Understanding the Mechanisms of Stress Corrosion Cracking

Karen Kruska

Linacre College

Oxford University

A thesis submitted for the degree of Doctor of Philosophy

Department of Materials Trinity Term 2012

A scientist in his laboratory is not a mere technician:
He is also a child confronting natural phenomena that impress him
as though they were fairy tales.
Marie Curie

Für Mama und Papa.

Abstract

Austenitic stainless steels are frequently used in the cooling circuits of nuclear reactors. It has been found that cold-worked 304 stainless steels can be particularly susceptible to stress corrosion cracking at the operating conditions of such reactors. Despite more than 130 years of research underlying mechanisms are still not properly understood. For this reason, the effects of cold-work and applied stress on the oxidation behaviour of 304SS have been studied in this thesis.

A set of samples with/without prior cold-work, and with/without stress applied during oxidation, were oxidized in autoclaves under simulated pressurised water reactor primary circuit conditions. Atom-probe tomography and analytical transmission electron microscopy were used to investigate the local chemistry and microstructure in the different samples tested. Regions containing grain boundaries, deformation bands, and matrix material in contact with the environment, were extracted from the coupon specimens with a focused ion beam machine. Cross-sections of crack tips were studied with secondary ion mass spectrometry and electron backscatter diffraction. The compositions of oxides grown along the surface and the different microstructural features were analysed. Fe-rich spinels were found at the surface and Cr-rich spinels were observed along fast diffusion paths. Ni-enrichment was found at the metal/oxide interfaces and a Ni-rich phase was detected in precipitates ahead of grain boundary oxides. Li was observed in all oxidised regions and B segregation, originating from impurities in the alloy, was observed in grain boundaries and crack tip oxides. Cavities and hydrogen associated with Ni-rich regions were found ahead of the bulk Cr-rich oxide in some of the samples.

The implications of these findings for the understanding of SCC mechanisms are discussed. It is suggested that Ni precipitation as well as the presence of deformation bands may play an important role in controlling SCC susceptibility in 304 stainless steel. A modification of the film-rupture model including internal oxidation and fast diffusion along H-stabilised vacancies in strain fields at the crack front is proposed.

Preface

This thesis is an account of the work carried out by the author in the Department of Materials, University of Oxford, under the supervison of Dr S Lozano-Perez, Dr D W Saxey and Prof G D W Smith.

No part of this thesis has been previously submitted for a degree at this or any other university. The work of other authors has been freely drawn upon and is duly acknowledged in the text. A list of cited references is given at the end of this thesis.

Some of the work described in the thesis has been presented in the following publications and conferences:

Papers

K Kruska, S Lozano-Perez, D W Saxey, T Terachi, T Yamada and G D W Smith, *Selective grain boundary oxidation in cold- worked stainless steels: chemical characterisation at the nanoscale*, **Submitted for publication in Corrosion Science**.

S Lozano-Perez, K Kruska, I Iyengar, T Terachi and T Yamada, *The role of cold work and applied stress on surface oxidation of 304 stainless steel*, **Accepted for publication in Corrosion Science**.

S Lozano-Perez, K Kruska, T Terachi and T Yamada, *Understanding surface oxidation in stainless steels through 3D FIB sequential sectioning*, **Accepted for publication in Journal of Physics: Conference Series (JPCS), (EMAG 2011 6-9th September 2011, Birmingham)**.

K Kruska, S Lozano-Perez, D W Saxey, T Terachi, T Yamada and G D W Smith, *3D Atom-Probe Characterization of Stress and Cold-Work in Stress Corrosion Cracking of 304 Stainless Steel*, **Proceedings of the 15th International Conference on Environmental Degradation of Materials in Nuclear Power Systems - Water Reactors**, J T Busby, G Ilevbare, Peter Andresen (Eds.), pp 939 - 946 (August 7-11 2011, Cheyenne Mountain Resort, Colorado Springs, Colorado, USA).

S Lozano-Perez, N Ni, K Kruska, C Grovenor, T Terachi and T Yamada, *Characterizing*

environmental degradation in PWRs by 3D FIB sequential sectioning, **Proceedings of the 15th International Conference on Environmental Degradation of Materials in Nuclear Power Systems - Water Reactors**, J T Busby, G Ilevbare, Peter Andresen (Eds.), pp 993 - 1004 (August 7-11 2011, Cheyenne Mountain Resort, Colorado Springs, Colorado, USA).

S Lozano-Perez, N Ni, K Kruska, T Terachi and T Yamada, *FIB sequential sectioning as a tool to understand environmental materials degradation in 3D*, **INSS Journal 17** (2010), pp 188-199.

Conference presentations (where no proceedings were published)

K Kruska, D W Saxey, G D W Smith, T Terachi, T Yamada and S Lozano-Perez, *Atom-probe tomography of grain boundary oxides in stressed and cold-worked 304 stainless steel*, **DPG Spring meeting 2012**, Berlin, German, 25th - 31st of April 2012.

K Kruska, S Lozano-Perez, D W Saxey, T Terachi, T Yamada and G D W Smith, *High-resolution analytical characterization of stress corrosion cracking in stainless steels*, **EUROMAT 2011**, Montpellier, France, 7th - 11th September 2011.

K Kruska, S Lozano-Perez, D W Saxey, T Terachi, T Yamada and G D W Smith, *Influence of Stress and Cold Work on Stainless Steel Grain Boundary Oxidation Investigated by Electron Microscopy and Atom-Probe Tomography*, **8th International Conference on Microscopy of Oxidation**, Liverpool, UK, 11th -13th April 2011.

K Kruska, S Lozano-Perez, D W Saxey, T Terachi, T Yamada and G D W Smith, *Influence of Stress and Cold work on Stainless Steel Grain Boundary Oxidation Investigated by Electron Microscopy and Atom-Probe Tomography*, **Microscience 2010**, London, UK, 28th June - 1st July 2010.

Funding

This project was funded by the Institute of Nuclear Safety Systems Inc., 64 Sata, Mikata-gun, Fukui, 919-1205, Japan.
Further funding was obtained from The Worshipful Company of Armourers and Brasiers (Travel Grant) and Linacre College (Travel Grant).

Acknowledgments

The completion of this thesis would have been impossible without the help and support of a number of people. At first and foremost I would like to thank my supervisors. I am grateful to George Smith for believing in me and securing funding for me at the start of this project. Thank you for your unfailing advice whenever I was stuck and the phase diagrams from the British Library. I would like to thank David Saxey for teaching me everything about the LEAP. Thank you for spending days training me on the NVision FIB, for your on-going support and your valuable comments on all my work despite your move to Perth. Particularly I want to thank Sergio Lozano-Perez for being my supervisor, mentor and friend. Thank you for sacrificing your evenings to teach me on using the TEM, for trusting me to present our work in front of the community and for reading all my work in record times.

I would also like to thank my college advisor Victor Burlakov for the support throughout my DPhil, although you changed your working place twice. I thank you for caring and asking and for all the wonderful dinners.

I am grateful to the EM & technical support group for their help with the microscopes, namely S Lett, G Hughes, R Doole, C Salter, C Hetherington and G Chapman.

I thank Ben Britton for his help with EBSD techniques and strain analysis, Katie Moore for her help with the NanoSIMS and Ilya Iyengar for the FIB/SEM data reconstructions.

I wish to thank TMS and J T Busby, G Ilevbare and P L Andresen for organising the Environmental Degradation meeting in Colorado Springs that inspired me and remotivated me. Also thanks to Dan Schreiber for useful facebook discussions on range files and for showing me, how to create a proper line profile.

I would like to thank my parents Bärbel Kruska and Jürgen Haaren-Kruska for their endless unconditional support. Thank you, for providing a loving home I could return to whenever I needed to rest and believing in my dreams and trusting my decisions.

I would like to thank my colleagues from the Nanoanalysis and Atom-Probe Groups for the great working environment: Na, Haibo, Sean, Andy, Kate, Chris, Joven, Dan, Tong, Rong, Paul S, Alan, Hiroto, Phil and Paul B. In PARTICULAR I thank Dan Haley for

solving all my small IT problems, for InkScape, crack attack and group climbing. Thank you for proof reading my thesis, for driving me nuts, fighting back and always coming to the pub. ESPECIALLY I would like to thank Ceri Williams for always being there, sharing my love for sports, science and social events. For 35p cake and luxury gateaux. For 1001 cups of tea and as many chats. For the gossip, group croquet and group squash. For kicking my .. and shutting me up. Thank you for being such a great friend.

I am grateful to all the students/post-docs from the coffee list - Nick R, Nick G, Katie, Ben, Doug, Jenni, Susi, Claire, John and Dave - for good advice in hard times and light-hearted chat in good times. Especially I thank Stella Pedrazzini for girly nights in or out, SitC, pizza and ice cream.

Furthermore there are many old friends and new friends in Oxford, who supported me and kept me sane. Everyone from the judo club, particularly Amy, Vitek and Brad; Adam and Ash, Stu and Max from Linacre. I thank Quentin, Salva, Margreet and Tom for their friendship, gymming and dinner parties; Birte, who came from home; everyone at NOOC. I thank Shu-Ting Lee, my bouncy friend, who always had an open ear, some chocolate and a cup of tea for me, even at 3 am in the morning and Kate Ryan, my best friend and house mate, for walking, cycling, dancing, flamingos, alpacas and red wine.

Finally, I thank INSS (Japan) and in particular Takuyo Yamada and Takumi Terachi for providing the samples and funding and for the useful discussions at our annual meetings in Tsuruga.

Glossary

ADF	Annular Dark Field
AES	Auger Electron Spectroscopy
AISM	Adsorption Induced Slip Mechanism
appm	atomic parts per million
APT	Atom-Probe Tomography
ASM	American Society of Metals
ATEM	Analytical Transmission Electron Microscope/y
BF	Bright Field
BWR	Boiling Water Reactor
CGR	Crack Growth Rate
CERT	Constant Extension Rate Testing
CL	Constant Load
CSL	Coincident Site Lattice
CT	Compact Tension
CW	Cold-Work
DB	Deformation Band
DF	Dark Field
EBSD	Electron BackScatter Diffraction
EDS	Energy Dispersive X-ray Spectrometer
EDX	Energy Dispersive X-ray Spectroscopy
EELS	Electron Energy Loss Spectroscopy
EIR	Effective Ionic Radius
EM	Electron Microscope/y
ESCA	Electron Spectroscopy for Chemical Analysis
FE	Finite Element
FEG	Field Emission Gun
FFT	Fast-Fourier Transformation
FIB	Focussed Ion Beam
FICM	Film-Induced Cleavage Model
FRM	Film-Rupture Model
FWHM	Full Width at Half Maximum
GB	Grain Boundary
GIF	Gatan Imaging Filter
GND	Geometrically Necessary Dislocation

HAADF	High-Angle Annular Dark Field
HAC	Hydrogen Assisted Cracking
HE	Hydrogen Embrittlement
HELP	Hydrogen-Enhanced Local Plasticity
HT	High Tension
IG	InterGranular
IGSCC	InterGranular Stress Corrosion Cracking
IPF	Inverse Pole Figure
IQ	Image Quality
LEAP	Local-Electrode Atom-Probe
MAE	Mean Angular Errors
MCP	MicroChannel Plate
MSA	Multivariate Statistical Analysis
MVC	MicroVoid Coalescence
NanoSIMS	Nano Secondary Ion Mass Spectrometry
ND	Normal Direction
PWR	Pressurised Water Reactor
QC	Quasi Cleavage
RD	Rolling Direction
ROI	Region Of Interest
SCC	Stress Corrosion Cracking
SE	Secondary Electron
SHE	Standard Hydrogen Electrode
SMM	Surface Mobility Model
SS	Stainless Steels
SSRT	Slow Strain Rate Test
STEM	Scanning Transmission Electron Microscope/y
TCW	Tensile Cold-work
TD	Transverse Direction
TG	Transgranular
TDB	Twin Deformation Band
ToF	Time of Flight
VOI	Volume of Interest
ZLP	Zero Loss Peak

Contents

Abstract I
Preface III
Acknowledgments V
Glossary VII

1 Introduction **1**
1.1 Stress Corrosion Cracking in the Nuclear Industry 1

2 Literature **5**
2.1 Historical Introduction to Stress Corrosion Cracking 5
2.2 Suggested Models 7
2.2.1 The film-rupture model 8
2.2.2 The film-induced cleavage model 10
2.2.3 The surface mobility model 11
2.2.4 The role of hydrogen 12
2.2.5 Internal Oxidation 18
2.2.6 Recent developments 19
2.3 Influence of internal stress/ cold work 19
2.4 Experimental Approaches 22
2.4.1 Mechanical testing 22
2.4.2 Crack Growth Rate Measurements 24
2.4.3 Introduction to the microstructure of oxides formed 26
2.4.4 Sample preparation 27
2.4.5 Analytical methods 29
2.5 Summary and Research Objective 36

3 Experimental Methods **39**
3.1 Material 39
3.2 Corrosion tests 40
3.3 Optical Microscopy 41
3.4 Electron Microscopy (EM) 42
3.4.1 Historical Introduction 42
3.4.2 Electron Scattering 43
3.5 Scanning Electron Microscopy (SEM) 44
3.5.1 Secondary Electron Imaging 44

3.5.2 Electron Backscatter Diffraction . . . 45
3.6 Focussed Ion Beam Milling . . . 47
3.6.1 Introduction . . . 47
3.6.2 FIB-SEM Tomography/ 3D FIB-slicing . . . 48
3.7 Sample preparation with the FIB . . . 50
3.8 Analytical Transmission Electron Microscopy . . . 52
3.8.1 TEM BF/DF imaging . . . 53
3.8.2 Scanning Transmission Electron Microscopy . . . 54
3.8.3 Electron Energy Loss Spectrometry . . . 55
3.8.4 Elemental mapping - Energy filtered TEM . . . 57
3.8.5 The Microscopes . . . 58
3.9 Atom-Probe Tomography . . . 60
3.9.1 Historical introduction . . . 60
3.9.2 The Local-Electrode Atom-Probe . . . 62

4 Surface and Grain Boundary Oxidation 65
4.1 Results . . . 65
4.1.1 No stress/no cold-work . . . 67
4.1.2 Stress/no cold-work . . . 79
4.1.3 No stress/cold-work . . . 86
4.1.4 Stress/cold-work . . . 97
4.2 Discussion . . . 101
4.2.1 Comments on experimental technique . . . 101
4.2.2 No stress/no cold-work . . . 105
4.2.3 The influence of cold-work . . . 108
4.2.4 Oxidation under stress . . . 111
4.2.5 GB oxidation . . . 114
4.2.6 The role of lithium and boron . . . 116
4.2.7 The role of Ni enrichment ahead of GB oxides . . . 117

5 Deformation Band Oxidation 125
5.1 Results . . . 127
5.2 Discussion . . . 131

6 The Role of Hydrogen 139
6.1 Results . . . 139
6.2 Discussion . . . 145

7 Ideas towards an SCC mechanism 147

8 Crack Tip Analysis 155
8.1 Preliminary Results . . . 155
8.1.1 Electron Backscatter Diffraction and strain analysis . . . 155
8.1.2 NanoSIMS . . . 160

8.2 Discussion 165

9 Conclusions **167**
9.1 New experimental approaches 167
9.2 Implications for SCC mechanisms 168

10 Suggestions for Future Work **171**

A EBSD strain mapping data quality maps **175**
A.1 5 % cold-work sample 175
A.2 10 % cold-work sample 176
A.3 20 % cold-work sample 176

B Colour Code for Ions in APT Ion maps **177**
References 179

Chapter 1

Introduction

1.1 Stress Corrosion Cracking in the Nuclear Industry

In recent years the signs of global warming became increasingly apparent [1, 2]. A heated debate arose amongst scientists and politicians about the extent of human influence upon the problem [3–6]. In contrast to coal, oil and gas, nuclear power plants do not emit huge amounts of CO_2 in producing electrical energy. This is why, despite all the problems with nuclear waste and the fear of radioactive contamination of the environment or catastrophic accidents, nuclear power seems to be at least the short-term solution to secure the world's energy demand and reducing carbon output at the same time. Since the infamous reactor explosion in Chernobyl, Ukraine, in 1986 (which was caused by human error), people are more aware of the dangers connected with nuclear power and many are uncomfortable with this source of energy. Improved reactor set ups with extensive safety systems have been developed and even more reactors have been put into operation in the decades after the accident. In the absence of further disastrous failures the resistance died down and the trust in nuclear energy had slowly started to grow until the recent 2011 accident following an earthquake in Fukushima, Japan, refueled the nuclear debate and the public confidence in nuclear safety was shaken again. All these factors make it critical to eliminate every possibility of materials failure and create systems as safe and reliable as possible, so that nuclear power is to be a tool in combating climate change.

In December 2012 there were 441 nuclear reactors operating in the world [7]. The most common types of reactor are the pressurised water reactor (PWR) (see Figure 1.1) and the boiling water reactor (BWR). These systems were initially designed to operate for up

to 40 years although possible extensions to 60 years are now being considered in many cases [8, 9]. These time spans are much longer than in most other industries and so long-term operating experience is really only now being gained as power plants reach ages of 30 to 40 years. The materials in these systems are exposed to very high pressures and temperatures in aqueous environment and it is not surprising that corrosion-related failures occur [8]. One potentially hazardous corrosion-related problem is Stress Corrosion Cracking (SCC).

"SCC is a time-dependent process in which a metallurgical susceptible material fractures prematurely due to synergistic interaction of a corrosive environment and sustained tensile stress at the metal surface (see Figure 1.2). The tensile stress may be residual stress resulting from heat treatment or fabrication of the metal, it may be developed by external loading or a combination of these conditions [10]."

Modern nuclear reactors operate at temperatures between about 280°C and 340°C with different water chemistries [8]. PWR water is alkali treated and mostly oxygen-free, with the primary circuit also containing about 3 ppm of dissolved hydrogen to suppress water radiolysis [8]. While SCC in Ni alloys was observed frequently and has been researched for a long time, stainless steels were believed to be resistant against this form of corrosion under these conditions. Only in the last decade susceptibility of cold-worked stainless steel to SCC under PWR primary water conditions was predicted. The first SCC failure in this type of material was reported at almost the same time [8].

In PWRs corrosion and InterGranular Stress Corrosion Cracking (IGSCC), in particular, can for instance lead to steam generator tube failures. These tube problems may force most PWRs to replace their existing steam generators well before their design lifetime [12]. Other components affected by SCC within PWRs include steam turbines, reactor core internals, jet pump beams and feedwater nozzles [12]. It is not only the replacement of the failed components that causes enormous costs, but also the outage time of the reactors. This is why materials degradation has been troubling the nuclear industry for many years and research in this area is very important [12, 13].

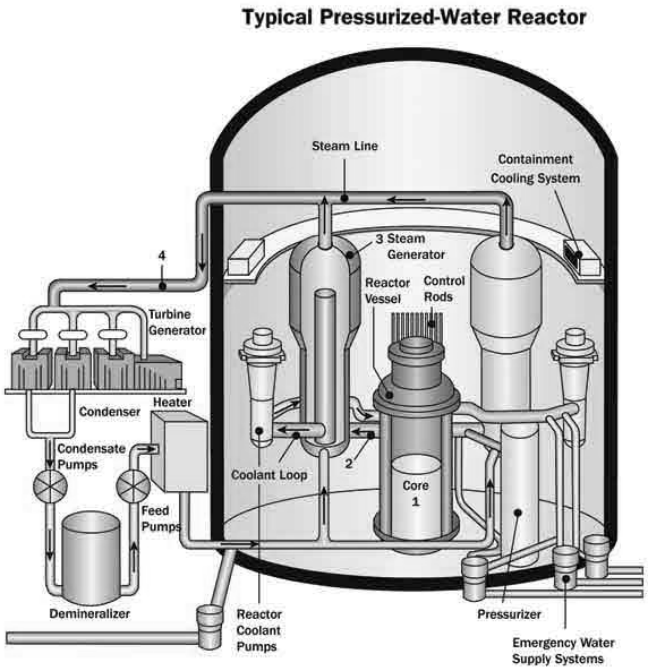

Figure 1.1: Schematic diagram of a PWR. In a typical commercial pressurised light-water reactor the reactor core (1) generates heat. Pressurised-water in the primary coolant loop (2) carries the heat to the steam generator (3) inside which heat from the primary coolant loop vaporises the water in a secondary loop producing steam. The steam line (4) directs the steam to the main turbine where it turns the turbine generator, which produces electricity [11].

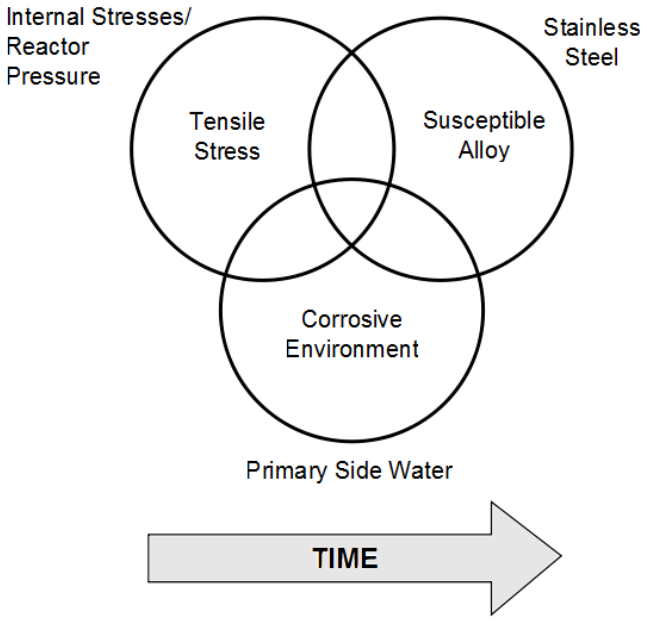

Figure 1.2: Conditions necessary for Stress Corrosion Cracking

Chapter 2

Literature

This review starts with a brief overview of the history of SCC research and a discussion of the most popular SCC models to put the research conducted in this thesis in a wider context. The field of SCC is very broad and none of the current theoretical models can be generally applied to new systems. Many reports on experimental SCC research in a number of systems were published over the last 50 years. The scope of this review therefore predominantly includes experiments that were conducted on austenitic stainless steels under PWR primary water conditions, i.e. hydrogenated water with added boric acid and lithium at 280°C - 340°C. Results that are relevant for these systems and techniques that are new to the field and likely to lead to new findings in the future are also reviewed. Special attention is paid to the influence of cold-work on SCC.

2.1 Historical Introduction to Stress Corrosion Cracking

The reported research concerning SCC goes back to 1873 when W. H. Johnson discovered that the tensile strength and resistance to torsion of iron and steel decreased if they were exposed to strong hydrochloric acid or dilute sulphuric acid [14]. These first experiments presented to the Manchester Literary and Philosophical Society piqued the curiosity of Professor O. Reynolds, who decided to conduct a few experiments himself. Between 1873 and 1875, Johnson and Reynolds presented several papers suggesting that hydrogen absorption might cause this effect [15–20]. These were undoubtedly the first studies into stress corrosion cracking and Hydrogen Embrittlement (HE), even though these expressions only appear in the literature much later. Although it might only have

been an intangible suspicion of the dimension of the impact of their discoveries at the time, Reynolds was the first to predict the importance of the observed hydrogen effects in engineering [16].

Some publications in the initial period [21–24] reported on the stress corrosion susceptibility of iron and steels, however, the main focus of research in the beginning of the 20th century was on SCC in brass and Cu-Zn alloys. This was due to the severe problems that the then rapidly growing electric power industry experienced with cracking of brass condenser tubes. Furthermore, the British army detected similar cracks in brass cartridge cases especially during the monsoon season in tropical stations [25]. Some of these failures occurred in brass and magnesium-bronze bolts that had never been exposed to stress by external loading, which led to the discussion of the influence of cold-work and internal stresses on cracking [26, 27]. It was demonstrated in 1921 that SCC in brass could be avoided if internal stresses were reduced by heat treatment [28].

In the early years of SCC research the phenomenon was generally referred to as "season cracking" [29, 30]. Opinions differ on whether this term originates from the time of year in which cracking was most prevalent or that cracks were thought to be similar to those appearing in timber during seasoning. Bassett commented in 1918 that the term was misleading either way, as this type of fracture was always accompanied by corrosion. He suggested the term "corrosion cracking", which was at first only commonly used in the US [31]. Other scientists in the field were more skeptical about the extent to which corrosion influences "season cracking" [32, 33]. Rosenhain, for example, was certain, that "chemical action plays a part in the production of cracks, [...] [but that] this part is essentially that of accelerating the action", he believed that cracking would also occur without the influence of corrosion, just more slowly [33]. Nonetheless it was universally recognised in the 1940's that the role of corrosion was of major importance for the "season cracking" of Cu alloys. By 1945 the term "stress corrosion cracking" was widely established in the entire community [34]. The term "season cracking" continued to be used for the spontaneous cracking of internally-stressed brass [26].

From the late 1930's, research partly returned to (austenitic) stainless steels. A number of service failures had been encountered in austenitic chromium-nickel steels exposed to pressurised, wet ethyl chloride environments. Hodge and Miller reported that both intergranular and transgranular cracking had occurred in these cases [35]. A number of studies

in the following years reported that aqueous chloride solutions caused SCC in all common types of austenitic stainless steel [26].

In 1941 Dix was one of the first to suggest a general SCC mechanism. His idea was based on the electro-potential difference between grains and grain boundaries (GBs) [36]. Many different models and mechanisms, trying to explain SCC in various systems, were published from the 1950's onwards.

The nuclear industry became involved in SCC research in the 1960's when the first materials failures led to plant outages and started producing enormous costs. The first such SCC failure was at the Shippingport Atomic Power Station, USA in 1957 [37]. Early steam generators were tubed with 304 stainless steels, but due to the increasing number of failures during the first 10 years of operation, the stainless steels were exchanged for the more corrosion resistant Alloy 600 (72 wt.% Ni, 15.5 wt.%Cr, 8 wt.% Fe, 0.5 wt.% Si, 1 wt.% Mn, 0.15 wt.% C, 0.5 wt.% Cu, 0.015 wt.% S) [26]. Although using Alloy 600 the life-times of steam generators were much increased, cracking in steam generator tubes still caused most outages in PWRs. A major advance in the field was the replacement of Alloy 600 with Alloy 690 (60.65 wt.% Ni, 29.7 wt.%Cr, 8 wt.% Fe, 0.35 wt.% Si, 0.29 wt.% Mn, 0.022 wt.% C, 0.2 wt.% Cu, 0.001 wt.% S, 0.007 wt% P, 0.02 wt.% Mo, 0.01 wt.% Co, 0.2 wt.% Ti), another Ni alloy with a higher Cr content. Although, the greater SCC resistance of Alloy 690 to SCC was quickly established and agreed on, the reasons for its better performance in tests and application are still not well understood [38].

2.2 Suggested Models

Scientists have conducted a large number of experiments and tests on various materials under a wide range of conditions in an attempt to obtain a general understanding of the mechanism of SCC. However, due to the large number of parameters that influence SCC, including the electrochemical potential, pH, identity and concentration of dissolved species, alloy composition, alloy structure, temperature and stress [39], no general model that gives quantitative predictions, especially for new systems, has yet been proposed. The problem is even harder as the parameters listed above are not independent. Nominal models or correlations of two or three of the parameters listed above do exist in the literature [40]

but they are not adequate for reliable quantitative predictions [39]. The SCC models most dominant in the literature will be discussed in this section.

2.2.1 The film-rupture model

A model that has been present in the literature for many decades is the Film-Rupture Model (FRM). It is sometimes referred to as the slip-dissolution model or a combinations of both of these terms [41]. The general cracking scheme is illustrated in Figure 2.1. The passivating film consisting of corrosion products on the surface of the metal, is ruptured by the applied stress and unprotected metal is revealed. The newly exposed metal starts dissolving in the surrounding environment until a new passivating film has developed. This new film is ruptured again and a crack grows as the cycle repeats. The name "slip-dissolution" model accounts for the idea that film-rupture can occur due to displacement along a slip band. This is, however, not always the case, therefore Gutman suggests that the process described above should be called a film-rupture model "because brittle films can break (or not) at small strains before the yield of the base metal, and, on the other hand, preferable slip dissolution can develop without any films" [41]. This review will go with the term FRM, independent of the cited authors preferences. This term shall cover any case where a passivating film is ruptured to expose underlying metal.

In 1952 Logan [40] described the FRM as part of a generalised theory of stress corrosion suggested by Maers *et al.* [43]. He proposed that the corrosion is caused by an electrochemical mechanism and moves along anodic paths (such as GBs) in the more electronegative metal matrix; the corroded areas in the metal will lead to high stress concentrations in the oxide regions. If the attack is becoming deeper and the radius of the affected area decreases, the stress concentration is more localised and stresses are higher. Such highly localised stress conditions can cause the metal to tear apart; the fresh metal surfaces are even more anodic and cause an increase in current from the base of the corroded area to the unaffected surface [43].

The FRM is rather intuitive if a constant strain or loading rate is assumed, but it becomes more complicated if static loading and therefore a non-constant strain rate is considered [44]. It was Vermilyea [45] who first proposed that this issue can be overcome by considering dissolution at the crack tip to move the crack forward into the plastic strain field around the former crack tip, which causes plastic deformation, i.e. the crack opens

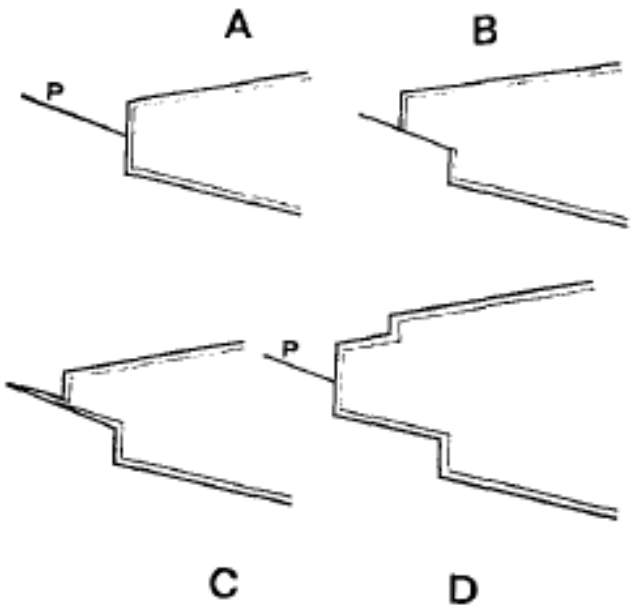

Figure 2.1: Schematic diagram of the sequence of events occurring at the tip of a propagating stress corrosion crack. (A) The tip of a crack. The surface is covered by a protective film. P is a slip plane. (B) The slip plane undergoes a shear and a new, reactive surface is created. (C) Corrosion attack occurs on the reactive surface while repassivation begins on the outer edge. (D) The crack flank repassivates after the corrosion attack. Together with plastic deformation, it has caused the crack to grow deeper into the material [42].

and generates a new strain field ahead the new crack tip. This means that the plastic deformation does not occur during the dissolution/repassivation stage but afterwards by a creep type mechanism. If this model is correct the stress corrosion cracks would grow in discrete steps. Vermilyea showed that his model gives good results for a 304-type stainless steel and a Mg alloy in certain environments [45].

In 1988 Andresen and Ford further reported that the FRM has been statistically validated for type 304 and 316 stainless steels, at least for the metallurgical and environmental conditions characteristic of light-water reactors [46]. This statement is supported by a number of earlier publications by these authors [47–50]. In 1982 Ford published a detailed diagram showing that the crack growth rate is proportional to the anodic current density which supports the FRM [51]. Nevertheless, the model has been criticised because the predicted anodic dissolution rates are not sufficiently high to account for the observed rates of crack propagation in some systems, including brass and austenitic stainless steels [52].

In the last two decades, various papers have been published trying to either simplify the model or introduce additional parameters [53–55]. Often the electrochemical part is considered in discrete stages (dissolution, passivation, film rupture, dissolution...) as suggested

by Vermilyea but the mechanical part is solved assuming a constant crack tip strain rate based on 'continuum' arguments from fracture mechanics [44]. Although this approach is less accurate than Vermilyea's original model, it is mathematically much more transparent and therefore, for example, supported by Lu and Shoji [56]. It was also shown [57] that, for the Vermilyea model, relatively large depths of corrosion are necessary in every film rupture cycle to obtain realistic plastic strain distributions ahead of the crack tip. These depths would also lead to much wider crack openings and more heavily corroded fracture surfaces, than experimentally observed. It was therefore concluded that the FRM model is not applicable for transgranular SCC [57] and the FRM became primarily associated with intergranular stress corrosion cracking (IGSCC) [58]. Gutman criticised that the FRM, although most of the experimental verifications are associated with IGSCC, does not contain any detail specific to intergranular corrosion [41]. Although Newman and Healey describe the FRM as a "relatively mature and successful attempt to rationalise the kinetics of SCC", they also point out that it does not apply to all systems [44].

In the last two years, Hall has published a few short papers evaluating the Shoji [59] and Ford-Andresen [60] models. He has also proposed his own model with a variable stress intensity factor [61]. Hall's ideas were used by Vankeerberghen *et al.* as a basis to model the propagation rates for 316SS in PWR conditions [62]. The authors concluded that, although their results are consistent with the published experimental data, they neither prove nor disprove the validity of the FRM mechanism. However, they still consider the model plausible and applicable to engineering calculations [62].

Gutman concludes in his paper from 2007 [41] that "experimental evidence and theoretical fundamentals suggest that a single mechanism cannot explain the entire range of stress corrosion processes, and creating new mechanisms is an endless process of their development and rejection [...]. It seems that the more realistic way today is to subdivide SCC into separate significant phenomena and to study these phenomena in the hope to use the results for stress corrosion prevention."

2.2.2 The film-induced cleavage model

The Film-Induced Cleavage Model (FICM) was developed more recently than the FRM. It was first proposed and described in detail by Sieradzki and Newman in 1985 [63], although the term film-induced cleavage is not mentioned in the paper. The model was first

developed to explain transgranular cracking and was later used to describe intergranular cracking in very ductile noble alloy systems [64]. It is therefore not particularly relevant for the system reviewed in this report but will briefly be described for completeness.
SCC in α-brass in cuprous ammonia solutions was shown to produce discontinuous, cleavage-like fracture surfaces [65]. The FICM attempts to explain the development of such surfaces as follows: A brittle layer of corrosion products such as oxides or chlorides forms on a material in a corrosive environment. If a crack that has developed in this brittle film grows at a high enough speed it can penetrate into the underlying substrate resulting in a cleavage-like fracture.

2.2.3 The surface mobility model

A rather different idea for an SCC model was put forward in 1987 by Galvele [66]. The proposed surface mobility model (SMM) is probably the most fiercely criticised model in the literature [67–69]. The model assumes that the corrosive environment increases surface mobility and that cracks grow due to the injection of surface vacancies at the highly stressed crack tip or by the emission of ad-atoms from the bottom of the crack [66] as illustrated in Figure 2.2.

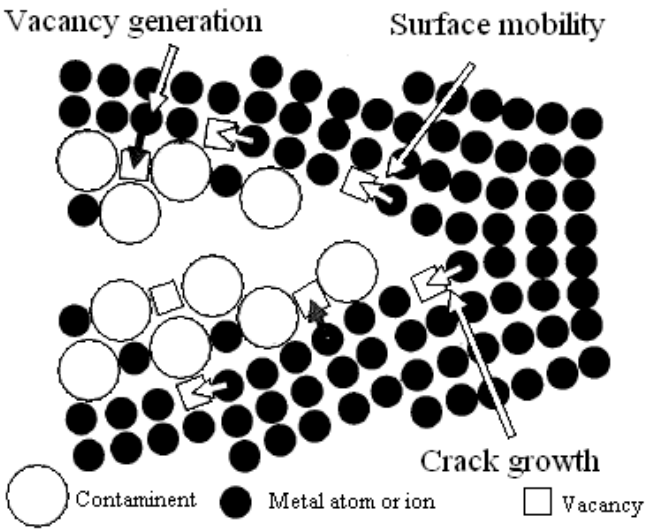

Figure 2.2: Crack propagation by surface mobility in the presence of an ionic contaminant [70].

Sieradzki and Friedersdorf [67] noted that there are a number of errors in Galevele's derivation of the surface mobility model and that it overestimates crack velocity by as much as 14 orders of magnitude. They also argue that while stress corrosion crack propagation

could, in principle, occur via a surface mobility like mechanism, the effects of other mechanisms suggested in the literature are more dominant. Galvele responded to their note [70] defending his original work by emphasising his point that stress corrosion cracking is not simply a mechanical phenomenon (like normal fracture) and that more attention must be drawn to the (electro-) chemical environment if a general model is to be developed. A few years later, Gutman published a comment on Galvele's reply [68] stating that Galvele failed to embrace the suggestions by Sieradzki and Friedersdorf and concluding that the whole model is "built on a contradictory base". He suggests subdividing the SCC process into separate phenomena at the crack tip and then studying these, but he does not give any specific details on how one might do this. Galvele again responded to these notes [71], repeating the points he made previously and giving examples where his model corresponds to experimental data. Galvele's SMM highlights the importance of electro-chemistry on developing a suitable SCC model.

2.2.4 The role of hydrogen

Johnson and Reynolds, the first to observe stress corrosion cracking, already attributed this type of materials failure to hydrogen inclusions [16,17]. In a lecture from 1959 Troiano commented that it was well-known that hydrogen can severely embrittle steel and other metals [72]. He also pointed out that the embrittlement is enhanced by slow strain-rates and elevated temperatures [72]. Shreir reported in a paper from 1970 that the embrittlement can either be caused by gaseous hydrogen (H_2), or in solution from $(H_3O)^+$ or H_2O [73]. He noted that the effects of delayed failure and HE have to be carefully distinguished from SCC. According to Shreir SCC is anodic dissolution moving along a favoured path. Therefore SCC can only occur, if the corrosion process

$$Fe \longrightarrow Fe^{+2} + 2e^- \tag{2.1}$$

is not stopped by a negative potential within the metal (cathodic protection). This negative potential, however, is exactly what causes hydrogen charging and and leads to HE [73]. In the box in Section 1.1 SCC was defined as the failure of materials in a corrosive environment exposed to tensile stress, where neither the environment nor the stress alone would cause failure. This definition includes Hydrogen Assisted Cracking (HAC). Lynch [74]

wrote in a report from 1988 that the similarities in appearance of HAC and SCC have led some workers to suggest that both processes occur by a common mechanism. Although this idea has not been widely accepted, Lynch believes that HAC and SCC follow the same "adsorption induced slip mechanism" (AISM).

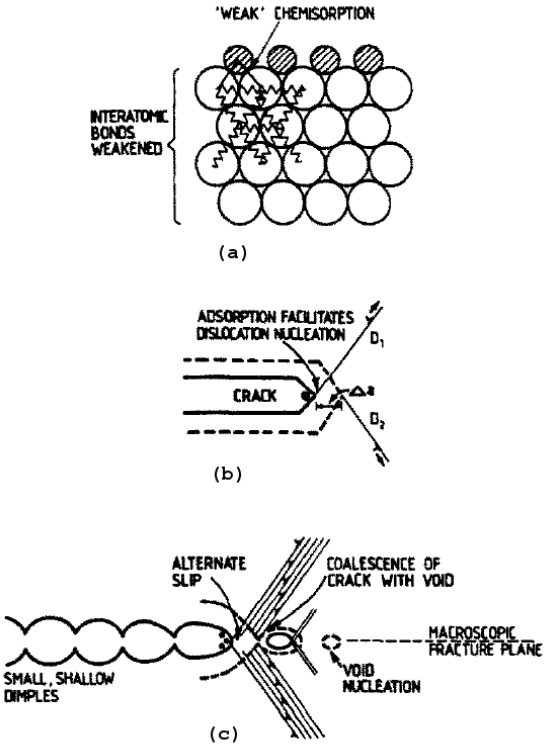

Figure 2.3: Schematic diagrams illustrating the adsorption-induced localised-slip process for environmentally assisted cracking. a) Adsorbed H weakens the bonds near the crack surface. b) The weak bonding facilitates the nucleation of dislocations. c) The crack is progresses by an alternate slip mechanism until the crack tip reaches a void [74].

Adsorption Induced Slip Mechanism

In ductile materials large strain fields ahead of the crack tip are produced by stress-activated dislocation sources ahead the crack tip (see Figure 2.3b). These strain fields produce voids ahead of the crack tip, which on joining up cause the crack to advance. In brittle materials higher stresses are necessary for extensive dislocation mobility to occur. Lynch suggests that hydrogen atoms are adsorbed to the crack surfaces near the crack tip after dissociation of hydrogen molecules, hydrogen-sulphide, or water molecules or after electrochemical reactions in an external environment. These adsorbed hydrogen atoms weaken inter-atomic bonds and give rise to higher dislocation activity in the crack tip

region. Strain fields are formed ahead of the crack due to dislocations nucleating at the crack tip, which will again lead to the growths of microvoids. The coalescence of these voids with the crack tip by an alternate slip mechanism will result in macroscopic crack growth of cleavage-like appearance. Lynch mainly bases this hypothesis on a number of studies of fracture surfaces. The appearance of larger and smaller dimples on the observed fracture surfaces complements the suggested model. Lynch emphasises in his conclusions that there are systems where adsorption is not responsible for HAC/SCC. In these cases Lynch supports the FRM reported above [74]. A very similar model was published in 2008 by Liu [75] and commented on by Lynch [76]. Lynch criticises that Liu ignored large parts of the previous literature and does not acknowledge his and other earlier work on the topic. He notes that Liu has redone some of the work Lynch published in his 1988 paper without analysing it as thoroughly [76].

The Troiano-Oriani Decohesion Hyposthesis and Variations

Barth and Steigerwald [77] report that Troiano suggested that hydrogen in the lattice can reduce the cohesive strength of the base metal bonds. They further reports that Troiano's model proposes that hydrogen atoms interact with the 3d electron shell of the metal atoms to lower their binding energy. If hydrogen concentrates in the regions of tensile stress ahead of the crack tip in sufficient quantity the weakened bonds between the metal atoms lead to an increase in crack growth. Hydrogen then diffuses to the new position of the crack front and the process is repeated. The mechanism was later referred to as the "Troiano-Oriani decohesion hypothesis" [78]. Chen *et al.* presented some data on Fe-Si single crystals, which was consistent with this mechanism [78]. Troiano and Oriani assumed that the cohesive force between atoms decreases linearly with a rising hydrogen concentration. Lee and Unger picked up on this approach and introduced a means of evaluating the cohesive force pointwise in relation to the hydrogen concentration in the "cohesive zone" [79]. Schneider *et al.* performed some finite element (FE) simulation supporting the decohesive model [80]. Raykar *et al.* recently published an improved model combining FE simulations with an analytical approach [81].

Although decohesion hypothesis was a promising approach, it could not be applied to material systems without voids experimentally observed ahead of the crack tip; this includes austenitic stainless steels at low temperature. Therefore, Magnin *et al.* developed a

model fitted to ductile fcc single phase materials, such as austenitic stainless steels [82,83]. They combined the decohesion hypothesis with an idea suggested by Jones in 1985 [52]. Because the rate of anodic dissolution in the FRM could not account for crack growth rates in some materials, Jones wrote: "Proportionality between crack velocity and anodic dissolution of a straining electrode does not guarantee that the crack actually grows by anodic dissolution. Instead, anodic dissolution may control some subsequent consecutive process which actually causes the fracture" [52]. Because of the appearance of fracture surfaces, Jones suggested introducing a brittle element instead of electrochemical dissolution to the FRM mechanism. Magnin *et al.* incorporated this idea to the decohesion hypothesis; they assume that dislocations moving in the decohesive zone pile up at the interface to the surrounding material. The high stresses at the dislocation pile-ups cause cracking. Magnin's model is illustrated in Figure 2.4. The model is further developed in [84] and supported by experiments on a 316 type stainless steel.

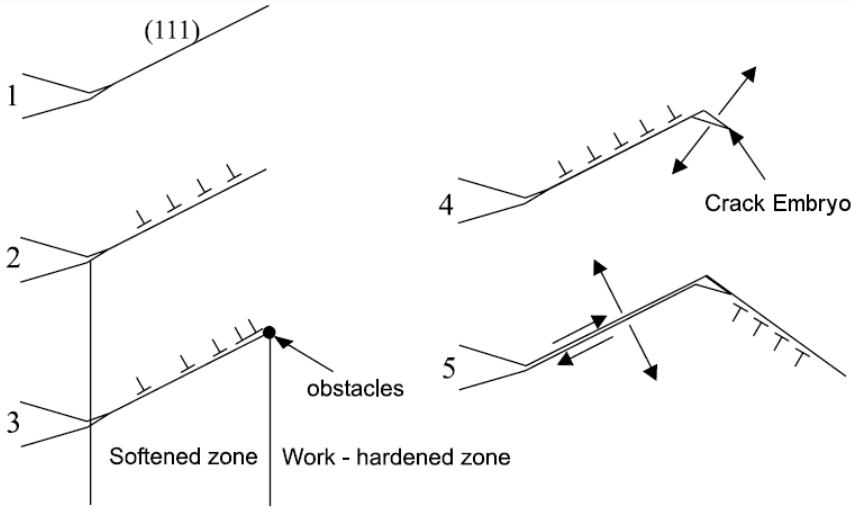

Figure 2.4: The steps of the corrosion enhanced plasticity model by Magnin *et al.* (1) The (111) slip planes are activated at the very crack tip. (2) Anodic dissolution causes vacancy production and hydrogen absorption in (111) planes. This leads to more mobile dislocations and a locally enhanced plasticity in the crack tip region. (3) When the dislocations pile up at obstacles at the edge of the more plastic region, they create a high local stress concentration. (4) If the critical stress intensity is reached a crack embryo will form. This is even more likely, if the critical stress intensity is lowered by hydrogen absorption in the (111) plane. (5) Hydrogen lowers the cohesion energy of the (111) microfacets and the stress normal to these facets can be sufficient to open the crack along the (111) plane. Dislocations are emitted on a plane symmetrical to the crack plane, shielding the new crack tip [82].

Hydrogen-Enhanced Local Plasticity

A mechanism first suggested by Beachem and based on detailed analysis of fracture surfaces of 4 different ferritic steels [85]. The mechanism is based on four interactions between hydrogen and steel [85]:

1. Evolving hydrogen enters the metal matrix at growing crack tips.
2. Molecular hydrogen dissociates at clean deforming surfaces and subsequently diffuses into the metal matrix [86].
3. Hydrogen migrates to regions of higher triaxial tensile stresses [72, 87].
4. Dissolved hydrogen aides the deformation of the ferrite matrix (in mild steels) [88,89].

It had been previously reported that the pH of crack tip solutions during "freely corroding" SCC experiments is approximately 3.5 regardless of the pH of the bulk solution [90–92]. This pH favours the evolution of hydrogen, which supports the existence of interaction 1. Interactions 2, 3 and 4 are backed up by the literature as indicated. Beachem suggests that hydrogen diffuses into the lattice ahead of the crack tip and aids whichever type of deformation the matrix will allow. The stress intensity factor and the hydrogen concentration in solution at the crack tip will determine, if MicroVoid Coalescence (MVC), quasi cleavage (QC) or InterGranular (IG) fracture occur [85]. A sketch of the suggested mechanism is shown in Figure 2.5. For case (a), a large K causes a large zone of plastic

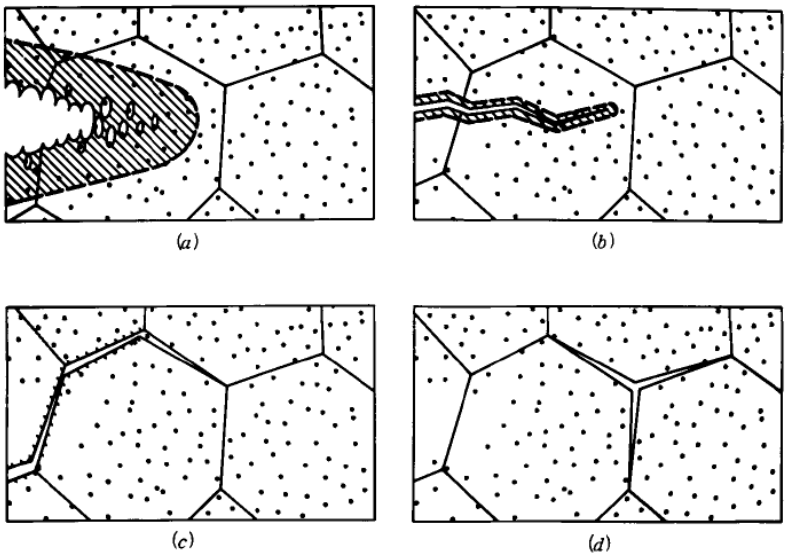

Figure 2.5: Sketches of microscopic fracture modes observed as a function of decreasing stress intensity factor K from high in a) to very low in d) [85].

deformation at the crack tip at sufficient hydrogen level. The plastic zone is big enough to include numerous inclusions that act as void nuclei and the resulting fracture mode is MVC. K decreases with the crack length and so does the plastic zone in case (b). It does not contain many inclusions that lead to void formation, but is still extended enough to allow QC. At still longer crack lengths and lower K further crack growth occurs by IG fracture in case (c). If K is insufficient to cause crack growth by any of these mechanisms, further cracking can occur only if hydrogen diffuses into the metal and segregates to GBs or other extended defects in high enough concentration to weaken the GBs and cause IG fracture in case (d). The crack growth rates are much lower at low K, so the time for hydrogen diffusion is longer and higher concentrations and therefore higher GB plasticity can be achieved [85]. This mechanism was in later years mostly promoted by Birnbaum and coworkers at Illinois University [93–97]. In recent work [98] they present a high-resolution study of fracture surfaces of steels tested under hydrogen gas pressure. TEM cross sections reveal an extremely high dislocation density in the entire sample. As the sample history is not thoroughly described in the publication and no uncharged material was examined, it remains unclear to what extent the dislocations are caused by hydrogen. Apparently, a reduction in fracture toughness was observed compared to hydrogen poorer conditions. It is argued, that the continuous dislocation density and the microscopically rough fracture surfaces rule out a decohesive mechanism. However, the presented micrographs show a dark layer about 50 nm wide near the fracture surface, which is not mentioned in the paper and could relate to a higher dislocation density region.

A recent paper by Barnoush and Vehoff [99] presents a thorough study of in-situ electrochemical nano-indents in a number of materials, including Ni. They observe an earlier onset of dislocation nucleation or motion in hydrogen-charged materials, which is consistent with molecular dynamics simulations by Wen *et al.* [100]. Both papers conclude that their results neither confirm the Hydrogen-Enhanced Local Plasticity (HELP) mechanism as presented by Birnbaum in [95] nor an adsorption-type mechanism as suggested by Lynch [74]. They agree, however, that the process of HE is controlled by a decrease in the defect formation energy and the interatomic bonding energy and suggest a hydrogen-enhanced decohesion mechanism based on the model suggested by Troiano [72].

2.2.5 Internal Oxidation

In 1993 Scott and Le Calvar reviewed experimental data for SCC in Ni and Ni-base alloys and found it "difficult to reconcile conventional ideas of film rupture/anodic dissolution or hydrogen embrittlement with either the influence of corrosion potential or the high activation energy" [101]. This led them to suggest a diffusion-controlled internal oxidation mechanism as traditionally associated with high-temperature corrosion [102]. Internal oxidation means that less noble alloying elements are oxidised, while the balance (in the discussed case the Ni) remains metallic. Scott and Le Calvar argue that such a mechanism is particularly important for Ni-based alloys in atmospheres with low partial pressures of O as the Ni/NiO equilibrium is at a higher potential then the respective equilibria of typical alloying elements. They suggest that grain boundary embrittlement could be controlled by

1. gas bubble formation (CO/CO_2)
2. internal oxide formation or
3. formation of a layer of O atoms at the GBs.

Rebak and Szklarska-Smialowska criticise that in the equation provided for the first case the CGR is proportional to the stress intensity factor at the crack tip and the predicted CGR are too high [103]. In the other cases Scott and Le Calvar assume oxygen diffusion rates which are not stress dependent and consequently obtain stress independent CGRs. The CGRs predicted, if it is assumed that O diffuses into the GB without oxidising all the Cr along the GB, are in reasonable agreement with experimentally observed CGRs in Alloy 600 [101]. Thomas and Bruemmer found fine scale oxides along GBs at the crack path in a TEM study supporting the internal oxidation mechanism [104]. Due to the fact that the major component of an alloy needs to be more noble than the main alloying elements to allow for internal oxidation in the classical sense, this mechanism was almost exclusively associated with Alloy 600.

Although a number of elaborate models have been suggested there is still no unified solution. McEvily and Le May commented in 1991 that it is very possible that there is no single mechanism for HAC/SCC, but that one or the other might be more appropriate in a given situation, or that in fact a combination of the mechanisms applies [105].

2.2.6 Recent developments

Stress corrosion cracking has many facets depending on the system, but also on the scale on which it is looked at. For example, if a tube or bolt failed, fracture surfaces are exposed. These can be examined with the naked eye, under an optical microscope or an electron microscope [74, 98]. The cross sections of progressing or matured cracks can be examined at different levels of detail, too. In addition to structural analysis, it is possible to analyse the local chemical composition, electrochemical potentials and the propagation speed with increasing accuracy. What is learned about the microscopic processes in a crack or at a crack tip can help the design of large-scale material systems for engineering applications. In other words, stress corrosion cracking is a multiscale problem [39, 84]. Staehle has reviewed the available analytical transmission electron microscopy (ATEM) studies in the field, and has found that it is again necessary to change the scale of SCC research. As crack tips have been found to be only a few nm in diameter he suggests a "paradigm shift" in considering the mechanics of SCC. These cracks are so narrow that they cannot be treated on a continuum basis, but must be looked at on an atomic level [39].

2.3 Influence of internal stress/ cold work

The models reviewed above tried to accommodate the effects of chemistry (corrosion, dissolution) or applied tensile stress (deformation, fracture) or both. In chloride solutions at elevated temperature, the small residual stresses are sufficient to cause SCC in austenitic stainless steels [52, 106]. This environment is quite aggressive and cracking is probably driven by an FRM anodic dissolution type mechanism where stresses hinder passivation and lead to crack opening. In the less corrosive PWR primary water environment, austenitic stainless steels were, until recently, believed to be resistant to SCC [107].

The reason why SCC often leads to unexpected and therefore disastrous failures is that cracks subtly grow over longer periods of time in less corrosive environments. Cold-working, i.e. plastic deformation at low temperature, causes displacement, mostly along slip planes resulting in the formation of twin deformation bands. It also induces additional dislocations in the material and increases its hardness. Irradiation with neutrons or ions also simultaneously changes the microstructure in several ways and can induce dislocation loops, voids, segregation and hardening [108]. The higher the density of dislocations, the

more energy is needed to move them or create new ones; and thus, the harder the material. The dislocations accommodate tension that cannot be stored in the crystal lattice via relatively minor variations in the bonding lengths. This type of tension stored in the lattice and defects is commonly referred to as internal stress. Just like an externally applied load it can cause stress corrosion cracking. This is why many studies on austenitic stainless steel consider cold-worked [109–113] or irradiated [108, 114, 115] samples, which can be susceptible to SCC PWR primary water conditions.

Dislocations introduced by cold-work can be removed by heat treatment and recrystallisation of the material. This can also happen "accidentally" and uncontrolled for example in the heat affected zone during welding. There are many publications concerning these "sensitised" materials [116–120]. The sensitisation causes Cr carbide formation and therefore Cr depletion at the the GBs. The decrease of the Cr content locally increases the general corrosion susceptibility and leads to a much more rapid failure especially in oxidising environments. The mechanism is different from that of unsensitised steels as studied in this thesis and will therefore not be further discussed. Irradiation changes the microstructure in several ways and the irradiation dose has major effects on the SCC susceptibility [114]. The interactions of these processes are very difficult to quantify and great efforts are undertaken to improve understanding [115]. However, the effects of radiation are not relevant to the work undertaken in this thesis and will therefore not be further discussed.

Any form of deformation at low temperature leads to the formation of slip bands, dislocations and induces internal stress. To characterise the effects of cold deformation or cold-work, steels are commonly rolled to obtain a uniform reduction in thickness. The defects created are strongly dependent on the rolling direction. A steel described to be with 20% cold-work was cold-rolled to 80% of its original thickness.

That cold-work and internal stress have an effect on SCC behaviour has been known nearly as long as SCC itself. A number of reports on this topic from the early 20th century are mentioned in a 1921 article on failure mechanism of metals caused by internal stress [27]. At about 300°C, cold-work was identified to increase crack growth rates and reduce the estimated crack initiation time for austenitic stainless steels in oxygenated water, but the electrochemical potential at the surface of these steels is considerably lower in hydrogenated PWR conditions. As it falls significantly below the critical potential for SCC initiation, austenitic stainless steels are widely used in PWRs [121]. However, in the last

decade, a limited number of cases of IGSCC have been detected in components of French PWRs [122]. Furthermore, two publications by Szklarska-Smialowska show that severely cold-worked austenitic stainless steel specimen are susceptible to SCC in a Slow Strain Rate Test (SSRT) (see Section 2.4.1) [123, 124]. Raquet *et al.* [121] also found a strong susceptibility for SCC in heavily cold worked austenitic stainless steels in hydrogenated primary water typical of PWRs. The susceptibility to cracking increased with increasing level of cold-work and/or localisation of deformation. The amounts of cold-work applied in the study were high compared to cold-work levels commonly encountered in PWRs. However, surface-near defects from grinding or deformation due to improper manufacturing could lead to locally high levels of cold-work in some components. It was also shown that the presence of significant triaxiality of stress promotes cracking. Crack initiation was observed under static and dynamic loading but in the static case no propagation occurred. Under dynamic deformation conditions (SSRT, cyclic loading) the cold-worked austenitic stainless steels showed SCC susceptibility (cf. section 2.4.1). A recent study by Terachi *et al.* compares the results from 53 cold-worked CT specimens (316SS and 304SS) (and further specimens reported in the literature) and developed an empirical formal to calculate the crack growth rate $\frac{da}{dt}$ in dependence of the yield strength at the testing temperature σ_y and the apparent stress intesity factor K_a [125]:

$$\frac{da}{dt} = 9.5 \times 10^{-10} \times \sigma_y^{2.9} \times K_a^{1.0} \times \exp \frac{-84 \times 10^3}{RT} \tag{2.2}$$

where R is the gas constant and T the absolute testing temperature. This formula however is only valid in a temperature range beween 250 °C - 320 °C. As testing was only performed in the T-S direction and cracking was branched, the authors warn that precise prediction of CGRs for operating plants is not possible. Further more Terachi *et al.* report increasing crack growth rates with increasing CW level. CGRs at 320 °C increased from $\sim 1.5 \times 10^{-8}$ mm/s in specimens with 5% CW to $\sim 1.1 \times 10^{-7}$ mm/s in specimens with 20% CW [125]. Tribouilloy *et al.* performed tensile cold-working (TCW) and cold-rolling on austenitic stainless steels [122]. They found that 304 SS favoured IGSCC after TCW, whereas the cold-rolled 304 SS favoured transgranular SCC (TGSCC). No cracking was observed in 304 SS after TCW up to 26%. The 316 SS was much less sensitive to SCC than the 304 SS. Couvent *et al.* have also studied the effect of strain hardening on CGR and crack growth

path and concluded that pre-straining was necessary for SCC initiation and intergranular cracking was enhanced by combining strain pathes [122, 126–128].

Although a lot of research has been performed on cold-worked materials, the data is hard to compare due to different preparation and testing methods. The direction of the deformation seems to be as important as the stress mechanism and a more systematic study with reproducible conditions would be desirable.

2.4 Experimental Approaches

Stress corrosion cracking has been studied extensively over more then 130 years. During this time several standardised methods of testing for SCC have been developed. The resolution of the existing characterisation methods has significantly improved and new techniques have been become available.

2.4.1 Mechanical testing

The technical and historical information in this subsection is based on the *Metals Handbook Volume 8: Mechanical Testing* from the *American Society of Metals* (ASM) [10], unless stated otherwise.

(Failed) components from field experience in light water reactors have been characterised [130–132], but these specimens are rare as failures and service exchanges are rare and operating conditions cannot be varied easily. Furthermore it is often unwanted modification of standard conditions that causes enhanced degradation. Therefore, it is useful to perform laboratory tests that simulate plant operating conditions. To test for SCC susceptibility it is necessary to expose a specimen to appropriate environments whilst applying a load or strain to it. Until 1965, constant-load or constant-strain tests were most widely used to make SCC testing under well controlled conditions possible. But as SCC is a time-dependent process, and often only occurs after years of operation, two types of accelerated tests were developed in the 1960's. The first method uses static load and pre-cracked samples, while the second technique uses a constant (slow) strain rate on both pre-cracked and non pre-cracked specimen. However, whilst these tests frequently produce SCC, identical alloy/solution systems do not exhibit cracking in non-accelerated tests. Thus, results from accelerated tests and the derived predictions of the service life

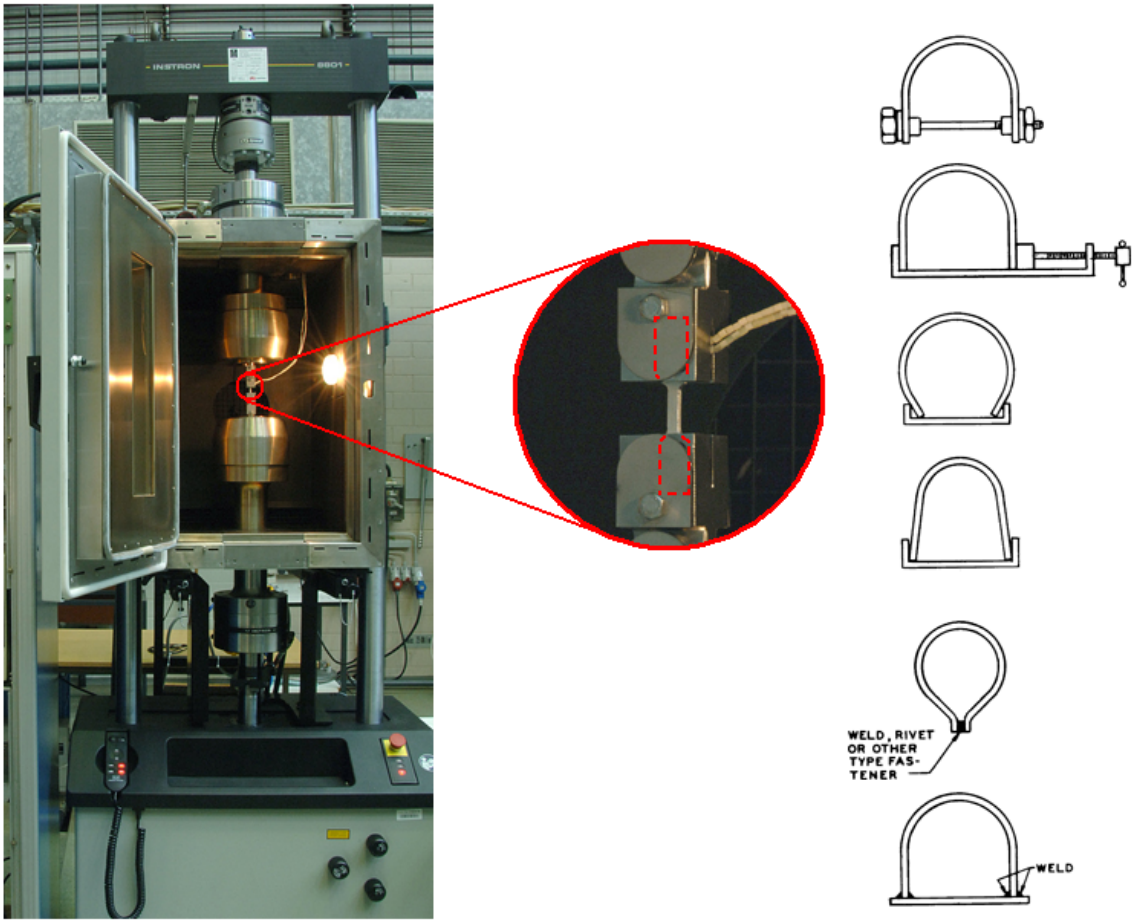

Figure 2.6: The image in the left side shows a flat tensile test specimen in a climate chamber [129]. The graphics on the right show typical geometries for U-bend tests [10].

times of structural components should be evaluated cautiously.

For SCC, the processes of crack initiation and propagation are often considered separately. Pre-cracking of samples reduces the initiation period and accelerates the test. In fact initiation occurs much more randomly in pre-cracked specimens and the initiation period can not be neglected; it also does not relate to "real" initiation periods. To obtain reproducible and comparable data, SCC tests had to be standardised. In 1985, there were 12 ASTM (the American Society for Testing and Materials) standards concerning statically loaded stress-corrosion tests. At that time, neither ASTM nor ISO (the International Standards Organisation) had any standards for pre-cracked specimens or slow strain rate tests.

Constant-strain tests work with a fixed displacement, i.e. a load is applied to the sample with a fixed lever system and not readjusted during the test. When the crack opens, the dimensions of the sample will change, and because the displacement is not increased accordingly, the applied load will decrease. This can lead to incomplete failure (fracture) of

the materials and difficulty in determining whether SCC has occurred. Sometimes springs are included in the stressing systems; this allows complete cracking, but the test will no longer be a strictly constant-strain test. To conduct a constant-load test in its simplest form, a hanging weight is suspended from the specimen. If a crack opens in the sample the load will stay constant, but the stress at the crack tip will increase. Specimens can be loaded to various levels of applied stress until they fail as defined by ASTM standard G49 [133]. Historically, U-bend tests were the most extensively used, because of the large variety of simple techniques (as illustrated in the right side of Figure 2.6). However, the state of stress in a U-bend specimen is much more complex than in a tension specimen. The tensile stress is theoretically uniform through and around the cross-section of the tension specimen, whereas the tensile stress in a bend specimen varies on the surface as well as through the thickness. Therefore, it can be concluded that applying uniaxial tension stress provides optimum control of the stress and more severe testing conditions.

The most recently developed method is slow strain rate testing (SSRT) (sometimes also referred as Constant Extension Rate Testing (CERT)). SSRT is a modification of the constant load tension test as shown in Figure 2.6. Instead of a applying constant load, in this case, the extension of the specimen is slowly increased until it fails. A more detailed description of this test method is given in the ASTM standard G129, which was only established in 2006 [134]. The benefit of SSRT is that it produces a result in a reasonably short time. The time to the onset of cracking in susceptible materials is reduced by the application of the dynamic plastic straining, and furthermore the results are very consistent and reproducible. SSRT always ends in specimen fracture and the fracture mode can then be compared with SCC criteria. It is very important in SSRT to choose a relatively slow strain rate, because high rates will lead to ductile fracture before corrosion reactions can occur. However, if the strain rates are too slow, continued corrosion will be prevented due to film repair.

2.4.2 Crack Growth Rate Measurements

Crack Growth Rates (CGRs) are often measured during the different SCC tests with potential drop methods [135]. Alternating or direct currents are passed through the sample

during the SCC test and the development of the potential is monitored. If a defect, such as a crack, is developed between the two measuring points, the resistance or impedance will increase and lead to an increase in voltage. This can be interpreted as crack initiation or propagation.

Andresen et al. have determined crack growth rates in a range of materials depending on a range of conditions, such as corrosion potential, test temperature, yield strength (CW level), stress intensity factor and concentration of impurities in the testing environment, with varying success [136–138]. A major problem, when trying to find a relationship between one parameter and the CGR is, that parameters are interdependent and small changes in pH, corrosion potential or temperature can mask (or feign) trends in the others. This is particularly apparent in Figure 2.7. Andresen *et al.* tried to combine over a hundred data from different labs to obtain a relationship between CGR and corrosion potential, but small changes in the experimental parameters made it impossible in this case.

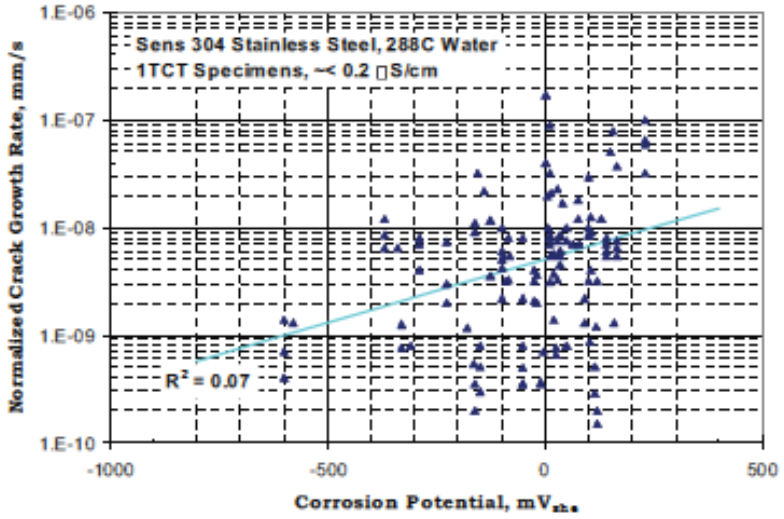

Figure 2.7: Crack growth rate vs. corrosion potential for type 304 stainless steel. Attempt of statistical validation by screening over a hundred data from "good laboratories". The large scatter in the data makes it effectively impossible to determine effects of individual variables [136].

Arioka *et al.* measured CGRs of SUS316 with different levels of CW (different yield strength) in dependence of the temperature and found the maximum CGRs to be $\sim 5 \times 10^{-6}$mm/s at 340°C [139]. The results are ploted in Figure 2.8. Furthermore the effect of water chemistry (oxidised/hydrogenated) was examined. CGRs of up to 10^{-6}mm/s were measured in oxidising environment.

Although it seems from a number of sudies [138–140] that the crack growth rate in

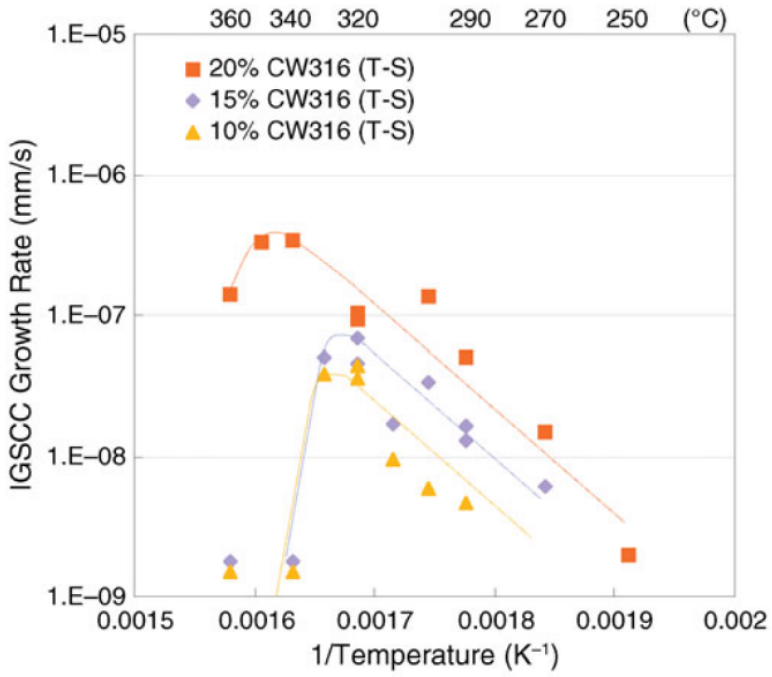

Figure 2.8: Crack growth rate vs. temperature for type 316 stainless steel in simulated PWR primary water [139].

austenitic stainless steels increases with increases with the corrosion potential, this is very hard to show, due to the interdependence with other parameters. This seems to be the reason that there are no more recent reports of this type of experiment.

2.4.3 Introduction to the microstructure of oxides formed

In 1987 Lister *et al.* tested the effect of lithiated water at 279°C on corrosion of 304 stainless steel [141].They examined the corrosion products on their specimen with SEM and AES. Although the Auger depth profiles were not always straightforward to interpret they suggest a $Ni_xFe_{3-x}O_4$ structure for the outer oxide and a mixed spinel consisting of $FeCr_2O_4$ and $NiCr_2O_4$. As shown in Figure 2.9, Lister *et al.* believe the outer oxide to be precipitates or mixed corrosion products.

Robertson also reported oxides formed at $\sim$ 300°C on stainless steel to have a duplex structure. Contrary to the Cr_2O_3 film formed at temperatures above 600°C, the oxides are spinel oxides [142]. He further suggests that the high temperature corrosion of stainless steels is controlled by solid state diffusion of metal ions through the oxide layer. He explains the formation of the inner oxide by water ingress along micropores in the oxide and attributes to metal ion diffusion along GBs [142].

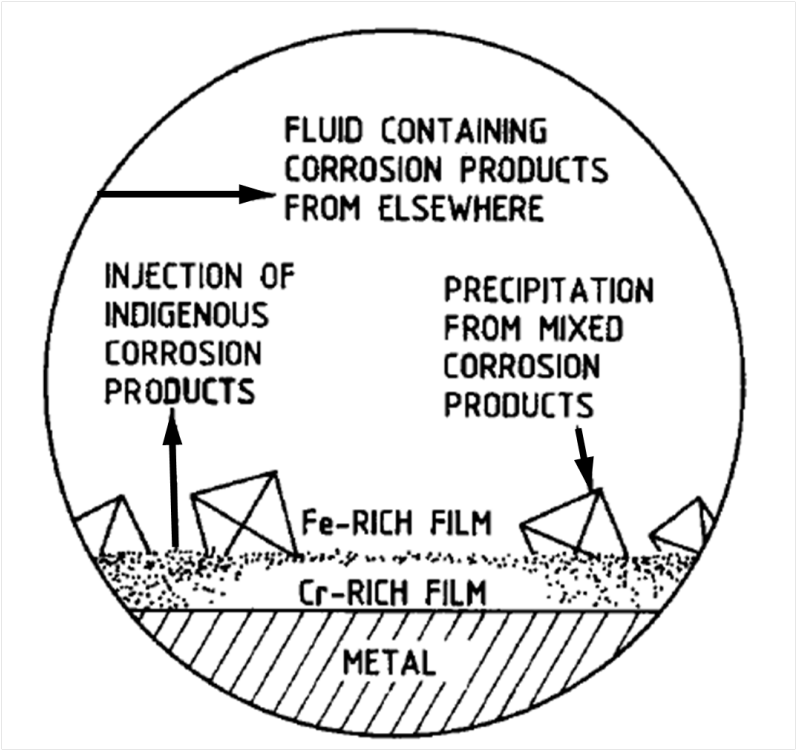

Figure 2.9: Crack growth rate vs. temperature for type 316 stainless steel in simulated PWR primary water [141].

The formation of non-stoichiometric spinels at the surface was later confirmed by Terachi [111] with high resolution EDS. Terachi [111], Bruemmer and Thomas [109] and Lozano-Perez [143] found silimar oxide compositions in stress corrosion cracks.

2.4.4 Sample preparation

Sample preparation for analytical transmission electron microscopy

Although, the first TEMs were available in the late 1930's they have only been used to study SCC in the last two decades. The main reason is that suitable sample preparation techniques have only then become available. Traditionally, TEM samples were prepared by (chemical-)mechanical grinding/polishing, ion-beam thinning, or electropolishing. With these techniques it is not possible to systematically extract and thin localised features, such as crack tips, from larger specimen. Electropolishing may even change the chemical composition of crack oxides.

The arrival of Focussed Ion Beam (FIB) milling made it possible to carefully select small sample regions and thin them to thicknesses of under 100 nm without major changes in the sample chemistry or structure. Some FIB systems (see section 3.6) use the ion beam

for imaging as well as milling. To avoid damaging the sample surface during imaging, a protective layer of a metal (typically W or Pt) or C can be deposited. Langford and Petford-Long introduced two different techniques to prepare samples with a FIB in 2001 [144]. For the first technique a "thick" slice of the sample is mounted on a support and a small section in the middle is then thinned to the required thickness. For the second technique a small filament is directly cut out of the larger specimen, which is then taken out of the FIB system. The TEM filament is lifted out with a micromanipulator and placed on a support membrane, such as holey carbon film [144]. Sivel *et al.* produced TEM lift-out samples using a dual-beam FIB/SEM system, which allows imaging during the sample preparation without causing damage [145]. With the right set of detectors, such a system allows Energy Dispersive X-ray Spectroscopy (EDX) and Electron BackScatter Diffraction (EBSD) maps of cross sections and even series of slice-by-slice maps. A more recent paper by Lozano-Perez introduces an in-situ lift technique, with a micromanipulator in the vacuum system. The TEM samples are welded on a copper support and can still be thinned after preliminary examination in the TEM. Lozano-Perez also suggested leaving a thicker frame around samples containing crack tips to improve their mechanical strength [146]. This latter method was employed for sample production in this thesis. It is described in more detail in section 3.7.

Sample preparation for APT

With the onset of laser fitted systems it has become possible to study oxides in the Local-Electrode Atom-Probe (LEAP). The predominant method to prepare the needle-shaped APT samples is electropolishing of wire-type specimen [147]. This method is obviously not suitable for surface oxides or even stress corrosion cracks, which are buried in a relatively large volume. FIB milling again allows extracting the desired region of interest. Miller describes techniques to extract the volume containing the desired feature with the FIB and weld it on to a suitable support. The specimen can then be sharpened into an APT tip with annular FIB milling. Hudson *et al.* [148] used the technique to study metal/oxide interfaces on Zircaloy-4. Lozano-Perez also describes a technique to prepare APT needles containing crack tips using the FIB [146]. He emphasises how challenging this work is at many stages. Even if a sample is successfully prepared with FIB milling the brittle corrosion crack tip is likely to fracture during the LEAP experiment. Nonetheless the report shows some

APT data of a crack tip proving that APT can be a useful technique to study SCC [146]. Pre-manufactured silicon coupons with microtip arrays allow serial production of multiple APT tips [149]. This technique was employed for sample preparation in this thesis. A more detailed description can be found in section 3.7.

Sample preparation for EBSD

Sample preparation for EBSD experiments is not trivial if samples of locally varying hardness (i.e. composite materials, multiphase materials or cold-worked materials) are to be studied. Saito *et al.*, who performed an EBSD study on a cracked, cold-worked 316-type stainless steel, successfully prepared his samples by mechanical polishing with SiC abrasive paper and diamond paste followed by mechano-chemical polishing [150]. The maps presented in the report show many scratches that can complicate the interpretation of actual features in the sample. The presented data reliably showed deformation bands in the grains; however, very high resolution is required to perform detailed strain analysis as suggested by Wilkinson [151, 152].

2.4.5 Analytical methods

SEM and TEM

One of the first electron microscopy studies on SCC was carried out by Scamans *et al.* in 1978 [153]. They performed high-voltage TEM on jet-polished U-bend specimens of about 0.5 μm thickness and revealed slip bands and corrosion grooves at the surface. A study on fracture surfaces of cold-worked type 304 and type 316 stainless steels was published by Cigada *et al.* in 1982 [154]. They show SEM micrographs of fracture surfaces and TEM of the microstructure of 50% cold-rolled samples that had been treated in H_2O with 1000 ppm Cl^- and boiling $MgCl_2$ solution. Nisbet *et al.* prepared austenitic stainless steel cross-section samples with atom-beam thinning and obtained some early images of SCC cracks [155]. Several studies of stress corrosion cracking using ATEM have been conducted by Thomas and Bruemmer and their co-workers [104, 109, 156–158]. They presented one of the first papers with ATEM data on GB oxidation in 1980 and were also the first to do detailed TEM analysis of crack tips in U-bend Ni alloy samples in 1999 [104]. Another report followed in 2001 with data on alloy 600 and a 316-type stainless steel. These publications showed how much potential ATEM has for the analysis of stress

corrosion cracks. Lozano-Perez and Titchmarsh were amongst the first to use FIB milling to produce cross-section samples containing SCC cracks in Ni alloys [13]. With this new sample preparation technique, micrographs of much higher quality could be obtained. In 2005 Bruemmer *et al.* [109] published TEM micrographs of cold-worked austenitic stainless steels. They prepared their samples by filling the cracks with a thermosetting resin whilst in the U-bend test, followed by a chemical-mechanical polish of the cross-section to electron transparency. They found that films of corrosion products had developed in the cracks. Near the crack tips the films were approximately 5 nm in thickness and strongly enriched in chromium. They also found the Cr-rich films to be crystalline and observed large-grained Fe spinels in wider parts of the cracks. Terachi *et al.* [111] reported a TEM study of a FIB-prepared CERT-tested type 316 SS in the same year. They observed the same double layer of oxide films with a Cr-rich oxide on the inside and Fe_3O_4-type oxide particles on the sample surface and in the wider areas of the crack. This lead them to suggest that there is no large potential gradient within or outside the crack, in this case. Further Terachi *et al.* reported Ni enrichment on the oxide/metal interface and at the crack tip. The crack followed a slip step-like pattern and no GB oxidation was observed ahead the crack tip. Another notable TEM study on cold-worked type 304 and type 316 stainless steels was published by Tribouilloy in 2007 [122]. Cracks were filled with epoxy resin and embedded in a brass insert, before slicing, dimple grinding, and subsequent ion polishing. The study reports limited alpha prime martensite (<1%) at the crack tip of cold worked 304 SS, which could play an important role in crack advance.

Chemical Analysis: STEM, EELS, EFTEM, EDX, NanoSIMS and APT

To understand chemical aspects of SCC, diffusion, dissolution, adhesion, and oxidation, it is desirable to study the local chemical composition at matured and propagating crack tips. This research requires maximum spatial resolution and chemical sensitivity simultaneously. High spatial resolution often results in a limited field of view, especially for scanning techniques.

Takeda *et al.* analysed the thickness, electric properties and composition of surface oxides partially cold-worked 316-type SSs after SSRT in BWR conditions using ESCA depth profiling [159]. They discovered a variation of the Cr content in the inner oxide depending on the strain rate and CW. Cr in the oxide was predominantly found to be in a +III oxida-

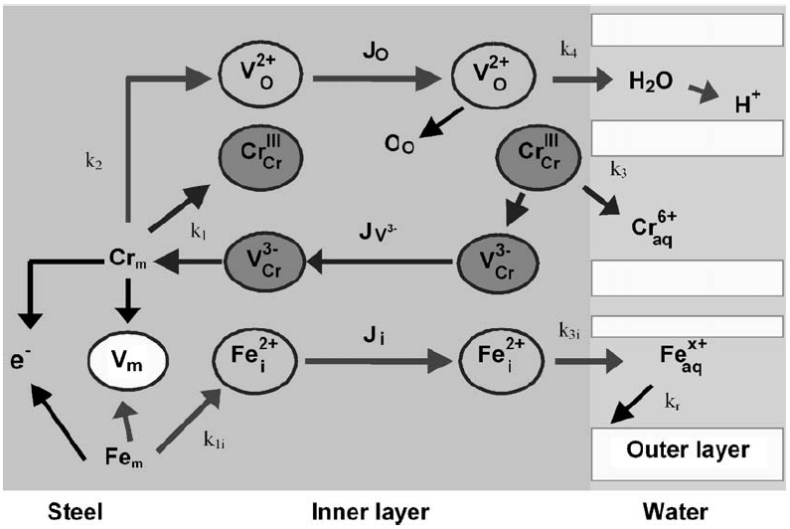

Figure 2.10: Schematic representation of the processes during oxidation/dissolution of stainless steel in high-temperature water according to MCM. The k_x are the reaction sequences, V marks a vacancy, m stands for metallic and J_x shows the directions of the currents involved [159].

tion state and metallic in the matrix. Slight variation of the Fe and Ni in the outer oxide depending on the strain rate and CW were also observed and an oxidation/dissolution mechanism based on the mixed-conduction model for corrosion was suggested [160–162] as illustrated in Figure 2.10.

Arioka and co-workers [112] used scanning Auger electron spectroscopy (AES) to study crack tip cross sections. They found a Fe depleted and Ni enriched zone, in the region from just ahead of the crack tip to about 100 nm in the GB. These results correspond with ATEM data from Terachi *et al.* mentioned above. A study by Lozano-Perez *et al.* from 2008 used NanoSIMS to investigate cracks in type 304 SS tested under constant load in simulated PWR primary water [163]. The focus of the study was on minor constituents, such as boron, phosphorous and sulphur. These trace impurities are known to have a strong influence on intergranular fracture. The crack was methodically divided in three parts as shown in Figure 2.11: the top surface, the crack flanks and the crack tip.

Lozano-Perez *et al.* found NanoSIMS a suitable technique for the chemical investigation of SCC cracks. The sample preparation proved to be much easier than for ATEM and APT analysis and a lateral spatial resolution of <50 nm could be achieved. In addition to the previously found dual oxide layer, oxide-penetration along crystallographic deformation bands was also observed, a discovery in which the authors wish to invest further research. Moreover, Lozano-Perez *et al.* were the first to observe B segregation to the GBs, which

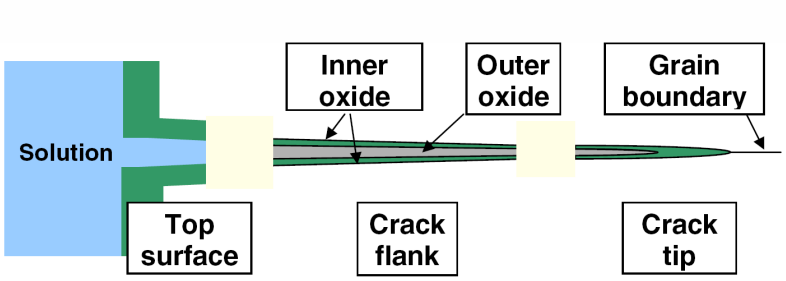

Figure 2.11: Schematic representation of a stress corrosion crack and its representative features [163].

could not be detected with TEM or scanning AES, with NanoSIMS. Data from crack tips, acquired with different techniques were presented to prove that using a range of different experimental methods in parallel was the best approach to achieve to obtain a full set of high-resolution data [164].

In a further publication Lozano-Perez *et al.* combined EBSD with NanoSIMS and conducted (S)TEM together with EELS, EDX and EFTEM for the characterisation of cold-worked 304-type stainless steels with varying Cr content [110]. A range of new insights into crack chemistry in these materials was presented. Oxidised deformation bands were frequently found along the crack path and the length of their oxidation increased with decreasing Cr content in the alloy. The lengths of deformation bands intersecting the crack were much higher than those originating at the unstressed surface, which led the authors to conclude that deformation band oxidation is stress assisted. The oxide species in the oxidised bands was identical with the one on the free surface. It was found that oxidation in the bands proceeds by formation of individual cells that only join up at a later oxidation stage and the authors therefore suggest that oxygen ingress and Fe outwards diffusion probably occurs via the cell boundaries. B enrichment could not be detected at the deformation bands. Lozano-Perez *et al.* also found that oxidation at crack tips is not symmetric. The oxide grows mainly in one of the two grains adjacent to the crack. The authors suggest that the orientation of the deformation bands (which is dependent on the crystallographic orientation) with respect to the propagation direction seems to play an important role. No evidence for selective GB oxidation ahead of the crack tip was found. In most crack tips a B-rich region at the interface between the oxide and fresh GBs was found. The extent of oxidation ahead of the crack tip increased with decreasing Cr content in the alloy. Lozano-Perez and co-workers also observed a Ni-enriched region

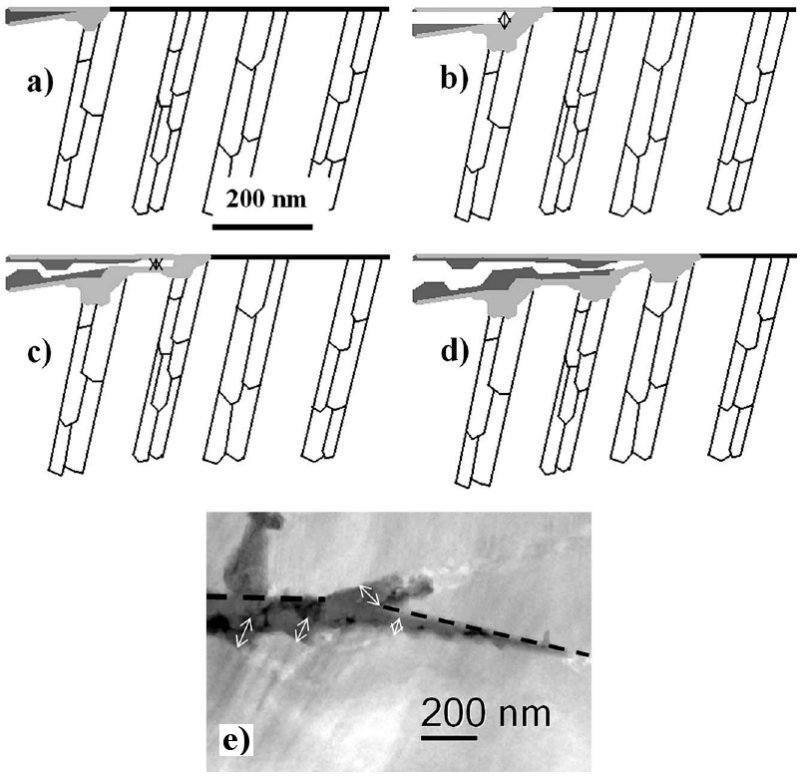

Figure 2.12: Schematic representation of the crack growth sequence. a) The bottom grain has a typical family of deformation bands in a suitable orientation for oxidation, as opposed to the top grain. Deformation bands have an internal structure of cells and micro-twins. Some of the cells have a more favourable orientation for oxidation. Cr-rich oxide has been represented in light grey and Fe-rich oxide in dark grey. b) A continuous layer of Cr-rich oxide has formed in the deformation band ahead of the crack tip. Its brittle character and the accumulated stress induce a localised shearing at the deformation band and, therefore, the Cr-rich oxide breaks and the crack grows. c) The crack encounters a portion of the GB "free" of deformation bands and slows down its propagation although, eventually, in reaches the next deformation band and b repeats. d) The accumulated stress promotes oxidation of the deformation bands, which will eventually shear. e) HAADF image showing a real crack tip with the shearing at deformation bands indicated by the white arrows and the original location of the GB by the black dashed line [110].

at the GB ahead of the crack tip beyond the Cr-rich oxide. Evidence of localised shearing along deformation bands intersecting the crack path was found in STEM High-Angle Annular Dark Field (HAADF) images. B, Si, Mo, C and P were found to segregate to high angle boundaries as a consequence of the final solution treatment. This is a lots of new information about the geometries of stress corrosion cracks in this system and the authors concluded their report by suggesting a new SCC model as illustrated in Figure 2.12 for this alloy system based on their findings.

A review paper by Cerezo *et al.* [165] shows an APT map of the vicinity of a crack tip. This technique has a higher lateral resolution than NanoSIMS and a very high chemical

sensitivity and, although sample preparation is difficult, APT has great potential for the investigation of features as small as crack tips in great detail. Although the study of oxides has become possible with laser-assisted APT, the accurate quantification of the oxides, and spinel oxides in particular was found to be difficult [166, 167]. Bachhav *et al.* have found that the measured oxygen concentration in a wüstite varied by several percent depending on the laser wavelength. The best results were obtained with an infrared laser. However, the authors have found the most accurate oxygen concentration in a spinel oxide with a green laser [168]. They also mention an ambiguity concerning assignment of the peak at 16 Da. As

$$[\text{Time of Flight (ToF)}]^2 \propto \frac{\text{ion mass}}{\text{ion charge state}} , \tag{2.3}$$

the ions at 16 m/z could be attributed O^{+1} or O_2^{+2}. In the latter case the ions causing this peak would contain twice as much oxygen. It has further been suggested, that certain ions of a multiple element material can preferentially cause multiple hits and not be counted [169]. However, the effect of this was shown to be negligible in oxides [170]. Ions can also be lost because of preferential surface diffusion and DC evaporation. Viskari and Stiller have presented APT data of the GB region directly ahead of the crack oxide [171], but so far the dataset in [165] remains the only example of a successful APT experiment analysing an oxidised crack tip.

Structural Analysis: EBSD strain analysis etc.

It was found that stress corrosion crack propagation comes to a halt at certain "special" GBs [172, 173]. Watanabe suggested that identifying these GBs and increasing their number in a material could possibly stop cracks from progressing and would avoid stress corrosion failure [174]. Watanabe's idea has been picked up by many researchers and in the literature is referred to as "grain boundary engineering".

Usually, it has been assumed that "special" GBs are Coincident Site Lattice (CSL) boundaries. The grains adjacent to these GBs have misorientations where some of the atoms are at coincident lattice points. These GBs are labelled with the letter Σ and a number representing the reciprocal density of coincident lattice points. If, for example, $\frac{1}{3}$ of the lattice points of the two grains are identical, the GB between them would be labelled a

Σ3 boundary. This type of GB is often associated with low energies [175]. Orientation mapping by application of EBSD in an SEM can identify and quantify the proportions of CSL boundaries in a fully automated manner [173]; a typical map is shown in Figure 2.13. A more detailed description of the CSL model can be found in [176].

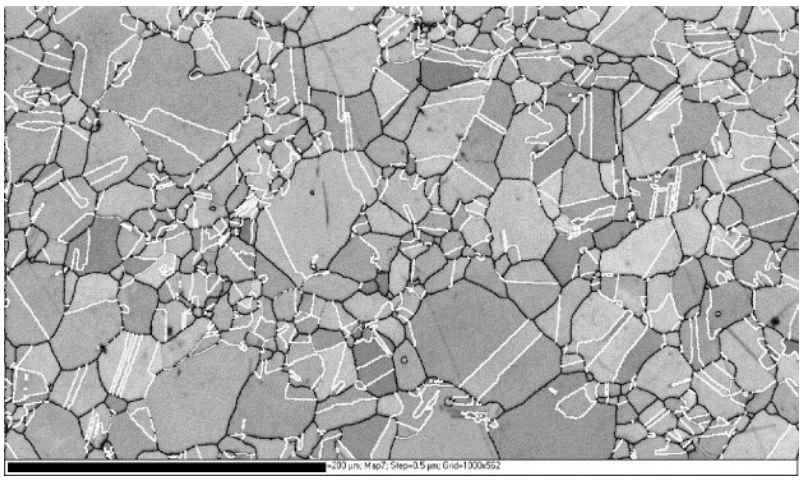

Figure 2.13: Example of an orientation map from a nickel-based superalloy. Σ3 boundaries are represented as thick white lines, Σ9 boundaries are thin white lines and all other boundaries are black. There were 47% Σ3 and 9% Σ9, expressed as a proportion of total GB projected area (length) in the map [173].

In a study by Crawford and Was [177] on alloy Ni-16Cr-9Fe none of the low-angle boundaries ($\leq 15°$) cracked. Although CSL boundaries were more resistant than random GBs, they were not completely immune to cracking. Most CSL boundaries in this type of Ni alloy were observed to be twin Σ3 boundaries [178]. A study by Pan (on a different Ni-alloy) found that Σ3 boundaries are crack resistant, but all other low-Σ boundaries were present in the observed crack paths [179]. In a study on 304 and 316 stainless alloys Σ3 boundaries did not show complete cracking-resistance and all other low-Σ boundaries showed no special behaviour [172]. Considering these results, it seems hardly possible to realise any form of GB engineering. Gertsman and Bruemmer believe that even low-angle boundaries may be susceptible to cracking, but there were too few such boundaries in the studied materials to obtain statistically valid results [172]. Randle commented that the most meaningful reference structure for GBs in polycrystals is the periodicity in the plane of the GB, rather than the misorientation-based CSL [173]. The orientation of GBs with respect to applied stresses turned out to be important, however, some boundaries did not crack despite being favourably orientated. Twins intersecting random GBs can stop crack advance. The authors conclude that investigation of the GB crystallography is not

sufficient to determine IGSCC susceptibility, and that chemical parameters also need to be considered [172].

Another reason for structural analysis around crack tips is to obtain measurements that help determining the crack tip strain rate which is used to model crack propagation and opening in some of the models described in section 2.2. Young *et al.* [55] point out that the crack growth rate $\dot{a}$ in the FRM is directly related to the crack tip strain rate:

$$\dot{a} = \frac{M}{z\rho F}\frac{Q_f}{\varepsilon_f}\dot{\varepsilon}_{CT} \tag{2.4}$$

where M is the atomic weight, ρ is the density of the material, F is the Faraday constant, z is the overall number of electrons involved in the overall oxidation of an atom of metal, Q_f is the oxidation charge density passed between rupture events, ε_f is the fracture strain of the oxide at the crack tip, and $\dot{\varepsilon}_{CT}$ is the crack tip strain rate. They noted that the crack tip strain rate is the most experimentally and theoretically challenging parameter to quantify in the equation. Wilkinson *et al.* [152] suggested using cross-correlation functions to determine small shifts in features from one EBSD pattern to the next. They interpreted the data they had obtained from a fatigue crack in a Ni alloy to yield the local strain tensor within the sample volume of the specimen. They showed maps indicating the misorientation from a low-index orientation and the rotation about an axis parallel to the crack front (which is the largest of the rotation components). Their method to analyse the Geometrically Necessary Dislocation (GND) density distribution is very promising and could also be used to analyse stress corrosion cracks in austenitic stainless steels.

Lozano-Perez and Gontard suggested electron tomography as a new promising approach to structural analysis. Their idea is to use STEM tilt series to measure crack openings, characterise the 3D crack morphology and visualise crystallographic features, such as subboundaries and deformation bands [113].

2.5 Summary and Research Objective

Cold-worked 304 and 316 stainless steels crack in PWR primary water conditions. In these materials mainly IGSCC was observed, but TGSCC has also been reported. The crack path mostly followed a slip-step-type pattern. Surface oxides and oxides in the crack have been found to be very similar, with a double-layer consisting of a Cr oxide phase on the

covering the matrix and ferrite particles on top/in the middle of the crack. Ni enrichment was found on the interface between surface oxide and matrix as well as ahead of the crack tip. One study reported oxidised deformation bands with the same composition as the surface oxide and asymmetric oxidation at crack tips, i.e. the oxide grows in one of the two grains adjacent to the crack. The study further reports a B-rich region at the interface between the oxide in the crack and fresh GBs. Another study reports martensite formation in the crack tips of SCC cracks in cold worked 304 SS. A number of models have been suggested to predict SCC susceptibility in new systems and predict life times, but SCC behaviour is very different in different systems and no general model seems to exist. Furthermore, experimental confirmation of estimated parameters in the models has not yet been provided.

With high-resolution ATEM, APT tomography and EBSD strain mapping a remarkable set of techniques is available to investigate a carefully prepared set of cold-worked specimen provided by the Institute of Nuclear Safety Systems, Japan (INSS). It would be desirable to determine the role of the rare Li and B participants in surface oxides and in the crack, to quantify strain around cracks and built them into a model, to understand the chosen crack path and to get an idea about the role of hydrogen in this system.

In PWRs boric acid and lithium hydroxide are added to the primary coolant. The former is added for reactivity control whilst the latter is added for pH control, resulting in a substantial buffering of the solution [180]. B and Li are found in the samples in such low quantities that they can only be detected with NanoSIMS or APT. Sample preparation for both techniques has proven to be possible and experiments are carried out in this research. The distribution of B and Li in and around the oxides and segregation to microstructural features is studied. Their role in SCC mechanisms is discussed.

Angus Wilkinson's group in Oxford Materials has only recently found a way to efficiently map strains with an EBSD based technique. This technique makes it now possible to quantitatively measure strains around cracks and crack tips. Sample preparation is difficult. For the high resolutions required, very smooth surfaces are necessary. Furthermore, part of the strain in the samples will be relieved when the samples are sectioned. However, this technique is a powerful tool that is used to map strains around crack tips.

The role of hydrogen in SCC has been discussed for many years (see Section 2.2.4). The predominant problem is, that hardly any experimental data exists. Hydrogen is hard

to detect with electrons or X-rays and for a long time neutrons were the only possible "probe" to study hydrogen. Furthermore, hydrogen can diffuse into the material after the experiments during sample preparation. The significance of hydrogen observed in Ni-rich regions with APT is discussed. Future experiments based on the findings of this study may finally bring the community a step closer to answering the question that has been posed in 1874.

The development of new techniques enables the scientific community to provide advice and guidance to the nuclear industry in the choice of materials and material systems to make nuclear power as reliable and safe as possible. However, further work is still necessary to solve this enormously complicated phenomenon: stress corrosion cracking.

Chapter 3

Experimental Methods

To investigate SCC on the nanoscale a combination of high definition sample preparation techniques and high resolution analysis techniques are necessary. FIB milling was used to obtain sample geometries for APT Tomography (APT) and ATEM. A combination of FIB milling and Scanning Electron Microscopy (SEM) was used to do 3D structural analysis. Finally vibropolishing was employed to obtain the smooth surfaces required for EBSD and Nano Secondary Ion Mass Spectrometry (NanoSIMS).

3.1 Material

The material studied in this thesis is a nuclear grade stainless steel, SUS304, commonly used in PWR components. Its composition is illustrated in Table 3.1. SUS304 is an austenitic stainless steel, which means it has a face centered cubic crystal lattice and paramagnetic properties. Cr improves the uniform corrosion properties of the steel, while Ni and Mn stabilise the austenite phase. SUS304 is known to exhibit excellent corrosion and SCC resistance in the operating environment of a PWR. However, it was found that it is susceptible to SCC particularly if it is cold-worked prior to the exposure to stress and oxidising conditions [181].

Alloy	Fe	C	Si	Mn	P	S	Ni	Cr	Mo
SUS304 (wt. %)	Bal.	0.04	0.31	1.6	0.003	0.001	9.2	18.3	<0.01
SUS304 (at. %)	Bal.	0.19	0.62	1.6	0.005	0.002	8.8	19.6	<0.005

Table 3.1: Chemical composition of SUS304

3.2 Corrosion tests

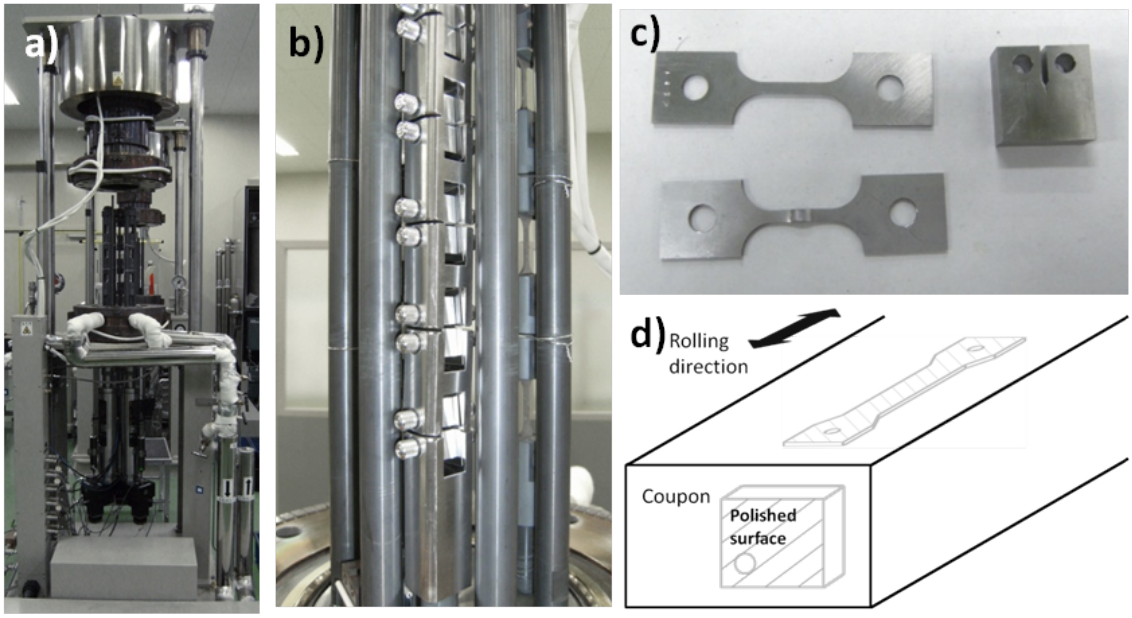

Figure 3.1: a) An open autoclave in the INSS labs in Tsuruga, Japan. b) Tensile specimen and stress coupons under constant load in an open autoclave. c) Tensile and compact tension specimen geometries. d) Schematic of the sample orientations with respect to the rolling direction of the bulk piece.

To simulate PWR operating conditions, autoclave testing was performed at the INSS laboratories (Japan). The nuclear grade 304 stainless steel (SUS304) was solution treated at 1060 °C for 100 min and water-quenched. Some of the samples were unidirectionally cold-rolled to a 5, 10 or 20 % reduction in thickness prior to the corrosion tests. Coupon and tensile specimens were cut from the bulk pieces as indicated in Figure 3.1d and their surface was polished down to mirror finish with colloidal silica. Oxidation was performed in simulated PWR primary water (hydrogenated water, containing 500 ppm B, 2 ppm Li and 30 cm^3/kg H_2O dissolved H) in an autoclave. Figure 3.1b shows how the specimens were mounted in the autoclave.

The SCC process can be divided into several stages, usually initiation, propagation and failure. Sometimes these stages are subdivided further. As the diagram in Figure 3.2 shows, SCC initiation is a long complicated process, which depends on many conditions. This is beyond the scope of this thesis.

To study the influence of stress and CW on SCC propagation, GB oxidation in the near surface region (without SCC initiation) was studied in standard tensile specimen. To observe SCC propagation **pre-cracked** CT specimens were used. This led to crack growth

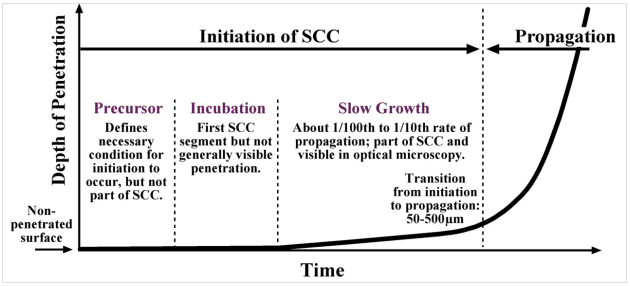

Figure 3.2: Overall SCC initiation and progagation process [182].

in between 1 and 6 months, depending on the level of CW.

Grain boundary oxidation

A selection of samples with 0% cold-work and 20% cold-work, either as simple coupons for a corrosion test or in the shape of a standard tensile specimen for testing under stress, were kept in the autoclave for 1500 h at 360 °C. Stress was applied to the tensile specimen with a Constant Load (CL) tensile test. The load was 1.21 kN or 3.62 kN, which corresponds to applied stresses of 151 MPa and 451 MPa respectively. These stresses lie just below the yield strengths in non cold-worked and cold-worked material, respectively.

Crack oxidation

A selection of pre-cracked standard Compact Tension (CT) specimens (ISO 7539-6) (Figure 3.1c) with 5 % cold-work, 10 % cold-work and 20 % cold-work were tested at 320 °C. The test geometry was such that a theoretical target stress intensity factor of 30 MPa $m^{\frac{1}{2}}$ was reached. The 20 % cold-work specimen was tested for 666 h, the 10 % cold-work specimen was tested for 982.4 h and the 5 % cold-work specimen was tested for 4356 h.

3.3 Optical Microscopy

A *Zeiss Axioscope* fitted with a *Nikon* digital camera and the *Nikon NISD* software was used for optical microscopy. The microscope has objective lenses for 2.5 - 100 x magnification and a 1.25 x magnifier in the column. It was employed to analyse the surface quality during/after polishing and to obtain an overview about the crack paths in a cracked specimen before sectioning in the FIB.

3.4 Electron Microscopy (EM)

3.4.1 Historical Introduction

Between 1925 and 1927 Hans Busch discovered that an inhomogeneous, rotationally symmetric magnetic field can be used as an electron lens to shape an electron beam just like a glass lens can be used for light [183]. He was later referred to as the "Vater der Elektronenoptik", the father of electron optics. This principle was used by Max Knoll and Ernst Ruska, who built the first transmission electron microscope in 1931. Ernst Ruska was awarded the Nobel Prize for his fundamental work in electron optics in 1986 [184].
In 1937 Manfred von Ardenne used an electron beam to raster across the sample surface and collected the secondary electrons to produce a magnified image of the sample [185]. Figure 3.3 shows how he suggested geometries for BF and ADF STEM as well as SEM in his 1938 paper.

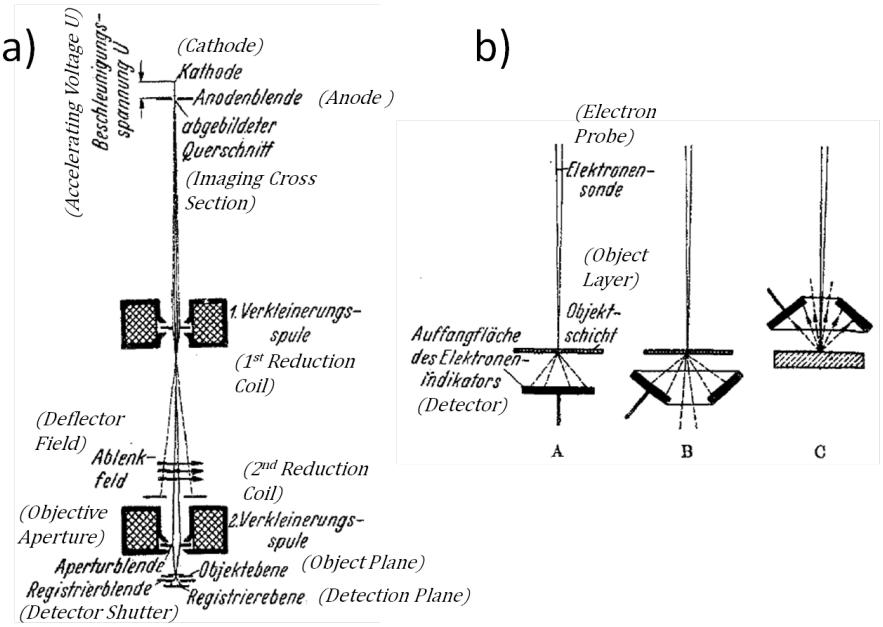

Figure 3.3: Figures from von Ardenne's 1938 paper: a) Course of beam in a scanning electron microscope. b) Schematic of the different types of exposure in a scanning electron microscope. A. Bright-field, B. Dark-field, C. Top View [185].

The first scanning electron microscope with a greater resolution than temporary optical microscopes was developed by Ruska and Borries for Siemens in 1938 [183]. In the 1930s both Siemens and AEG opened the first electron microscopy laboratories and research quickly progressed in both institutions. In the 40s Philips in Holand as well as companies in the USA, Russia, Japan and other countries joined the race. A number of commercial

TEMs were on the marked in the mid-40s [183]. Research into scanning electron microscopes was only taken up again by Sir Charles Oatley. One of his students, Garry Steward played a major role in the development of the first commercial instrument, the Stereoscan SEM by Cambridge Instruments in 1967 [186].

3.4.2 Electron Scattering

In all types of EMs, information about a sample is obtained because electrons are interacting with the atoms in the characterised material in some manner. The average distance that an electron can travel before this interaction occurs is called the mean-free path λ (not to be confused with the wavelength!). Figure 3.4 shows a schematic of the spatial distribution of signals generated in a bulk sample by electron interaction. The size of the pear-shaped interaction volume depends on the elements in the analysed sample.

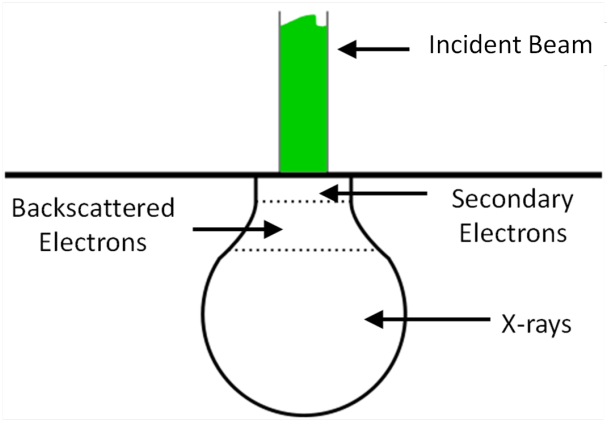

Figure 3.4: Schematic of the the interaction volume for an electron beam penetrating a bulk sample.

Elastic scattering

Electrons can be deflected in the field of the atoms in the sample and change the direction of their movement. In this process the direction of the momentum changes, but no energy is lost or transfered. This type of scattering is called elastic scattering or Rutherford scattering. The probability for an electron with energy E_0 to be elastically scattered at an angle α is characterised by

$$p(\alpha) \propto \frac{1}{E_0 \sin^4 \alpha}. \tag{3.1}$$

It is immediately apparent that small scattering angles are much more likely then large ones. The mean-free path for elastic scattering decreases rapidly with the atomic number

(mass) Z of the scattering atoms.

Inelastic scattering

If electrons transfer an amount of energy during the scattering process, it is referred to as inelastic scattering. The electrons can excite phonons, lattice vibrations, which are macroscopically notable as heat or plasmons, vibrations of the valence electrons. The most valuable form of electron energy loss during scattering (for electron spectroscopy), is, probably, by energy transfer to an inner shell electron. The energies that are necessary to knock an inner shell electrons out of an atom are characteristic for each element. Furthermore the process can lead to x-rays, secondary-electrons and Auger electrons being created, all of which are useful for the chemical analysis of the specimen.

3.5 Scanning Electron Microscopy (SEM)

3.5.1 Secondary Electron Imaging

In an SEM an electron beam is scanned over the surface of a sample and the generated secondary-electrons are detected for every point. The most obvious advantage of an EM over a light-microscope follows from the Rayleigh criterion: due to the small wavelength of electrons compared to light an EM has a much higher angular resolution. Another major advantage using an SEM is the large depth of field. Because the electron beam has very little divergence, there is not only a focal plane, but a "layer" of significant thickness in which the object is "almost" in focus. Furthermore the secondary electrons commonly used for image generation are by far not the only signal emitted under electron bombardment. Backscattered electrons, Auger electrons, X-rays, and photons are also generated and can, if the right set of detectors is in place, provide useful information about the sample's properties. The penetration depth of the electrons is dependent on the crystallographic orientation of the analysed material with respect to the electron beam. If the orientation of the crystal is close to a main crystallographic axis, the atomic spacings of the surface layers projected in 2D are much wider than at a random orientation and therefore the mean-free path of the electrons is much longer in this direction. This effect is called electron channelling. The further the incident beam penetrates the sample, the harder it is for backscattered electrons to reach the detector. The resulting channelling

contrast was used in this thesis, to identify the location of GBs and select suitable regions for sample preparation.

3.5.2 Electron Backscatter Diffraction

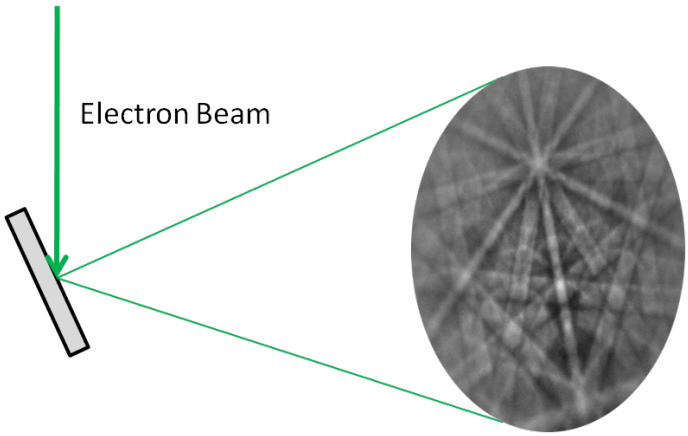

Figure 3.5: Schematic of an EBSD experiment.

For EBSD the sample is mounted at a 70° angle with respect to the horizontal (see Figure 3.5) and an electron beam is scanned across the surface. For an electron beam with a 20 kV accelerating voltage the electrons that enter the sample are scattered in the top 20 nm below the entering point. In every point, the (inelastically) scattered electrons are diffracted by a set of lattice planes on their path to the sample surface and form a Kikuchi-type diffraction pattern. The pattern is collected on the EBSD detector, a phosphor screen in front of a CCD camera, which is normally placed at about 90° with respect to the electron gun facing the sample surface. A computer analyses the position of the bands in the diffraction pattern and the angle between them and compares it to the ones predicted for the respective crystal structure and operating conditions. From this information the orientation of the grain can be determined. If the crystal orientation is analysed in an array of points, a typical EBSD Inverse Pole Figure (IPF) map as presented in Figure 3.6 can be created. For EBSD mapping the sample surface is required to be extremely flat, as any irregularity or any type of faceting influences the orientation at the sample surface.

The EBSD experiments were performed on a *JEOL-6500 FEG SEM* with *TSL OIM DC v4* software, at 20 kV and using a probe current of approximately 1 nA. The instrument operates with a Field Emission Gun (FEG) which allows a resolution of ∼1 nm at 20 kV. Samples were vibro-polished for 24 h in 3:5 colloidal silica : deionised water mixture to

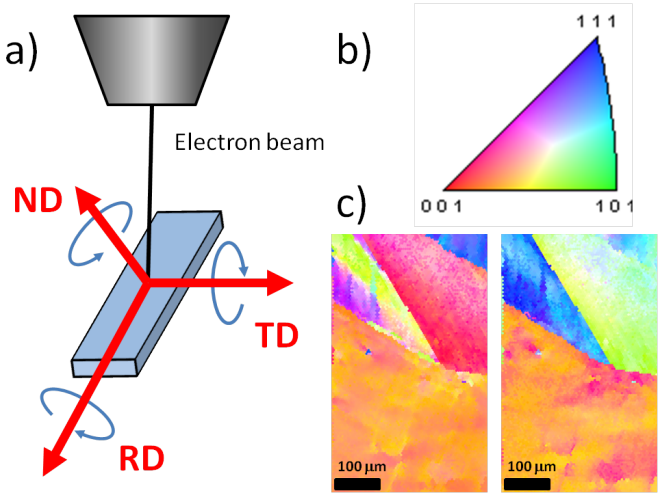

Figure 3.6: a) Schematic showing the Normal Direction (ND), the tranverse direction (TD) and the rolling direction (RD) in an EBSD experiment. b) Colour key presenting all possible crystallographic directions. c) TD IPF (left) and ND IPF (right) of a cold-worked stainless steel.

obtain a smooth surface finish.

EBSD strain analysis

If there is any elastic strain in the material, the features in the Kikuchi pattern will be shifted relative to a pattern of the unstrained material and the band width of the Kikuchi bands will be changed, due to the difference in lattice spacing. Plastic strain is equivalent to the presence of defects and dislocations. They disturb the symmetry of the crystal lattice and cause the Kikuchi patterns to blur. Slip bands and twins mean a local change in the crystal orientation which becomes evident in the diffraction patterns. A comparison of the patterns of the strained material with a pattern of unstrained material allows one to quantify the local deformation of the lattice and therefore the local strain. Unfortunately, truly unstrained material is hardly ever at hand, especially if strain fields expand beyond single grains. However it is still possible to analyse the relative strain within a grain with respect to a reference point. More detailed descriptions of the method used can be found in [151, 152, 187, 188].

3.6 Focussed Ion Beam Milling

3.6.1 Introduction

In focussed ion beam milling, charged particles are focused into a narrow beam and accelerated towards the sample surface. The systems used in this thesis operate with a Ga^+ beam, but ions from other elements such as Au or In are possible [189]. Similar to the electrons in a Scanning Electron Microscope a low current ion beam is rastered over the sample surface creating secondary electrons, which are collected to form a secondary electron (SE) image. A high current ion beam, controlled by a patterning function, can be used to locally sputter a thin surface layer away. Repeated or prolonged sputtering of small areas leads to formation of well defined holes or trenches in the sample surface. This way it is possible to cut complicated sample structures with very small dimensions. If a metal or metal precursor is evaporated in the chamber, a low current ion beam can be used to selectively deposit a thin metal layer in well defined areas. Two different instruments were used for the experiments in this thesis.

FEI FIB 200

The *FEI FIB 200* is a single beam instrument operating with a Ga source. The ion beam can be set to operate at either 30 kV or 5 kV with beam currents between 10 pA and 20 nA. Its gas injection system allows Pt deposition. One of the unused gas injection needles was modified to hold a static *in-situ* micromanipulator, consisting of an electro-polished tungsten wire.

Zeiss NVision 40

The *NVision* is a dual beam FIB, meaning that it is equipped with an electron gun as well as the Ga source. The electron beam does not only allow entirely destruction-free imaging (as in any conventional SEM), but, because of the 54° angle between beams, it also permits a more 3-dimensional view on the sample and its surroundings. The *SIINT Zeta* Ga^+ column can be operated at 1 to 30 kV and currents between 0.1 pA and 45 nA. The Schottky field emission *Gemini* column of the SEM can be operated at beam energies from up to 100 V to 30 kV. Furthermore the NVision is fitted with a Kleindieck *in-situ* micromanipulator, which can be rotated on three axes via a piezo system and enables the

user to lift-out sample parts and place them on a support precisely. W, C and SiO_2 can be evaporated through a multichannel *SII* gas injection system, thus allowing welds of different strength and conductivity.

The FIBs were mostly used for preparation of TEM and APT samples in this thesis, but the dual beam FIB was also employed for a technique called 3D-FIB-slicing.

3.6.2 FIB-SEM Tomography/ 3D FIB-slicing

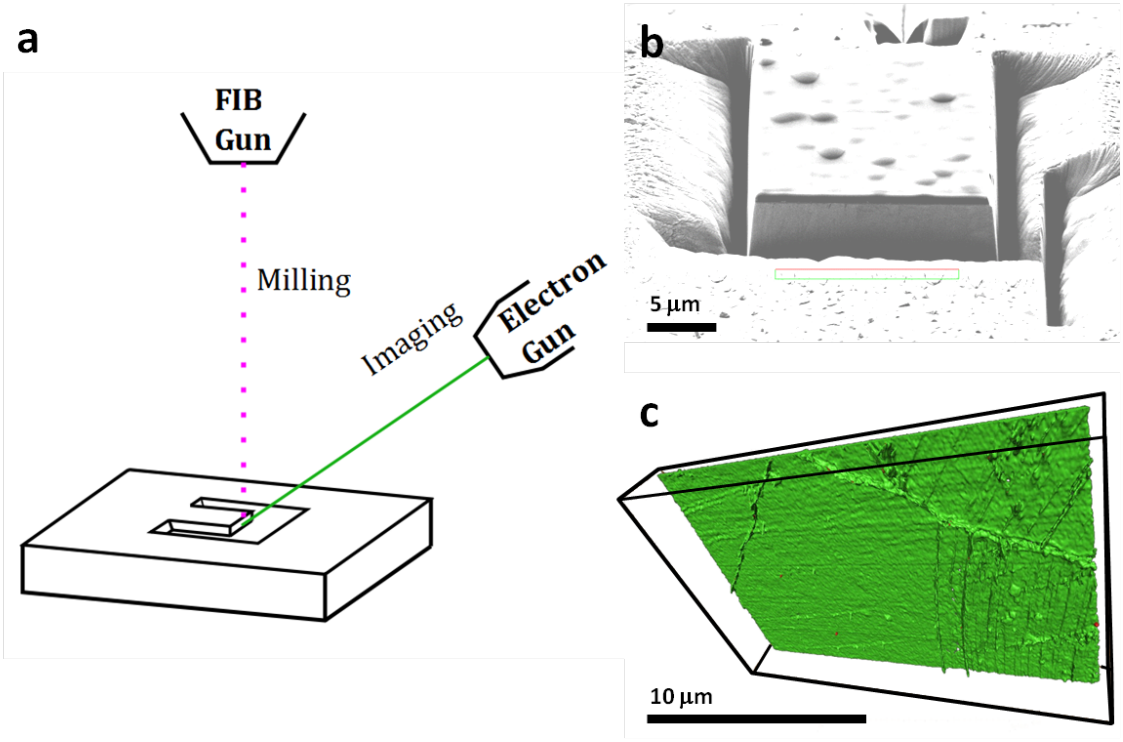

Figure 3.7: a) Schematic of the experimental set up for FIB-SEM Tomography. b) SE image of isolated material with view on the cross-section recorded during the experiment. c) View from below (from the matrix) on the volume of the oxide regions near the surface of a steel sample reconstructed from the data of a FIB-SEM experiment.

A schematic of the experimental set-up is shown in Figure 3.7a. The angle between the electron beam and the ion beam in the *Zeiss NVision* is 54°. For this technique an area of roughly 30 × 30 μm^2 is isolated from the bulk as displayed in Figure 3.7b. The sample is mounted flat, so that the ion beam is normal to its surface. This way the electron beam can be used to image a cross section of the material. SE-images of one side of the isolated block of the material are taken with the SEM and about 50 nm wide slices are subsequently milled away from the same side. A beam current of 700 pA was used to carry out the sectioning. This process is repeated until the whole block is milled away. The

Z-contrast in the SE-images allows identification of different phases within the material. After aligning all the SE images, the volume of the block can be reconstructed in 3D and different phases, such as the oxide phase shown in Figure 3.7c can be extracted and analysed.

The 3D reconstruction was carried out using Mercury Software Avizo. The different regions of interest appearing in the 2D images, such as metal, oxides, voids, etc., have different intensities. They were automatically selected using intensity thresholding methods. In some cases no automated segmentation method was good enough to overcome the channelling contrast present in some SE images, then the areas were manually selected. The dimensions of the reconstructed volumes were typically $\sim$20$\times$20$\times$5 μm with a voxel size of $\sim$11$\times$11$\times$40 nm.

A 3D model of the inner Cr-rich oxide was created for all the characterised specimens. The models show the view onto the oxide volume from below. The top surface, which is not visible in the selected model orientations, is the one exposed to the environment and generally flat due to the final polishing step with colloidal silica prior to autoclave testing. In addition, a top projection of the model, will be displayed to visualise the different depths of oxidation. This image, though it resembles an SEM micrograph, is artificially created. Brighter areas signify deeper oxidation in projection.

The Cr-spinel segmentation was performed in a semi-automatic way, relying on intensity thresholding to separate the Cr-rich oxide from the other phases and drawing the boundaries manually when this was not satisfactory. The error in the location in the boundary can be considered to be of $\pm$1 pixel, therefore the error in the calculation of the oxide thickness could be assumed to be $\pm$2 pixels. For most reconstructions the pixel size in the y direction was $\sim$12 nm, so the uncertainty in the oxide thickness determination would be $\sim$24 nm.

The depth of oxidation was measured in over 500,000 points per reconstructed Cr-rich spinel models and subsequently statistically analysed. The nature of the data allowed the individual analysis of features such as grains, GBs or twin deformation bands, as will be shown in Chapter 4.

3.7 Sample preparation with the FIB

The surface-oxide specimens were prepared using an *in-situ* lift-out technique [146, 164] in the *NVision* dual-beam FIB operated at 2-30keV and using 40 pA - 27 nA currents. Some preliminary milling was performed in the *FIB 200*. As can be seen in Figure 3.8, channelling contrast in the SEM SE images can be used to infer the location of the GBs and choose the regions where the TEM and APT samples will be prepared, so that they contain portions of the same GB, separated by $\sim$10 μm. The sample preparation procedure is sketched in Figure 3.9. While only one TEM sample of each GB was produced, 6 - 10 AP samples were extracted from each lift-out rod following the method described in [139]. At first, the regions of interest (ROI) are protected with a layer of carbon. As the oxide will be studied, it is important not to damage the surface and limit Ga implantation from the ion beam to a minimum. Then a small trench is cut across the GB; imaging of the exposed cross section reveals the angle of the GB with respect to the surface. Those with angles greater 45° are lifted out preferentially, because this way it is easier to capture a significant portion of them in the APT needles. For the fabrication of the APT specimens a long beam has to be lifted out from the bulk (see Figure 3.9c). To achieve this, two cuts are placed on either side of the protected area sectioning the sample at a 30° angle with

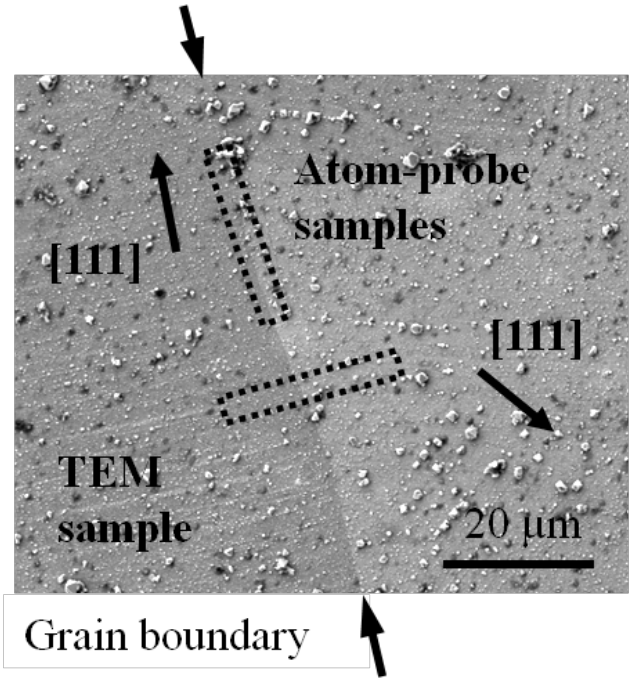

Figure 3.8: SEM SE image showing the region chosen for the APT and TEM sample preparation. Note that both samples contain the same GB.

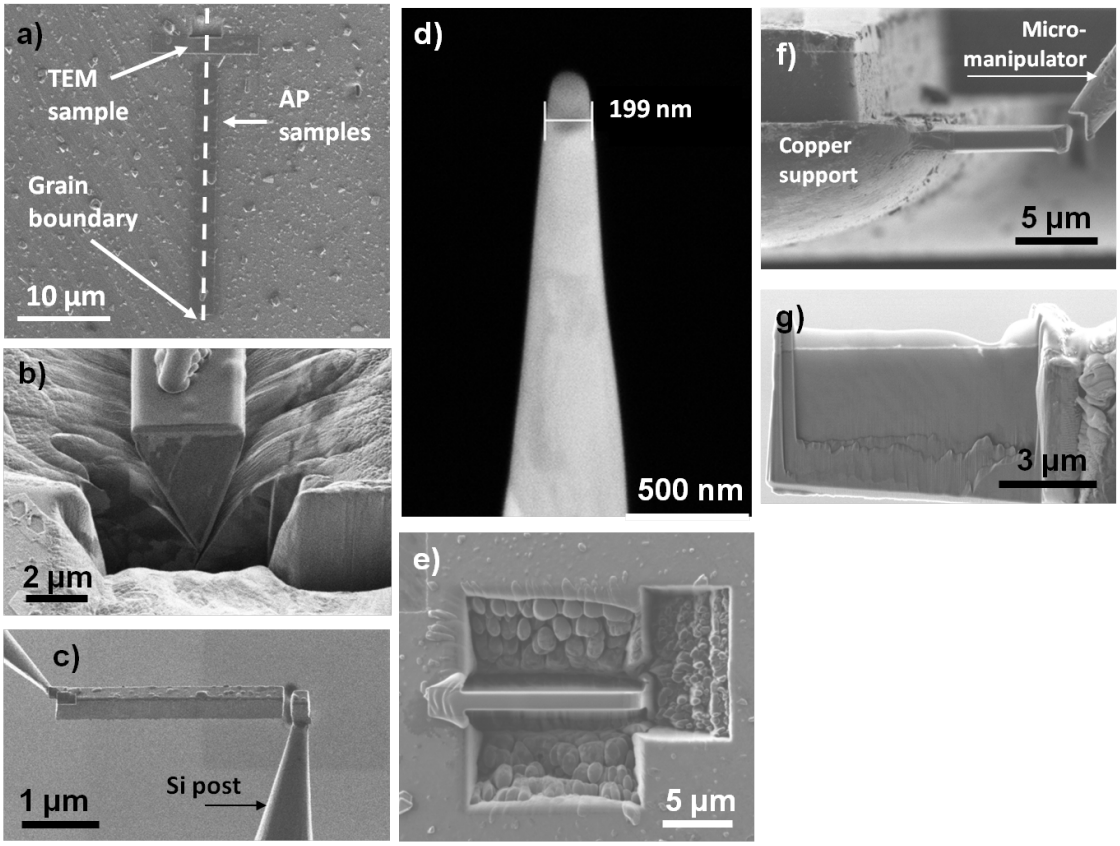

Figure 3.9: a) A carbon layer is deposited to protect the surface oxide above the GB in the areas chosen for sample preparation. b) The area reserved for the APT sample is undercut and a long beam with a triangular cross section is produced. c) The beam is lifted out with a micromanipulator and a small wedge shaped portion is welded on a pre-manufactured Si post. d) The specimen material is milled into a thin needle shape. e) Three trenches are milled around the area reserved for the TEM specimen. f) The TEM specimen is lifted out with a micromanipulator and welded onto a Cu support. g) The TEM specimen is thinned to electron transparency.

respect to the normal. The wedge shaped beam is lifted out with a micromanipulator and 1 - 3 μm wide portions are welded onto Si posts on a pre-manufactured coupon as shown in Figure 3.9c [149]. Welds are placed on both sides of the wedge to ensure a safe connection and good conductivity. Annular milling patterns are used to shape the wedge into a needle of $\sim$200 nm width. During this process most of the protective C layer at the surface is usually lost. Any remaining C has to be removed before the experiment. As a last step a low-energy ion beam with only 2kV accelerating voltage and with a low current (40pA) is rastered over the entire needle, to decrease the thickness of the layer, which is damaged by Ga implantation at the surface.

The TEM specimen is prepared in a similar fashion. A thin slice of 1 - 2 μm thickness is lifted out. To achieve this, deep trenches are cut on three sides of the protected ROI,

then the sample is undercut from each of the long sides with the beam at a 45° angle with respect to the normal. To avoid redeposition the undercuts have to be at least 1 μm wide. The sample is lifted out and welded onto a pre-manufactured Cu support fit for use in the TEM. The lift-out specimen is thinned to about 50 - 100 nm. In the NVision, electron imaging with a 5 kV electron beam can be used to check for electron transparency. The sample is thin enough when it becomes transparent for the 5 kV electrons. Finally, a low-energy clean of the specimen is performed on both sides to reduce Ga implantation.

3.8 Analytical Transmission Electron Microscopy

The TEM is a very versatile instrument. If the electron beam is used to illuminate a "large" region of the specimen, its crystallographic properties and defect structure can be imaged. Limiting the illumination to an area of homogeneous crystal structure (an undeformed grain, a single crystal) and recording of its diffraction pattern at different tilt angles allows detailed analysis of this structure and therefore determination of the analysed phase.

If the electron beam is rastered across the sample and the electron signal is collected for every "spot" on the sample, the technique is called Scanning TEM (STEM). Using a high angle annular detector it is possible to collect only the incoherently diffracted electrons. The number of these electrons, or the number of incoherent scattering events respectively, is largely dependent on the size of the nuclei in the illuminated spot. Therefore HAADF imaging makes it possible to obtain Z-contrast images.

Additionally, a number of electron-based spectroscopy techniques are possible, if the instrument is fitted with the necessary detectors. For this thesis EFTEM, EELS and EDX were used to analyse the local chemical composition of samples.

An overview over the techniques used in this thesis will be given in this chapter. The interested reader can find more detailed information in the well-known series on electron microscopy by Williams and Carter [190].

In a conventional TEM, electrons emitted from the electron gun by thermionic, Schottky, or field emission are focussed into an almost parallel beam with a set of electron lenses. Modern instruments also have an aberration corrector in the column to further increase resolution. The beam is used to illuminate a thin foil-type sample (typically 30 - 100 nm

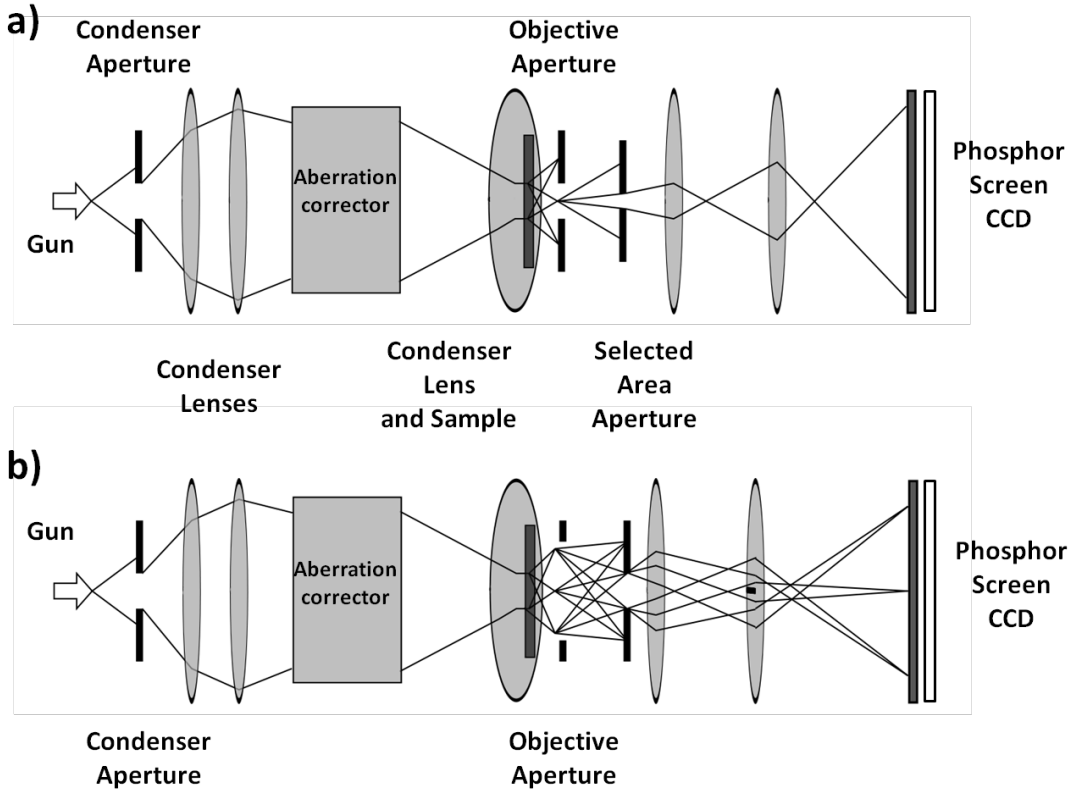

Figure 3.10: Schematic of a TEM. a) Set-up for bright-field imaging. b) Set-up to collect a diffraction pattern.

thickness). If the sample is crystalline, the electrons are diffracted in the sample and form a diffraction pattern in a plane below the sample. This diffraction pattern can be magnified and made visible on a phosphor screen or recorded on film or on a CCD (Figure 3.10b). If the camera length L and the wavelength of the incident electrons λ are known, it is possible to determine the crystal structure and lattice spacing of an unknown structure with good accuracy.

3.8.1 TEM BF/DF imaging

When the electrons pass through the sample, they are scattered as described in Section 3.4. One way to obtain imaging contrast is to only select the signal of one of the maxima of the diffraction pattern with an aperture. An objective aperture can be used in a set up like in Figure 3.10a to select the most intense middle part of the electron beam to obtain a BF image or it can be centered around one of the second order diffraction spots to form a dark-field (DF) image.

The ordered regions of the sample produce an intensity maximum in the diffraction plane

if the Bragg condition is fulfilled. However, if the symmetry of the material is disturbed, for example by dislocations or slip bands, these areas will not contribute to the diffraction pattern. Therefore, these features will stand out in BF and DF images. As many electrons pass the sample unscattered and therefore contribute to the intensity of the central beam, this type of contrast, which is also referred to as diffraction contrast, is most prominent in DF imaging. The probability for scattering is higher in thicker samples, therefore thicker regions will appear darker in the BF image (thickness contrast). Similarly, regions that contain atoms with higher Z numbers will appear darker in the BF image (Z contrast).

3.8.2 Scanning Transmission Electron Microscopy

For TEM imaging the electron beam is spread until it is parallel to illuminate part of or even the entire specimen. In contrast, for STEM the electron beam is focused into a small probe and rastered across the sample at great speed. In every point a great amount of information can be gathered with the right set of detectors. The BF image obtained in STEM mode is identical to a conventional TEM image, but it is always computer generated, from a detector signal acquired for each image point. The resolution in a STEM is limited by the size of the probe used for imaging. As the current in the probe decreases with decreasing size, the smallest probes can only be obtained if the current in the original beam is high. The highest currents are reached if a FEG is used. No post specimen lenses or apertures are required to separate the electrons depending on their scattering angles. BF images are acquired by only taking the electrons hitting the central BF detector into account. Annular detectors are used to acquire DF images, in STEM mode this is therefore often referred to as annular dark field (ADF) imaging. To be able to separate the electrons like this, it is of course necessary that the scanning electron beam is parallel to the optic axis at all times. The main advantage of the technique is, that no post specimen lenses are required, therefore there is a lot of room for a number of different detectors and spectrometers to analyse scattering angles and energy spectrum of the transmitted electrons.

In section 3.4 the different modes of scattering were discussed. Although only few electrons are Rutherford scattered at greater angles, these are the ones that interact with the nuclei. If a HAADF detector with a fairly large radius is placed around the ADF detector, it is possible to use only these electrons for image generation. As the mean free path for

Rutherford scattering strongly depends on the Z-number of the scattering atoms, the contrast in the resulting STEM image will be representative of the mass of the atoms in the sample. Of course the thickness and the density of the sample will also have an effect on the number of scattered electrons, so instead of pure Z-contrast, mass-thickness-contrast is obtained. As the Bragg scattered electrons will have smaller scattering angles (and hit the ADF detector) there will be very little intermixing with the crystallographic information.

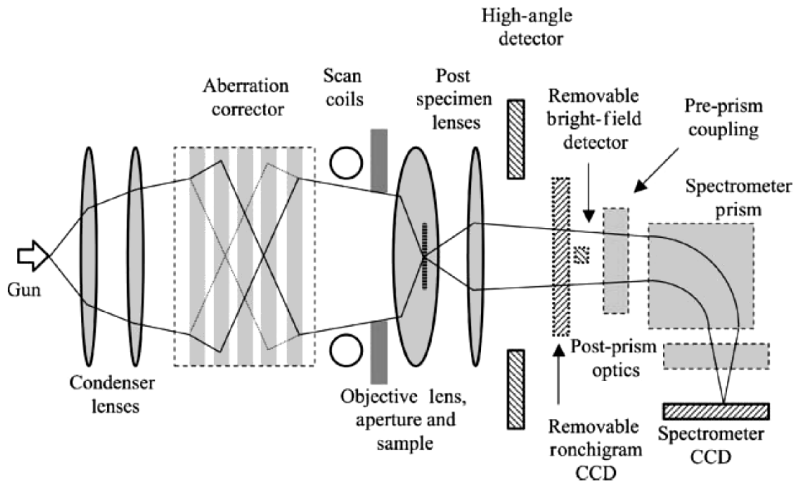

Figure 3.11: Simplified schematic of an aberration-corrected STEM; examples of electron trajectories are indicated. In the (quadrupole-octupole) aberration corrector, the different trajectories in the XZ and YZ planes are indicated with dotted and solid lines, respectively. The electrons are accelerated from the gun; condenser lenses are used to adjust the beam current and beam coherence and to couple to the aberration corrector. The objective lens focuses the probe, which is scanned across the sample by the scan coils. The high-angle detector collects electrons scattered to high angles. Removable bright field and Ronchigram detectors are shown as well as the important components of the spectrometer [191].

3.8.3 Electron Energy Loss Spectrometry

One way of analysing the electrons transmitted in one point is to measure their energy-loss spectrum. It is especially important to have the "right" thickness of specimen (about 50 nm for steels) for this technique, to avoid multiple scattering in too thick samples and evaporation of sample material under a high-energy beam in too thin samples. Ideally, the thickness of the sample is of the order of magnitude of the mean-free path of the electrons for the analysed material and the beam energy used.

Of course many electrons will be scattered elastically (zero loss) and will not lose a detectable amount of energy. These electron are irrelevant for chemical analysis with energy-

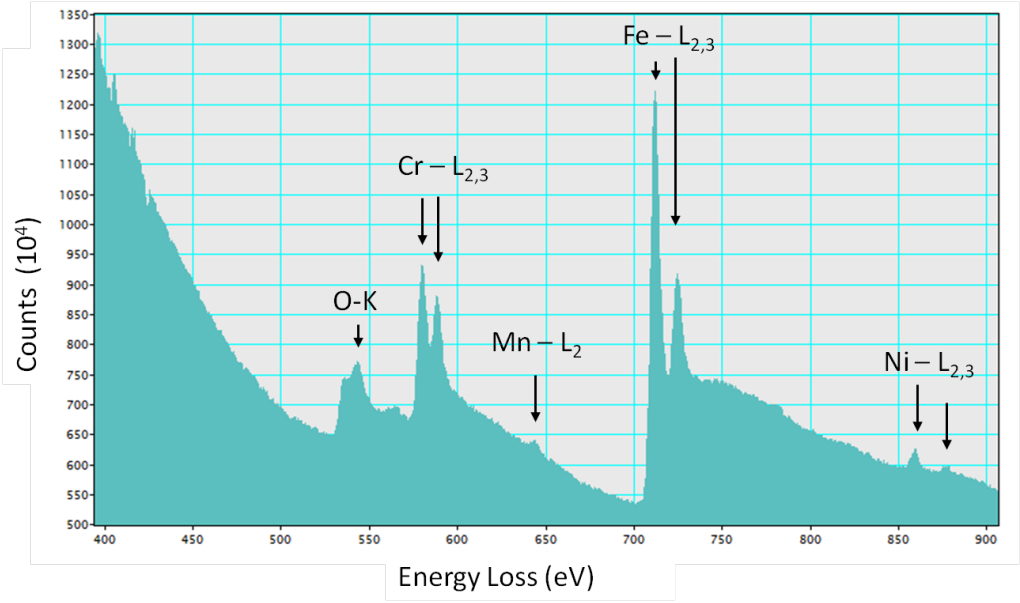

Figure 3.12: EELS spectrum of the oxide on a 304 stainless steel specimen showing all the major absorption edges.

loss spectroscopy, however the Zero Loss Peak (ZLP) can be used to align and focus the beam precisely on the ROI and to measure the sample thickness. A certain amount of energy is needed to lift an electron from an inner shell to vacuum level and ionise an atom bound in the sample. This energy is characteristic for every electron orbital in every element. A selection of the typical energies for the main alloying elements of SUS304 and oxygen is shown in Table 3.13(a). Electrons that have lost energy in an inelastic scattering process carry valuable and accessible information. The energy loss spectrum is expanded with a magnetic-prism system. The plasmon peak and the signal of valence and conduction band electrons are in the low loss region (<50 eV energy loss) of the energy-loss spectrum. The interactions with inner shell (core) electrons give rise to absorption edges at higher energies. This part of the spectrum is often referred to as the core-loss region. A typical EELS core-loss spectrum is shown in Figure 3.12.

Quantification

The core-loss spectrum can be used to perform quantitative analysis. A software package, such as *Gatan Digital Micrograph* can be used to remove the plural-scattering background. To do so, a curve is usually fitted to an energy window just before the edge onset and subtracted from the energy. This process is repeated for every edge. Then the number of atoms (N), which cause the remaining intensity (I) needs to be quantified. The intensity

I_A of a particular edge A is

$$I_A = P_A I_T \tag{3.2}$$

where P_A is the probability of ionisation and I_T the total transmitted intensity. In a thin specimen I_T can be assumed to be the incident intensity as backscatter and absorption events are negligible. P_A can be estimated to be $N\sigma_A$ with σ_a being the ionisation cross section of element A. It follows that

$$N = \frac{I_A}{\sigma_A I_T}. \tag{3.3}$$

To obtain the ratio between element A and an element B the expression can be extended to

$$\frac{N_A}{N_B} = \frac{I_A \sigma_B}{I_B \sigma_A}. \tag{3.4}$$

σ can be calculated theoretically or determined with a standard spectrum. With consideration of the collection angle and the specimen thickness it is now possible to do quantitative composition analysis. More detail on quantitative EELS analysis can be found in Williams and Carter, Chapter 39 [190].

3.8.4 Elemental mapping - Energy filtered TEM

In the TEM the electrons that contribute to the image are only restricted by the objective aperture. Therefore, electrons scattered at a large angles are the only ones that contribute to the image contrast (as they are the ones cut out by the aperture). The different energies of the electrons after they pass through the sample stay unaccounted for. As already explained in the previous section, it is possible to split the electrons up with regard to the energy that they have lost. EFTEM uses this to analyse the chemical composition of a specimen. An Ω-filter or a Gatan Imaging Filter (GIF) is used to select electrons of the desired energies. A series of images is acquired, each one only recording electrons with a narrow range (typically 5 eV) of energy loss. If, for example, only electrons that have lost 574 eV are used to generate the image all areas that contain Cr will appear bright. If the signal in all the separate energy channels for a certain region are added up, as in Figure 3.13(b), they form an energy loss spectrum, which energy resolution limited by the slit width of the filter. Spectra with higher resolution can be achieved by integrating

the counts over a larger area. This can be performed for every pixel in the image and elemental maps can be extracted. Multivariate Statistical Analysis (MSA) as explained in [192, 193] was used for noise reduction on elemental maps shown in this thesis.

EFTEM acquisition in this thesis was performed in a window from 450 eV to 900 eV, in steps of 10 eV, using a 10 eV energy slit. This window contains the edges listed in Table 3.13(a). In order to maximise the beam current used for the EFTEM acquisitions, the beam was focused on the region of interest with a diameter slightly bigger than the CCD and a 12.2 mrad half-angle objective aperture was used in the JEOL 3000F and a convergence half-angle of ∼5 mrad was measured in the JEOL 2200MCO.

Z	Element	Edge	Energy(eV)
8	O	K	532
24	Cr	$L_{2,3}$	574
26	Fe	$L_{2,3}$	708
28	Ni	$L_{2,3}$	854

(a) Principal EELS edges for the main alloying elements of SUS304 and oxygen [194].

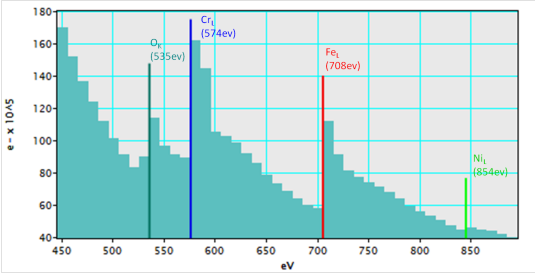

(b) EELS spectrum showing the edges presented in the adjacent table.

Figure 3.13: EELS parameters which were used in this thesis.

3.8.5 The Microscopes

Four (S)TEM systems were used in this thesis, the JEOL 2010, the JEOL 3000F, a prototype JEOL 2200MCO, which was operated by Dr Lozano-Perez and a JEOL 2100 at the Department of Physics, Warwick University. Unless stated otherwise, TEM data acquisition for this thesis was carried out with the JEOL 3000F.

JEOL 2010

The JEOL 2010 is an analytical TEM with a LaB_6 electron gun and which can be operated between 80 and 200 kV. The instrument is equipped with an Oxford Instruments LZ5 windowless Energy Dispersive X-ray Spectrometer (EDS) controlled by INCA and a bottom mounted Gatan Orius CCD camera.

JEOL 3000F

The JEOL 3000F is a FEG-(S)TEM equipped with a Fischione HAADF detector, an Oxford Instrument Isis EDX system and a post-column GIF. It operates at an accelerating voltage of 300 kV and can achieve a spatial resolution of 0.16 nm in imaging mode. The EDX system consists of an Oxford Instruments EDS with a super atmospheric thin window detector and an INCA processor. The STEM unit can be operated with two annular dark field detectors, a JEOL detector and the Fischione HAADF detector, which is placed at a position to allow EELS spectra to be acquired during STEM operation. Simultaneous acquisition of EDX is also possible. The GIF is equipped with a 2k MegaScan CCD camera, a 1k Gatan MultiScan camera is placed before the GIF.

JEOL 2200

The JEOL 2200MCO FEG TEM is a prototype instrument developed by the JEOL and Department of Materials (University of Oxford). The microscope is operated at 200 keV, with an improved High Tension (HT) stability ($\Delta V/V \sim 3 \times 10^{-7}$) due to its dual HT tank. It is equipped with two spherical aberration (C_S) correctors (for probe and image mode) and an Ω-filter. C_C is measured to be 1.2 mm (with only the image C_S-corrector on). The spherical aberration coefficient (C_S) is minimised to values around 3 μm. A Gatan 4 k CCD is used for the image acquisition.

C_S-correction increases the spatial resolution of the images and allows the use of a larger 200 μm condenser aperture, which increases the probe current. The microscope can be operated remotely, which improves stability in the microscope room.

JEM-2100 LaB_6

The JEM-2100 is operated with an LaB_6 filament at 200kV accelerating voltage. The instrument is very similar to the JEOL 3000F and equiped with a similar set of detectors. The STEM unit can be operated using a probe as small as 1.5 nm. BF and ADF images can be collected simultaneously and EELS and EDX acquisition during STEM operation are also possible.

3.9 Atom-Probe Tomography

3.9.1 Historical introduction

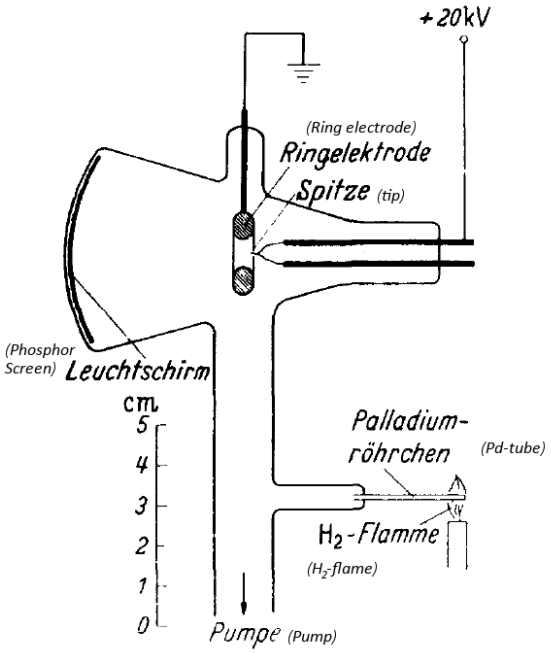

Figure 3.14: Schematic of the first field ion microscope as designed by Müller [195].

In his PhD thesis, which initially was a general study of field electron emission [196], Erwin Müller designed the first field electron microscope [197], which consisted of a needle specimen in an evacuated glass tube and a phosphor screen. In 1951 the addition of hydrogen as imaging gas and the reversion of the polarity of the tip from negative to positive, led him to the invention of the first field ion microscope [195]. A schematic of the instrument used by Müller can be found in Figure 3.14. Müller reported,

> "Das Feldionenmikroskop ermöglicht zum ersten Male eine Abbildung mit genügendem Auflösungsvermögen, um das atomare Gitter sichtbar zu machen."

English: The field ion microscope allows for the first time a projection with sufficient resolution to make the atomic lattice visible. He also suggested cooling the tip and discusses possibilities to decrease the necessary desorption field strength. This was the first time that imaging gas atoms, field ionised by electrons tunnelling through the free space between the ion and the surface of the needle, were made visible and revealed the atomic structure of a tungsten tip surface [196].

The strength of the field, F, on the apex of the needle is given by

$$F = \frac{V}{kr_t}, \tag{3.5}$$

where V is the applied voltage, r_t is the radius of the tip and k a numerical constant ($k \approx 2-5$) [196], dependent on the shape of the needle. As it was now possible to achieve a field large enough to cause desorption of positively-charged ions, it did not take long before Müller reported the field evaporation of other elements [198]. Finally the addition of a mass spectrometer led to the construction of a prototype 1D atom-probe in 1967. At this time an aperture was used to only allow atoms from selected regions to enter the mass spectrometer and be analysed. A high voltage pulse on the needle is superimposed on the standing voltage to stimulate field evaporation, so that the time of flight could be measured accurately.

If the voltage at the needle is V_0 and the charge of the evaporating ion is $n \cdot e$ with e being the elementary charge, the electrostatic potential energy of the ion at the tip can be expressed as $E_{pot} = neV_0$. The kinetic energy at the detector is approximately $E_{kin} = \frac{1}{2}m\frac{d^2}{t^2}$ if m is the mass of the ion, d the distance to the detector and t the time of flight. This approximation is correct, if we assume a grounded counter electrode directly in front of the tip, so that the ions reach their final speed instantly [199]. With the laws of energy conservation it follows that

$$neV_0 = \frac{1}{2}m\frac{d^2}{t^2}. \tag{3.6}$$

From this it is easy to see that the mass-to-charge ratio is proportional to the square of the time-of-flight t^2

$$\frac{m}{n} = 2eV_0\frac{t^2}{d^2}. \tag{3.7}$$

This way single selected atoms could be identified for the first time.

This concept was picked up by Cerezo *et al.*, who added a position sensitive detector and constructed the first fully operational 3D atom-probe in 1988 [200]. Several improvements to the technique have been implemented and become commercially available since. Tsong *et al.* showed that field ionization and field evaporation can also be photon-stimulated [201] and laser field ion microscopes and atom-probes were implemented.

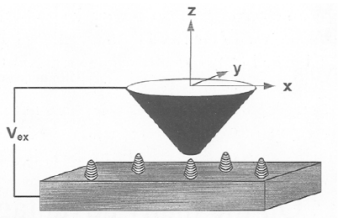

Figure 3.15: Schematic of a local electrode positioned relative to a planar microtip specimen [202].

The addition of a local electrode has improved mass resolution and field of view and requires lower applied voltages to achieve sufficient field strengths for ion evaporation. It also allows the examination of multi tip coupons, as sufficient evaporation fields are only achieved for one tip at a time [202, 203]. A disadvantage of the local electrode is that material from fractured specimens can contaminate the electrode, which will then start field evaporating itself. Therefore these electrodes have to be easily exchangeable in a sensible set-up.

3.9.2 The Local-Electrode Atom-Probe

Figure 3.16: LEAP HR Microscope [204].

Although the LEAP 3000X HR as shown in Figure 3.16 looks a lot more complicated than the simple apparatus in Figure 3.14 the basic principle remains the same. Atoms and molecules are field evaporated and field ionised from a thin, needle specimen. This can be achieved by traditional voltage pulsing or laser pulsing. As mostly less-conductive oxides were studied in this thesis, laser-pulsing was used throughout. The ions are accelerated in the field of an exchangeable local electrode as sketched in Figures 3.15 and 3.17. They pass

the reflectron, which further improves mass resolution. The time-of-flight is recorded when the ions hit a MicroChannel Plate (MCP) which locally amplifies the signal at the point of ion impact before it is detected with a position sensitive detector. With a thorough knowledge of the instrument geometry and an estimate of the field at the tip it is possible to reconstruct the sample in 3D.

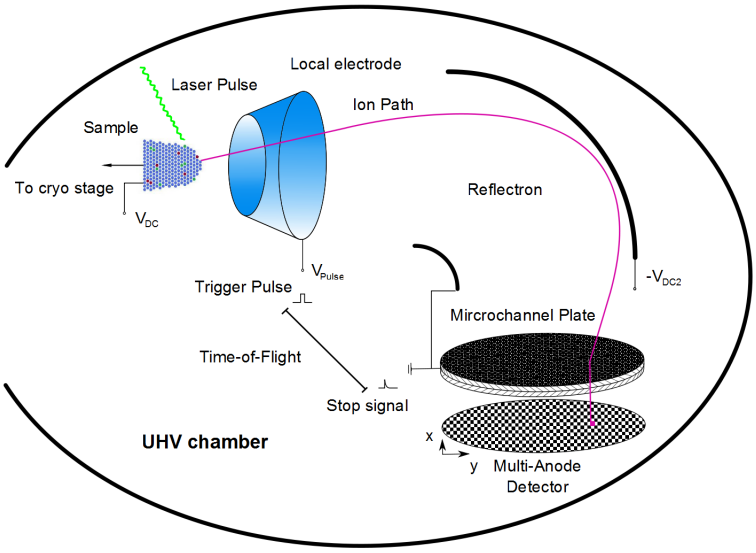

Figure 3.17: Schematic of an APT Experiment [204].

Specimen preparation was performed with FIB milling and specimen were mounted on microtip arrays as shown in Figure 3.18. The LEAP features a maximum field of view of ~150 nm. A laser pulse rate of 200 kHz, a pulse energy of 0.6 nJ and a wavelength of 532 nm was used for the experiments in this thesis.

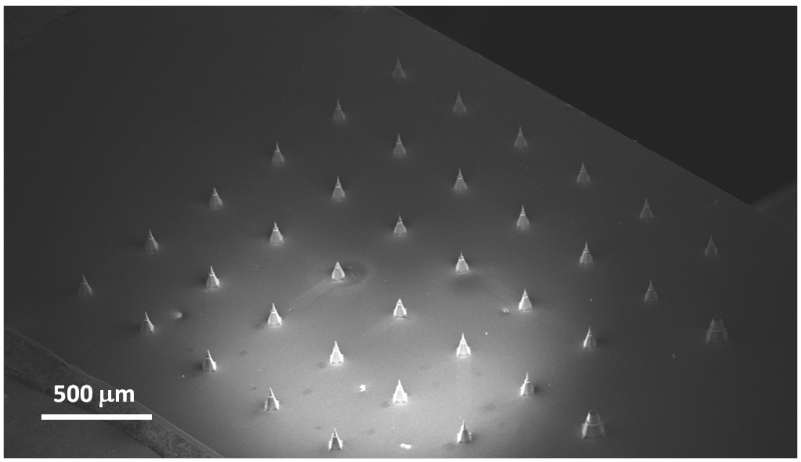

Figure 3.18: SEM image of a microtip coupon.

Data reconstruction was conducted with *Cameca IVAS*. A colour key and a list of the

m/z-ranges used to identify common ions can be found in Apendix B. The software has two ways to reconstruct the data. In the first case it uses the voltage progression and the theoretical evaporation field of the most common element in the sample to calculate the original tip radius and the shank angle of the tip. This type of reconstruction was chosen in most cases. The evaporation field for Fe in a +2 charge state (most common) is 33 V nm^{-1} [205]. However, after comparison of similar features in the APT and TEM data, the evaporation field was corrected to 28 V nm^{-1}. This value is cannot be correct for all parts of a sample containing metal and oxide, as the evaporation fields for those regions are different. In the data this becomes apparent in form of a change of shank angle at the oxide/metal interface.

In the second case, the user puts a tip radius and a shank angle into the software and the data is reconstructed with these starting conditions. If this method is chosen, it results in a constant shank angle (which is more realistic). However, as the real tip radius and shank angle were unknown and had to be estimated, this method was only used, where unstable operating conditions (temperature) had influenced the voltage progression.

In both cases it cannot be guaranteed, that the shape of the features presented is not mildly distorted. However, the reconstruction parameters have no influence on the measured compositions.

Where concentration profiles are shown, the ROI for the profiles was optimised to maximise the information.

Chapter 4

Surface and Grain Boundary Oxidation

The 3D FIB slicing data analysis presented in this chapter has been conducted in collaboration with Dr Lozano-Perez and Mr Iyengar. Much of the data reconstruction was conducted by Mr Iyengar and the statistical analysis was conducted by Dr Lozano-Perez. The data can also be found in [206].

Austenitic stainless steels were thought to be immune to SCC in PWR primary water conditions until controlled autoclave testing recently confirmed SCC susceptibility of highly cold-worked stainless steels in simulated PWR primary water [181]. Shortly thereafter SCC was reported in an operating PWR plant [128]. To understand the role of corrosion in intergranular SCC, surface and GB oxidation was studied in a set of samples with/without cold-work and tested with/without applied stress. A necessary step towards understanding the mechanisms controlling SCC and the influence of cold-work is the development of better methods for characterising oxidation at the nanoscale. The samples studied for this chapter were tested as described in section 3.2. 3D FIB slicing combined with statistical analysis, SEM, ATEM and APT were used to study the extent of oxidation and the chemistry at the oxidation front.

4.1 Results

As only highly cold-worked stainless steels were found to be susceptible to SCC in PWR primary water conditions, the cold-worked samples and the samples with applied stress

	Mean	Sigma	Minimum	Maximum
No CW no stress	139	42	1	268
No CW no stress II	101	56	0	581
No CW stress	189	79	0	1202
CW no stress	132	59	0	934
CW stress	191	77	1	1388

Table 4.1: Statistical analysis of the depth of oxidation (only including Cr-rich spinel) in the different samples analysed. All values in nm [206].

were expected to exhibit greater depths of oxidation, particularly at GBs. 3D reconstructions of the Cr-rich surface oxide of all four samples were produced and the oxidation depth was measured. The results for the maximum oxide depths in Table 4.1 are in line with expected oxidation behaviour. However, GBs and DBs, that had formed in all but the no stress/no cold-work sample, were found to be preferentially oxidised. The mean values given in the table are averaged over several grains, GBs and DBs. Although they correctly display the general trend in the corrosion behaviour, they are not sufficient to describe it accurately. To separate the oxidation depth of different oxidised features, the frequencies of each oxidation depth from the surface for every sample are plotted in histograms in this chapter. Most of the histograms show a bimodal distribution where two peaks can be fitted with Gaussian curves. Each curve is described by

$$I = A\frac{\exp\left(-\frac{4\ln 2(x-x_c)^2}{w^2}\right)}{w\sqrt{\frac{\pi}{4\ln 2}}} \tag{4.1}$$

where I is the intensity to be fitted, A is the amplitude (height) of the Gaussian, w is the width at half height (also known as full-width-half-maximum) and x_c represents the location of the centre of the Gaussian curve. The first Gaussian normally accounts for the matrix oxidation (lower) and the second one for the oxidation of microstructural features such as GBs, dislocations or DBs (higher). The fitting was performed using a Levenberg-Marquardt algorithm [207]. The results obtained from this type of analysis describe the corrosion behaviour in the different samples much more accurately.

All samples were also studied with ATEM. During sample preparation, stresses in the more deformed samples started to relax during the final thinning steps. This led to buckling of the samples, and in some cases prevented sufficient thinning to allow for EFTEM mapping. EFTEM maps are shown for the samples oxidised without applied stresses and the composition of surface and GB oxides was analysed. STEM imaging was performed

for the remaining samples. This did not allow for compositional analysis to be conducted in the GB region, but Z contrast still provides some information about elemental distributions. The thickness of the surface and GB oxide was measured and can be compared with the values obtained from the 3D FIB slicing.

All but the stress/cold-work sample were also studied with APT. Part of the GB oxide could be extracted for every sample and the composition was measured. The results were subsequently compared with the compositional analysis from EFTEM mapping. Additionally, the distributions of the trace elements B and Li, which are present in the PWR water during testing, was studied.

4.1.1 No stress/no cold-work

In the no stress/no cold-work sample neither internal nor external stresses should have been present during oxidation, so a uniform layer of passivating corrosion products was expected to grow at the sample surface. But as will be seen in the results presented, small amounts of deformation that had remained in the near-surface region from the final grinding and polishing steps had an effect on oxidation.

3D FIB slicing

Two regions in this sample were characterised with 3D FIB slicing. The first analysed region covered an area of 18.5×11.8 μm^2 at a data resolution of 10×10×69 nm^3. The 69 nm corresponds to the thickness of each FIB slice. This region includes two grains separated by a GB. Figure 4.1 shows a view from below onto a 3D model of the Cr-rich spinel and the respective thickness plot, generated as explained in section 3.6.2. The oxidation depth was analysed in the different regions and the results are shown in Table 4.2.

	Average Oxidation Depth
Grain 1	141±28 nm
Grain 2	137±53 nm
GB	no preferential oxidation

Table 4.2: Statistical analysis of the depth of oxidation (only including Cr-rich spinel) in Region 1 of the no stress/no cold-work sample [206].

The oxidation depth distributions for both grains are visualised in the histogram in Figure 4.2a. The frequency of occurrence of the particular oxidation depths measured perpen-

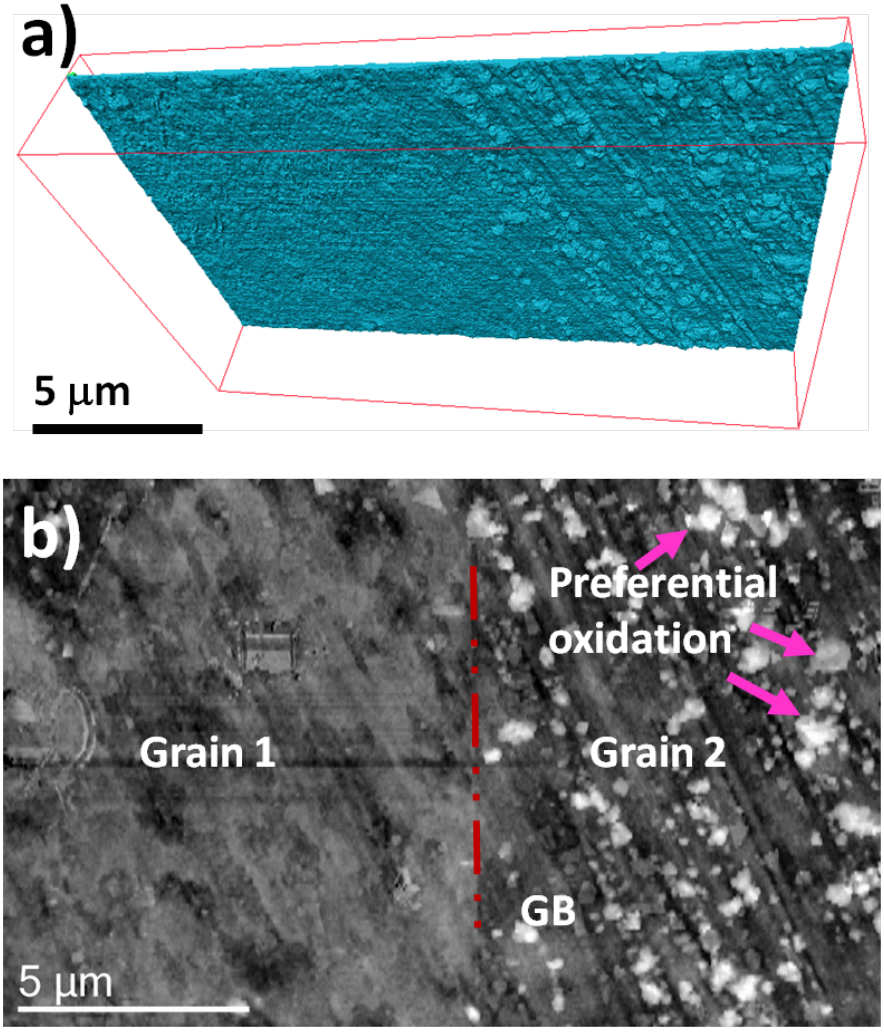

Figure 4.1: a) 3D model of the Cr-rich spinel oxide and b) Oxide thickness plot from the no stress/no cold-work sample (Region 1) [206]. The scale ranges from 0 nm (black) to 375 nm (white).

dicular from the surface is plotted on the vertical axis and the different oxidation depths are on the horizontal axis. The average oxidation depths of the two grains are slightly different, which can be attributed to the different crystallographic orientations in the grains. An individual histogram for Grain 2 is shown in Figure 4.2b; the data was fitted by two Gaussian peaks, due to the observed bimodal distribution. The origin of the second peak can be easily identified in both the 3D model of the oxide and the thickness plot. The peak corresponds to the preferentially oxidised regions that appear bright in the thickness plot of grain 2. The GB (vertical in Figure 4.1), did not oxidise preferentially.

The second analysed region covered an area of 19.1×8.7 μm^2 and the voxels used in the reconstruction were 13×13×59 nm^3 in size. The 59 nm corresponds to the thickness of

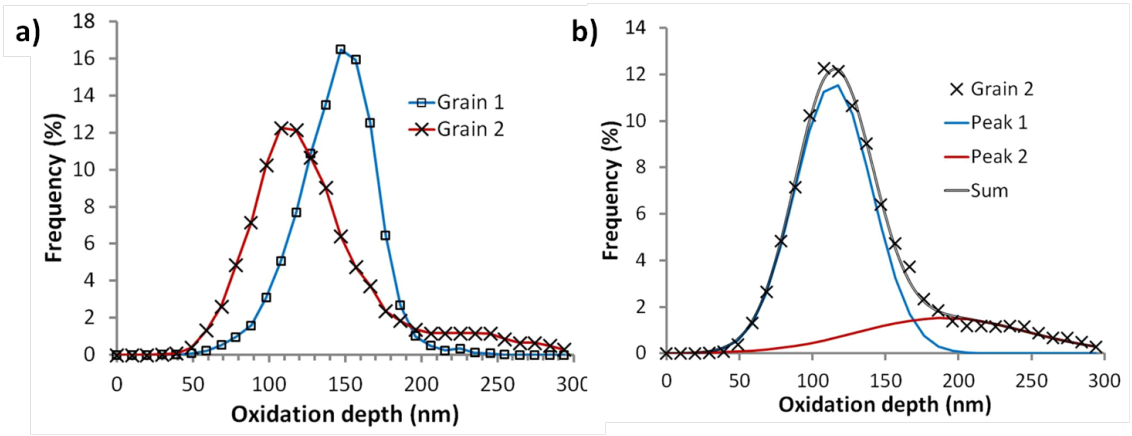

Figure 4.2: Plots showing the frequency of occurrence the particular oxidation depths. a) Histogram showing the different oxidation behaviour in the grains and b) fitting of the bimodal distribution in Grain 2 by the sum of two Gaussians, for the no stress/no cold-work sample (Region 1) [206].

the FIB slices. This region included 3 grains separated by 3 different GBs. A 3D model of the Cr-rich spinel and its thickness plot, generated as explained in section 3.6.2, are shown in Figure 4.3. The oxidation depth in the separate areas was analysed, the results can be found in Table 4.3.

	Average Oxidation Depth
Grain 1	86±57 nm
Grain 2	120±38 nm
Grain 3	102±57 nm
GB1	234±109 nm
GB2	no preferential oxidation
GB3	243±98 nm

Table 4.3: Statistical analysis of the depth of oxidation (only including Cr-rich spinel) in Region 2 of the no stress/no cold-work sample [206].

Histograms plotting the frequency of oxidation depth, for the different grains are shown in Figure 4.4a. Grain 1 and grain 3 both have a bimodal distribution. As above the lower peak at greater oxidation depths is due to the near-surface defects. Grain 2 is generally oxidised to a greater depth, but the respective histogram does not show a second peak corresponding to oxidised defects. This region contained some preferentially oxidised GBs (GB1 and GB3). A volume containing the GB region around GB3 was extracted from the data set and an individual histogram, which can be found in Figure 4.4b, was generated. The bimodal distribution in this histogram is due to matrix areas that were contained in the analysed volume. Peak 2, the peak at greater oxidation depth, describes the GB oxidation. GB2 did not seem to be preferentially oxidised.

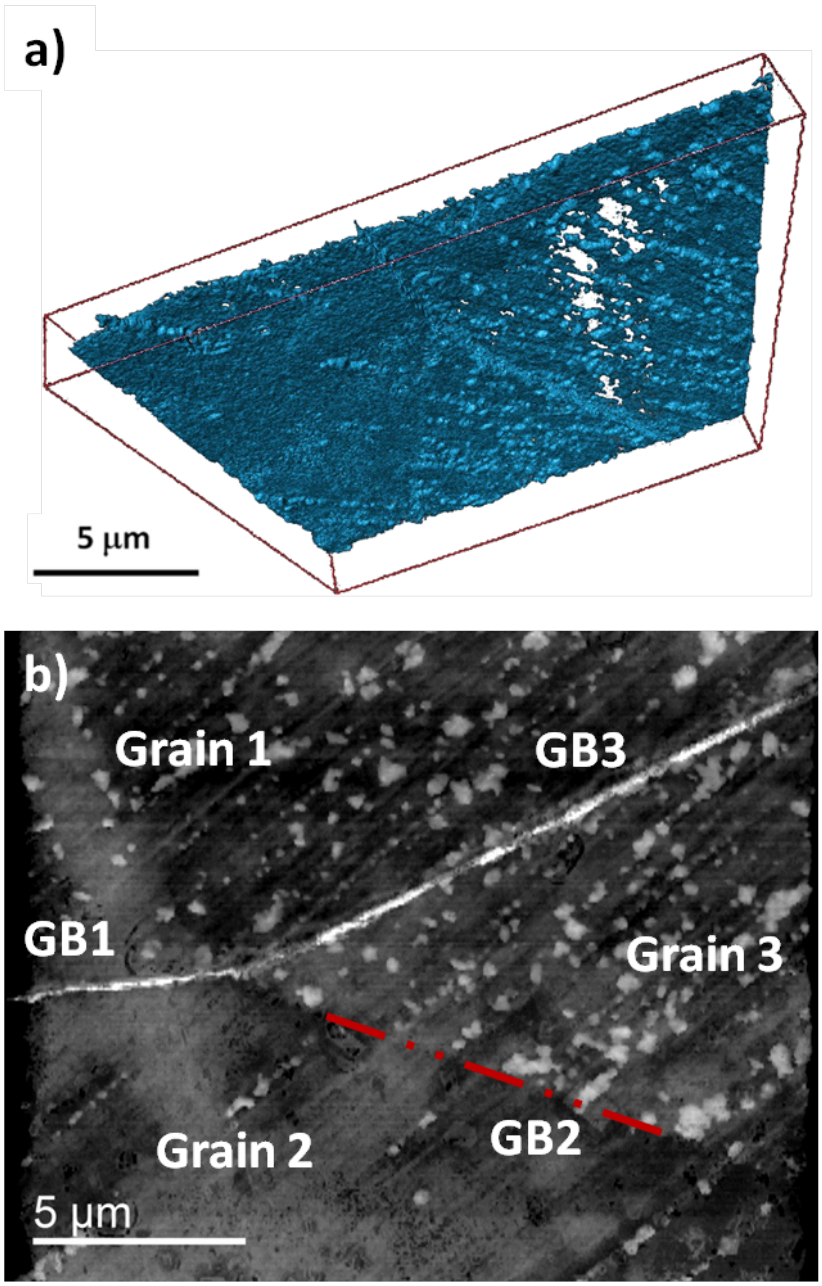

Figure 4.3: a) 3D model of the Cr-rich spinel oxide and b) oxide thickness plot from the no stress/no cold-work sample (Region 2). The scale ranges from 0 nm (black) to 570 nm (white).

Analytical Transmission Electron Microscopy

The ATEM data in this section was acquired using the JEM-2100 following FIB lift-out as described in section 3.7.

Figure 4.5 shows a TEM BF image of the no stress/no cold-work sample. The GB in the sample corresponds to GB1 in Figure 4.3, the left grain corresponds to Grain 1 and the right grain corresponds to Grain 2. The displayed region contains the oxidised surface

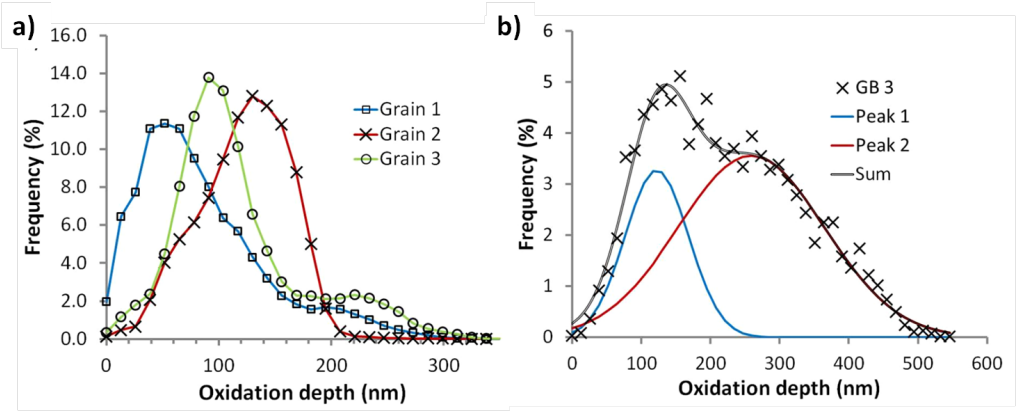

Figure 4.4: Histograms showing a) the frequency of the different oxide depths (measured from the original surface) of the two grains and b) the oxidation behaviour of GB 3 fitted by the sum of two Gaussians, in the no stress/no cold-work sample (Region 2) [206].

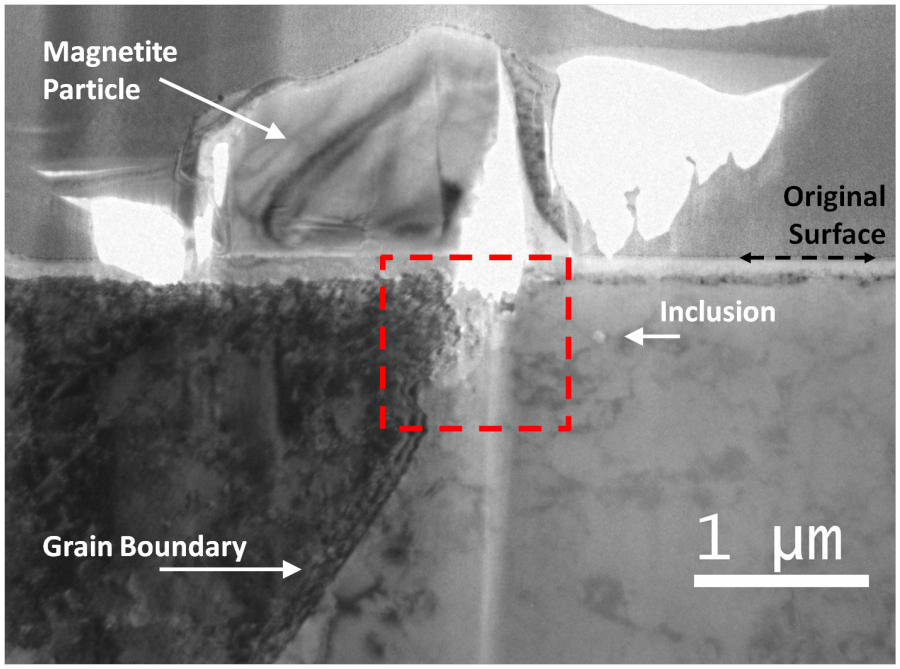

Figure 4.5: TEM BF image showing a cross-sectional no stress/no cold-work sample containing an oxidised GB. Elemental maps of the boxed region can be found in Figure 4.6.

(inner oxide) and an oxidised GB. A magnetite particle has grown on top of the original surface over the left grain (outer oxide). The holes in the protective C layer and the surface oxide region at the top half of the sample are FIB damage from the final thinning step. The brighter streak vertically in the centre of the image is also a thickness effect from the FIB preparation. In the BF image the left grain appears darker, because it is near a zone axis, allowing the observation of its high density of dislocations.

The thickness of the surface oxide was measured to be 127±23 nm on the left grain and 98±10 nm on the right grain. This is consistent with the measurements from 3D FIB

slicing. The GB oxide depth at this part of the GB is 680 nm, which is much deeper than the average depth of GB1 measured in the 3D FIB slicing data (234±109 nm). The oxide regions can be identified more easily in the EFTEM elemental maps of the boxed region. The maps are shown in Figure 4.6.

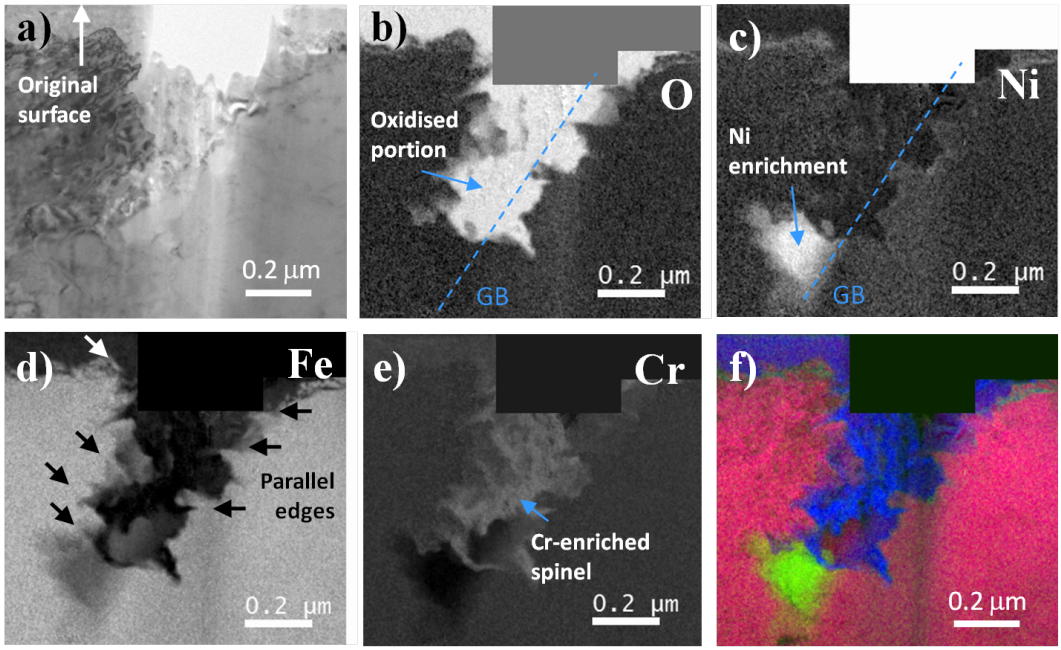

Figure 4.6: a) TEM BF image showing a close-up on the GB oxide in the boxed region in Figure 4.5. The original sample surface of this no stress/no cold-work sample lies horizontally at the top edge of the map. b) Thickness map of the same region. c)-f) EFTEM elemental maps. f) RGB map showing the Fe in red, Ni in green and Cr in blue.

A thickness map was obtained from the boxed region with t/λ (thickness/mean free path) having an average value of ~1 in the matrix. The GB oxide in Figure 4.6b was 320±67 nm wide on average, it extended predominantly into the left grain, but the right grain was also affected. The outer edges of the oxide portion had a zig-zag shape on both sides. The arrows in Figure 4.6d indicate some parallel edges of the oxide portion. Figure 4.6c shows Ni enrichment at the interface between the surface oxide and the matrix and to a limited extent at the edges of the GB oxide. A large Ni-rich particle was found at the oxide front. The Ni EFTEM map shows a gradual increase in the Ni concentration from the outer edges of this particle to its centre. The average Ni concentration in this particle was over 60 at.%. The projected dimensions of the Ni enriched particle were $\sim 220 \times 200$ nm. Comparison of its position in the Ni map with the BF image in Figure 4.5 reveals that the Ni enrichment is mostly confined to the left grain. A schematic of all the described features is shown in Figure 4.7.

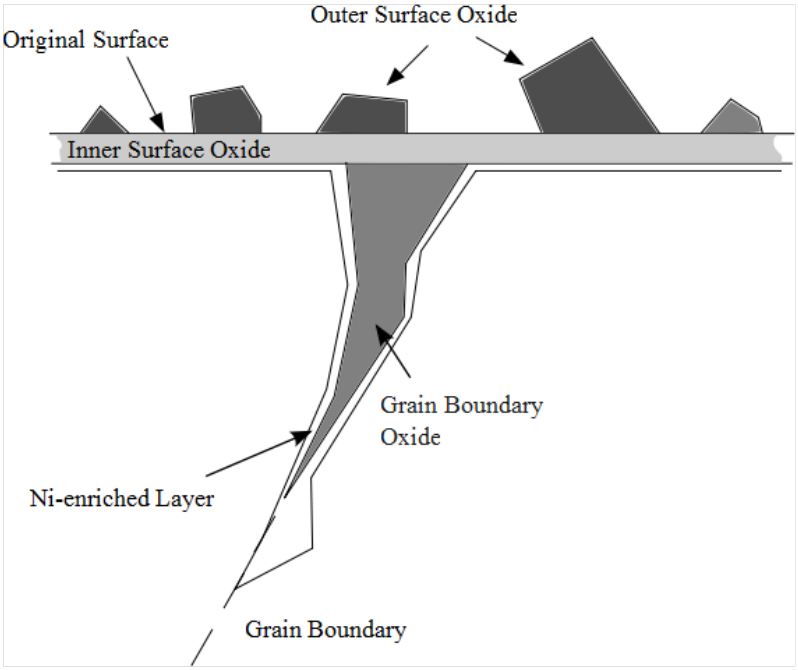

Figure 4.7: Schematic of the oxide structures forming during oxidation of austenitic stainless steel at moderate temperatures in aqueous solution [142, 208, 209].

EELS spectra were extracted from the EFTEM data set and the local compositions were analysed. The measured compositions are given in Table 4.4.

Conc. (at.%)	**Fe**	**Cr**	**Ni**	**O**
Matrix	71±2	19±1	10±1	omitted
surface oxide	20±2	22±2	3±1	56 ± 7
GB oxide	16±3	27±2	3±1	54±7
metallic Ni enriched region	36±2	4±1	61±10	omitted

Table 4.4: The concentrations measured in the EFTEM maps in Figure 4.6. Oxygen was omitted in the EFTEM quantification of the metallic features, as it can be attributed to surface oxidation of the TEM foil (6 at. % were measured).

The ratio of the main elements, Fe, Cr and Ni, in the matrix region were consistent with the nominal composition. The O and Ni concentrations measured in the surface and GB oxides were consistent within the margins of error. However, the Fe:Cr ratio in the surface oxide was almost 1:1, while the Cr content was much higher in the GB oxide. This also shows in the Cr elemental map (Figure 4.6e), where parts of the GB oxide are bright, while there is no difference in contrast between matrix and surface oxide. The O map (Figure 4.6b) shows that the GB oxide extends beyond the Cr-rich regions. Part of the GB oxide seems to be more similar to the surface oxide.

The surface oxide present was characterised with TEM BF imaging (see Figure 4.8a). The original sample surface lies horizontally at the top edge of the map. Although the

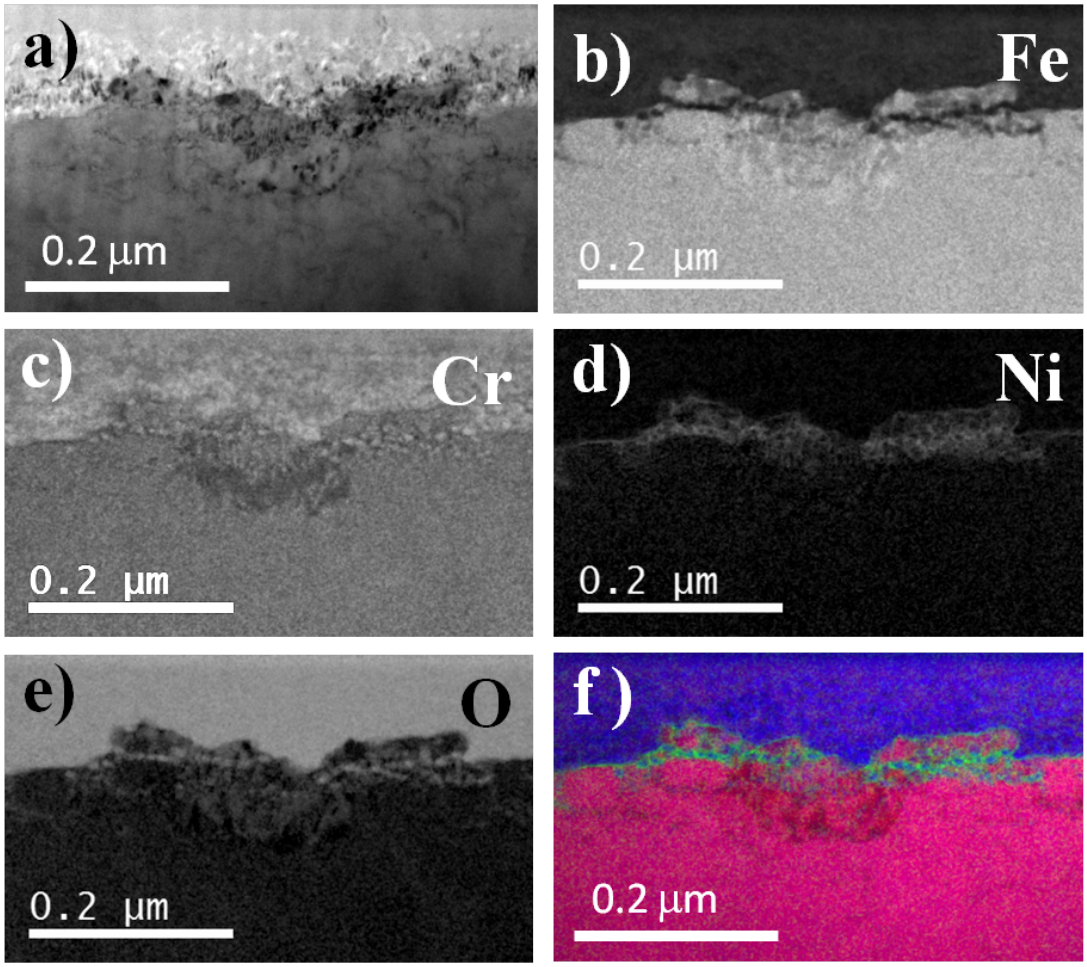

Figure 4.8: a) TEM BF image showing the surface oxide and the near surface defects of a no stress/no cold-work cross-sectional sample. The original sample surface lies horizontally at the top edge of the map. b)-e) EFTEM elemental maps. f) RGB map showing the Fe in red, Ni in green and Cr in blue.

sample was not exposed to stress or CW, a dislocation network can be observed extending 200 nm from the original surface at the top edge of the maps into the sample. The surface oxide seems to be thinner in the central area of the map and the oxide/metal interface is not parallel to the original surface, but seems to follow the dislocation structure near the surface. In the areas, where the oxide appears thinner, the EFTEM oxide map in Figure 4.8e shows oxidised dislocations ahead of the bulk oxide. Every oxidised portion is surrounded with a Ni enriched layer. The Ni enrichment seems to be particularly enhanced around the oxidised dislocations.

Atom-Probe Tomography

The same GB as above was studied with APT. The samples were lifted out as described in section 3.7. The marked region in the elemental map in Figure 4.9a shows where the APT needle was lifted out. All ions of data set A are displayed in Figure 4.9b and a schematic with its most important features in Figure 4.9c. Figure 4.9d shows the individual ion maps generated from the APT data reconstruction. When looking at 3D ion maps in a 2D projection, it is important to be aware of density effects. A higher density of dots (ions) in the map can represent a greater concentration of the ion type or a higher density of all detected ions. An ion density map with all detected ions is shown in the left of Figure 4.9d. This shows decreased density in the surface oxide and the bulk of the GB oxide in data set A and increased density in the GB and dislocation oxide with respect to the matrix.

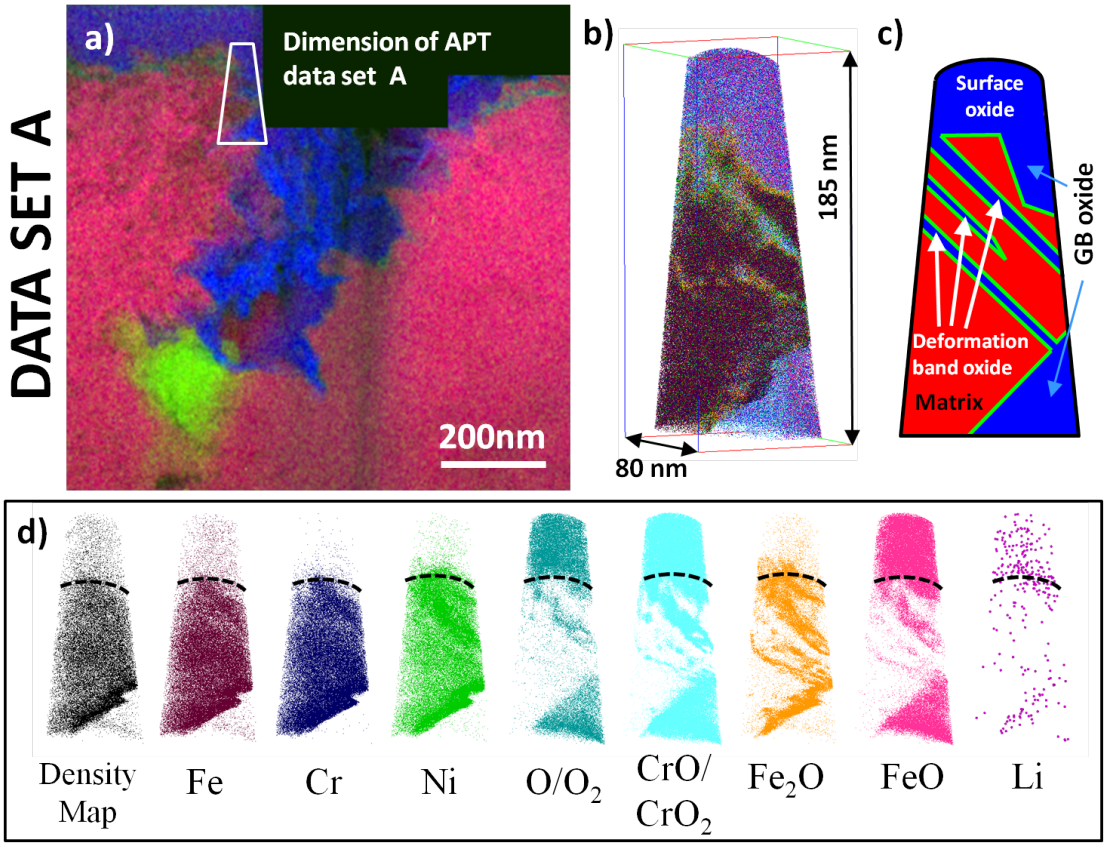

Figure 4.9: a) EFTEM elemental map, showing a position representative for the position the APT data set A was collected from. b) All ions of data set A, acquired from the no stress/no cold-work sample. c) Schematic showing the main features of data set A. d) Ion maps showing the distribution of the individual ion types within the data set. The dashed lines indicate the position of the interface between the surface oxide and the other features of the sample.

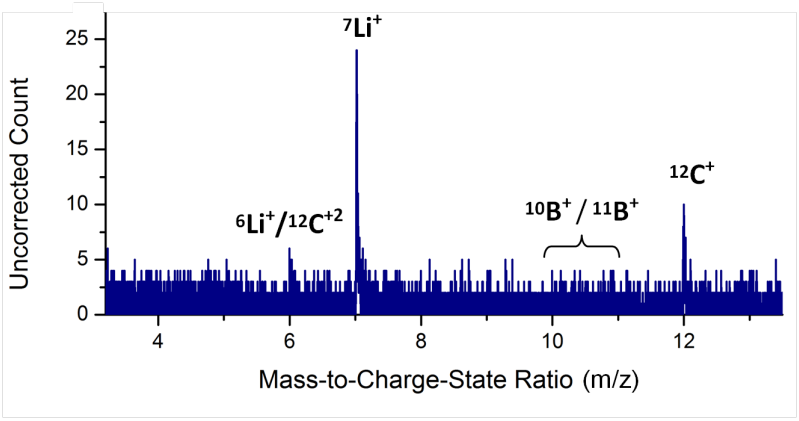

Figure 4.10: Part of the mass spectrum for data set A showing the Li peaks at 6 and 7 m/z and the absence of any B signal above the noise.

The APT data does not contain the centre of the GB oxide, but a portion from the left side. At the top of the data set is the surface oxide, below lies the metallic matrix disrupted by oxidised dislocations running across the entire data set. At the bottom right of the APT data set the GB oxide comes into view. Although the analysed oxide is about 50 nm wide at the bottom of the data set, this is only a small part of the widespread GB oxide around this part of the GB as the white box in Figure 4.9a indicates. It is striking that the O/O_2, CrO/CrO_2 and FeO ions were evaporated from all core oxide regions, while Fe_2O ions were only evaporated from the interface regions and the probably more weakly oxidised regions in the oxidised dislocations. This will be a common observation in this chapter. The author believes that Fe_2O was evaporated from regions in which oxides were only starting to grow, but no stoichiometric phase had formed at the the end of the corrosion test. The last of the individual ion maps in Figure 4.9d shows the Li distribution in the data set, which was present in all oxide regions. As shown in the extract from the mass spectrum of data set A (Figure 4.10), no B peak is discernible above the background noise found for this sample.

APT data of a different, only mildly oxidised GB (comparable to the GB in Figure 4.1 or GB2 in Figure 4.3) is shown in Figure 4.11. In the edge-on view it can be seen that the oxidation in data set B is mostly limited to the GB plane. The oxide that started to grow in the neighbouring dislocations has not extended sufficiently far into the metal matrix to form a bulk oxide as in data set A. A side-on view on the extracted GB plane in Figure 4.12 shows that the GB oxide is discontinuous. The oxide particles in the GB plane are too small for analysis of their internal composition, but the concentration profile through a

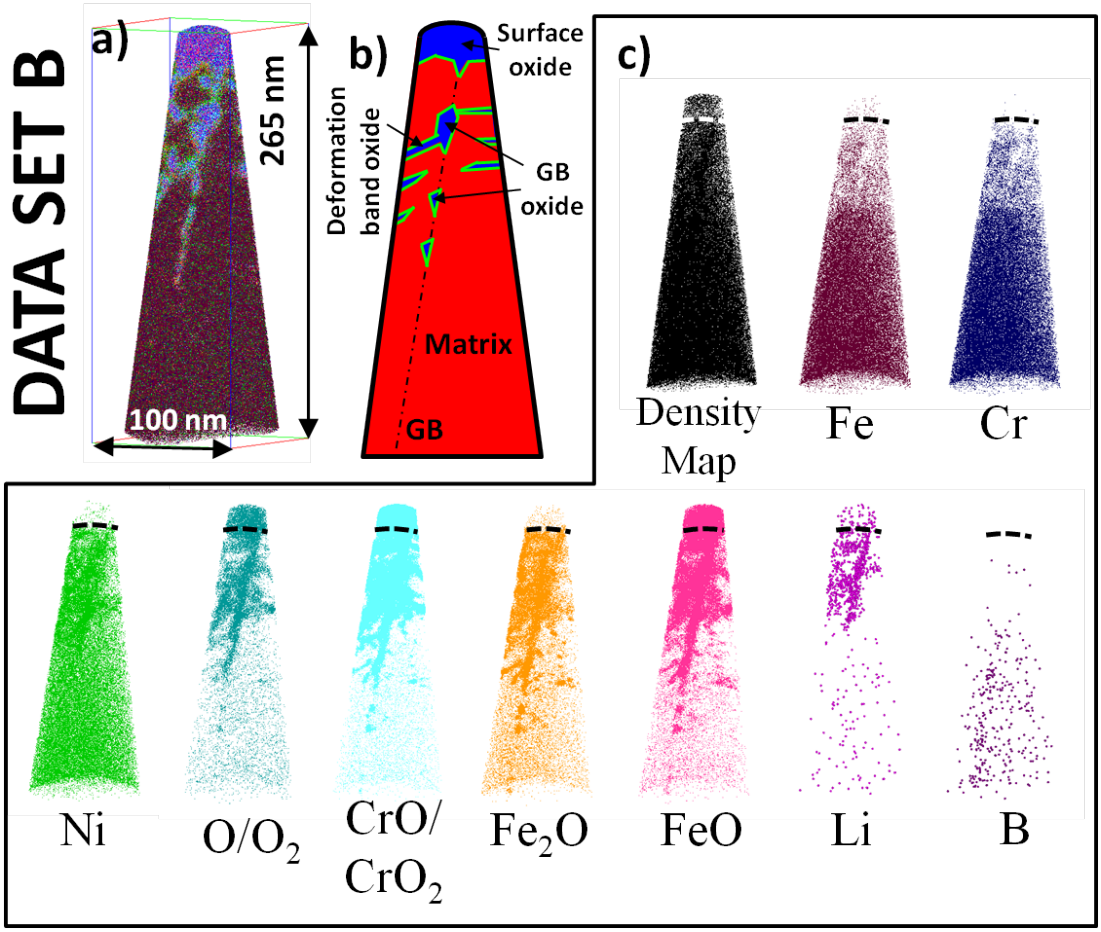

Figure 4.11: a) All ions of data set B, acquired from the no stress/no cold-work sample. b) Schematic showing the main features in data set B. c) Ion maps showing the distribution of the individual ions in data set B. The dashed lines indicate the position of the interface between the surface oxide and the other features of the sample.

slightly bigger representative particle in Figure 4.12d shows that the O concentration in the centre of the particles still reaches about 30 at.%. The ion maps in Figure 4.11c show that O and O_2 ions are only evaporated from the regions with the highest O concentration. The Fe_2O map shows that some oxygen is still present in many small clusters outside the GB plane. As in section 4.1.1, this ion species is not evaporated at all from the bulk surface oxide (position indicated by the dashed line). While the density of metallic Cr and Fe is lower in the dislocation rich region near the surface oxide, the density of metallic Ni is higher, suggesting that Ni enrichment is lining oxidised dislocations, as observed in the EFTEM data (Figure 4.8). While Li is only present in the oxide regions on the surface and in the GB, B can only be found in the unoxidised part of the GB (see Figure 4.12b).

The respective regions of three APT needles were analysed to obtain the local composi-

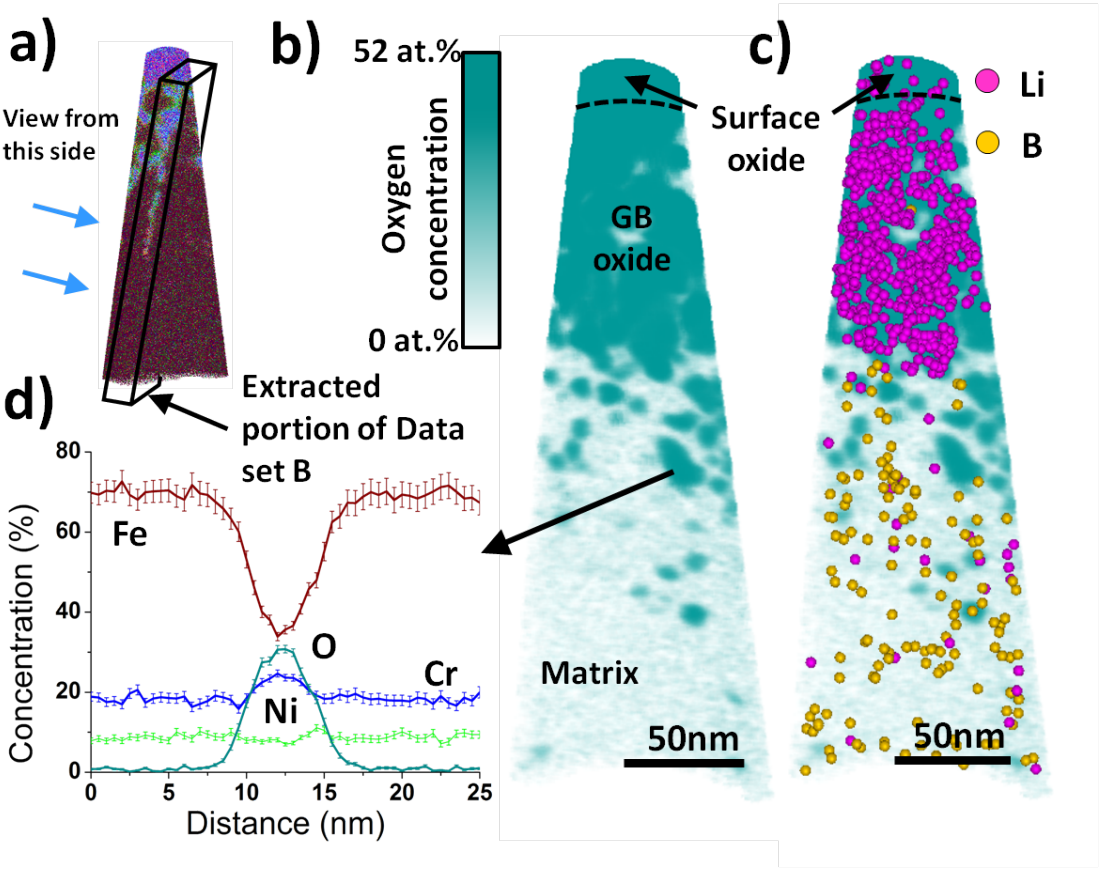

Figure 4.12: Extracted GB from data set B in plan view. a) Schematic showing how the GB plane was extracted. b) Oxygen concentration in the GB plane in projection. 52 at. % O was measured in the surface oxide. c) Map in b overlaid with the distribution of B and Li atoms in the GB plane. d) Concentration profile through indicated oxide particle in the GB plane (bin size used $\approx$ 0.5nm).

tions. All compositions measured with APT can be found in Table 4.5. Only the two data sets presented contained GB oxides. The errors indicated in the table account for the variations between datasets. The core regions of the GB oxide in data set A and the surface near "bulk" GB oxide in data set B were analysed to obtain the GB composition. The concentrations of some lower concentration elements are also listed.

Conc.	**Fe**	**Cr**	**Ni**	**Mn**	**Si**	**C**	**O**
Matrix	68.2±0.7	19.6±1.2	9±0.4	1.4±0.2	0.49±0.01	0.07±0.03	0.7±0.1
Surf Ox	23.1±1.9	21.9±0.2	2.6±1.5	0.8±0.2	0.02±0.01	0.3±0.1	50.8±0.2
GB Ox	28.6±4.1	23.4±2.2	2.4±1.6	1.2±0.1	0.01±0.01	0.19±0.01	43.7±8.2

Table 4.5: Compositions of the different features in the no stress/no cold-work sample measured with the APT in at. %.

4.1.2 Stress/no cold-work

The sample analysed in this section has been oxidised with an applied load, so that the stress remained below the yield strength (see Section 3.2). The sample was solution treated at 1060 °C prior to the corrosion test, so potentially present residual DBs should have been removed. It will be shown that, although no plastic deformation was expected, DBs were frequently observed in the stress/no cold-work sample after the corrosion test. A more detailed analysis of the preferential oxidation observed in these DBs can be found in Chapter 5.

3D FIB slicing

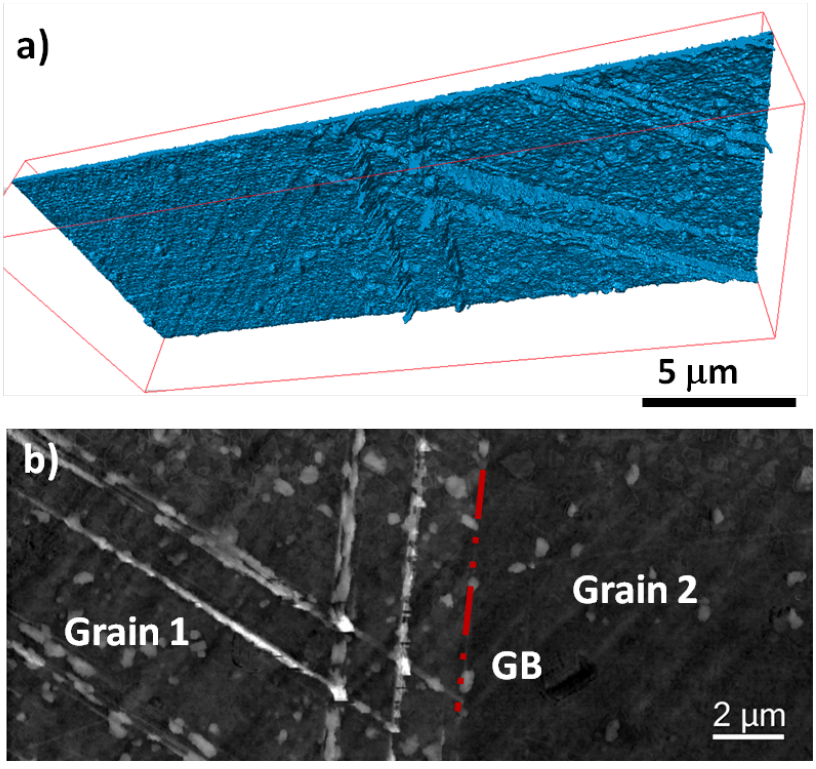

Figure 4.13: a) 3D model of the Cr-rich spinel oxide and b) oxide thickness plot from the stress/no cold-work sample [206]. The scale ranges from 0 μm (black) to 1.2 μm (white).

A region of 22.5×9.3 μm^2 at the surface was analysed with 3D FIB slicing. The voxels used in the reconstruction were 12×12×42 nm^3 in size. This region included one GB and two grains. A 3D model of the Cr-rich spinel and its oxide thickness plot, generated as explained in section 3.6.2, are shown in Figure 4.13. The view on the 3D model is from below, so that the oxides that have grown into the DBs, can be seen. The GB did not seem to be preferentially oxidised.

	Average Oxidation Depth
Grain 1	214±95 nm
Grain 2	159±35 nm
GB	no preferential oxidation

Table 4.6: Statistical analysis of the depth of oxidation (only including Cr-rich spinel) in Region 1 of the stress/no cold-work sample [206].

The depth of the oxides in the different regions was measured and the results can be found in Table 4.6. Several preferentially oxidised DBs are crossing grain 1 leading to a greater average oxide depth. The histogram in Figure 4.14a shows that the maximum of the first peak for grain 1 is much closer to the maximum of the peak for grain 2, at about 180 nm. Even considering this, the average oxidation depth is greater than that of all grains observed in the no stress/no-cold-work sample. A histogram describing the oxidation of an individual DB is shown in Figure 4.14b. Peak 1 can be attributed to the matrix oxide and peak 2 describes the oxidation in the extracted DB, the average oxide depth was 397±418 nm.

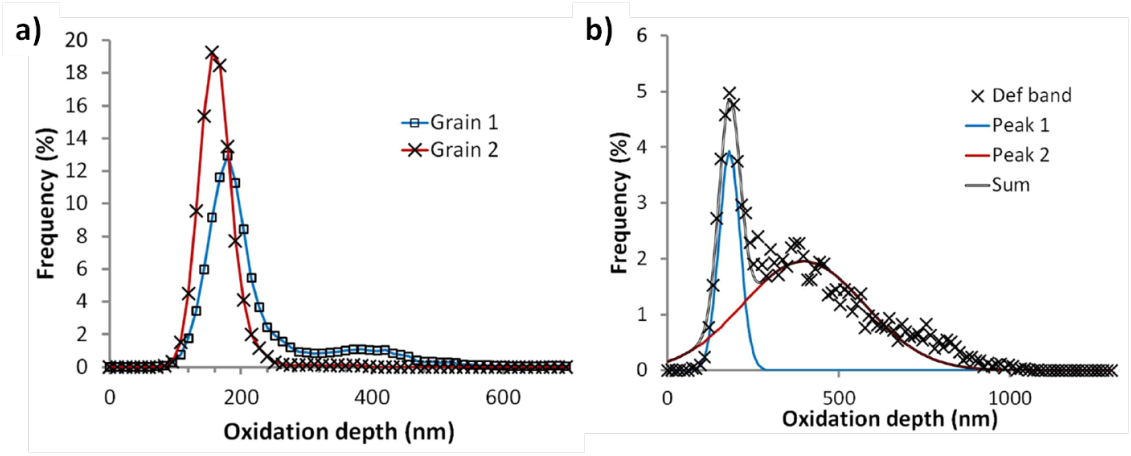

Figure 4.14: Histograms showing a) the different oxidation behaviour of the two grains and b) oxidation behaviour of one of the oxidised deformation bands fitted by the sum of two Gaussians, in the stress/no cold-work sample.

For the FIB sample preparation, GB sections were selected and cut free from the surrounding material as described in section 3.7. During this procedure, cross sections through the sample were revealed. One of these cross sections of the stress/no cold-work sample, imaged with SEM, is shown in Figure 4.15. Figure 4.15a shows an SEM in-lens image, with a mildly oxidised GB indicated by the blue arrow. The centre shows a deformation band, with a narrow localised oxide extending about 800 nm deep in the material. The right side shows a region where two systems of slip bands crossed (see pink and blue arrows

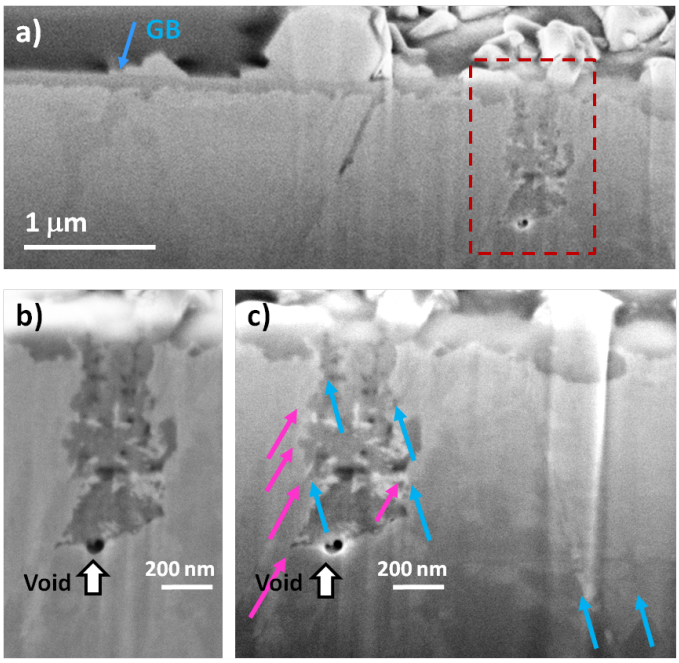

Figure 4.15: SEM images of cross-sections in the stress/no cold-work sample. a) SEM in-lens image showing a GB on the left side, an a heavily oxidised crossing point of two systems of slip bands in the dashed red box. b) SEM SE image of the oxidised region. The white arrow points at a very dark circular region. c) The circular region is still visible in the SEM in-lens image.

in Figure 4.15c). The oxide is about 1 μm deep and 300 - 400 nm wide. Figures 4.15b and c both show a close-up on the boxed oxide region. Figure 4.15b shows the secondary electron image. A round dark region of about 75 nm in diameter, indicated by the white arrow, is located at the oxidation front. In this micrograph it could be a void or an inclusion consisting of lighter elements (Z-contrast). In the more edge-sensitive in-lens image (Figure 4.15c) however, the feature looks like a hole or bubble. Although this was not an observation commonly made in the analysed samples, it appears that the formation of voids ahead of stress enhanced oxide regions is possible.

Analytical Transmission Electron Microscopy

STEM imaging was used to characterise a GB in the stress/no cold-work sample. The internal stress caused the sample to bulge during the final thinning steps in the FIB and prevented sufficient thinning for EFTEM imaging in the GB region. However, the Z-contrast allows some assumptions about local compositions. The matrix and surface oxide were characterised with EFTEM in other, thinner regions of the sample. The maps are presented in Chapter 5. Figure 4.16a shows a BF image of the GB and Figure 4.16b shows

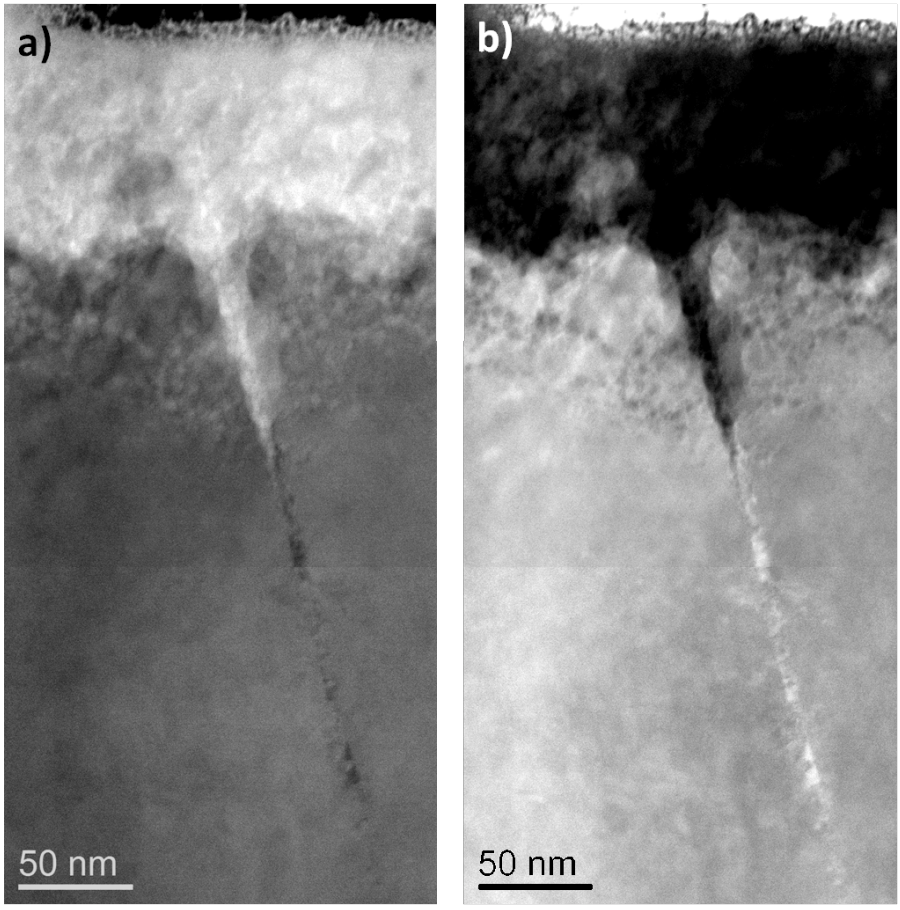

Figure 4.16: STEM micrographs of the stress/no cold-work sample. a) BF image. b) ADF image.

the ADF image. The oxide region appears bright in the BF image and dark in the ADF image. There was no significant difference in the surface oxide thickness in the two grains. The thickness of the oxide on the right grain was 103±18 nm and on the left grain it was 99±21 nm. The oxide in the GB has an oxide depth of 208 nm.

Atom-Probe Tomography

The GB studied with APT does not correspond to the GB shown in the STEM data in Figure 4.16. Figure 4.17 shows all ions of the data set from different sides and Figure 4.17a shows a schematic with the main features of the data set. The dark maroon areas were the steel matrix, the blue and purple regions were Fe and Cr-rich oxides and the green regions were Ni-rich. The black region at the top is the C cap from the FIB sample preparation. One side of the data set was occupied by the GB oxide. It is in full view at 180° rotation. Additionally, there were many oxidised fingers and curved surfaces, that may be oxides that have grown along dislocations pervading the matrix near the bulk oxide.

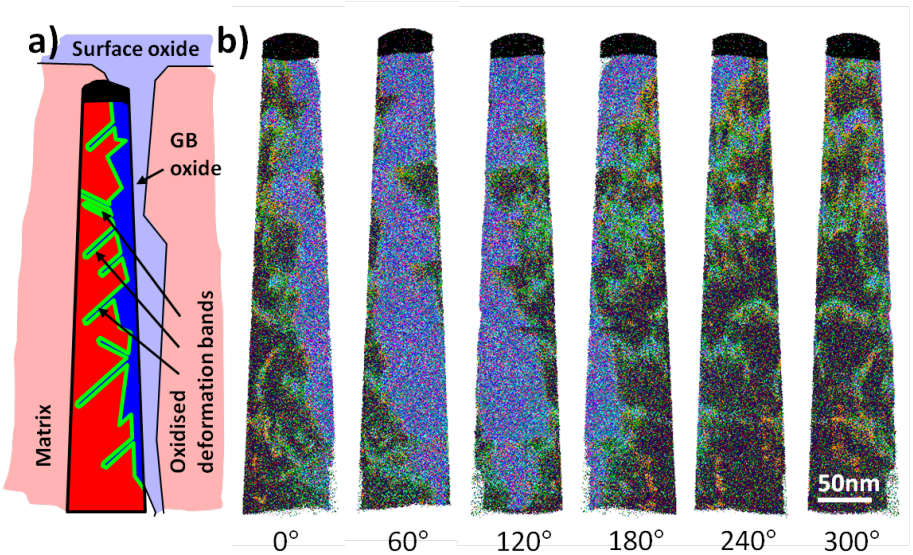

Figure 4.17: APT data set of the stress/no cold-work sample. a) Schematic showing the main feature in the data set and its origin in oxidised sample. b) Distribution of all ion types from different angles. A colour key for all ions can be found in Appendix B. The black region at the top is the C cap from the FIB sample preparation.

Figure 4.18 shows the separate ion maps of the stress/no cold-work sample. The GB oxide is at the top edge of the images. The Li map on the bottom of the figure seems to show higher Li concentrations in the oxide portions away from the GB than in the bulk oxide. The composition of the dominant features in this and two other sample were also determined. The errors given account for the variations between analysed regions. A reason for repeated fracture of this sample type might be the high number of oxidised dislocations in the GB region. The matrix composition in this material was consistent with the previously reported data. The composition of the regions can be found in Table 4.7.

Concentration	**Fe**	**Cr**	**Ni**	**Mn**	**Si**	**C**	**O**
Matrix	66.6±1.5	18.3±0.1	9.7±0.7	1.5±0.1	0.53±0.17	0.1±0.02	2.5±1.2
Surface Oxide	19±0.5	23.7±0.7	2.6±0.9	0.8±0.1	0.03±0.02	0.5±0.4	52.8±0.1
GB Oxide	23±1.1	21.9±1	3.3±2.8	1.1±0.1	0.02±0.01	0.5±0.4	49.3±2.2

Table 4.7: Compositions of the different features in the stress/no cold-work sample measured with the APT in at.%.

Figure 4.19 shows a slice of 3 nm thickness through the APT data set. Iso-concentration surfaces of 22 at.% O and additionally at 12 and 22 at.% Ni are shown. The value of 22 at.% O was chosen in this case, in order to highlight the oxide particles away from the GB oxide, which are only completely oxidised in their centre. The respective high concentration sides are shaded. The GB oxide is the large oxide region on the left side

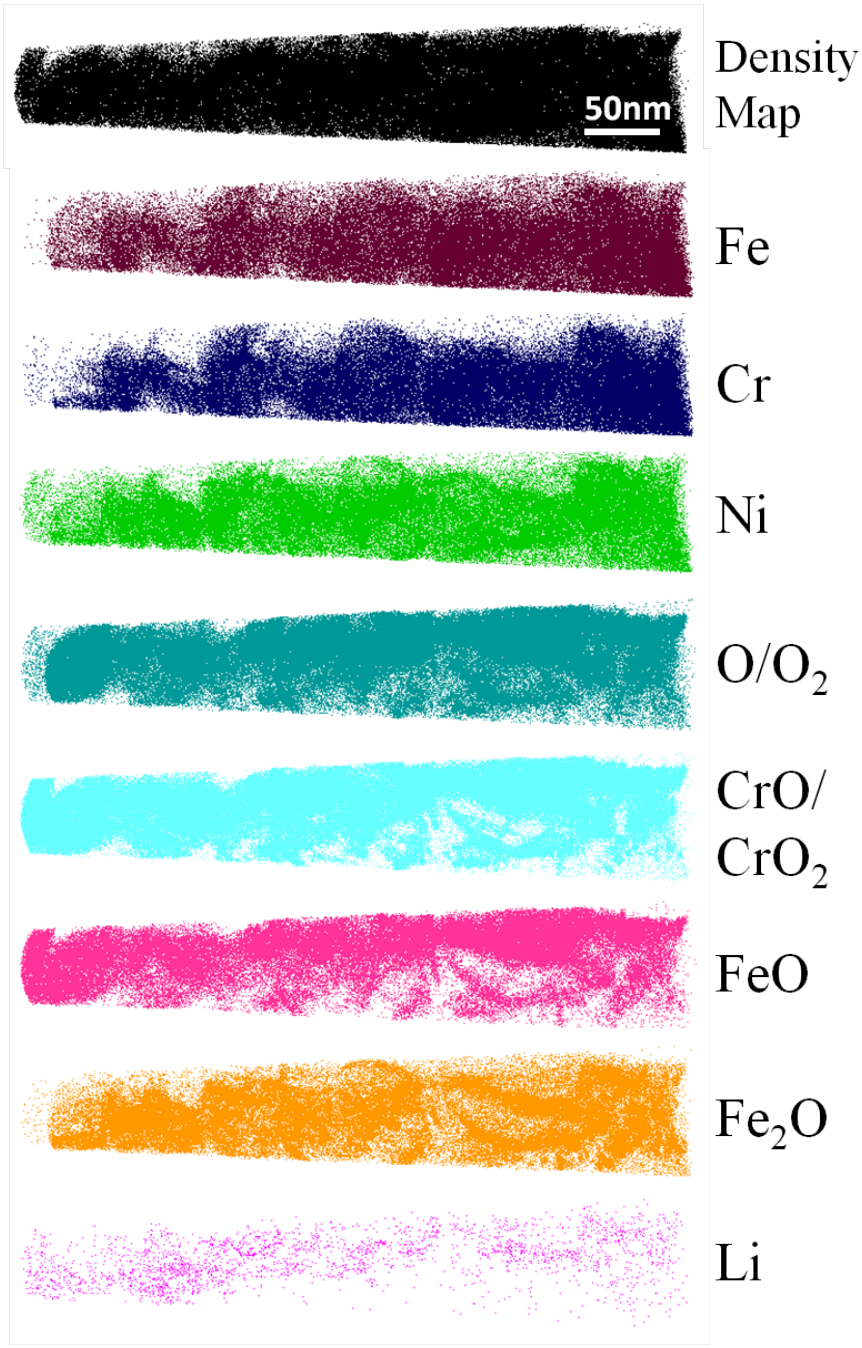

Figure 4.18: Ion maps of the stress/no cold-work data set introduced in Figure 4.17. The GB oxide is in cross sectional view at the top edge of the samples in this orientation (corresponding to the 0° angle in Figure 4.17).

of the slice. The bulk Ni concentration is about 9 at.%. It can be seen that the Ni concentration is greater than 12 at.% near the GB oxide and around the oxide particles along the two marked dislocations. The right side image shows an iso-concentration surface at 22 at.% Ni. It becomes evident that the highest Ni concentrations can be found around and in between the oxide particles along the dislocations.

Figure 4.20 shows two presentations for three different slices extracted from the same data

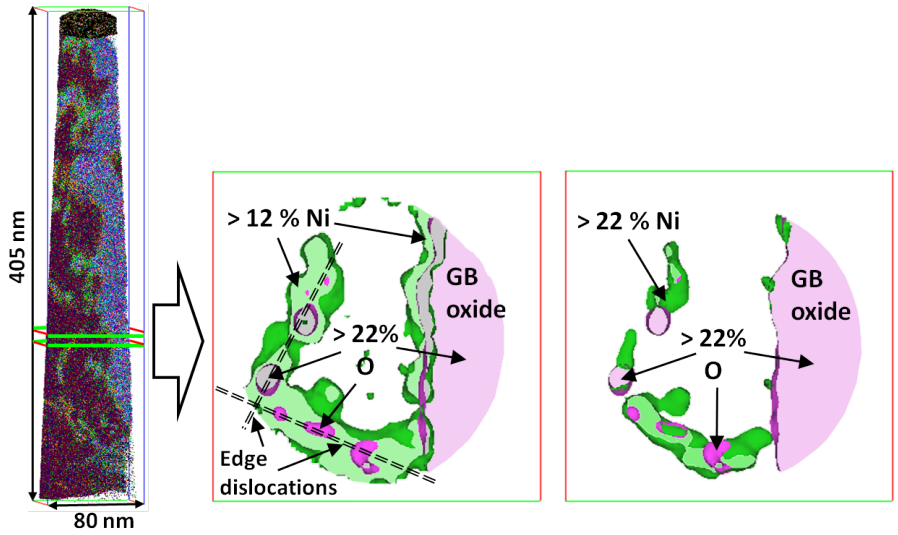

Figure 4.19: Two presentations of a 3 nm thick slice perpendicular to the z-axis of the stress/no cold-work data set as indicated in the full data set on the right. In both versions an iso-concentration surface at 22 at.% O is inserted in pink and the high gradient side is coloured in accordingly. The left image shows how Ni enrichment (>12 at.%) envelopes all oxide regions. Double dashed lines mark the position of two edge dislocations lined with oxide particles. The right image shows where Ni in higher concentrations (>22 at.%) is located. Only small regions are at the GB oxide/matrix interface, but much Ni has concentrated around and in between the oxide particles along the dislocations.

set as indicated. Each slice is 2 nm thick (this corresponds to about 8 close-packed lattice planes). In all three slices, some of the Li atoms (blue) seem to have accumulated in some areas away from the oxide regions (pink). These areas are circled in the presentations on the left side. All areas circled in the images on the left side, show Li accompanied by an enrichment of Ni in the absense of oxide particles. In some cases these areas coincide with an enrichment of Fe_2O ions (circled on the right of Figure 4.20) even though these areas do not contain enough oxygen to lie within the O iso-concentration surface. As can be seen in Figure 4.18 (and also in Figures 4.9, 4.11 and 4.26), Fe_2O ions are often evaporated from regions of low O concentrations and only rarely from the bulk oxide in the GB or at the surface.

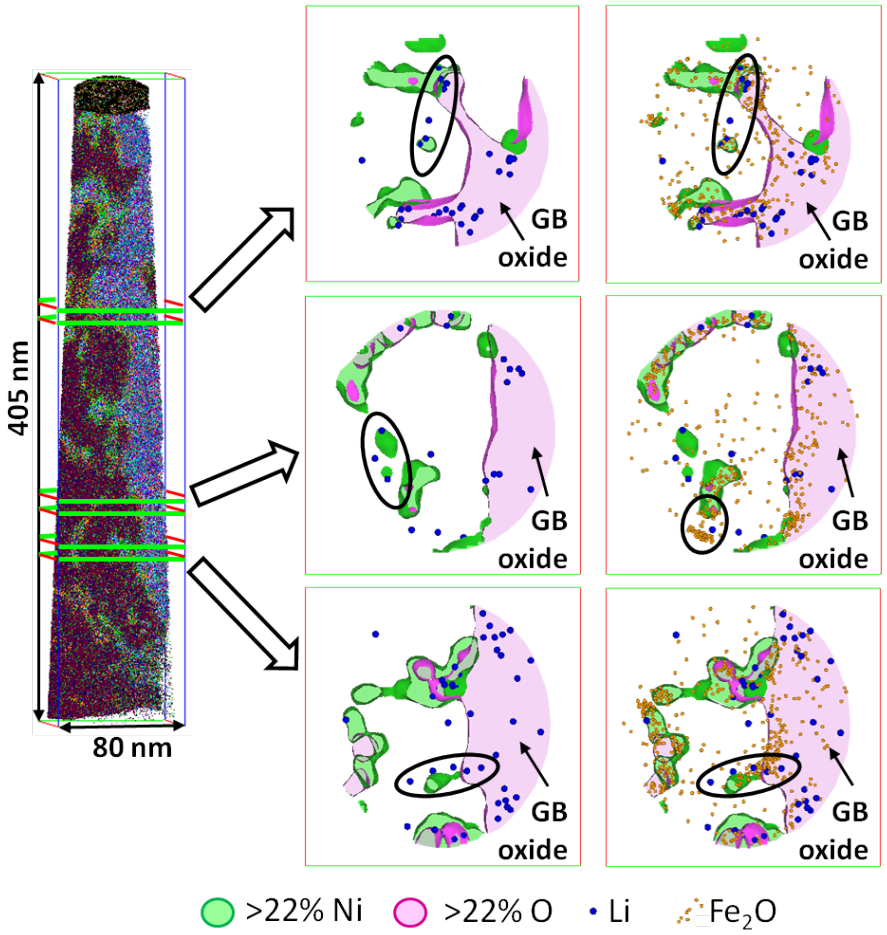

Figure 4.20: Three 2 nm slices each perpendicular to the z-axes of the stress/no-cold work data set. The left presentation of each slice shows Li atoms additionally to the iso-concentration surfaces at 22 at.% O and Ni. The high gradient sides of the isosurfaces are coloured in. Areas with Li atoms away from the oxide regions are circled. The right presentations of each slice also shows Fe_2O ions. Areas, where they coincide with Li atoms outside oxide regions are circled in these images.

4.1.3 No stress/cold-work

The sample described in this section was cold-rolled to 20% reduction in thickness prior to oxidation. It was reported in the literature that 304 stainless steel prepared in this way is susceptible to SCC in PWR primary water conditions [128]. The sample was plastically deformed homogeneously. The traces of the plastic deformation in the microstructure of the material and their influence on corrosion are studied in this chapter.

3D FIB slicing

The region in the no stress/cold-work sample that was analysed with 3D FIB slicing covered an area of 19.5×3.4 μm^2 at the surface. It contains two GBs and three different

grains.

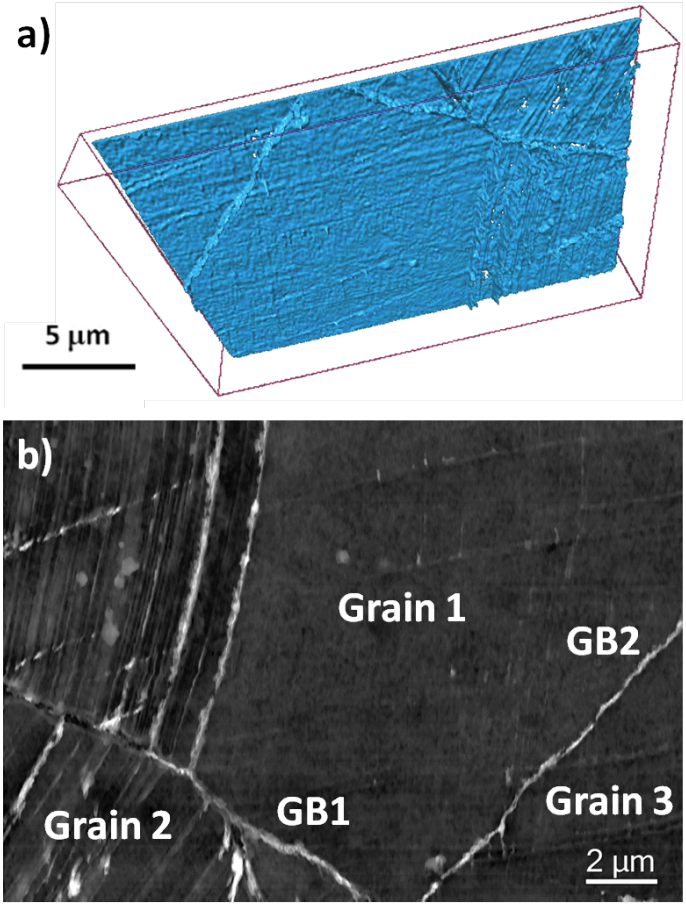

Figure 4.21: a) 3D model of the Cr-rich spinel oxide and b) oxide thickness plot from the no stress/cold-work sample [206]. The scale ranges from 0 nm (black) to 870 nm (white).

A 3D model of the Cr-rich spinel and its oxide thickness plot, generated as explained in section 3.6.2, are shown in Figure 4.21. The voxels used in the reconstruction were $11\times11\times42$ nm^3 in size. The oxidation behaviour in grain 2 and 3 was statistically analysed and the resulting histogram is shown in Figure 4.22a. A contribution from DBs can be seen in the peak for grain 2 above 200 nm oxidation depth. All GBs were preferentially oxidised. An individual histogram for GB1 can be found in Figure 4.22b. A summary of the results can be found in Table 4.8.

	Average Oxidation Depth
Grain 1	132±53 nm
Grain 2	153±93 nm
Grain 3	105±23 nm
GB1	203±107 nm
GB3	210±123 nm

Table 4.8: Statistical analysis of the depth of oxidation (only including Cr-rich spinel) in no stress/cold-work sample [206].

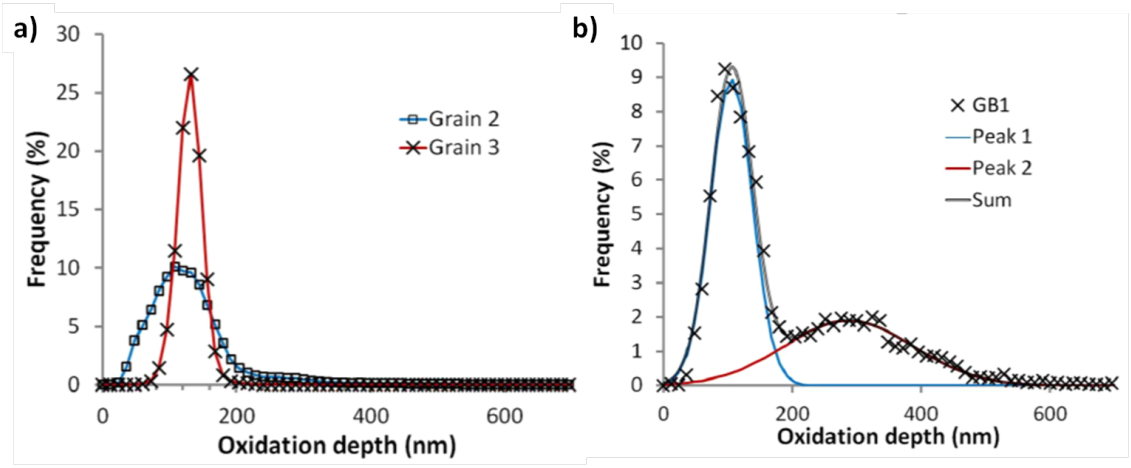

Figure 4.22: Histograms showing a) the different oxidation behaviour of the two grains and b) the oxidation behaviour of GB 1 fitted by the sum of two Gaussians in the no stress/cold-work sample.

Four series of six SEM images are displayed in Figure 4.23. In every series of images the GB oxide becomes wider somewhere along the oxidation front. In some cases a region of bright contrast can be seen ahead of, or even partly enclosed by, this wider oxide region. These regions are indicated by the red arrows. The length of these regions where the oxide has become wider and extends sideways into the grains is only a few tens of nanometers. The thicker oxide appears to mostly occupy one grain. In neighboring regions further along each GB, the oxide becomes narrow and pointed in the direction of the GB again.

Analytical Transmission Electron Microscopy

The ATEM analysis of this sample was conducted on the JEOL 2200. The local microstructure in the analysed region was revealed by TEM BF imaging, as shown in Figure 4.24a. The sample contains a GB which intersects the surface exposed to the environment (top) as well as various DBs in the right-hand grain. The oxide at the surface was damaged by FIB preparation, however, it can be seen that it is much thicker on the left grain than the right one. Dislocation networks next to the surface are also visible. These were caused by the last mechanical polishing steps before the autoclave test.

The same region was characterised by EFTEM, which reveals oxidised regions more easily (see elemental maps in Figure 4.24c–f). A thickness map was also obtained with t/λ having an average value of $\sim$0.7 in the matrix (the mean-free path, λ, was calculated to be $\sim$91 nm, according to [210]). The oxygen map shows that the GB was selectively oxidised, with Cr-rich oxides observed up to 190 nm below the end of the Cr-rich surface

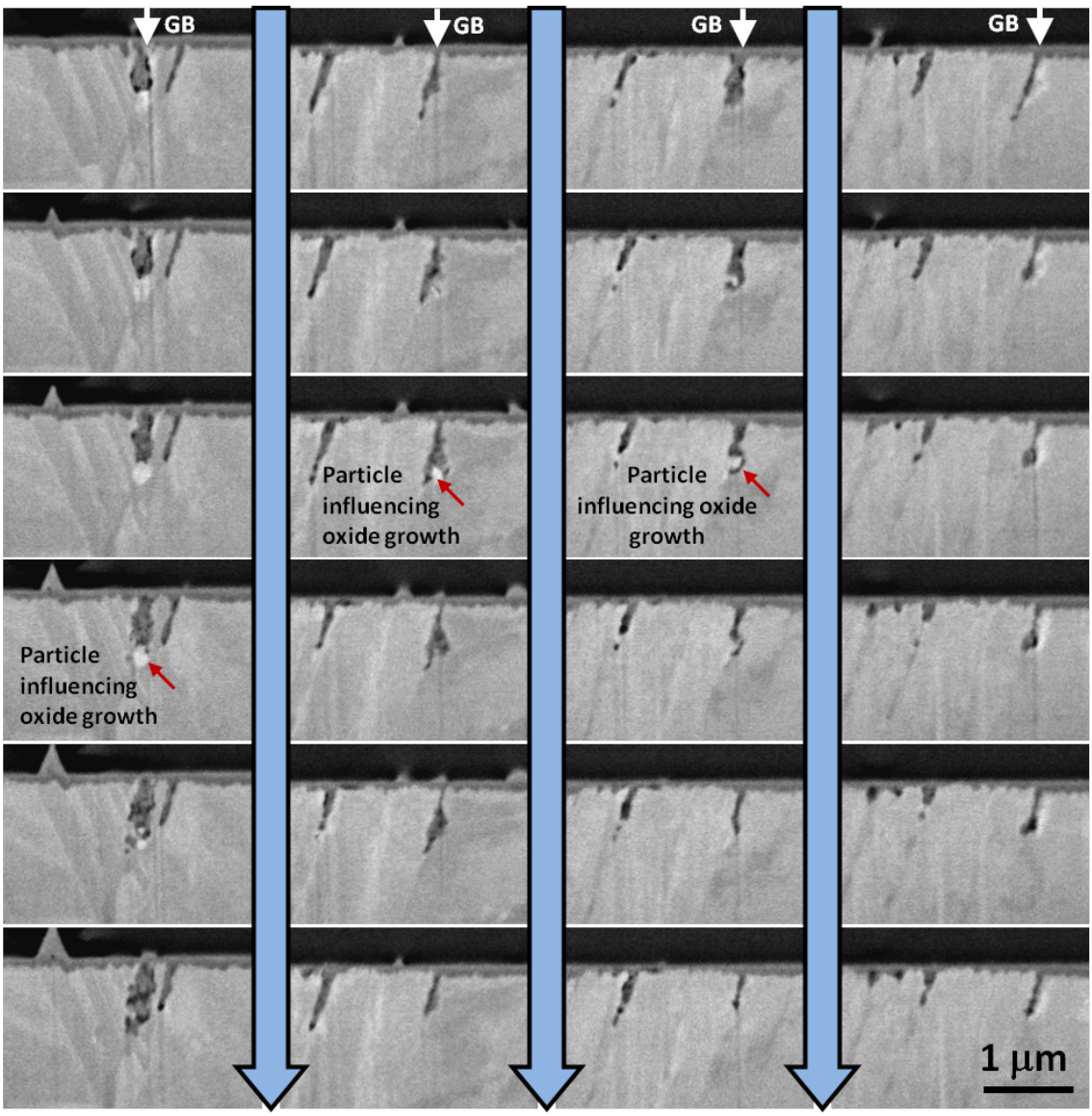

Figure 4.23: SEM images from the FIB SEM slicing data set in the no stress/cold-work sample. Every column contains a series of slices of about 10 nm distance. The white arrows point at the same GB in different places. The red arrows point at bright areas ahead of the oxidation front.

oxide layer. Oxides have also formed along DBs and dislocation networks, as previously reported in [211]. The elemental maps in Figure 4.24c–f show selectively oxidised DBs in the left grain. These features will be discussed in more detail in section 5.

A Ni enriched layer was found at the interface between Cr-rich oxides and metal. This Ni enrichment seems to be characteristic for the metal/oxide interfaces surrounding all Cr-rich oxide regions (surface, GBs and DBs) in this material, with measured Ni concentrations as high as 45 at. %. Furthermore, in all TEM foils containing oxidised GBs, regions of extremely high Ni concentration (55 - 65 %) were observed adjacent to the GB

plane, just ahead of the oxidised portion of the GBs.

EELS spectra were extracted from the EFTEM data set and the local compositions were analysed. The results are listed in Table 4.9.

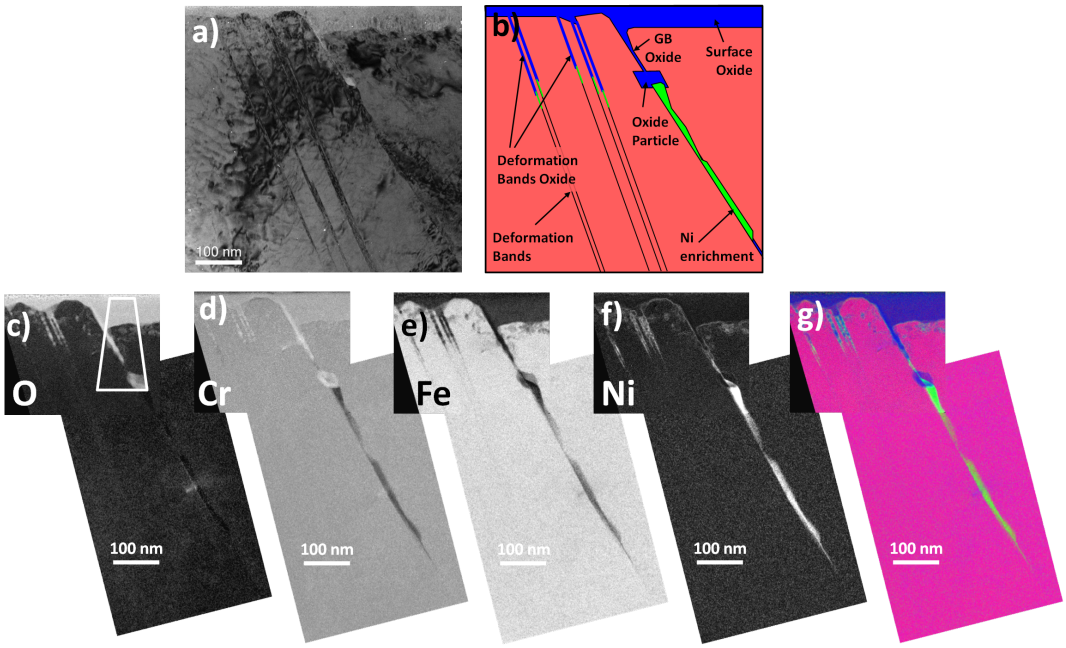

Figure 4.24: a) TEM BF image showing a no stress/cold-work cross-sectional sample containing an oxidised GB and some twin deformation bands in the left grain. The original sample surface lies horizontally from left to right towards the top of the map. Note the different oxidation rates in the two grains. b) Schematic showing the main features of the maps. c)-f) EFTEM elemental maps. The boxed region displayed in the oxygen map represents the approximate region analyzed by APT, shown in Figure 4.25a. The original surface of the sample coincides with the flat termination of the oxide right at the top of the images (horizontal). g) Relative composition RGB map showing Fe in red, Ni in green and Cr in blue.

Conc.	**Fe**	**Cr**	**Ni**	**O**
Matrix	70±3	20±1	10±1	Omitted
Outer Oxide	21±1	9±1	13±1	57±8
Inner Oxide	18±1	21±1	4±1	57±8
GB Oxide	8±1	24±2	20±1	47±5
Ni particle	23±3	4±2	73±10	Omitted

Table 4.9: Composition analysis with EFTEM showing the local concentrations of the main elements in the no stress/cold-work sample. All concentrations shown in at. %. Oxygen was omitted from the quantitative analysis of the metallic features as the O signal (5 at. % was measured) can be attributed to surface oxidation of the foils.

Atom-probe tomography

The APT data were fully consistent with the ATEM results. Two APT data sets of different size are shown in Figure 4.25. Both show part of the same GB that was characterised in the TEM. Schematics are presented to highlight the main features of each data set. The experiment represented in Figure 4.25a was stopped after the detection of 65 million ions (referred to as data set A), while the APT needle in Figure 4.25b fractured in an oxide-rich region after the detection of only 13 million ions(referred to as data set B). The 3D reconstructions in Figure 4.25 have been rotated so that the GB plane is edge-on. In this orientation the features can easily be related to those in the TEM sample, and the left and right grains are the same in both presentations.

The datasets contain a number of regions with different compositions: the surface oxide at the top, the bulk metal at the bottom and an oxidised GB going almost vertically down the centre. Separating the metal and oxide regions is a thin Ni-rich interface layer. The concentration profile in Figure 4.25c illustrates how the composition changes across this layer. Similar concentration profiles were extracted at the oxide/metal interfaces in all data sets of the no stress/cold-work material. The maximum Ni concentration in the layer varied. The graph displays the oxide composition on the left side and the metal composition on right. In the example shown, the interface layer is 6 nm wide, the composition changes abruptly, and the Ni concentration peaks at more than 30 at. %. In addition to the concentrations of the main elements, Fe, Cr, Ni and O, the graph also shows the Li distribution across the interface. Li was found throughout the oxide, but is completely absent in the steel matrix.

Maps of the different species in both data sets are shown in Figure 4.26. Different ion types are prevalent in the surface oxide compared to different parts of the GB oxide. Li is present in all oxidised regions.

It is possible to extract a 3D Volume of Interest (VOI) from the original data set, which can be analysed separately. A useful analysis technique for dividing a data set into relevant VOIs is the iso-concentration surface. With this technique it is possible to extract regions that contain more (or less) than a given concentration of a particular element.

Figure 4.27 shows only the oxidised regions of dataset A. The GB plane is almost perpendicular to the plane of the image. This VOI was extracted to study the Li concentration in the cap oxide and along the GB. An iso-concentration surface at 9 at. % O was chosen

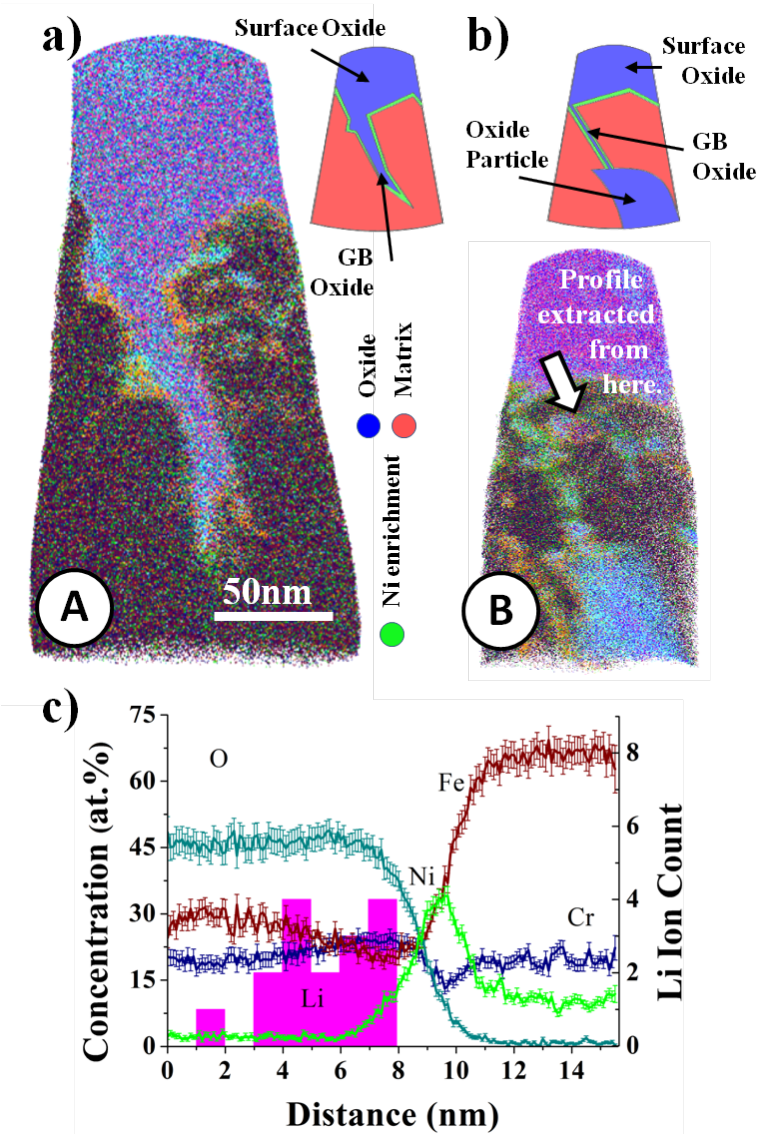

Figure 4.25: a) and b) Two no stress/cold-work APT data sets and schematics, showing the same GB intersecting with the surface in different places. Both maps are the same scale. Both maps show Cr-rich oxide on top and an oxidised GB below. The data presented corresponds to the region boxed in Figure 4.24c, but the APT samples are displaced with a spacing of about 10 μm along the GB. c) Concentration profile across the oxide/matrix interface of data set B. The atomic concentration of the major elements displayed was calculated in at. %. Ionic species were decomposed for the calculation of their local concentrations. Li ions are represented as individual ion counts. The bin size for the major elements is 0.1 nm, the bin size for the Li is 1 nm.

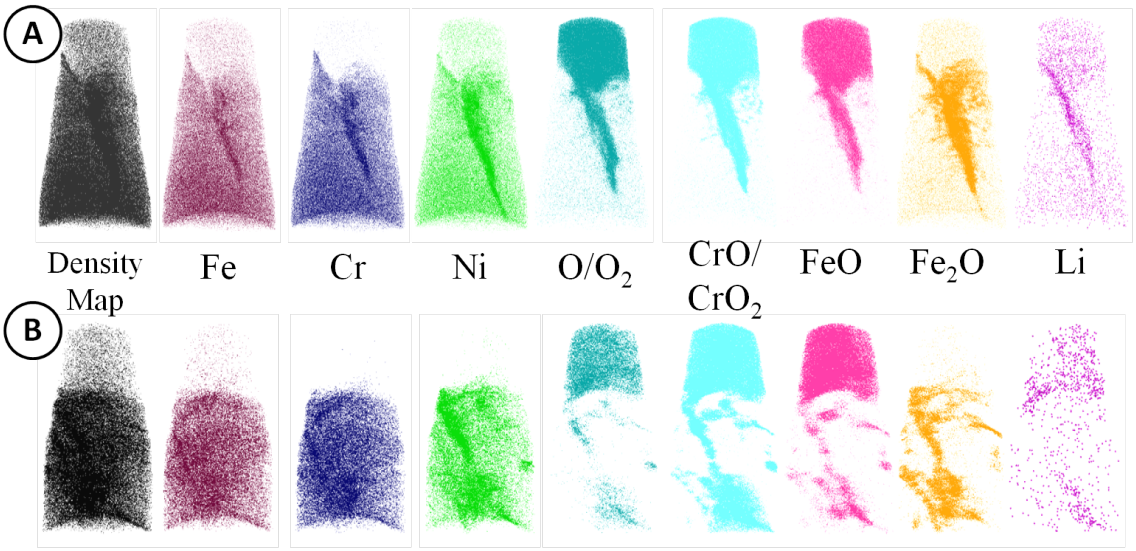

Figure 4.26: Maps showing the most commonly evaporated ions for data set A (top) and data set B (bottom). Both data sets in this Figure are aligned, so that the GB is shown edge on, the same way as in Figure 4.25a and b, where all ions of these data sets are shown in the same map.

to extract the dataset. This gave rise to a connected VOI with an overall high oxygen content. However, the oxide could not be entirely separated from the Ni-rich interface layer. This interface layer is discussed in more detail later in this section.

The Li concentration was 27±19 atomic parts per million (appm) in the cap oxide and the 108±40 appm in the GB oxide.[1] Thus the average concentration in the GB was measured to be almost 4 times higher than the average Li concentration in the surface oxide. As the extracted VOI of the GB oxide also includes some of the surrounding (mostly metallic) interface layer, which is Li-free, the real Li content must be even higher than this.

To analyse the composition of all regions in and around the GB oxide, a series of APT needles was prepared from the same GB. Six of the needles were characterised successfully. However, only the two data sets presented above contained GB oxides and only one of the other data sets (not shown) contained part of the outer oxide. The relevant regions of all six data sets were used to obtain the best possible statistics. The measured compositions can be found in Table 4.10. All errors given account for the variations between the analysis volumes of the different datasets. Only one specimen contained part of an Fe-rich outer oxide particle and only one interface layer was extracted. In these cases a Poisson error [2] is given.

[1] The given errors lead to negative numbers in a 95 % confidence interval, this is of course not possible and a consequence of the symmetry of the Gaussian model.

[2] Poisson statistics are applied, if measured quantity is a number of counts (such as the ion counts at the

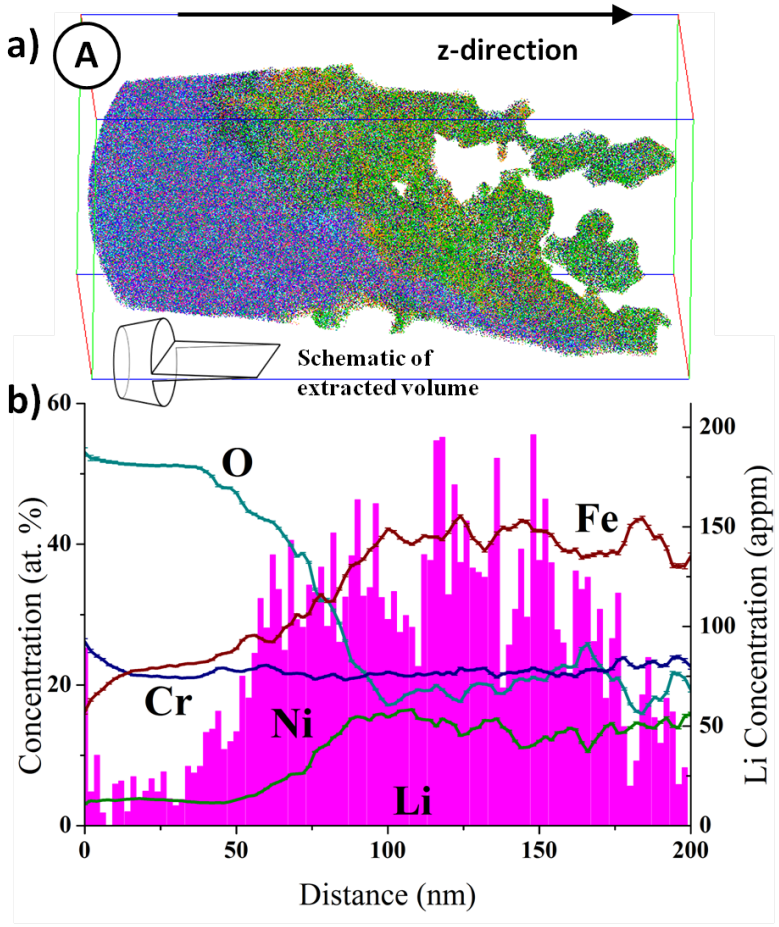

Figure 4.27: a) Oxide extracted from the no stress/cold-work sample (data set A), the surface oxide is on the left, the GB oxide is on the right. b) Li concentration in appm measured along the oxidised portion (down the z-axis of the needle specimen) of data set A. The Li concentration (bars) is plotted on the right axis. The other atomic species are calculated in at. % and plotted on the left axis (the bin size used is 2nm).

Conc.	Fe	Cr	Ni	Mn	Si	C	O
Outer Oxide*	42.2±0.06	5.3±0.02	3.1±0.01	1.3±0.01	0.02±0.001	0.6±0.008	51±0.07
Inner Oxide	22.4±1.2	22±0.8	2.9±1.1	0.9±0.2	0.02±0.01	0.2±0.1	51±0.2
Interface Layer*	42.7±0.2	18.7±0.1	25.4±0.2	1.3±0.03	0.08±0.008	0.05±0.007	10.1±0.1
Matrix	69.1±1.3	18.9±1.3	8.9±0.2	1.3±0.2	0.44±0.15	0.07±0.02	0.6±0.3

***Data from only one measurement.**

Table 4.10: Change of the chemical composition across the interface layer between the surface oxide and the matrix in the no stress/cold-work sample. All concentrations shown in at. %.

The GB oxide composition was determined from the analysis of the two presented data sets only. The map in Figure 4.28a shows the extracted GB plane from data set A, which shows how the oxidation in this plane is not homogeneous. Figure 4.28b shows the exact location of the volume that was extracted from the original data set. As can be seen in Figure 4.28c the oxygen concentration decreases from ∼50 at.% in the bulk oxide (red) to ∼0 at.% about 200 nm deep into the GB. Figure 4.29 shows a concentration profile through one of the oxide particles in the GB plane. An apparent concentration gradient of Fe, O and Cr was observed over a range of a few nanometres. The Ni concentration is increased in the region around the oxide particle. To analyse the composition of the core oxide only, iso-concentration surfaces at 35 at.% oxygen were chosen to separate the oxides from the surrounding material. The average composition of the oxide particles within the GB was determined to be 10.7±5 at.% Fe, 32.4±3.3 at.% Cr, 5.7±5.7 at.% Ni and 48.7±8.2 at.% O.

Ni-enrichment was observed in a 3 - 4 nm thick layer at the interface between the matrix and oxide (Figure 4.25c, page 92). The measured composition of the extracted interface layer was 42.7 at.% Fe, 18.7 at.% Cr, 25.4 at.% Ni and 10.1 at.% O. However, the concentrations of the major elements change gradually in this interface layer. In its centre the Ni concentration reached peak values of between 30 and 45 at.%. The observed Ni-rich layer surrounded the oxide portion all the way down the GB. In one APT needle a large Ni-rich "particle" similar to the one observed with TEM (Figure 4.24f) was observed. The dataset is discussed in detail in Chapter 6. The composition of the particle was determined to be 33.9 at.% Fe, 2.3 at.% Cr, 57.8 at.% Ni and 3.2 at.% O.

---

detector of an APT experiment), the appropriate formula for the error in the mean is: $\sigma_P = \frac{1}{n}\sqrt{\sum_{i=1}^{n} x_i}$ with n being the number of measurements and x_i the measuring values. In the case of only one measurement the error is $\sigma_P = \sqrt{x_1}$

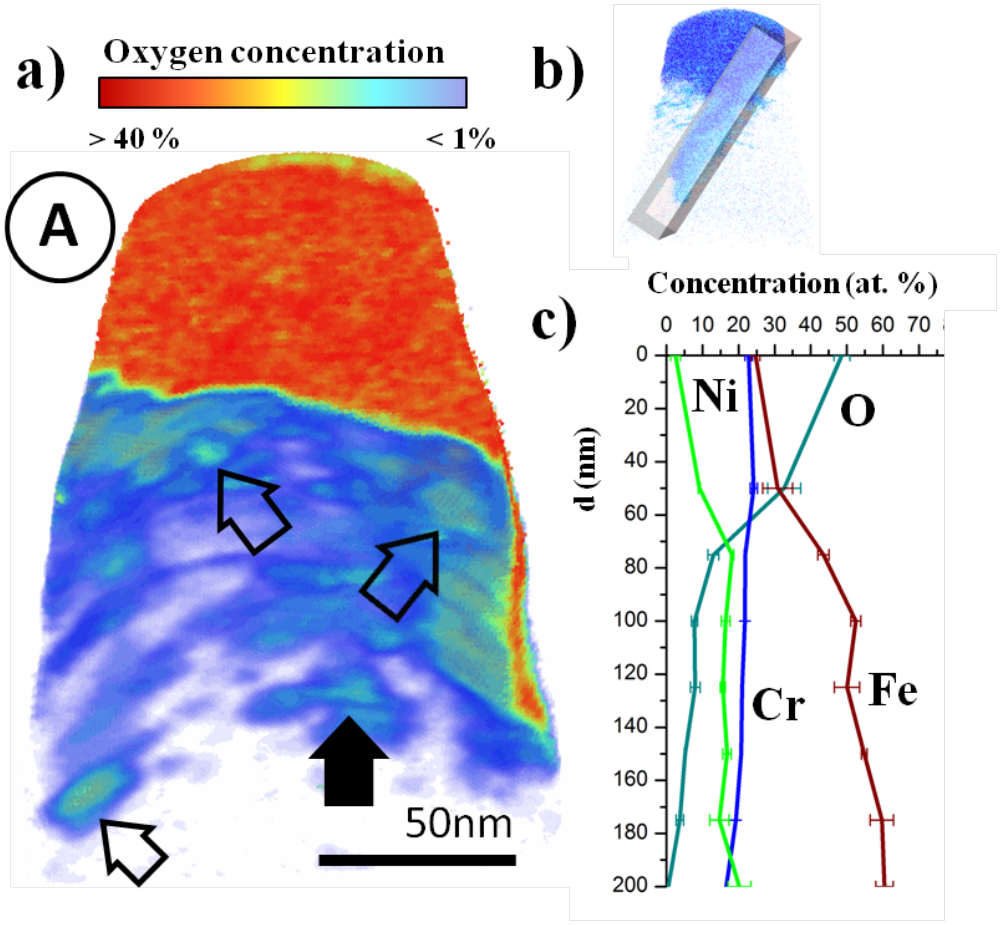

Figure 4.28: Oxygen concentration (at. %) in the GB plane of data set B (Figure 4.25b). a) Two dimensional concentration map (a projection through the 3-D atom map). The arrows point at particles with high oxide concentration. White regions contain no oxide at all. b) Schematic showing where the GB plane in (a) was extracted from the APT data set. The extracted portion was rotated 90°. c) Plot of metal and oxygen concentrations within the GB.

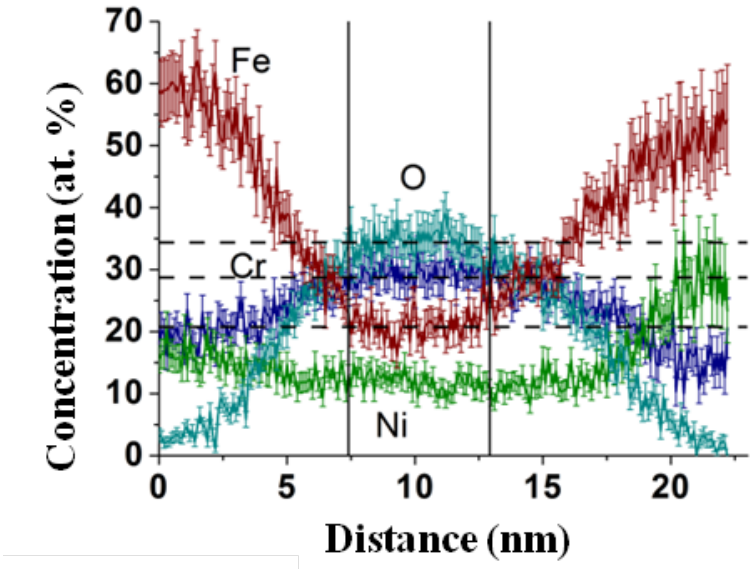

Figure 4.29: Concentration profile through the particle indicated by the solid black arrow in Figure 4.28 (bin size used is 0.1 nm).

4.1.4 Stress/cold-work

The sample described in this section was cold-rolled to 20% reduction in thickness prior to oxidation under stress. It was shown in the previous section, that the internal stresses induced by cold-work are sufficient to enhance oxidation at most GBs. The study of the influence of external stresses during oxidation of these cold-worked samples is presented in this section.

3D FIB slicing

The region analysed covered an area of 18.9×18.1 μm^2 and the voxels used in the reconstruction were 12×12×57 nm^3. This region includes three GBs and three grains. A 3D model of the Cr-rich spinel and its oxide thickness plot, generated as explained in Section 3.6.2, are shown in Figure 4.30. The average oxidation depths of the regions are listed in Table 4.11.

Analytical Transmission Electron Microscopy

STEM imaging was performed on three oxidised GBs in this material. Again buckling of the samples during sectioning prevented sufficient thinning for EFTEM mapping. Figure 4.32 shows BF and ADF STEM images. A close-up of the oxidised region of the GB in the BF is also displayed. The thickness of the surface oxide is 112±27 nm in the left

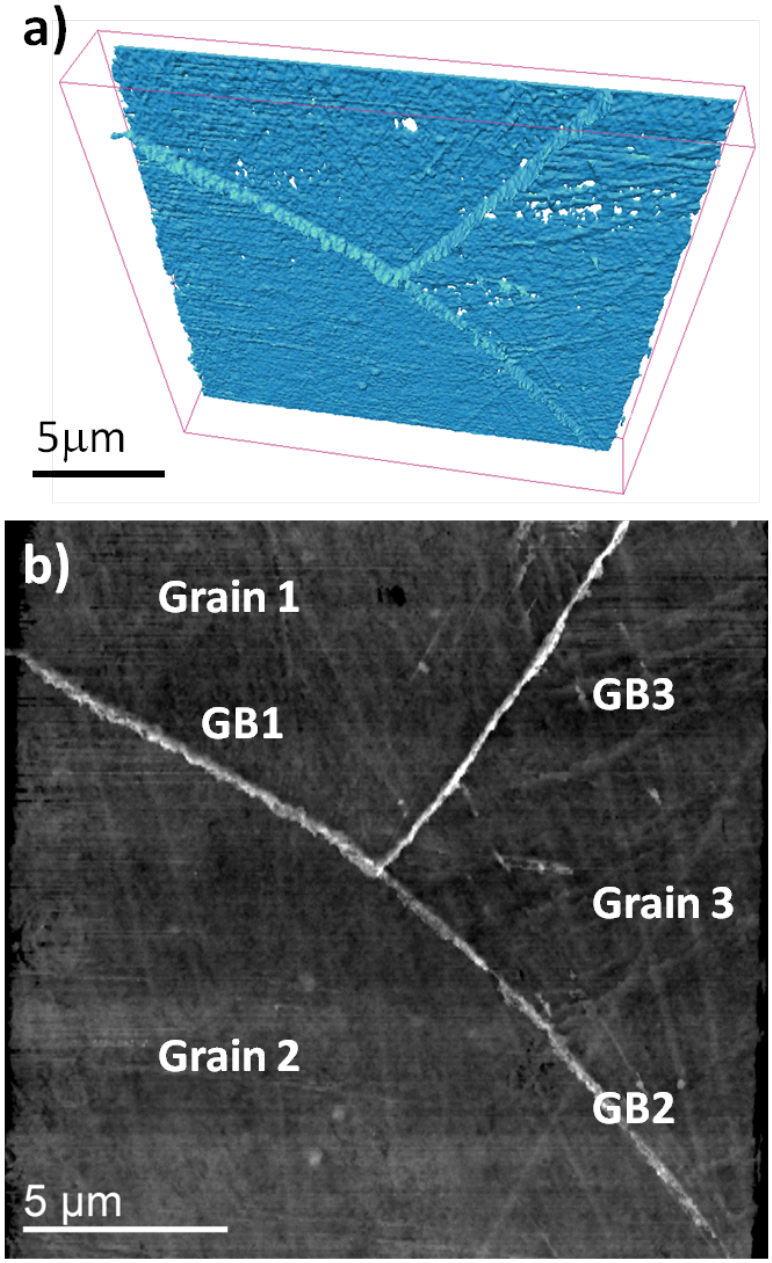

Figure 4.30: a) 3D model of the Cr-rich spinel oxide and b) oxide thickness plot from the stress/cold-work sample [206]. The scale ranges from 0 μm (black) to 1.4 μm (white).

grain and 111±21 nm in the right grain. The thickness of the surface oxide in both grains is almost identical, so it is likely that the grains have similar orientations and the GB is a low-angle GB. The oxide thickness at the GB is 243 nm, which is about 130 nm deeper than the surface oxide. The GB oxide is present in both grains, but the biggest portion is in the left one, where an oxidised slip plane is located only about 100 nm away from to the GB.

Figure 4.33 shows TEM and STEM BF images of two oxidised GBs. The original sample

	Average Oxidation Depth
Grain 1	177±48 nm
Grain 2	224±52 nm
Grain 3	160±42 nm
GB1	394±151 nm
GB2	381±133 nm
GB3	426±282 nm

Table 4.11: Statistical analysis of the depth of oxidation (only including Cr-rich spinel) in the stress/cold-work sample. An individual histogram for GB1 can be found in Figure 4.31b [206].

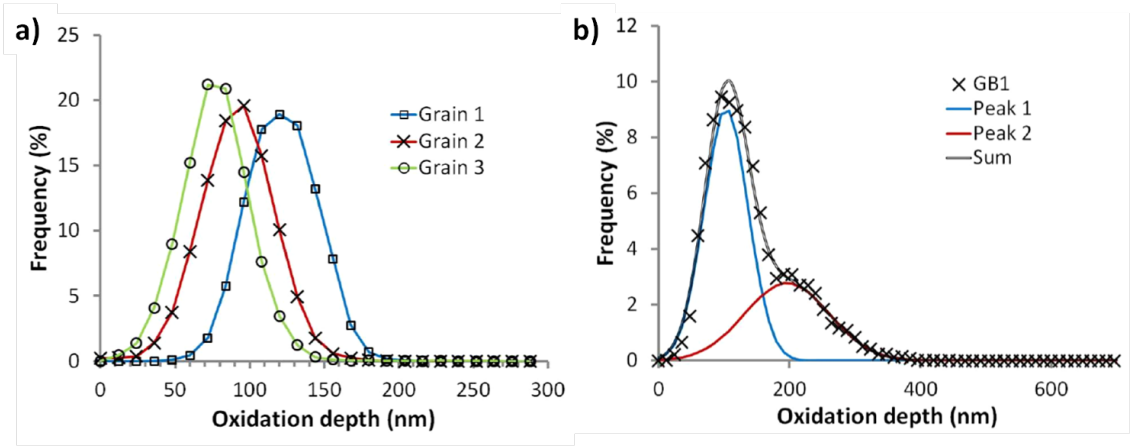

Figure 4.31: Histograms showing a) the different oxidation behaviour of the two grains and b) oxidation behaviour of one of the oxidised deformation bands fitted by the sum of two Gaussians, in the stress/cold-work sample.

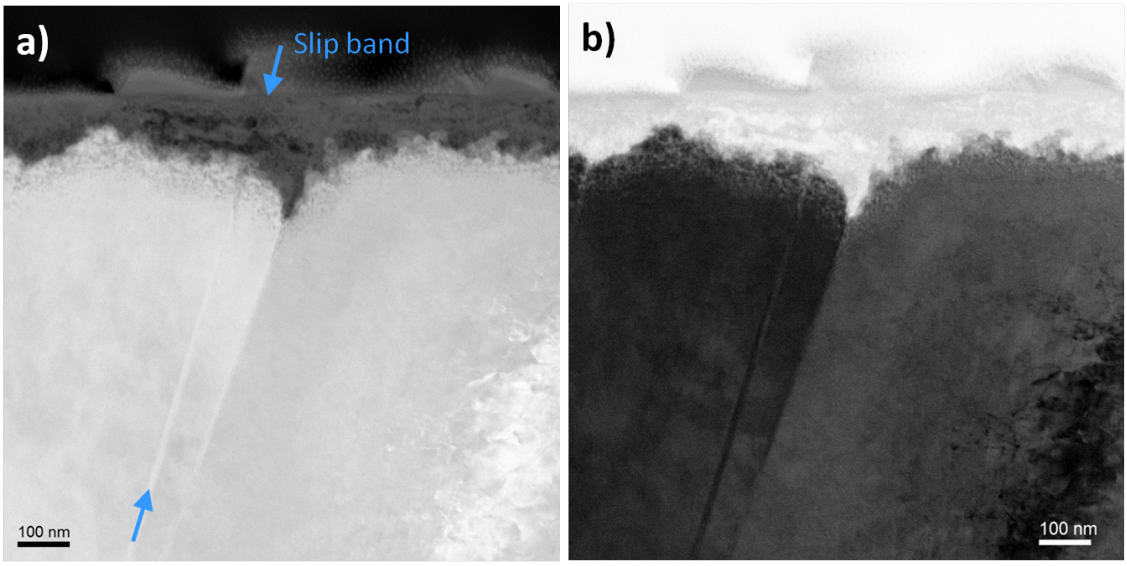

Figure 4.32: STEM micrographs of the stress/cold-work sample. a) BF image. b) ADF image.

surface lies horizontally at the top edge of the image. The GB shown in Figure 4.33a and b is oxidised to a greater depth than the one described above. The right grain is more

heavily oxidised than the left, associated with deformation bands almost parallel to the surface. The oxide thickness is 94±25 nm in the left grain and 102±19 nm in the right grain. The GB oxide depth is 502 nm. In the part closest to the surface both sides of the GB are oxidised. At a greater oxide depth the oxide has grown solely in the right grain. The TEM image in Figure 4.33b shows that a deformation band lies next to the GB. At greater depth, the oxide path follows the deformation band. On the left side of the deformation band, at the front of the oxidised region is a brighter area, indicated with the blue dashed line in the close up on Figure 4.33a. As Z-contrast is common in STEM images and Ni atoms are heavier than Fe and Cr, this region could be interpreted as the Ni enrichment observed in similar regions of the no stress/cold-work sample. The 350 nm deep and 70 nm wide area could also be caused by a thickness effect from the FIB sample preparation. However, curtaining[3] from the ion beam is observed perpendicular to the surface in this micrograph and the marked region has a well-defined curved phase boundary, which suggests a change in composition.

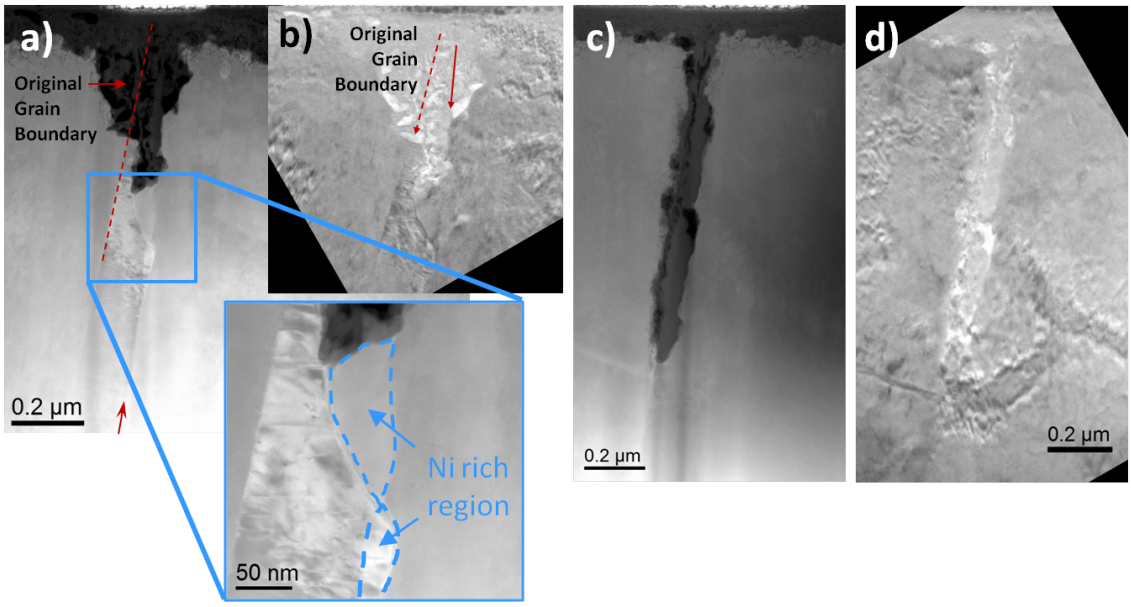

Figure 4.33: (S)TEM micrographs of the stress/cold-work sample. a) and c) STEM BF images of 2 different GBs. b) and d) respective TEM BF images.

The GB shown in Figure 4.33c and d is oxidised to a much greater depth than any other GB shown in this chapter. The oxide depth at the GB is 1.15 μm. The oxide thickness is 98±15 nm in the left grain and 90±17 nm in the right grain. Both sides of the GB

[3]The so called curtain effect consists of the formation of striations vertically across the TEM foil, if samples have surfaces with uneven topography or changing chemical composition [212, 213]

are oxidised; however, the oxide in the right grain is more homogeneous and continuous, whereas the oxide in the left grain appears patchy and inhomogeneous. The oxide has grown deeply into the GB, but it is not very wide (87±22 nm). A change in contrast, as in Figure 4.33a indicates that Ni enrichment is present at the end of the GB oxide. The wide oxide in the GB in Figure 4.33a and b seems porous and brittle, whereas the oxide in Figure 4.33c and d looks solid and mostly homogeneous. The TEM image in Figure 4.33d shows a deformation band almost perpendicular to the GB ahead of the GB oxide in the left grain. This could be a sign of high stress concentration at the oxide front.

4.2 Discussion

The results presented in this chapter demonstrate a new, comprehensive experimental approach to the study of the influence of stress and cold work on GB oxidation in an austenitic stainless steel tested in PWR primary water. The combination of techniques allowed the acquisition of high-resolution, high-sensitivity 3D data, with APT, validation of the chosen analysis parameters and measured compositions by comparison with ATEM, and its positioning in the context of its environment, in the reconstructed 3D block from the 3D FIB slicing.

New information about the influence of stress and cold-work on the oxidation rate and the controlling mechanisms was gathered and the role of the minor additions, B and Li, to the PWR water was studied. Additionally to the Ni enrichment at the metal/oxide interface, Ni-rich precipitates were found along the oxide front at GBs. These may play an important role in controlling SCC in austenitic stainless steels.

4.2.1 Comments on experimental technique

Information from reconstruction and statistical analysis of 3D FIB slicing data

The application of 3D FIB sequential sectioning to the characterisation of surface oxidation in stainless steels under simulated PWR conditions produced high volumes of data that have been statistically analysed. In comparison to previous characterisations of surface oxidation, it provided a better description of the phenomena, by sampling many more points at a higher spatial resolution. This revealed a different oxidation behaviour for different grains, GBs and deformation bands. The results confirm some initially expected

trends, such as the increase in oxidation rate in samples with prior CW and/or oxidised under applied stress.

Sample	**Region**	**Peak 1** x_c	**Peak 1** w	**Peak 2** x_c	**Peak 2** w
No Stress/no cold-work 1	Grain2	114	62	190	135
No Stress/no cold-work 2	Grain3	94	69	205	119
No Stress/no cold-work 2	GB 3	122	108	259	249
No Stress/cold-work	Grain 2	114	101	254	188
No Stress/cold-work	GB 2	122	54	227	424
No Stress/cold-work	GB 1	106	76	287	235
Stress/no cold-work	Grain 1	178	66	317	276
Stress/no cold-work	Grain 2	159	53	190	86
Stress/no cold-work	DB	180	72	397	418
Stress/cold-work	GB 1	103	79	196	151
Stress/cold-work	GB 2	94	45	199	186
Stress/cold-work	GB 3	71	50	261	333

Table 4.12: Parameters from curve fitting (Sum of two Gaussians) of oxide depth distributions in regions which showed a bi-modal distribution [206].

The plots of the oxidation depths in many of the analysed regions have bimodal distributions, which were fitted with the sum of two Gaussians (see Figure 4.2b). As can be seen, the first peak is related to the part of the sample with shallower oxidation, which is always the undeformed matrix. In Figure 4.2b for example, the oxide on the undeformed matrix can be described on average by a Gaussian centred at ∼120 nm with a FWHM of ∼70 nm. The second peak corresponds to features that oxidise faster than the matrix. In Figure 4.2b the second peak was caused by the area on and around the scratch lines which have oxidised preferentially.

Orthorhombic volumes containing the GBs and DBs were separated from the remaining datasets and extracted. As these features are not perfectly straight, some neighbouring voxels from the surrounding matrix are also included in the analysis. Their contribution appears in the histograms in form of a smaller peak of shallow oxidation (see Figures 4.4b, 4.14b, 4.22b and 4.31b). Both peaks are fitted with Gaussians, so that the GB or DB oxidation, which is represented by the second peak, can easily be quantified. The values for comparable features (such as GBs and grains) as listed in Table 4.12 were averaged to obtain more statistically relevant numbers. The results are presented in Table 4.13.

If the sample volume has been reconstructed in 3D, information and visualizations in arbitrary orientations can be extracted. The resolution of the resulting data depends on the thickness of the slices during data acquisition and the orientation of the respective

Sample	Region	Mean	FWHM
No Stress/no cold-work	Residual Deformation	197	127
Stress/no cold-work and no Stress/cold-work	DB	253	183
All	Preferentially oxidised GBs	238	263

Table 4.13: Average values for oxidation depths in different regions of different samples averaged [206].

data within the data set. The plane containing GB 2 in the no stress/cold-work sample (Figure 4.21b) was extracted. The result, which looks similar to an SEM image, but is artificially created, can be seen in Figure 4.34. The resolution is not as high as in a real SEM image, but still sufficient to extract valuable information. The oxidation along the GB plane is inhomogeneous and seems to progress selectively down certain areas. These areas were probably subject to higher deformation, which resulted in a locally higher dislocation density. The image contains several darker regions (indicated by arrows). The arrangement of these regions (at the oxide front) suggests, that these might be voids, like the one observed in Figure 4.15.

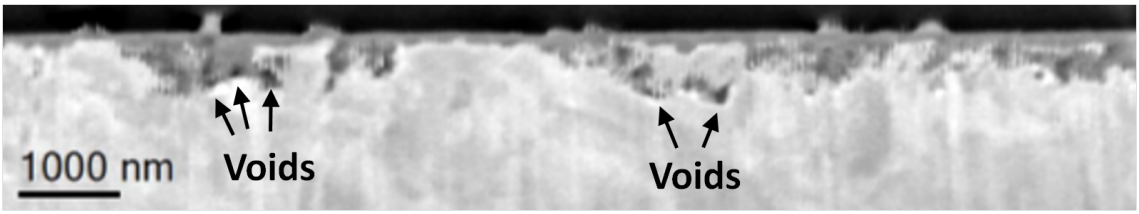

Figure 4.34: GB plane from the no stress/cold-work sample extracted from the 3D reconstruction. The GB plane corresponds to GB 2 in Figure 4.21b. Oxide appears as a darker grey. Top surface was the surface exposed to the environment, where some Fe-rich spinel faceted particles have grown.

Although the statistical description of the oxidation behaviour by Gaussians is very useful, it does not account satisfactorily for the long "tails" towards deeper oxidation observed in GBs and DBs. For example, although the oxidation of deformation bands in the stress/no cold-work sample is described by the second peak in Grain 1 (See Figure 4.13) which is centred at 317 nm and has a width of 276 nm, it does not reveal that the highest oxidation observed along one of the DB is over 1 μm deep; GB 3 in the stress/cold-work sample (Figure 4.30) is described by a Gaussian centred at 261 nm and with a width of 333 nm, but has a record oxidation depth of almost 1.4 μm. This suggests that there are at least three oxidation regimes operating in the samples. The first regime is described by the first Gaussian peak (lower oxidation rate) and accounts for the oxidation of the undeformed

matrix. The second regime is associated with the second Gaussian peak and describes the oxidation of regions or features with high dislocation density (GBs, deformation bands, etc.) under no applied stress. The third regime is revealed in the form of extended tails towards higher oxidation depths and only appears in samples oxidised under stress.
Although statistical analysis is a great tool to analyse large volumes of data, it should be remembered that it is best suited to describe average oxidation behaviour. Extreme cases are possible and those are relevant if a worst-case-scenario is to be constructed.

Compositional analysis of oxides with APT

When oxidised under PWR primary water conditions, 304-type stainless steel has been reported to form a double layer consisting of an inner $(Fe_xCr_{1-x})_3O_4$ chromite-type oxide layer ($x \approx \frac{2}{3}$) and an outer layer of $(Ni_yFe_{1-y})_3O_4$ magnetite-type particles ($y \approx 0.7$) [208, 209]. A stoichiometric spinel oxide consists of 57.1% oxygen and 42.9% metal. The EFTEM quantification of the surface oxides of all samples is in good agreement with these figures. The composition analysis of the APT data gives consistently lower oxygen concentrations. Summaries of measured compositions can be found in Table 4.14 and 4.15. As the oxide portions that were analysed with the two techniques are from the same sample region and contain comparable volumes of oxide (oxide depth, proximity to GB oxide) it appears unlikely, that this is caused by local non-stoichiometry of the oxide. It has previously been reported, that the analysis of oxide compositions is difficult with APT [166, 214]. The mass/charge peak at 16 m/z can be attributed to O^+ or O_2^{2+}. For the compositions reported in this thesis the peak was ranged as O^+, therefore it is possible that O_2 was evaporated in a 2^+ charge state and some atoms were not counted. However, only about 3 % of the oxygen in the oxide can be attributed to the peak at 16 m/z, so this could not fully explain the missing oxygen. Possible explanations for "losing" oxygen in APT experiments include DC evaporation, preferential surface migration, or a bias for oxygen in multiple-ion events. Bachhav *et al.* reported that the oxygen concentration measured by laser assisted APT can depend on the wavelength and pulse energy of the laser [166]. They found that the measured oxide concentration can vary by more than 20 % depending on the particular analysis conditions. Tsukada *et al.* have suggested the accumulation of holes as a precondition for evaporation [215]. Oxygen loss in the form of neutral molecules also appears possible from less conducting materials such as oxides [216].

4.2.2 No stress/no cold-work

Conc.		Fe	Cr	Ni	Mn	Si	C	O
Matrix	Nom.	Bal.	19.6	8.8	1.6	0.62	0.19	
	APT	68.2±0.7	19.6±1.2	9±0.4	1.4±0.2	0.49±0.01	0.07±0.03	0.7±0.1
	EFTEM	71±2	19±1	10±1				Omitted
Inner Oxide	APT	23.1±1.9	21.9±0.2	2.6±1.5	0.8±0.2	0.02±0.01	0.3±0.1	50.8±0.2
	EFTEM	20±1	22±2	3±1				56±7
GB Oxide	APT	28.6±4.1	23.4±2.2	2.4±1.6	1.2±0.1	0.01±0.1	0.19±0.01	43.7±8.2
	EFTEM	16±1	27±2	3±1				54±7
Ni particle	APT	not available						
	EFTEM	35±2	4±1	61±9				Omitted

Table 4.14: Compositions of the different features measured with the different techniques in the no stress/no cold-work sample. All concentrations shown in at. %.

Although the general trend showed increasing oxidation after CW and under applied stress, the amount of oxidation found in the no stress/no cold-work sample was higher than expected. This is the reason why two regions from this sample were characterised with 3D FIB slicing and APT. Region 2 (Figure 4.3b) was less oxidised on average than Region 1 (Figure 4.1a). However, GB1 and GB3 in Region 2 are the only boundaries that show preferential GB oxidation. The TEM data in Figures 4.5 and 4.6 as well as the APT map in Figure 4.9 correspond to GB1 in Region 2. The APT data in Figure 4.11 corresponds to the GB in Region 1. The oxide thickness plots of both regions show bright parallel lines running diagonally across the data. These features, which are more oxidised than the surrounding matrix, cover the entire area, independent of the grain. This suggests that they are related to scratches on the surface, which were present prior to the autoclave exposure. The final polishing step had been performed to mirror finish with colloidal silica. No scratches were observed optically or in the SEM on the exposed surface. Therefore, residual deformation, consisting of dislocations in the near-surface region, is believed to have caused enhanced oxidation along the lines. The EFTEM maps in Figure 4.8 show that surface near dislocations are oxidised preferentially. Some dislocations oxidised ahead of the bulk oxide front and enclosed metal "pockets". Although the material in these "pockets" is mostly metallic, small amounts of non-stoichiometric oxide have already formed. It appears that the dislocation plane would have been the new oxide front if oxidation continued. Ni enrichment was mainly observed around the dislocation plane. Only a thin layer of Ni could be observed at the bulk oxide front. This suggests, that Ni was initially rejected from the oxide, but then removed from the interface. Ni

diffusion into the steel matrix is slow [217], so diffusion along the interface seems to be the dominating mechanism. As the Ni enrichment is most striking around the oxidised dislocations, it seems plausible that Ni also uses the dislocations at a fast diffusion path. Alternatively, Ni rejected from the bulk oxide might be diffusing into the metal and the oxidised dislocations could act as a diffusion barrier at which some of the Ni "in transit" accumulates. Self-diffusion of Ni from the interface layer into the matrix would have caused a Ni concentration gradient. The absence of such a concentration gradient in the region below the surface oxide indicates that Ni diffusion occurs primarily along dislocations.

Figure 4.3b shows the importance of grain orientation for the extent of enhanced oxidation related to the scratches. While grain 1 and 3 oxidised considerably along the linear features caused by the scratches, grain 2 was almost unaffected. This could also be due to the depth of the initial damage depending on the grain orientation. In the samples oxidised under applied stress or with prior cold work, the effect of the surface condition was not so obvious, mostly because the oxides are thicker and the contribution from the near-surface damage is likely to be masked after the first 100 nm of oxide. In some samples, such as the stress/cold-work sample in Figure 4.30b, the analysed area seems to have more random and weaker signs of preferential oxidation caused by shallow scratches, indicating a better finish was achieved by polishing. It appears that the last polishing step was not sufficient to remove all the residual deformation near the surface and a longer colloidal silica polish is suggested for future studies.

The orientation of GBs seems to have an effect on their oxidation behaviour, especially in the no stress/no cold-work sample. As reviewed in Chapter 2, a number of studies [172, 177, 179] showed limited or no SCC susceptibility of low angle and $\Sigma 3$ boundaries. All SCC mechanisms include a chemical (corrosive) part and a mechanical part. The local corrosion behaviour of the GB may play an important role as well as its fracture toughness. Some SCC models assume that brittle oxides form in high defect regions and under tensile stress are susceptible to cracking. The presented results suggest that the SCC resistance of low angle and $\Sigma 3$ boundaries is not only due to the greater fracture toughness of these GBs, but due to the lower corrosion susceptibility.

The GB in Figure 4.5 and 4.6 shows a much deeper than average oxidation depth. Although the oxidation depth is not representative for this material, the large oxide portion and its shape contain information about the oxidation mechanism.

1. The oxide is mostly on one side of the GB.

2. The oxide front is blunt and the oxide is very wide spread.

3. The oxide is not homogeneous and changes its composition.

4. The oxide has fuzzy zig-zag shaped edges.

5. A Ni-rich region can be found in the left grain ahead of the oxidation front.

From these observations we can draw some conclusions about the growth mechanism.

1. Figure 4.6a shows many dislocations in the left grain, whereas the right grain seems much more uniform. Regions which contain many dislocations seem to oxidise preferentially.

2. Intuitively, one assumes that the GB is the fastest diffusion path for oxygen, however there is no sign of oxide growing into the GB beyond the dislocations at the sides. Rather it appears as if the foremost oxidation front consists of a dislocation in the left grain, that curls back towards the GB.

3. The Cr map in Figure 4.6e shows part of the oxide around the GB as being Cr rich. Part of the oxide looks porous, like a network of lines. It appears that the Cr-rich oxide has grown at first along the dislocations. The oxygen map in Figure 4.6b shows that the oxide regions go far beyond these Cr-rich (and Fe-depleted) parts. In the bottom centre of the GB oxide there is an area of Cr-depleted, Fe-rich oxide surrounded by Cr-rich lines, it seems that the Cr rich oxide at the oxidation front might form a barrier to further oxygen diffusion or at least slow it down, so that oxidation of the enclosed metal is favourable over diffusion deeper into the matrix.

4. The oxide has grown further in the left grain and forms pointy spikes. It appears that dislocations, especially in the left grain act as much faster diffusion paths, than the GB itself. Therefore, the oxide is widespread, rather than limited to a narrow area around the GB.

5. Ni enrichment was observed ahead of the oxidation front. The entire oxide region is Ni depleted. It appears that Ni was rejected from the oxide, as it is more noble than Fe and Cr and can only be oxidised minimally at the present potential. It was

also accommodated in the dislocation rich left grain, rather than in the GB. As Ni diffusion should happen by substitution, it appears that the left grain contains a higher number of vacancies, probably in dislocations, than the GB.

The compositional analysis of the matrix and surface oxide performed with APT and EFTEM was mostly in good agreement (see Tables 4.4 and 4.5), except for the consistently low values for oxygen in the APT data, discussed in Section 4.2.1. The variations in the Fe and Cr and even the O concentrations for the GB oxide are easily explained by the inhomogeneity of the oxide. The larger errors on the values for the GB oxide indicate that there was much more local variation within the analysed volumes than for the surface oxide and matrix. Initially it seems likely that the high Fe concentration in the APT measurement is due to poor separation from the matrix, however isoconcentration surfaces at 35% oxygen were chosen to select only the core oxide regions. If the oxide had not been well separated, much higher Ni concentrations would also have been expected. Therefore it seems likely that the APT data contains more of the Fe-rich oxide between the Cr-rich regions around the dislocations.

4.2.3 The influence of cold-work

Conc.		**Fe**	**Cr**	**Ni**	**Mn**	**Si**	**C**	**O**
Matrix	Nom.	Bal.	19.6	8.8	1.6	0.62	0.19	
	APT	69.1±1.3	18.9±1.3	8.9±0.2	1.3±0.2	0.44±0.15	0.07±0.02	0.6±0.3
	EFTEM	70±3	20±1	10±1				Omitted
Outer Oxide	APT*	42.2±0.06	5.3±0.02	3.1±0.01	1.3±0.01	0.02±0.001	0.6±0.008	51±0.07
	EFTEM	21±1	9±1	13±1				57±8
Inner Oxide	APT	22.4±1.2	22±0.8	2.9±1.1	0.9±0.2	0.02±0.01	0.2±0.1	51±0.2
	EFTEM	18±1	21±1	4±1				57±8
GB Oxide	APT	10.7±5	32.4±3.3	5.7±2.7	1.5±0.1	0.03±0.15	0.07±0.1	48.7±8.2
	EFTEM	8±1	24±2	20±1				47±5
Ni particle	APT	33.9±1.6	2.3±1.2	57.1±3.2	0.13±0.08	0.04±0.03	0.28±0.01	3.2±1
	EFTEM	23±3	4±2	73±10				Omitted

*__Data from only one measurement.__

Table 4.15: Compositions of the different features measured with the different techniques in the no stress/cold-work sample. All concentrations shown in at. %.

The effect of cold work on surface oxidation can be described as follows. By increasing the density of defects in the sample (dislocations and deformation bands), it provides fast-diffusion paths. These are particularly effective, if high densities of dislocations accumulate at interfaces such as GBs. All GBs from cold-worked samples that were studied seem to

have oxidised preferentially compared to the adjacent grains.

The compositional analysis between the EFTEM and APT data is mostly consistent for the matrix and inner oxide, except for the lack of oxygen measured in the APT, which can be assumed to be an artefact of the technique as discussed in Section 4.2.1.

The difference in the Fe:Cr:Ni ratio in the outer oxide measured with the two techniques can be easily explained as different particles were analysed with each technique. The Ni content could be arbitrary or a size effect. In either case the composition of the outer oxide does not have an effect on GB oxidation and will therefore not be discussed further in this thesis.

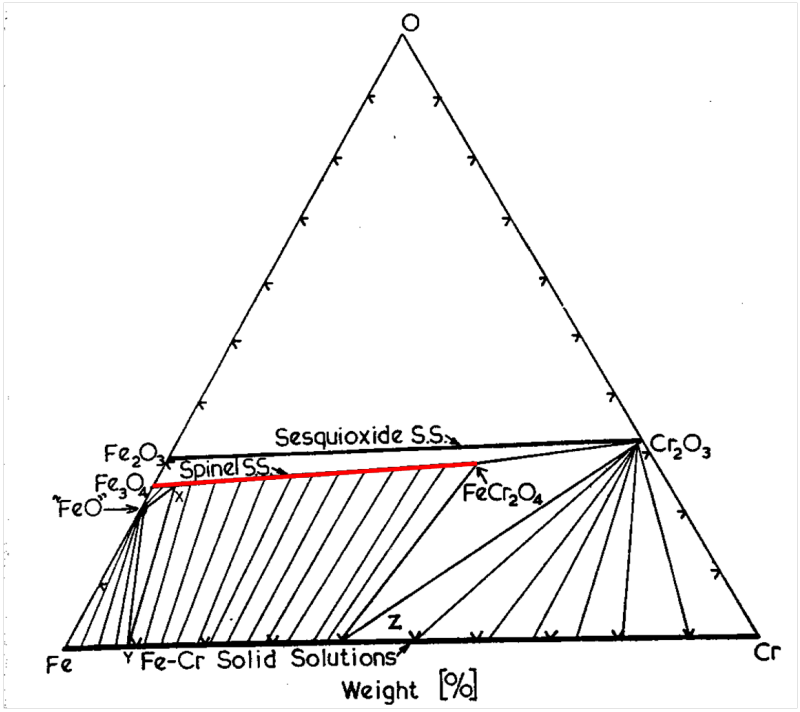

Figure 4.35: Tentative solid phase relations in system Fe-Cr-O at temperatures above 575° [218].

For stoichiometric chromite the Fe:Cr ratio should be 1:2, however the measurements of the surface oxide with both EFTEM and APT suggest a ratio closer to 1:1 (1:1 in APT and 1:1.2 in EFTEM). Even if it was assumed that Ni only occupies Cr sites this would only lead to a ratio of 1:1.1 in the APT data and 1:1.4 for the EFTEM. According to the ternary phase diagram shown in Figure 4.35 [218], Fe_3O_4 and $FeCr_2O_4$ are fully miscible. The phase diagram provided in Figure 4.35 is the lowest experimentally validated isothermal cross-section that could be found in the literature. However, an isothermal cross-section for 360° C, the testing temperature for the corrosion test in this study, has been calcu-

lated [219]. The spinel and sesquioxide phase fields in this calculated diagram are identical with the diagram in Figure 4.35. Therefore, the existence of a non-stoichiometric spinel is not surprising.

Regions of high defect density, such as GBs and deformation bands, show enhanced oxidation, despite being located below the passivating surface oxide [110, 211]. Due to the complex geometry and small dimensions of the GB oxide, it was difficult to separate the oxide from the surrounding metal. For the APT data an iso-concentration surface with 35 at.% oxygen was chosen to separate the oxide from the matrix. In the EFTEM quantification it was not possible to avoid the metal entirely as the data is projected along the thickness of the sample. The measured Ni content of 20 at.% (see Table 4.15) suggests that some of the Ni-rich interface layer was included in the analysis. However, the Fe:Cr ratio as obtained with both analysis methods is 1:3. The phase diagram in Figure 4.35 shows that there is no stable phase with such a composition. It appears that Ni^{3+} ions and possibly Mn^{3+} ions occupy some of the Fe^{3+} sites in the GBs to form a $Fe_{1-x}Ni_xCr_2O_4$-type spinel with $x \approx \frac{1}{3}$. Alternatively, a mixed phase containing some Cr_2O_3 is possible [218].

A possible reason why the surface spinel is more Fe-rich than the GB spinel seems to be that Fe is diffusing through the surface oxide to the surface. Another possibility is that solute Fe^{2+} from the environment might be reincorporated in the surface oxide. However, no obvious concentration gradient could be detected across the surface oxide as would be expected in either case. This would appear to rule out such a mechanism.

In the no stress/no cold work sample the GB oxide was Fe-rich and Cr-rich regions could be distinguished. The Cr-rich regions seemed to have formed first along dislocations in the GB region, where a high vacancy density enables fast Fe outwards diffusion. It appears likely that such regions dominate the GB oxide in the no stress/cold-work sample. So the reason for a more Cr-rich spinel oxide in the GB region could be in the enhanced Fe outwards diffusion. Contrarily, in the more Fe-rich surface oxide, the Fe is oxidised before it can diffuse outwards. This behaviour will be further discussed in Chapter 5.

Selective oxidation of dislocations has been previously demonstrated [211] and was observed in this study in the matrix region below the oxide/metal interface. Additionally Lozano-Perez *et al.* have shown that the oxidation depths can increase by up to an order of magnitude along DB interfaces or GB planes, the latter being the most effective diffusion paths [211].

Unlike ATEM data, which are always acquired projected along the direction of observation, APT data is 3D in nature and can reveal the real distribution of elements in the region of interest with high spatial resolution. This is particularly useful in understanding how the oxidation proceeds along the GB plane. While the oxygen concentration across the oxide-metal interface at any defect-free region near the sample surface changes abruptly from ∼49 to 0 at.%, the APT data shows that the oxygen concentration changes gradually across a greater length (∼200 nm) along defects (dislocations or the GB plane itself). In some places the surface oxide grows into the GB (see right hand side of Figure 4.28a), but in other regions oxygen diffuses along defects in the GB and oxide "particles" precipitate along the GB, seemingly unconnected to the surface oxide in other regions. The composition of the particles was similar to the surface oxide composition. The frequency of their occurrence decreases within the GB with increasing distance from the bulk Cr-rich oxide. Therefore, the decreasing oxygen concentration shown in Figure 4.28c should not be interpreted as the GB containing different oxides in lower oxidation states or even a linear decrease in oxidised metal atoms. Instead, the GB contains a decreasing number of particles with a spinel type oxide composition as discussed above. These results suggest that oxygen can diffuse through the metal along the GB without oxidising and an internal oxidation mechanism is present. The relevance of this finding to SCC mechanisms will be discussed in Chapter 7.

4.2.4 Oxidation under stress

The effect of applied stress on oxidation is not so straightforward. Although intentionally kept below the yield stress, the applied stress still caused the formation of DBs in the samples (see Figure 4.13b). However, it did not lead to enhanced oxidation in all GBs in the sample, as can also be seen in Figure 4.13b. The effect of cold work on oxidation is notably magnified by the presence of applied stress, especially along GBs or deformation bands. Stress assisted oxidation can be explained by means of lattice distortion at GBs and deformation bands which allows preferential diffusion along these features.

While the GB shown in both Figures 4.13 and 4.16 shows very little preferential oxidation, part of a more heavily oxidised GB was captured with APT (see Figure 4.17). The APT data also shows a large number of oxidised dislocations at the side of the GB oxide. Ni enrichment is found at the metal/oxide interfaces, particularly those of the oxide particles

along the dislocations. Figure 4.19 shows two presentations of a thin slice extracted the APT data set in projection. The left map shows an increased Ni concentration of >12% in a layer at the metal/GB oxide interface and around the oxide particles along two edge dislocations. The right map shows that the concentration is >22% in a narrow layer around the oxide particles along the dislocations. The Ni enrichment at the matrix/GB oxide interface is not that highly concentrated.

It appears that the Ni which was rejected from the oxide found fast diffusion paths in the edge dislocations and along the interface. It then accumulated along the dislocations and ahead of the GB oxide. The implications of the high Ni concentrations that can occur ahead of the GB oxides are discussed in Section 4.2.7.

Three boundaries with different oxidation behaviour were observed in the cold-worked sample that was oxidised under applied stress. Like all GBs in cold-worked materials, they are preferentially oxidised. Figure 4.32 shows an only mildly oxidised boundary. No diffraction was performed to determine the GB character, but if a broader section of the sample is examined as shown in Figure 4.36, both grains show almost parallel systems of slip bands. The angle between the two systems was 2.3°, so it seems, that the GB observed is a low-angle boundary. Dislocations that glide along slip planes can sometimes move across low-angle GBs and dislocation pile-ups are not as frequent as at ordinary GBs. If dislocation pile-ups are present at a GB, this GB is a less effective fast diffusion path for oxygen from the surface. Additionally, applied stress distorts the lattice more evenly across the two grains adjacent to low-angle GBs, rather then localised in the GB region. If the GB shown in Figure 4.36 is a low-angle boundary, it is not surprising that little preferential oxidation was observed.

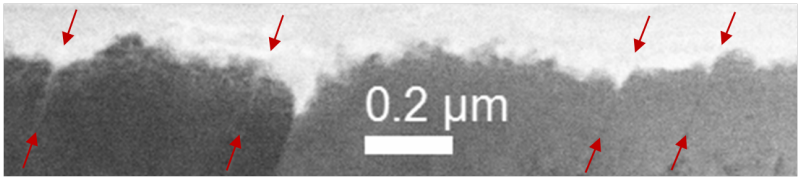

Figure 4.36: STEM BF image of stress/cold-work sample. Arrows mark slip bands.

The oxides around the two GBs shown in Figure 4.33 look very different from one another. Figure 4.33a and b shows a slip band, indicated by the arrow in the bottom of the image, in very close proximity to the GB. Initially the GB oxide surrounds the GB and the slip band and fills the entire space between them. In this region, the surface damage from

polishing appears to control the oxidation behaviour. Then the oxide grew along a path between both features, adjacent to the slip band on the right. Ahead of the oxide portion is a bright area, which probably corresponds to a Ni rich region with two cells.

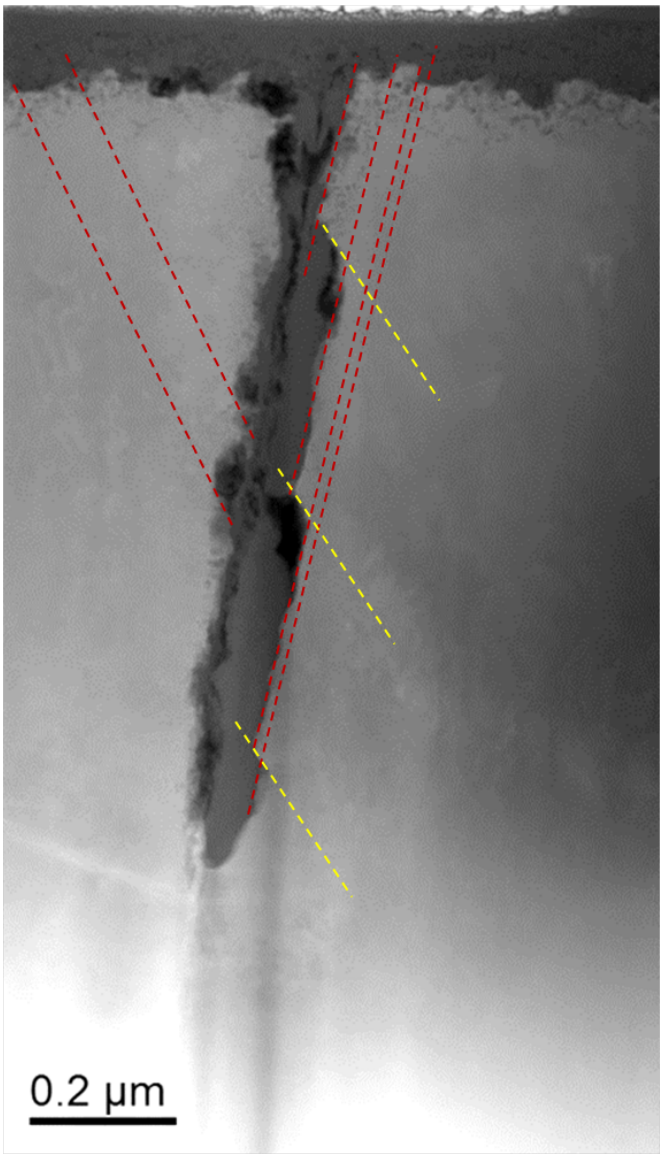

Figure 4.37: STEM BF image of the stress/cold-work sample. Slip planes indicated by dashed lines.

It is possible that the TEM foil initially contained more DBs then visible in Figure 4.33. The DBs might have vanished when the sample was sectioned and some of the stress stored in the lattice was relaxed. This seems to have happened around the GB in Figure 4.33c and d. The positions of some former deformation bands are indicated by the dashed lines in Figure 4.37. The GB oxide has a step-like pattern on the right side and the extensions of the edges coincide with enhanced oxidation at the surface. The oxide has filled the entire area between the GB and the deformation bands. It appears as if O diffused along

the DBs without oxidising the surrounding metal until it reached the GB. The left grain is not very oxidised. Little oxide has grown in local defects and along few deformation bands. Despite the great oxide depth no Ni enrichment was observed at the oxide front.

4.2.5 GB oxidation

Cold-work prior to oxidation induces dislocations and deformation bands into the material and activates existing dislocations. The dislocations cannot cross GBs and pile up in the slip planes of the material.

Applied stress during oxidation induces deformation bands, creates and activates dislocations and distorts the crystal lattice, particularly near irregularities, such as GBs, deformation bands and all other defects.

The flat surface of a perfect single crystal would have an oxide film of even thickness. However, the oxide thickness varies on polycrystalline materials, because oxidation is faster along some crystallographic directions. GBs have different properties, depending on the misorientation between the adjacent grains and therefore they have varying oxygen diffusion and oxidation rates. However, GBs are very localised features that represent very short range lattice disorder. A random GB, without any dislocation pile-ups or externally induced strain fields, should therefore not have significantly higher oxidation rates than the neighbouring grains (see Figure 4.38a).

The range of local disorder is extended, if dislocations move along slip planes in the material and pile up at a GB. This should only happen, if the material was plastically deformed, i.e. enhanced oxidation in this study was only expected in cold-worked samples.

In the no stress/no cold-work sample, dislocations were induced in the surface region by mechanical polishing prior to oxidation. This was not intended and should be avoided in future investigations. However, the results collected from the sample with surface defects are still valuable. They show the oxide growth mechanism if only dislocation pile-ups (no DBs) are present. Because of the dislocation pile-ups near the GB, a much wider region around the GB was oxidised (Figure 4.38b). It appears that oxygen diffusion along the GB was not faster than along the dislocations, as the oxide front was blunt. It was frequently observed that deformation bands are oxidised to a greater depth than GBs, this suggests that they are a faster diffusion path. If deformation bands and GBs are in close proximity, the room between them is often filled with oxide, whereas the other side of the

deformation band (away from the GB) is almost never effected (Figure 4.38c).

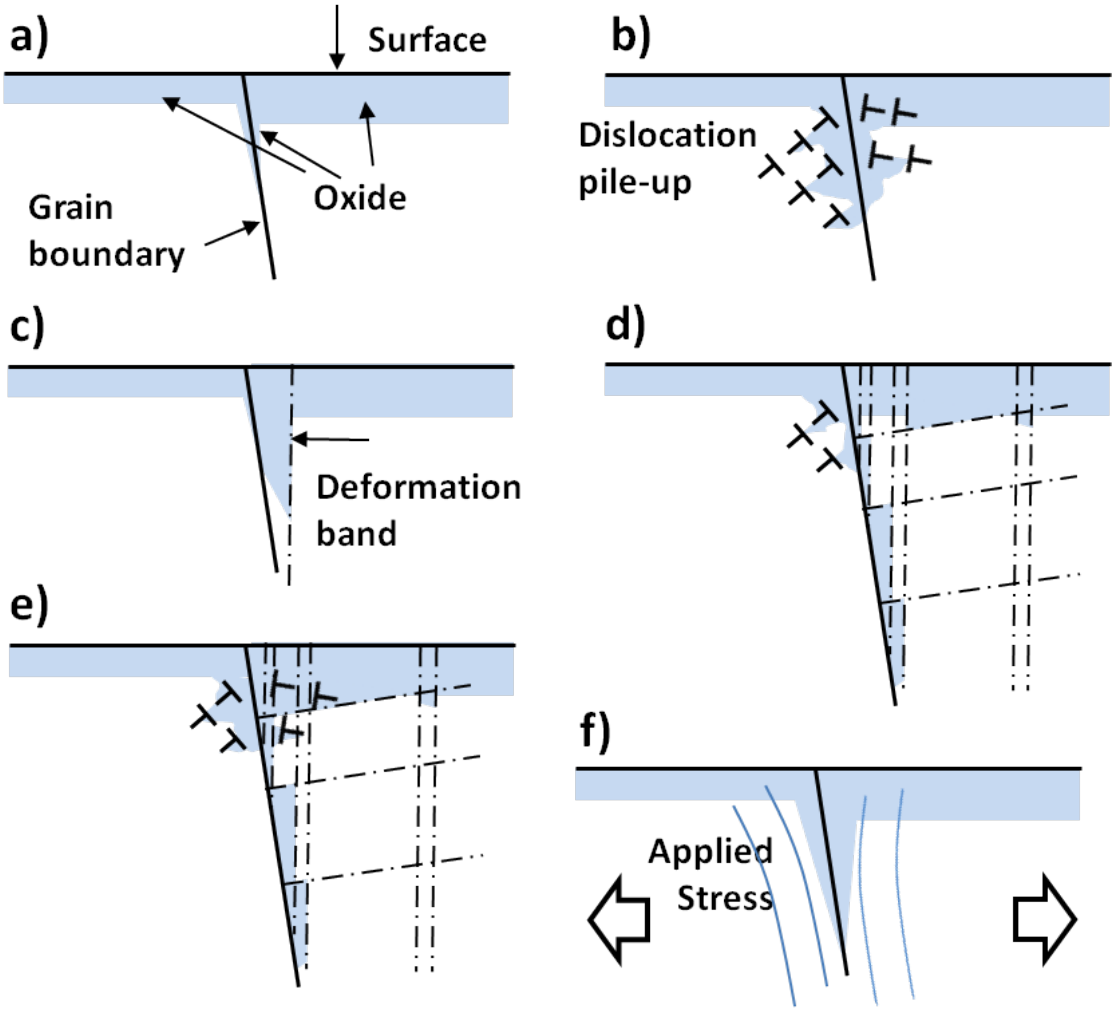

Figure 4.38: Schematic showing the oxidation behaviour around GBs intersecting the surface and other defects in the crystal lattice. a) Oxide at a high angle GB. b) Oxide at a high angle GB with dislocation pile-up in both grains. c) Oxide at a GB in close proximity to a deformation band. d) Oxide around a GB, with a complicated system of deformation bands in the right grain and a dislocation pile-up in the left grain. e) Oxide around a GB, with a complicated system of deformation bands in the right grain and a dislocation pile-ups in both grains. f) Oxide around a GB with lattice distortions due to externally applied stress.

From this behaviour it can be concluded that O diffusion and oxidation along the DBs is fast, but O diffusion across deformation bands does not normally occur, unless in combination with other defects. If several deformation bands are almost parallel to a GB especially in combination with dislocation pile-ups, rapid diffusion along the deformation bands and rapid oxidation in the dislocations piled up along a second slip system can lead to considerably higher oxide growth rates in GB regions as illustrated in Figures 4.38d and 4.38e.

Applied stress can induce more of those corrosion enhancing features. Additionally, before slip occurs and deformation bands are created, elastic deformation occurs. That means stress is stored in the distorted lattice. Figure 4.38f shows how the lattice distortion has enhanced oxygen diffusion at the GB.

4.2.6 The role of lithium and boron

APT results prove that Li segregates to the Cr-rich oxide, both at the surface and along the GBs, whereas no B could be detected in the oxide. To understand this, it is necessary to look at the behaviour of $B(OH)_3$ and LiOH if added to high purity water. Li has only one valence electron, and is a strong electron donor. B in contrast has three valence electrons and is an electron acceptor. It therefore also becomes a hydroxide acceptor. The respective equilibrium equations are:

$$LiOH \rightleftharpoons Li^+ + (OH)^- \tag{4.2}$$

$$B(OH)_3 + H_2O \rightleftharpoons B(OH)_4^- + H^+ \tag{4.3}$$

Tetrahydroxyborate $B(OH)_4^-$ as well as $B(OH)_3$ have large hydroxide shells, which hinder the diffusion into the metal and promote accumulation at the oxide surface. This theory is in line with previous findings from NanoSIMS measurements [163], where B was found only on the top surface of the oxide. Due to sample preparation procedures for APT this surface will, in most cases, be entirely removed, and therefore no B could be detected on the oxide surface with this technique. The concentration is too low for most other techniques to detect. LiOH, in contrast, dissociates to Li^+ and OH^-. The very small cation, Li^+, can easily diffuse into the oxide as an interstitial atom. The (oxidised) GB might operate as a fast diffusion path. As a result Li was easily detected in all the oxide regions, reaching concentrations up to 200 ppm in the GB oxide.

The panel in Figure 4.20 illustrates the distribution of Li in the oxidising regions of the stress/no cold-work sample. Three different slices, one in every row, have been extracted from the samples, each slice is 2 nm thick. The illustrations on the left show the position of the oxide and Ni enrichments >22 % and all the Li atoms in the plane. In some places high Ni concentrations were observed away from oxides. It appears that in these regions Ni has diffused along an unoxidised dislocation. Most Li atoms are in the oxide regions,

but some seem to line up in the same regions that are enriched in Ni (see circles in the left column of the panel in Figure 4.20). The illustration on the right show the positions of all Fe_2O ions in the slices. In most oxide regions, O is evaporated on its own or together with Cr, sometimes as FeO (see Figure 4.18). Only in the outer regions of the oxide two Fe atoms were evaporated together with only one O. In these regions oxidation was probably only about to start at the end of the corrosion test, and the local O concentration was still very low. In some cases these regions fall together with regions of Li enrichment outside the core oxide (see circles in the right column of the panel in Figure 4.20). This suggests that Li could diffuse into dislocations faster than oxygen. As discussed above it will most likely be present as Li^+ and therefore slightly change the local potential. It remains uncertain, whether this effect is strong enough to influence corrosion behaviour. Andresen *et al.* [136] did not observe any significant changes in the corrosion rates depending on Li concentration. However, that does not mean that it does not have any influence on the corrosion paths.

Ni is rejected from the oxide and diffuses along fast diffusion paths ahead of the oxide front. This it why it accumulates along dislocations and reaches such high local concentrations. The implications of this behaviour are discussed in the next section.

4.2.7 The role of Ni enrichment ahead of GB oxides

Ni enrichment at the oxide-metal interface as previously observed [111] and predicted by modelling [220], was confirmed in this study. Additionally, large highly Ni-enriched regions were found ahead of the GB oxides. Regions like this were observed with ATEM in a number of GBs (see Figures 4.39 and 4.40), including every single one that was examined in the no stress/cold-work sample. The last GB added to the bottom of the panel in Figure 4.39 is from a cold-worked sample from the same test series. It was exposed to a smaller load than the stress/cold-work sample during the corrosion test and is therefore referred to as low stress/cold-work sample.

However, the dimensions of the Ni-rich region varied and were not directly related to the dimensions of the oxide above. In most samples the Ni-enrichment was constrained to one grain. In others it alternated sides along the length of the GB (see Figure 6.2), but in no case had it accumulated on both sides of the GB at the same depth. The source of the Ni atoms in the Ni-rich regions was investigated using the EFTEM elemental map

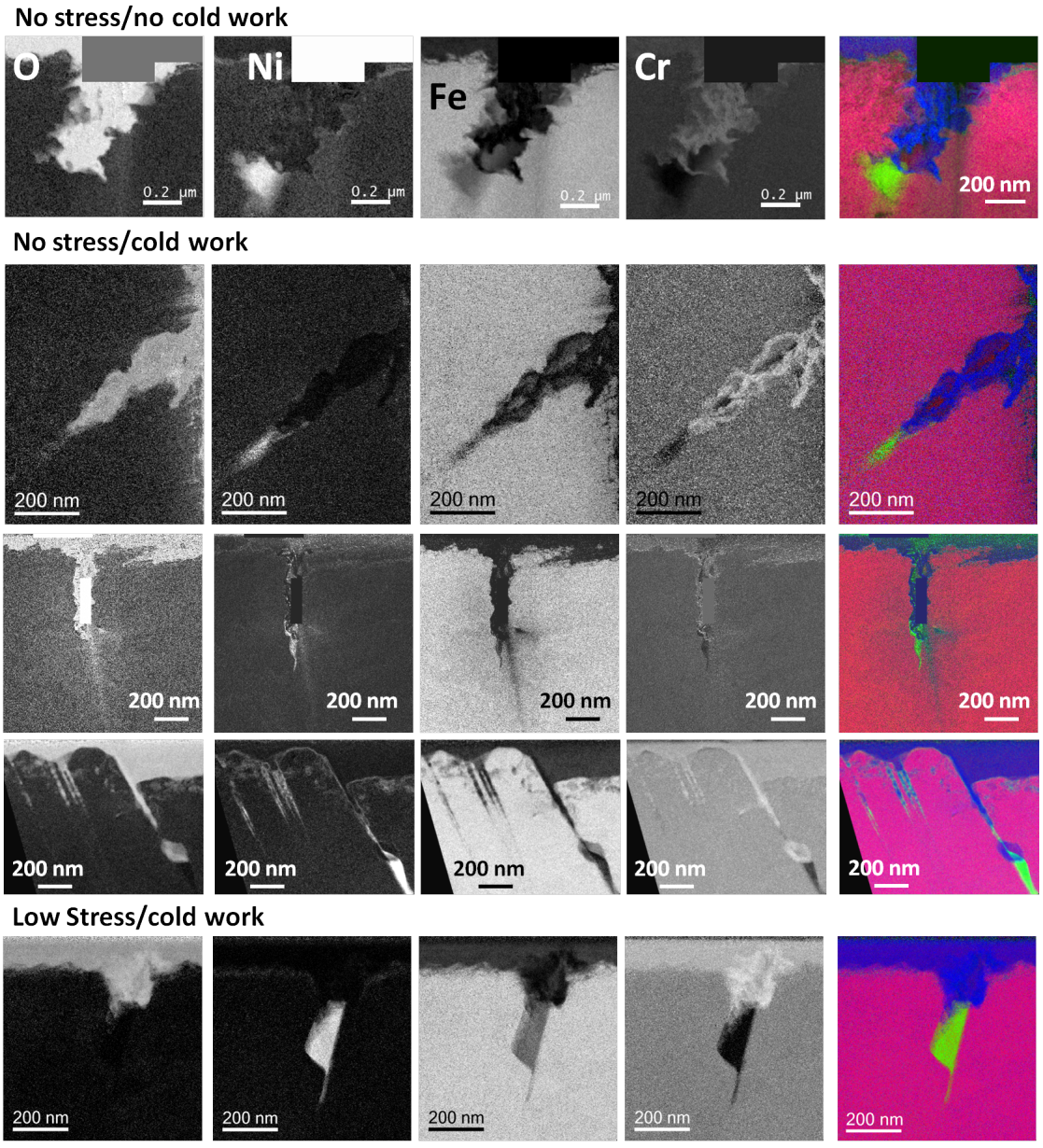

Figure 4.39: EFTEM data of 5 different samples each showing Ni enrichment at the oxidation front. The low stress/cold work sample has not been subject of this thesis. However, it shows pronounced Ni enrichment ahead of the GB oxide in this case.

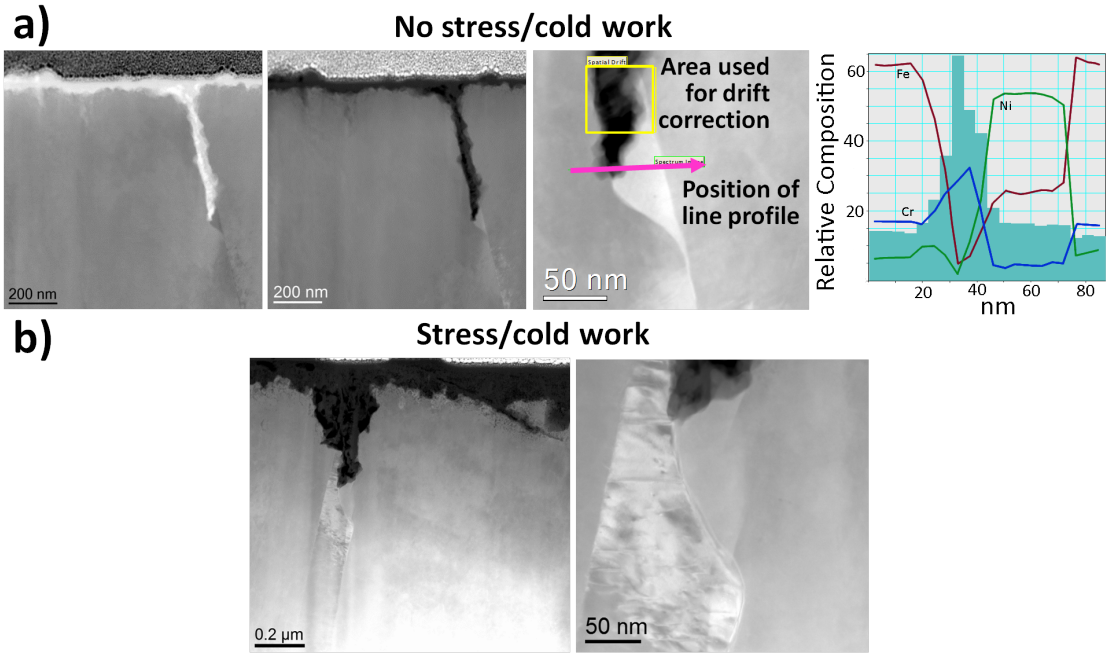

Figure 4.40: STEM data of 2 different samples each showing Ni enrichment at the oxidation front. a) GB oxide in the no stress/cold-work sample. From left to right: BF, HAADF, high-resolution HAADF of Ni-rich region, EELS line profile through Ni-rich region. b) GB oxide in the stress/cold-work sample, HAADF and high-resolution HAADF images.

(Figure 4.24) and the respective APT data (Figure 6.3). No Ni depletion was observed in the matrix around the oxidised regions, which suggests that the Ni was rejected from the volume occupied by the oxide. Figure 4.41 shows the Pourbaix potential-pH diagrams for the Fe-Cr-Ni-H_2O system at 300°C. The dashed blue lines mark the pH at PWR primary water conditions (7.2). At this pH the Ni/NiO phase boundary for the Ni-H_2O system (Figure 4.41c) is at approximately -780 mV compared to the standard hydrogen electrode (SHE). The $FeCr_2O_4/NiFe_2O_4$ phase boundary for the complete Fe-Cr-Ni-H_2O system also lies at about -780 mV compared to the SHE. From this it can be concluded, that the local potential at the oxide front is below -780 mV compared to the SHE, so that $FeCr_2O_4$ type spinels are stable, whereas Ni mostly remains in its metallic form.

Within the sample, the rejected metallic Ni enriches steel matrix. Given enough time, it would diffuse through the steel without any major changes in composition. However, Ni diffusion in steel is very slow at operating temperatures [222]. Therefore Ni accumulates in one of the grains adjacent to the GB ahead of the oxidation front. Depending on crystallographic orientation of the grains and vacancy concentration in the grain one side of the GB will be preferred.

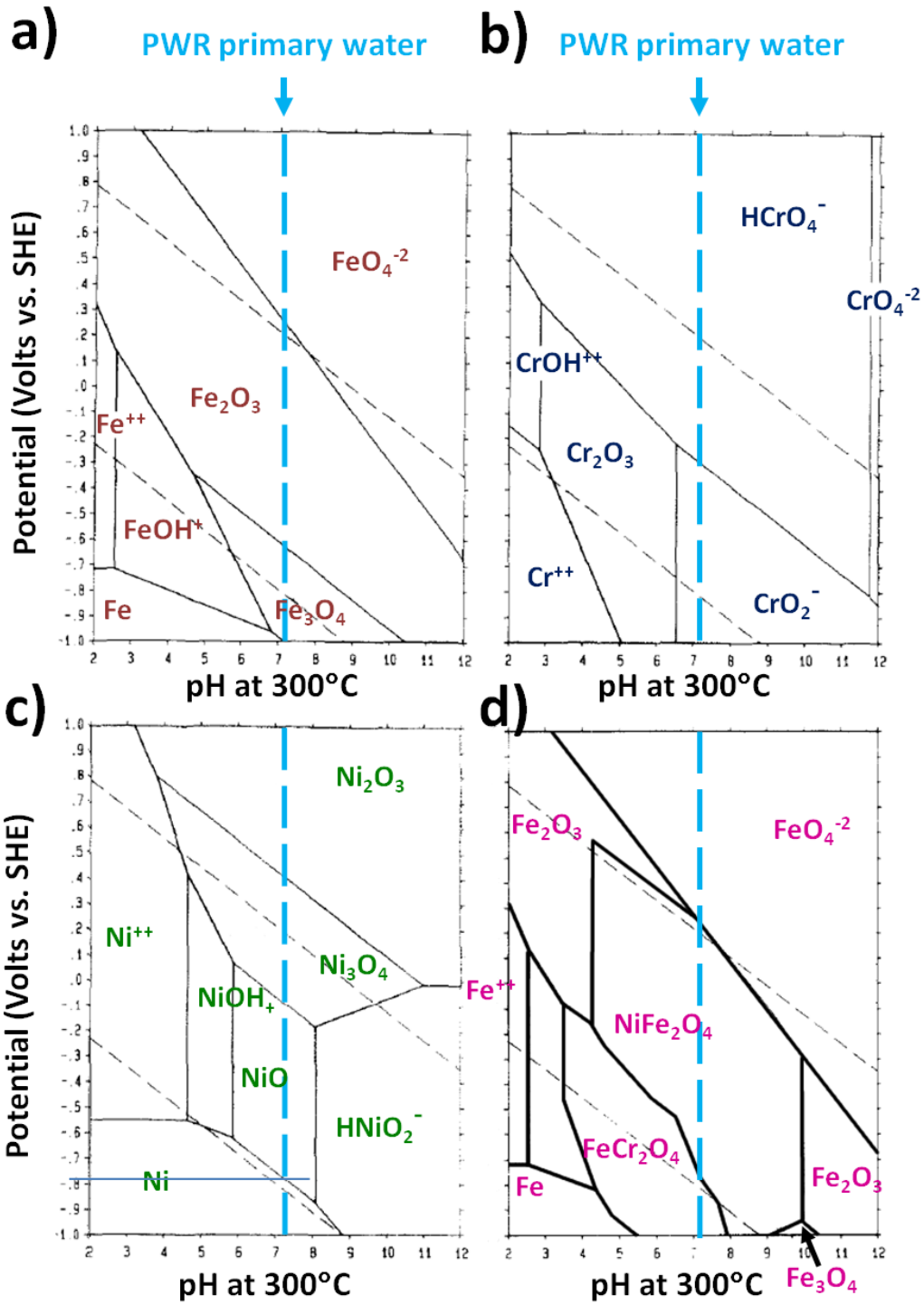

Figure 4.41: Pourbaix diagrams for the Fe-Cr-Ni-H_2O system at 300°C. Full lines separate the regions of stability for the species considered (dissolved species at activity = 10^{-6} mol/kg, solids at unit activity). Dashed black lines on each diagram represent water decomposition equilibria. The upper line is for decomposition to 1 atm oxygen gas and the lower line is for 1 atm hydrogen gas. Dashed blue lines represent the nominal pH of PWR primary water. a) Fe-H_2O diagram. b) Cr-H_2O diagram. c) Ni-H_2O diagram. d) Combined ternary system. Fe species for the ternary system are shown in pink [221].

The composition was analysed in all samples shown in Figure 4.39 and a summary of the measured compositions is shown in table 4.16. Interpreting this data, it is important to note that EFTEM data always represent the composition in projection. In this case that means that some matrix data could have been included in the analysis. If this was the case than the real Fe and Cr contents in the particle would be lower than measured and the Ni content would be even higher.

Concentration	**Fe**	**Cr**	**Ni**
No stress/no cold-work	36±2	4±1	61±10
No stress/cold-work	23±3	4±2	73±10
Low stress/cold-work	35±3	2±1	63±10

Table 4.16: Relative composition in the Ni-rich particles measured in the EFTEM data of the different samples in at. %.

All compositions measured with EFTEM, ATP and EELS were averaged and the result is presented in Table 4.17. The Ni-rich regions in the bottom three boundaries in Figure 4.39 and the two boundaries in Figure 4.40 all have abrupt borders to the Fe-rich matrix. This is even more clear in the EELS line profile on the right side of Figure 4.40a. A gradient would be expected, if Ni diffusion only depended on vacancy concentration around the oxide or rather the high-Ni region. The existence of such sharp boundaries suggests that a precipitate of a Ni-rich phase formed at the operating temperature. If that was the case, such a phase should show in the isothermal section at 360°C of the respective Fe-Cr-Ni phase diagram. However, due to the low self-diffusion rates of Fe, Cr and Ni at low temperatures, no experimental data on formation of equilibrium phases exists. The (experimentally validated) phase diagram for 750°C in Figure 4.42a shows a continuous fcc phase in the low Cr/high Ni region [222]. However, the calculated diagram in Figure 4.42b for 400°C suggests that the stable phases look very different at lower temperatures [223]. The extended gamma phase at Cr concentrations under 20 wt.% (that is frozen to form the austenite phase in 304 stainless steel) has separated into two slightly bigger and two very small regions. A small $L1_2$ phase field can be found at between 62 and 78 at.% Ni at Cr concentration of <0.2 at.%. The enlarged section in Figure 4.42c was provided in [224] in mass %, but as all species have similar masses, the difference to at.% can be neglected for this discussion.

The Cr (blue) and Ni (green) concentrations with there respective error ranges have been indicated by the shaded region in the phase diagram in Figure 4.42c. The phase of the

Fe	Cr	Ni
29±8	4±2	67±6

Table 4.17: Average of all available data (EFTEM, APT and EELS) in at. %. Errors account for the variation in the means.

Ni-rich particles would be in the boxed region, where both bars overlap. The fact that the boxed region does not coincide with any of the single phase fields seems to contradict the hypothesis that a Ni-rich phase has formed. The parent alloy composition lies in a three phase triangle with the Ni-rich fcc phase at one corner, suggesting this phase being a likely candidate to form at higher Ni concentrations. On the other hand, the $L1_2$ phase is exactly in the range of Ni concentrations, that were measured in the particles. It is possible, that the Cr, that was measured is due to the projection in the EFTEM and EELS data and trajectory aberrations in the APT data. Alternatively, the phase field in the calculated phase diagram could be too small. The isothermal cross section of the phase diagram is slightly higher than the testing temperature for the samples analysed in this study and there are limitations to the accuracy of calculated phase diagrams [225]. Synthesis of a phase of the measured composition and ageing at 360°C is recommended to test for and identify the structure of a possible equilibrium phase that may form at this temperature.

The formation of highly Ni-enriched regions at the oxidation front is very relevant to SCC. The plot in Figure 4.43 is just an example of how important the bulk Ni content in an alloy could be to SCC susceptibility [226]. The PWR primary water environment studied in this thesis is not as aggressive as the boiling $MgCl_2$, but for the boiling $MgCl_2$ environment it was shown how fracture time varied from >1000 h in Ni-free alloys to less than 1 h in alloys containing between 5 and 13 % Ni and back to >1000 h for alloys with >42 % Ni. This might be suggesting that the ability of Ni to influence the type of oxide that forms intergranularly (or to precipitate a Ni-rich phase) could be very important to understand SCC susceptibility.

In all the GBs shown, except the one in the second row from the top of Figure 4.39, which has the least pronounced Ni-enrichment, the oxide looks thicker, just above the Ni-rich regions. From this it appears probable that Ni enrichment can stop or at least delay further oxygen diffusion along the GB. This hypothesis is supported by some SEM images

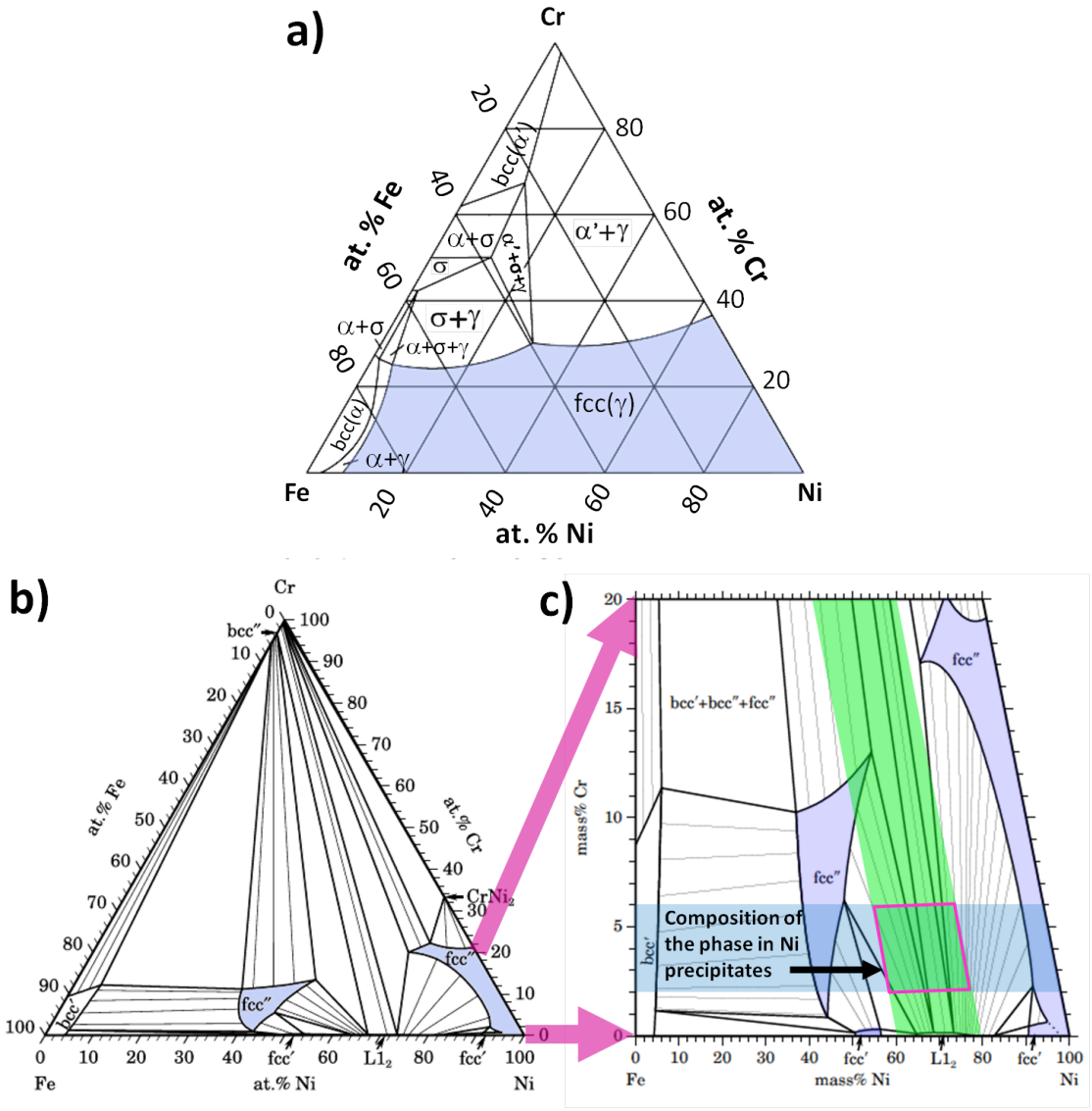

Figure 4.42: Ternary Fe-Cr-Ni phase diagrams. a) 750° C [222]. b) 400° C [223]. c) Magnification of the phase diagram in b in the range of the lower Cr contents [224].

extracted from a 3D FIB slicing experiment. Figure 4.23 show several regions, where the oxide has grown wider and in some cases even seems to grow around a bright contrast particle. The data also shows, that these bright regions seem to be particles next to or in the GB plane, rather than a continuous cylindrical region lining the entire oxidation front. The formation of more or less spherical particles or precipitates further supports the idea, that a new phase is forming in these regions as it will lead to minimal phase interfaces, which would be energetically favourable.

The implications of these findings for the SCC mechanism in the studied system are further discussed in chapter 7.

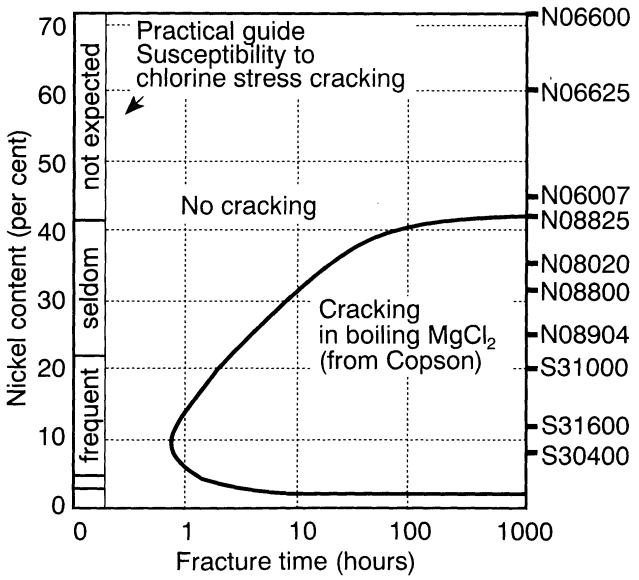

Figure 4.43: Effect of Ni on resistance to SCC [226].

Chapter 5

Deformation Band Oxidation

As SCC susceptibility in 304 stainless steel is enhanced by CW (see Chapter 2) it is important to understand the role of the different defects that the deformation causes in the crystal structure. This chapter is dealing with planar defects.

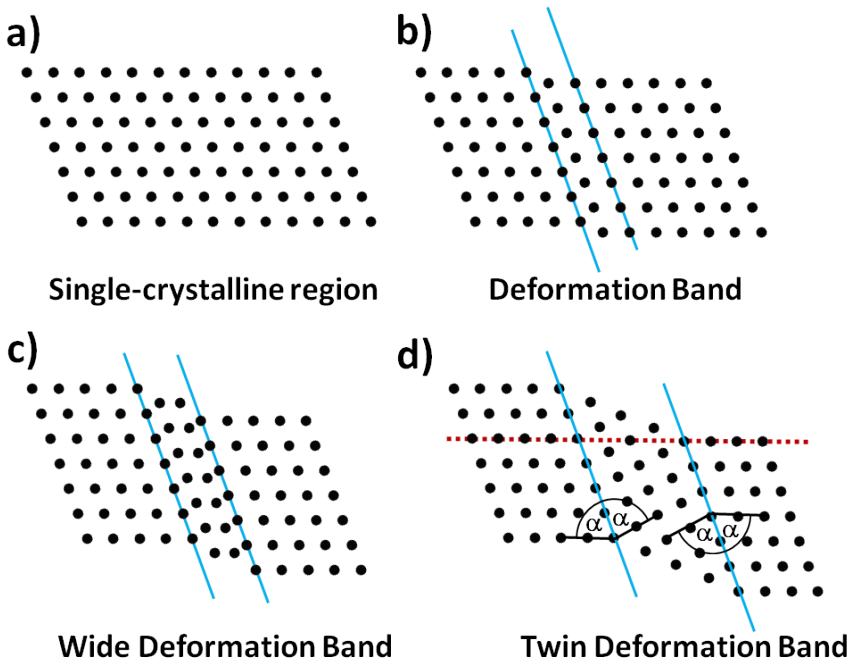

Figure 5.1: 2D Schematics illustrating different types of planar crystal defects. Each dot could be interpreted as a stack of dots perpendicular to the plane of the schematic. a) Undisturbed grain. b) Slip has occurred and a narrow region of lattice disturbance was created — a deformation band. c) Slip has occurred in several adjacent planes, and a wider region of lattice disturbance was created — also deformation band. d) Slip has occurred in several adjacent planes. This time each plane was displaced by a small amount, so that the crystal structure is mirrored at the DB plane. Long range order remained intact on either side of the deformation band and one third of the lattice points inside the band coincide with the lattice points of the surrounding grain — a twin deformation band.

The terminology in the literature is sometimes confusing — it mentions slip bands [63], deformation bands [154,227], deformation slip [228], deformation twins [154,229] and twin deformation bands [110]. In the cited sources, the first three and the latter two mean the same thing respectively. A schematic of the different defect types is shown in Figure 5.1. Only diffraction experiments or high resolution imaging can distinguish between two narrow Deformation Bands (DBs) as in Figure 5.1b and a single Twin Deformation Band (TDB) as in Figure 5.1d.

DBs were observed in all samples that have been either cold-worked or oxidised under applied stress. Oxide growth was mostly observed in DBs in contact with the surface, but also in some cases at intersections with GB oxides. Lozano-Perez *et al.* observed oxides in deformation bands along crack flanks of cold-worked 304-type stainless steels with nanoSIMS and Scanning Auger Microscopy (SAM) (Figure 5.2) [143]. The extent of the DB oxides (more than 2 μm measured from the crack flank in only 666 h exposure) was partly due to the reduced Cr content (15 wt.% instead of the 18 wt.% in commercial 304 SS) and hence the reduced general corrosion resistance of the alloy studied. The Ni map showed Ni enrichment associated with the oxidised DBs. The resolution of the technique was not sufficient to show the exact position of the Ni enrichment with respect to the DB oxides.

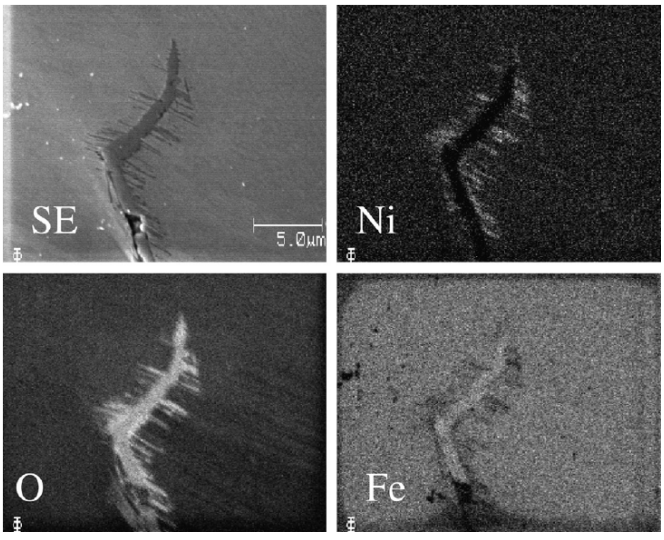

Figure 5.2: SAM images of a stress corrosion crack in a 20% cold-worked 304 stainless steel with 15% Cr [143].

Although SCC in austenitic stainless steels is found to be almost exclusively intergranular, it has been observed in this study that the maximum oxide depth in deformation bands

commonly exceeds the maximum oxide depth in GBs. These DB oxides are often much more constrained to a very narrow band and little metal is affected by the corrosion attack. In the present work, the composition of the DB oxides was analysed in EFTEM maps and compared to other oxide regions.

5.1 Results

Stress/no cold-work

Although the applied load during oxidation was chosen such that the stresses remained below the yield strength, and thus no plastic deformation should have been caused, DBs of variable width were frequently observed in the stress/no cold-work sample. This suggests that stresses in the sample during the oxidation were sufficient for localised plastic deformation. In places where the DBs end at the surface, oxides have grown along the lattice disturbances in the DBs and also in the spaces between tightly arranged DBs.
Figure 5.3 shows a TEM BF micrograph and the EFTEM elemental maps of the same region. The images containing oxidised DBs in the stress/no cold-work sample, where the original sample surface is horizontal across the top of the map. Oxides have grown in the area between the deformation bands, with oxide depths of 400 - 450 nm. The positions of some DBs are indicated by the black arrows in the TEM BF image. Pink arrows in the oxygen map (Figure 5.3b) show the the oxidation front terminating at straight parallel lines in each section. The white arrows in the Fe and Cr maps indicate the Fe depletion and Cr enrichment as compared to the bulk oxide in DBs on the oxide/metal interface. In these DBs Ni enrichment was observed in high concentration (about 26 at.%) ahead of the oxide front (Figure 5.3d). The remaining oxide was surrounded by a narrow Ni enriched layer, but no particular Ni enrichment was observed protruding into the DBs in the right half of the images.

Conc.	**Fe**	**Cr**	**Ni**	**O**
Deformation Band Oxide	18.7±0.6	22.6±1.8	5±4.3	54.1±3.5
Surface Oxide near DBs	22±1.5	19.5±0.5	3.7±2.8	55±1.4
Ni enriched area in DBs	54±6	20±3	26±3	Omitted

Table 5.1: Deformation band compositions measured in EFTEM maps of the stress/no cold-work sample in at. %.

The composition of the DB oxide was also measured in this sample and the results can be

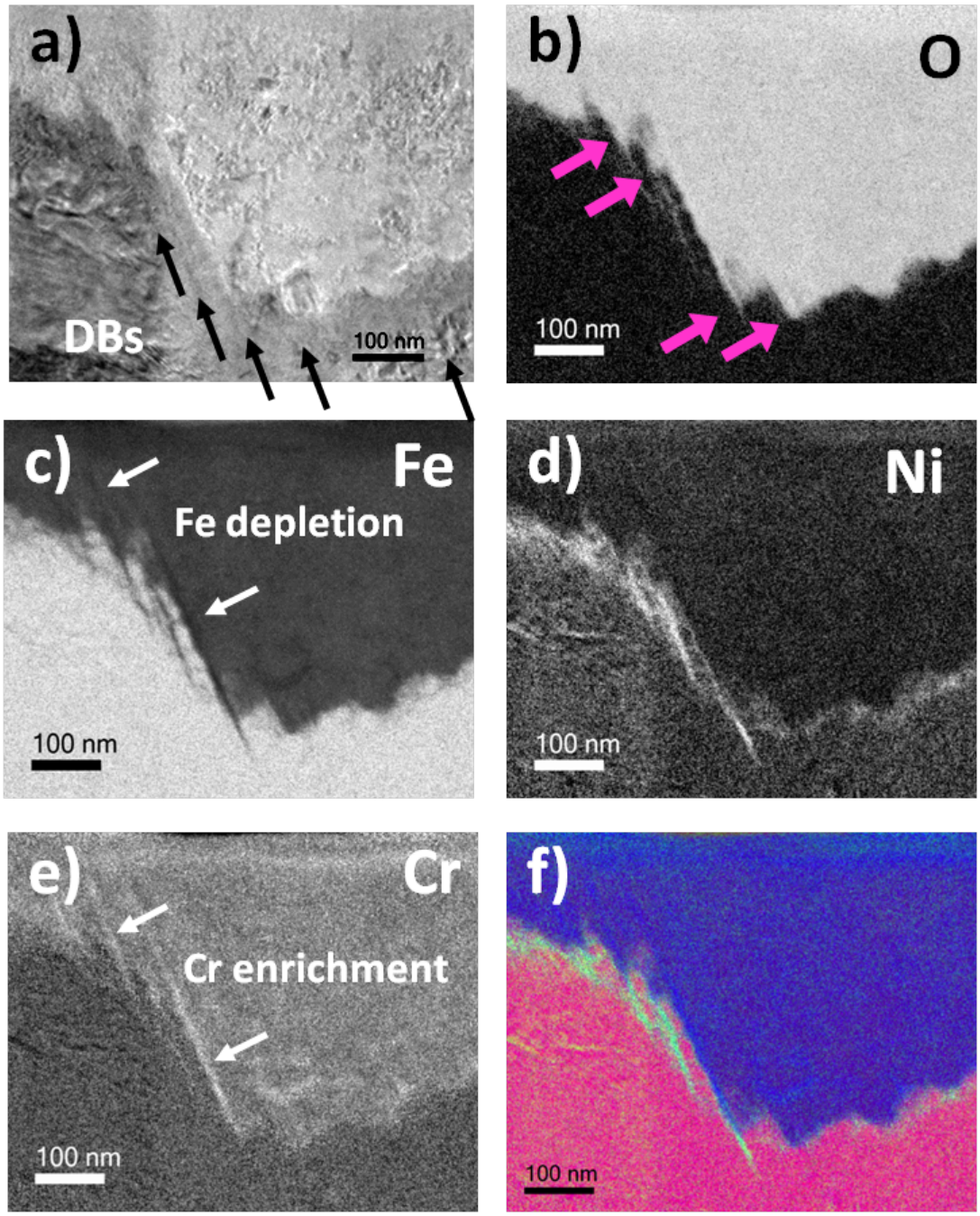

Figure 5.3: a) TEM BF image of TDBs in the stress/no cold-work sample. b-e) EFTEM maps of the sample. f)RGB map showing Fe in red, Ni in green and Cr in blue.

seen in Table 5.1. They confirm the trend that was already shown in the EFTEM maps (Figure 5.3); the oxide in the DBs contains more Cr and less Fe as compared to the bulk oxide between the DBs and at the surface.

No stress/cold-work

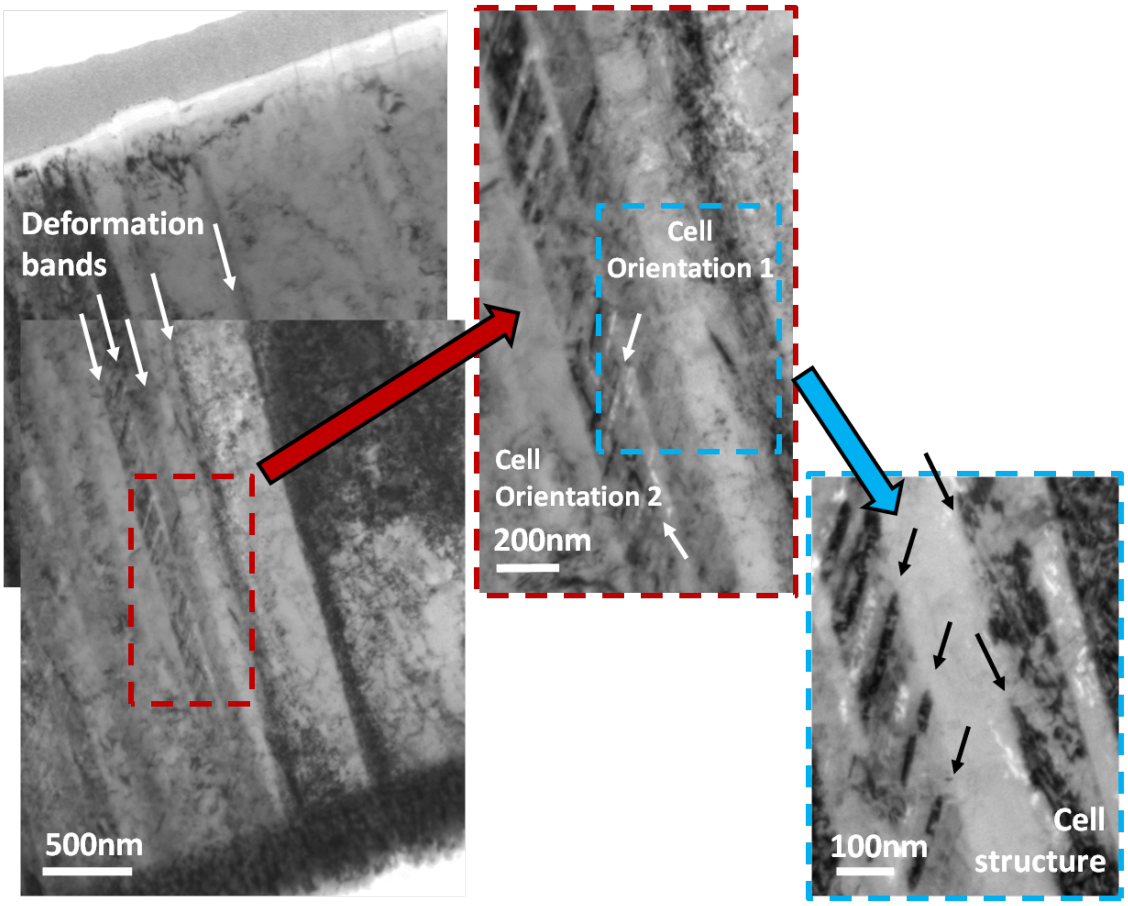

Figure 5.4: TEM BF images of DBs in the no stress/cold-work sample showing sub cell structure in widely spaced deformation bands.

The structure of the unoxidised DBs in the no stress/cold-work sample was analysed with BF TEM in the JEOL 2010. Figure 5.4 shows that the area between the DBs is divided into small cells, which are separated by short DBs in a second slip system. The right image (out of focus) reveals the sub cell structure. In the centre image it even appears as if two secondary slip systems were active at the same time (arrows) dividing the area between the DBs into even smaller sub-cells. The primary DBs in the displayed region are 100 - 150 nm apart.

It was frequently observed that the no stress/cold-work samples had been plastically deformed. Figure 5.5 shows a TEM BF image and the respective EFTEM elemental maps of several DBs in this material. The original surface lies horizontal across the top of the images. Other than in the stress/no cold-work sample above, these DBs appeared in pairs, with the distance between each pair about 5 nm. Little oxide has formed, mostly in the middle between the pairs. Some oxide can also be found in the areas outside the pairs, as

indicated by the white arrows in the RGB map in Figure 5.5f. The boxed region in Figure 5.5a is shown in high-resolution in Figure 5.6. It can be seen that the crystal structure is mirrored at the DB plane. Fast-Fourier Transformation (FFT) plots were generated for the boxed regions and the orientation of the patterns were compared. A 67° rotation about a [110] type axes was measured. The DB pairs observed here are TDBs.

The composition of the DB oxides was analysed in the no stress/cold-work sample and the results can be found in Table 5.2. The oxide along the DBs in Figure 5.5 contained more than 30 at.% Cr and less than 10 at.% Fe (much less in some areas).

Conc.	**Fe**	**Cr**	**Ni**	**O**
Deformation Band Oxide	9.3±5.3	32.6±1.7	2.3±2	55.9±6.5
Surface Oxide near DBs	21.1±2.2	19.7±2.4	5.6±2.3	53.5±6.5

Table 5.2: Deformation band compositions measured in EFTEM maps of the no stress/cold-work sample in at. %.

A close up of the O and Ni maps of the TDBs on the right side of the images in Figure 5.5 is shown in Figure 5.7. The oxide has grown in the areas inside the twins, while the twin boundaries themselves are highly enriched with Ni even beyond all oxidised regions. The oxide inside the twins (referred to as DB oxide in Table 5.2) is further separated by the indicated Ni-rich areas (Figure 5.7b). The oxide has grown in cells like the ones observed in Figure 5.4, while Ni, rejected from the oxide regions, has accumulated and diffused along the cell boundaries.

Two more DBs were observed in the same grain. The respective TEM BF image and EFTEM maps can be found in Figure 5.8. The oxide composition is the same as in Table 5.2. However, these DBs are separated by 47 nm and most of the oxide has grown along the DBs rather than in the area between them. The oxide is inhomogeneous and porous in the TEM BF image. The oxide depths are 185 nm and 230 nm respectively. No cell structure was observed between the DBs. Ni enrichment is observed ahead of the oxides in the DBs, but it does not surround the oxides to the same extent as in Figure 5.7.

At TDBs the oxide seems to grow in the band while Ni diffuses along the band edges, in the single DBs Ni is pushed into the band ahead of the oxide and the oxidation depth is greater.

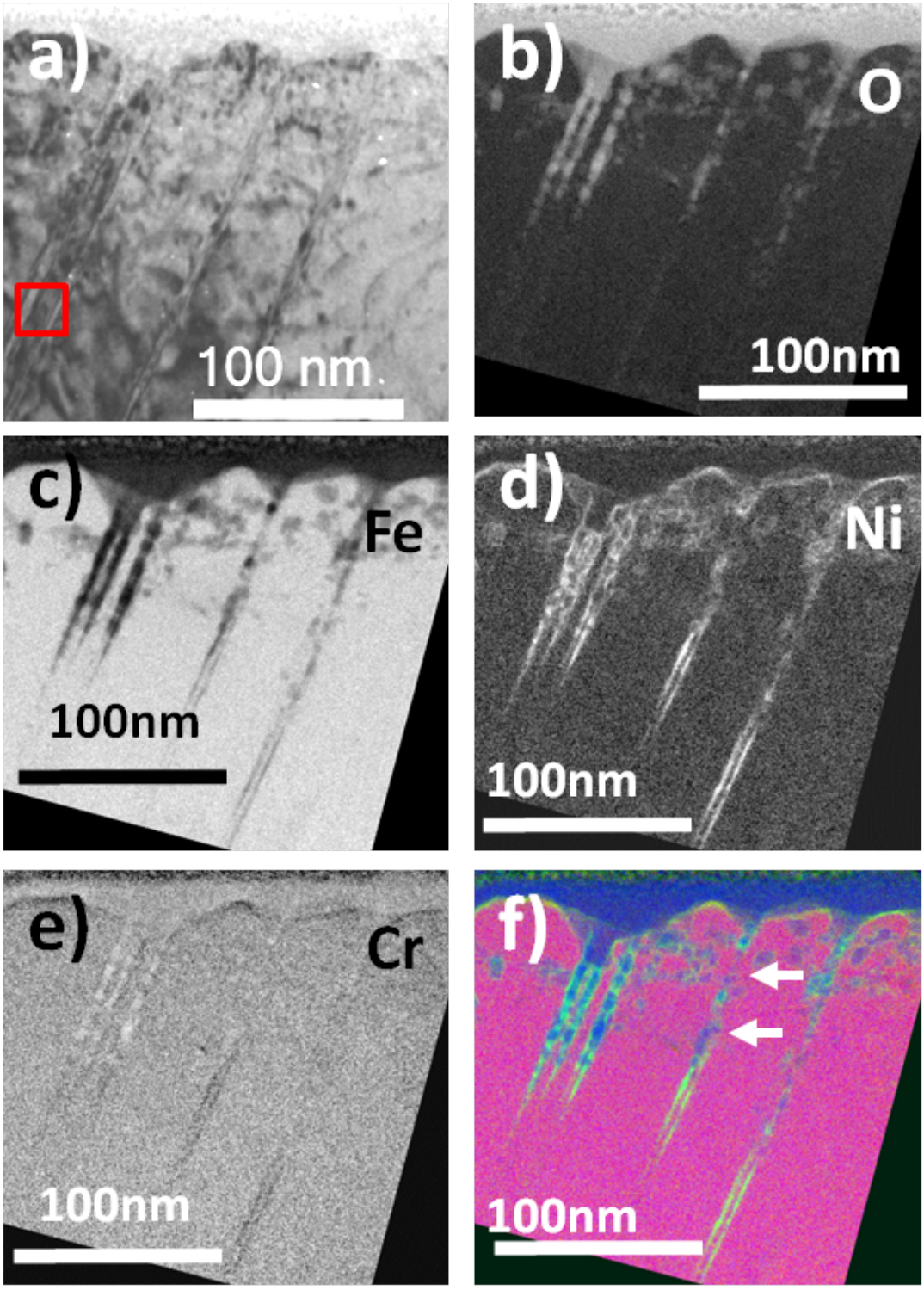

Figure 5.5: a) TEM BF image of DBs in the no stress/cold-work sample. A high-resolution micrograph of the boxed region is shown in Figure 5.6. b-e) EFTEM maps of the sample. f)RGB map showing Fe in red, Ni in green and Cr in blue.

5.2 Discussion

The surface near oxidation of GBs and DBs, although it looks similar at first glance, seems to follow different mechanisms. In this research it was commonly observed that DBs are

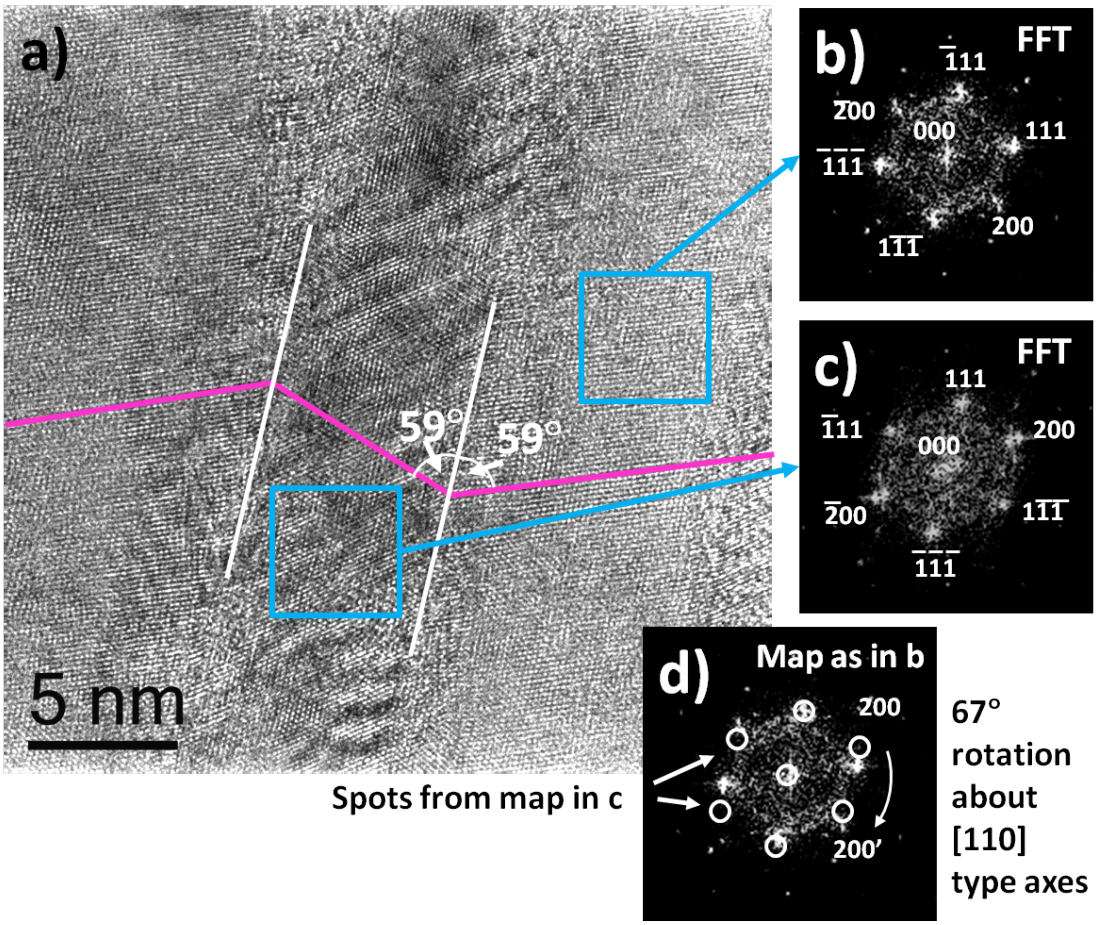

Figure 5.6: a) High-resolution micrograph of the boxed region in Figure 5.5a. Analysis of the orientation of the lattice planes shows mirroring of the crystal structure at the DB plane. b) FFT plot from the right grain. c) FFT plot from the region between the two DBs. d) Overlay showing the FFT plot from the right grain in the background and the position of the respective plot from between the DBs as white circles.

oxidised to the same or even greater depth than GBs. Both structures are regions of lattice disturbance, with higher defect density and therefore are fast-diffusion paths. However, the DBs are very local disturbances of the lattice, particularly if slip has occurred in a narrow band. Dislocations are likely to travel in other slip planes parallel to the DBs, so they are unlikely to pile-up or lock at the DBs, which frequently happens at GBs during deformation. For the experiment, the DBs are introduced by cold-rolling just before or during the oxidation. They were not present during the fabrication process, so there was no segregation to them and no change in potential at them at the start of the corrosion test.

TEM BF imaging has revealed that the areas between DBs or within twins can sometimes have sub-cells, as previously observed by Lozano-Perez *et al.* [110]. The complex sub-cell structure in these areas lead to locally higher dislocation densities, which may be a reason

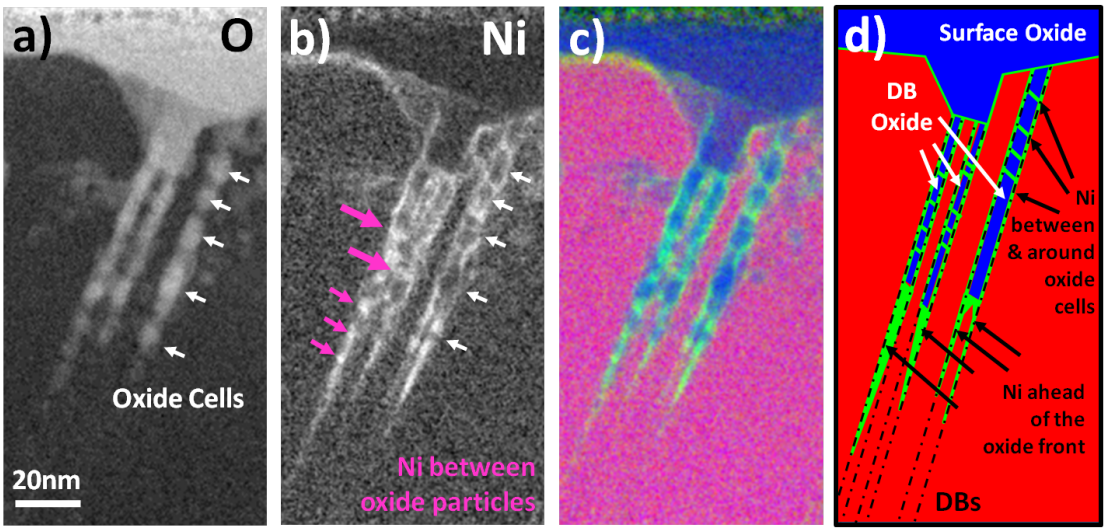

Figure 5.7: Close-up on the DBs on the left side of Figure 5.5 a) EFTEM O map. b) EFTEM Ni map. c)RGB map showing Fe in red, Ni in green and Cr in blue. d) Schematic showing the main features in the maps.

for enhanced oxidation within twins and between deformation bands. In the case where no cell structure was observed (Figure 5.8) the oxides had grown around the deformation bands and the area between was unaffected.

Independently of the existence of a cell structure between DBs, the resulting oxides were more Cr-rich than the surface oxide. In the case of the no stress/cold-work sample, an total concentration of 32.6±1.7 at.% Cr was measured. No spinel oxide with such a high Cr content exists. This suggests that the oxide has either a highly non-stoichiometric spinel structure with many Fe vacancies, or a completely different oxide structure is present. The ternary phase diagram in Figure 4.35 shows that a mixed phase containing Cr_2O_3 and $FeCr_2O_4$ is possible and, at higher O concentrations, Cr_2O_3 and Fe_2O_3 are fully miscible. The Pourbaix diagram in Figure 5.9 shows that small changes in the oxidation potential (along the blue arrow in the diagram) can change the dominant stable oxide structure from $FeCr_2O_4$ to Cr_2O_3. The sesquioxides (Cr_2O_3 and Fe_2O_3) have a hexagonal crystal structure and therefore it should be possible to detect the existence of such an oxide phase with a diffraction experiment. Local area diffraction in the DB oxide regions is suggested for future investigations.

This behaviour is different from oxidation in the GBs. However, the GB oxides were sometimes more Cr-rich than the surface oxides, particularly in the areas that look like oxidised dislocation pile-ups. Very little Cr diffusion seems to occur. Oxide growth is

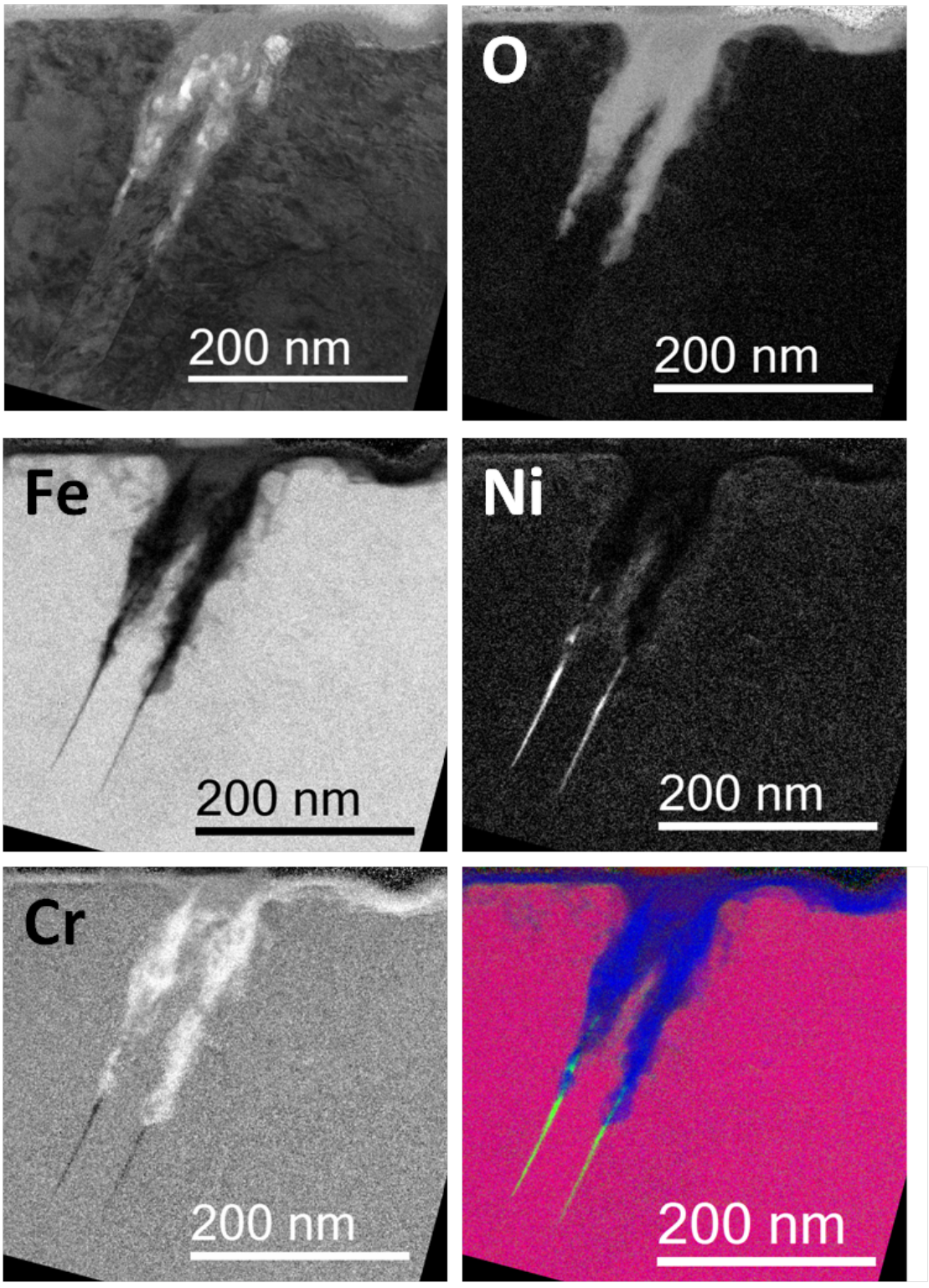

Figure 5.8: a) TEM BF image of TDBs in the no stress/cold-work sample. b-e) EFTEM maps of the sample. f)RGB map showing Fe in red, Ni in green and Cr in blue.

mostly subject of Fe outwards and O inwards diffusion. It seems that Fe can diffuse outwards easily along those high-vacancy paths. In the metal regions between these paths, where the crystal lattice contains fewer defects, interstitial O diffusion can still occur, but

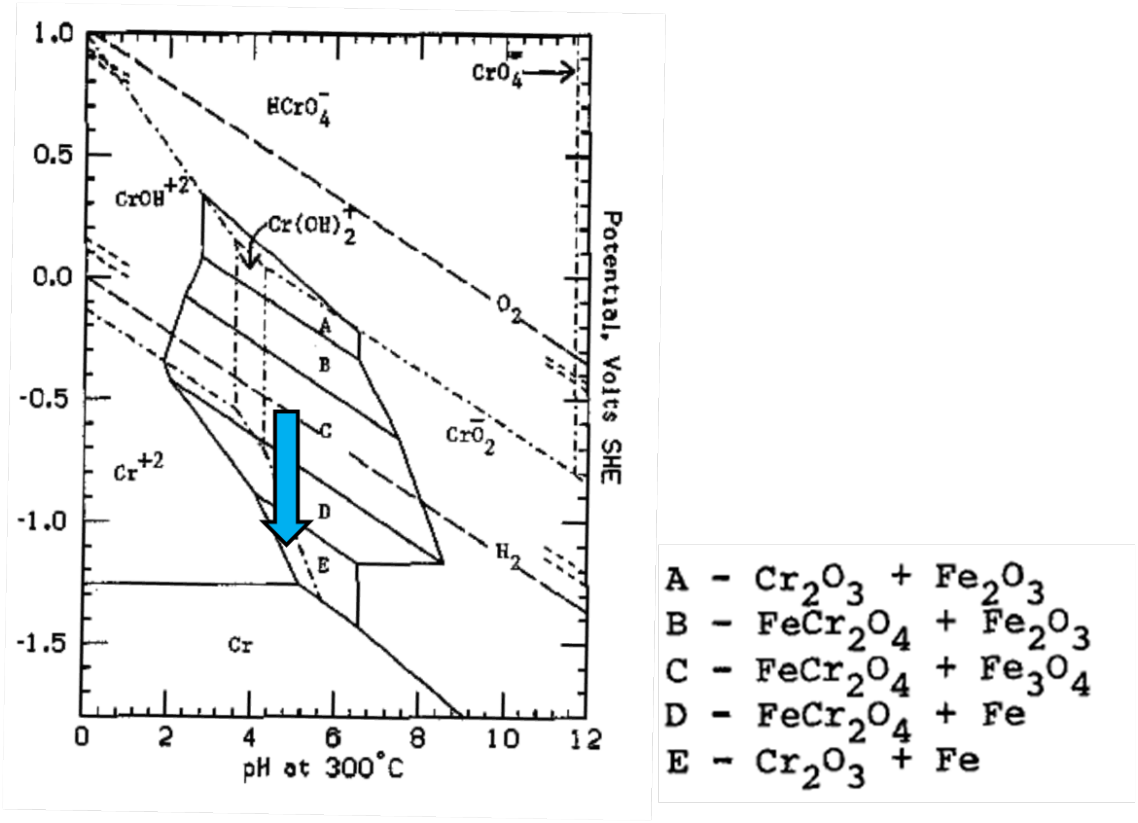

Figure 5.9: Pourbaix diagram for the Cr-H_2O System with Fe at 300°C. Full lines separate regions of stability for Cr in different states. Dissolved Cr species activities were 10^{-6} and metallic Cr activity 0.2 (to represent stainless steel) [230].

Fe outwards diffusion is limited. This may be why more Fe is left behind and oxidises in these regions.

At separate single DBs, where there are no dislocation pile-ups and no enclosed metal regions, Fe outwards diffusion is possible at the same rate as O inwards diffusion. This explains, why the DB oxides are more Fe depleted and why the outer oxides - the magnetite particles - seem to line up just above the DBs, but (at least in SUS304) not so commonly above GBs.

The appearance of Ni enrichment ahead of the oxide front in the DBs is also different from the appearance at GBs. It appears that the effect that hinders Fe diffusion out of oxide-enclosed regions also stops Ni diffusion through the oxide. Ni diffusion does not only seem to be slow, but in fact Ni seems to be rejected from all oxide regions and accumulates in high vacancy regions close to the oxide. It diffuses along the DBs and accumulates at the high-defect side of GBs. This is another sign that the DB itself is a very localised high-vacancy region. Ni diffusion, like Fe diffusion is substitutional. At the GB, where vacancy-rich dislocation pile-ups are present, a Ni phase with a minimal interface to the

steel matrix forms in one grain. In the DB, the Ni takes the vacancy-rich path down the band.

Regions of very closely spaced or very wide DBs as well as TDBs seem to behave slightly differently. These regions provide more diffuse regions of high defect density. The highest density of vacancies around single DBs is localised in the DB plane(s) and thus they allow Ni diffusion and accumulation. This includes the short deformation bands that frame eventually present sub-cells. As discussed in Chapter 4, Ni cannot be oxidised at the present potential. It is driven further into the material as oxidation of the high-defect metal regions progresses.

DBs are fast-diffusion paths for oxygen and metal atoms and they oxidise if one end is exposed to a surface (or crack surface). However, for crack opening and growth, mechanical displacement of the crystal system perpendicular to the crack plane is necessary.

Dislocations in the material glide along slip planes and pile up at GBs, these slip planes will, in most cases, lie parallel to the deformation bands. The dislocation pile-ups lead to enhanced oxidation in the GB region, therefore the oxide formation is much broader than at the DBs. In regions where two systems of deformation bands cross, the greatest oxidation depths are measured (see, for example, Figure 4.15). This makes sense, as many fast diffusion paths and boundaries for dislocation pile-ups come together here. In such regions TGSCC might occur, but these regions do not seem sufficiently common to play a major role in crack advance. If they do have an influence on crack initiation cannot be determined here.

The oxidation enhancing factor induced by stress and cold-work seems to be dislocation pile-ups rather than deformation bands. Although DBs that lie between the surface and a GB can enhance oxygen diffusion in the surface region, this effect is not relevant once crack growth has progressed beyond the first grain. The SAM maps in Figure 5.2 from [143] show Ni enrichment in DBs along the flanks of the open cracks. It appears that DBs along the crack provide “storage space” for the rejected Ni. This may be why no Ni enrichment of the extent observed ahead of the GB oxides in Chapter 4 was observed at crack tips. If it is assumed that such a Ni particle at the oxide front can stop further oxidation (Figure 5.10a), the DBs could be considered as a sort of “Ni bins” as illustrated in Figure 5.10b. If this is the case, the DBs do not enhance the oxidation, but they provide a fast diffusion path for the Ni, so that it will not accumulate at the oxide front and stop

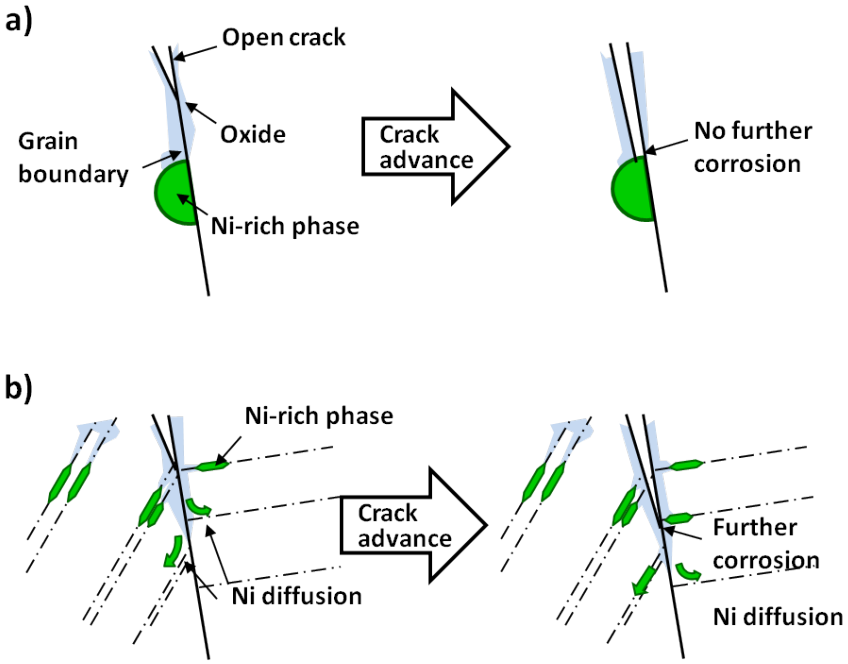

Figure 5.10: Diffusion at a cracking GB with and without DBs. a) Ni-rich phase forms ahead of oxidation front and stops further oxide growth and cracking. b) Ni diffuses into DBs. Corrosion and cracking continues to occur along the GB.

further oxidation. This theory could explain why austenitic stainless steel has good SCC resistance and also why this resistance is weakened by deformation.

Chapter 6

The Role of Hydrogen

The role of hydrogen in GB oxidation and SCC has so far remained a mystery. This has two reasons:

1. Hydrogen atoms are small and have only one electron, therefore they do not interact with other charged particles or x-rays very much. Auger processes are not possible (as they require at least 3 electrons) and neutron scattering does not have sufficient chemical sensitivity or spacial resolution.

2. Hydrogen in solid solution is very mobile and very volatile. In stainless steel at PWR operating temperature it diffuses 8 - 18 mm/year [231], that means it can leave a 100 nm thick TEM foil or APT needle in 3 - 7 min. Of course that also works the other way around; adsorbed hydrogen can diffuse through the samples in the same time. Although diffusion at RT is much slower [232], hydrogen is likely to be lost during ion irradiation in the FIB or when heating up under the electron beam.

This chapter shows hydrogen field evaporated from an APT sample and tries to explain, how this could be relevant to GB oxidation and interganular SCC mechanisms.

6.1 Results

An oxidised GB in the same no stress/cold-work sample as in Chapter 4 was studied with EFTEM mapping and APT. The models suggested by Lynch [74] and further developed by Oriani [233] and finally Magnin *et al.* [82, 83] suggest that hydrogen is injected into vacancies created in the stress fields at crack fronts. The GB observed in this chapter

was surrounded by residual stress fields from the cold-work that were sufficient to cause the GB to open during oxidation. Deformation bands ahead of the oxidation fronts are a further proof of the presence of stress fields. This is the conditions in which hydrogen trapping is predicted to occur.

Figure 6.1 shows the TEM BF image and EFTEM maps. The BF image in Figure 6.1a shows the surface oxide parallel to the top edge of the sample. The original surface was damaged during FIB preparation and a hole was produced in the GB oxide. In the right grain, the surface oxide has also grown into a DB almost parallel to the surface. Inhomogeneous oxide has grown down the GB vertically in the centre of the image. Particularly in the near-surface region, there seem to be voids in the oxide not caused by FIB damage. They appear bright in the BF image and dark in all related composition maps. These voids seem to have been caused by the opening of the GB and local fracture of the respective oxide regions. The oxidised part of the GB ends abruptly at a set of four deformation bands. They start at a curved phase boundary in the left grain and stretch across the entire right grain. The Ni elemental map in Figure 6.1d shows that the phase boundary in the left grain separates a Ni rich area from the steel matrix.

Figure 6.2a shows a higher resolution TEM BF image of the oxidation front and the Ni rich area and Figure 6.2b shows the respective relative composition map. The image is rotated 90° clockwise compared to Figure 6.1, so that the GB oxide is now coming in from the left side. The exposed surface is vertical to the right of the image. The matrix consisting mostly of Fe (red) and Cr (blue) appears pink, the GB oxide, which is rich in Cr, appears blue and the green regions corresponds to a Ni enrichment (58±3% were measured). Figure 6.2c shows an overlay of both maps. This overlay shows that the deformation bands do not only cross the bottom grain, but also the Ni-rich phase. The Ni rich phase does not extend across the GB, although it changes the side it accumulated on from the top grain to the bottom one. In both cases, the deformation bands cross the bottom grain and the Ni-rich area, but do not extend beyond.

The same Ni-rich feature was studied with APT. Sample preparation was carried out after the procedure described in Section 3.7. This means the APT sample contains a portion of the same GB shown in the EFTEM map, but displaced by a few μm. The white box in Figure 6.1f indicates the respective region in the EFTEM relative composition map. The main features that are contained in the APT data set are shown in the schematic in

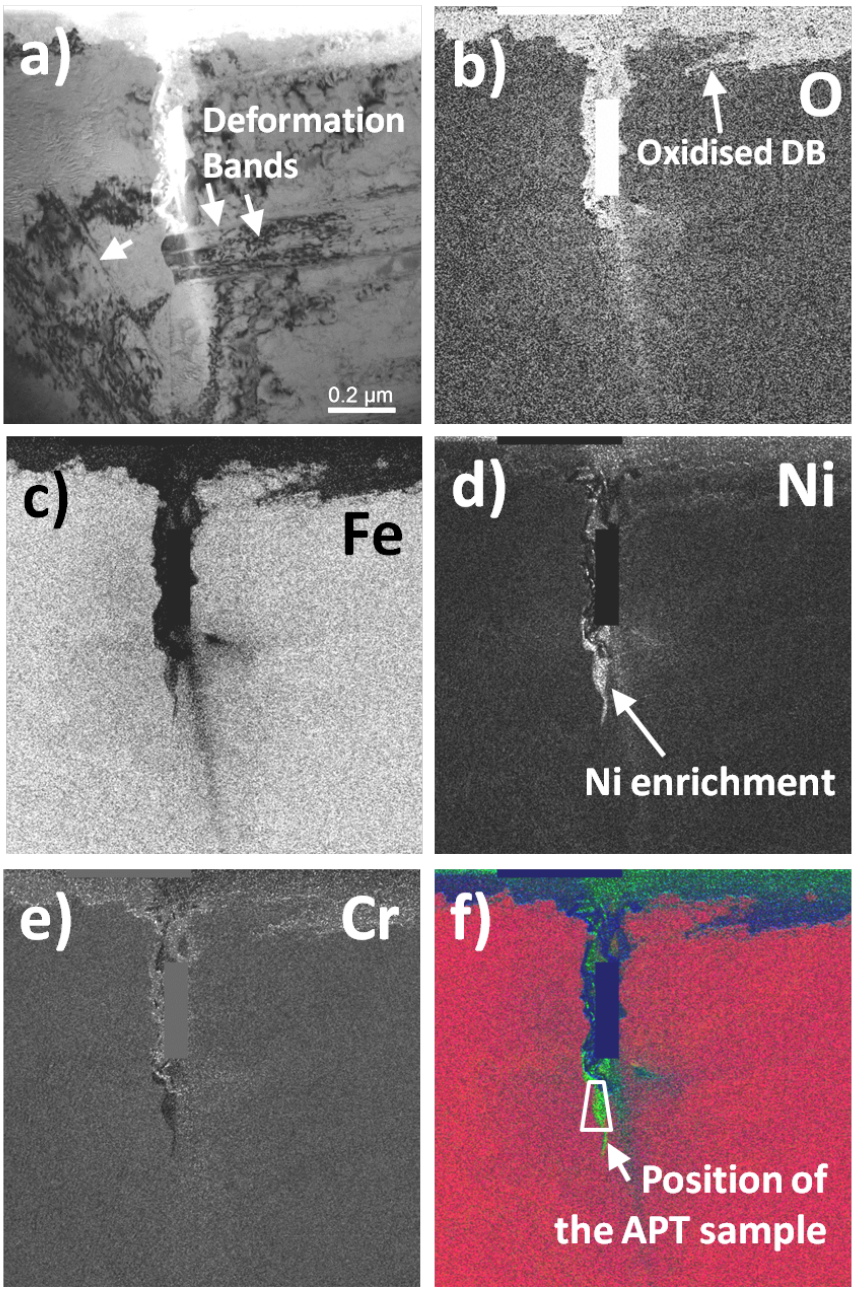

Figure 6.1: a) TEM BF image showing a cross-sectional no stress/cold-work sample containing an oxidised GB and some twin deformation bands. The original sample surface lies horizontally from left to right towards the top of the map. b)-e) EFTEM elemental maps. The boxed region displayed in the oxygen map represents the approximate region analyzed by APT, shown in Figure 4.25a. The original surface of the sample coincides with the flat termination of the oxide right at the top of the images (horizontal). f) Relative composition RGB map showing Fe in red, Ni in green and Cr in blue.

Figure 6.3a. Figure 6.3b and c show all ions of the data set from two different orientations. The view on the (green) Ni-rich region in Figure 6.3b corresponds to the view in the EFTEM map.

Figure 6.4a shows an extract from the mass spectrum of the APT dataset, showing how

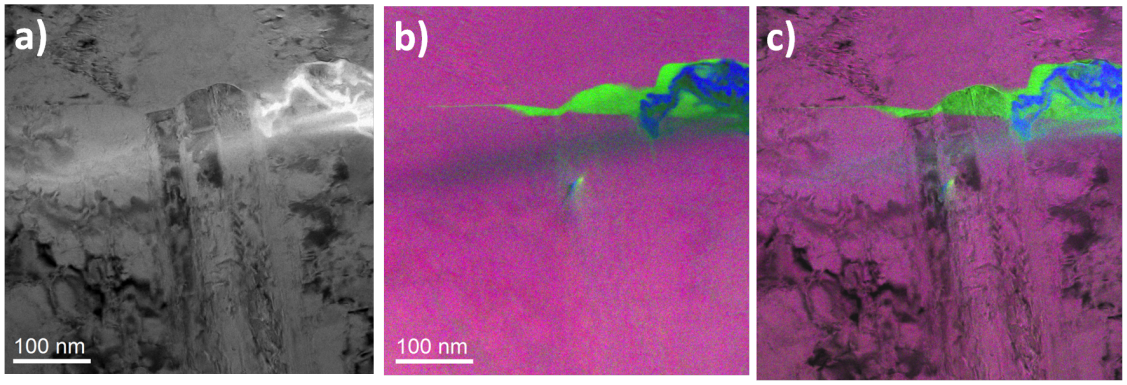

Figure 6.2: a) TEM bright field image showing a close up on the Ni-rich region. b) Relative composition RGB map showing Fe in red, Ni in green and Cr in blue. c) Overlay of TEM BF map and the elemental RGB map.

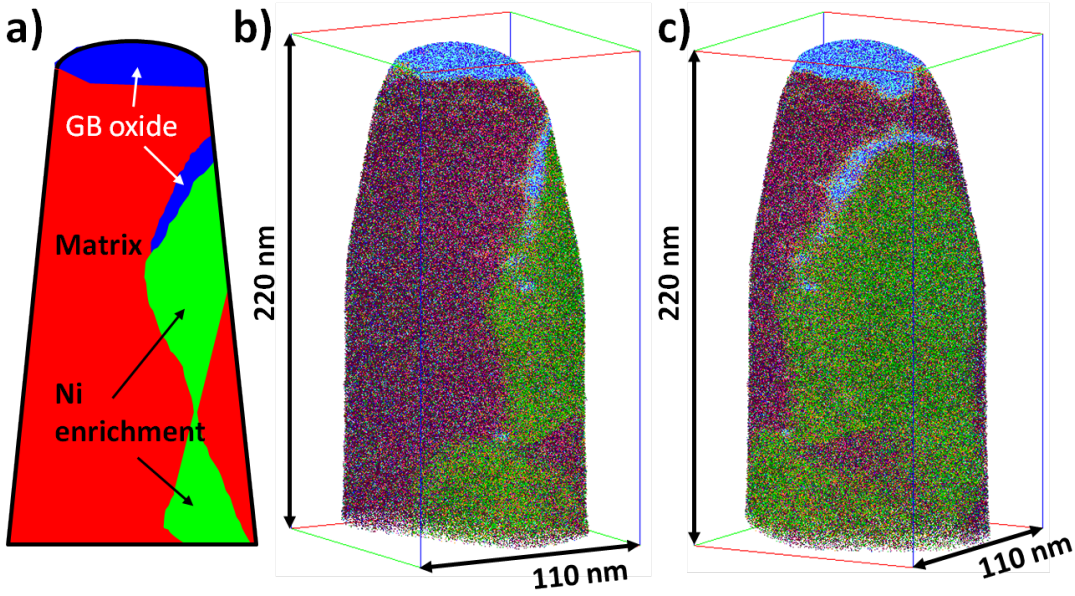

Figure 6.3: APT data set containing the Ni rich portion ahead of the GB as indicated in Figure 6.1f. a) Schematic showing the main features in the data set. b) Ion map showing all ions - side view. c) Ion map showing all ions - front view.

the peaks were ranged. The most common Ni isotope has a mass of 58 Da, but further isotopes of 60, 61, 62 and 64 Da exist. There are however no isotopes at 59, 63 or 65 Da. While the peaks at 63 and 65 m/z were ranged as Cu, the most probable cause of the 59 m/z peak seems to be NiH^+. The maps in Figure 6.4b show the distribution of NiH and Ni in the sample. The NiH is aligned along planes inside of the Ni-rich phase of the sample. Other possible ions of mass 59 include Co, AlO_2 and BO_3. However, no significant enrichment of AlO, B or BO_2 was found in the respective areas and the Co content of the alloy is low. The H map does not show any change in density across the

complete data set (peaks at 1, 2 and 3 m/z were ranged).

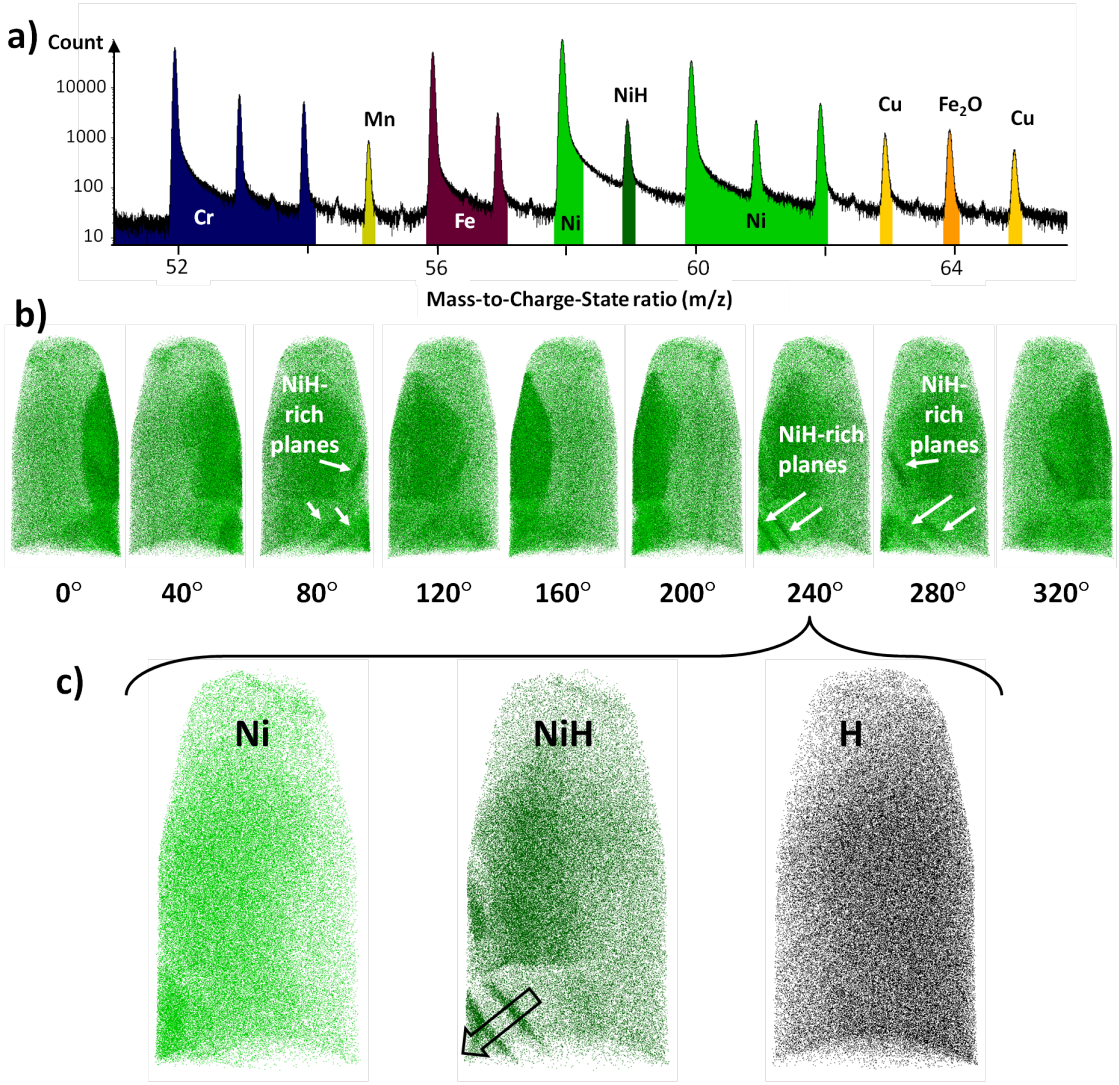

Figure 6.4: a) Extract from mass spectrum of the data set in Figure 6.3. b) Ion maps showing the distribution of Ni and NiH ions, Ni in light green and NiH in dark green. c) Ion maps showing the distribution of Ni, NiH and H ions within the dataset. The arrow in the NiH map shows the position where the 1D concentration profile in Figure 6.5 was taken from.

If the peak at 59 m/z is caused by NiH^+ ions, there should be further peaks at 61, 62, 63 and 65 Da. The peaks at 61 and 62 m/z are dominated by the minor Ni isotopes and 63 and 65 correspond to Cu, which is also present in the alloy. A concentration profile across two of the narrow bands (as indicated by the arrow in the NiH map of Figure 6.4c was generated. The profile in Figure 6.5 shows the concentration of NiH ions (peaks at 29.5 m/z and 59 m/z), H ions (peaks at 1 m/z, 2 m/z and 3 m/z) and Cu ions (peaks at 63 m/z and 65 m/z). The dashed lines show the 1D concentration profile generated with a 0.5 nm bin width, the solid lines show the trend in a coarser profile generated with

1.5 nm bin width. The most obvious change can be seen in the NiH concentration, as to be expected from the ion maps. It reaches a concentration of more than 1 % in two narrow regions of about 5 nm width. Although the effect is not strong enough to show in the ion map, there are small dips in the concentration of evaporated H atoms in the same regions. More notably the concentration of Cu ions evaporated from the areas seems also slightly increased. This suggests that the peaks at 63 m/z and 65 m/z which were assumed to be caused by Cu ions, are a convolution of the Cu signal with the NiH signal from the less common Ni isotopes of 62 Da and 64 Da. There is no alternative Co isotope, that could cause these signals. These results indicate that the 59m/z peak could be NiH^+.

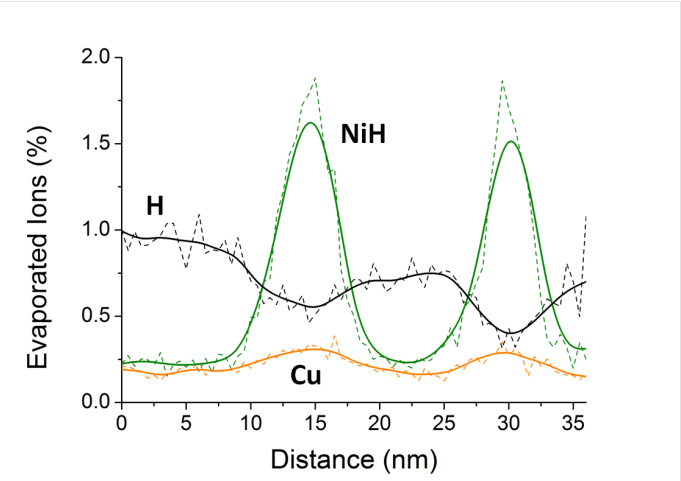

Figure 6.5: 1D concentration profile along the arrow in the NiH map in Figure 6.4. The dashed lines show the 1D concentration profile generated with a 0.5 nm bin width, the solid lines show the trend in a coarser profile generated with 1.5 nm bin width.

The isotope ratios of the Ni peaks with respect to the main peak at 58 m/z were analysed in the mass spectrum of the area in which the ion with 59 m/z is concentrated. If $^{58}NiH^+$ was evaporated, then $^{60}NiH^+$, $^{61}NiH^+$, $^{62}NiH^+$ and $^{64}NiH^+$ should be evaporated in the respective quantities. While the peaks at 58 m/z, 60 m/z and 64 m/z only contain the metallic Ni signal, the peaks at 61 m/z and 62 m/z should be a convolution of the signal from the respective Ni isotopes and the Ni-H ions. Table 6.1 shows, that the ratio between the peaks for ^{60}Ni and ^{58}Ni is consistent with the theoretical value as expected. The ratio of the peaks for ^{61}Ni and ^{58}Ni is more than twice as high as the theoretical value, suggesting that $^{60}NiH^+$ contributes to the peak at 61 m/z. This effect is less pronounced for the 62 m/z peak, as only 1.14% of all Ni atoms are ^{61}Ni. If no other elements were present the value for the ratio of the peaks for ^{64}Ni and ^{58}Ni should correspond to the theoretical

value. The deviation from the theoretical value is probably due to the fact that the peak is very small and therefore much more affected by noise in the mass spectrum.

Isotope ratios

[-]	**60/58**	**61/58**	**62/58**	**64/58**
Theoretical	0.385	0.017	0.053	0.014
Measured	0.388	0.038	0.057	0.016
Theoretical/Measured	1.007	2.256	1.063	1.161

Table 6.1: Isotope ratios of the metallic Ni peaks in the mass spectrum of an area in which the ion with 59 m/z is concentrated and comparison with the theoretical isotope ratios.

All the evidence presented support, with great level of confidence, that the peak evaporated as 59 m/z is originated by the joint evaporation of Ni and H. This demonstrates that trapped H can be mapped in 3D by APT in certain circumstances.

6.2 Discussion

The role of hydrogen in SCC has been an on-going subject of debate in the SCC community. Lynch suggested that adsorbed hydrogen could weaken interatomic bonds near (crack) surfaces [74], the Troiano-Oriani decohesion hypothesis states that hydrogen in the strained lattice lowers the binding energy of metal atoms [78] and the model by Magnin *et al.* [82,83] suggests the possibility of vacancy generation and hydrogen absorption due to anodic dissolution along (111) slip planes near crack tips.

The EFTEM maps and the TEM BF image from the same region in Figure 6.2 show that the Ni enriched regions ahead of the oxides in this sample are crossed by deformation bands. The DBs cross the Ni-rich phase originate in the bottom grain, which is the austenite grain in which the Ni-rich phase has **not** grown. This suggests, that the crystallographic orientation of the Ni-rich phase is aligned with that grain.

The corresponding APT data shows NiH segregated to parallel planar features within the Ni-rich phase. Von Pezold *et al.* have shown that theoretically small amount of dissolved hydrogen ($\sim$ 160 ppm) are sufficient to lead to hydride formation if strain fields are present [234]. However, the local H concentration is too low for a hydride phase. Furthermore the enriched areas are too localised. As H is the most common residual gas in ultra-high vacuum systems, the continuous adsorption onto and field evaporation from

the sample is easy to explain, and even the creation of MH ions is possible. However, the spacial segregation to parallel planes cannot be explained by such a mechanism.

The Ni enrichment can only be explained by substitutional diffusion, which requires the presence of vacancies. The more extended NiH regions in the APT data (Figure 6.4) are at the top of the Ni rich region near the interface with the oxide, where substitutional diffusion should be happening and where H could be contained in vacancies [235, 236].

Magnin *et al.* suggest the stress induced creation of vacancies and the absorption of hydrogen in (111) slip planes. If hydrogen was trapped in vacancies along the deformation bands visible in the EFTEM maps, it would be bound to the crystal lattice and would therefore not diffuse at the high rates quoted in the introduction of this chapter. As the data was acquired from the no stress/cold-work sample, strain fields are surely present within the sample. This would explain the observations and support Magnins model. Although it is likely that the observed NiH enrichment is due to H trapped in vacancies along deformation bands, it is impossible to say whether this has happened during the oxidation or during storage, sample preparation or the experiment after the oxidation. This could only be clarified if the experiment was repeated with deuterated water. Furthermore, hydrogen enrichment has only been observed in the Ni-rich region ahead of the GB oxide. Due to the complicated mass spectrum and the number of alloying elements it is unclear, if other metal-H ions are evaporated from other regions. At this stage, it can be conclusively said, that H can be trapped in deformation bands within high-Ni regions and that this can be observed with APT. From this it follows that the mechanism suggested by Magnin *et al* [82, 83] and illustrated in Figure 2.4 is at least relevant for high-Ni steels and Ni alloys.

Chapter 7

Ideas towards a stress corrosion cracking mechanism

The argument made in Chapters 4 and 5 suggests that Ni might play an important role in SCC of 304-type stainless steel in simulated PWR primary water. The potential in the alloy is such that Ni oxidises very little (Figure 4.41). Instead, the Ni diffuses away from the oxidising metal. It diffuses by substitution and favours high-vacancy regions such as GBs, DBs, twin boundaries and dislocations. If the Ni concentration exceeds a critical value, the Ni "precipitates" to form a region of a separate phase with a Ni concentration of 67±6 at.%. Once such a phase is formed, it will strive to reduce its interface with the steel to reduce the energy. However, formation of a particle as spherical as possible is very difficult given low diffusion rates of Ni in FeNi and the limited space. Extension into GBs and DBs might require much less energy. Only in regions with an extremely high vacancy concentration can the Ni phase expand and form a particle.

Looking back at the TEM and EFTEM data in Chapter 6, it appears that the deformation bands continue across the GB/phase boundary into the Ni rich particle that has formed. Dislocations normally cannot cross GBs, however, the Ni particle may have changed the GB nature locally. It appears, that the crystal orientation of the Ni-rich particle is aligned with the bottom grain in Figure 6.2 rather than the top one, which it expands into. The interface between the Ni-rich phase and the bottom grain is less coherent (due to the DBs) and the kinetics of atomic attachment easier and lead to an alignment of the new phase with the bottom grain. The vacancy rich dislocations seem to have either travelled across the phase boundary, or have triggered the creation of dislocations on the other side of the

boundary, so that fast-diffusion channels for the Ni to the outer regions of the particle were created. With regard to the APT data in Figure 6.4 it is possible that the hydrogen, which is thought to be trapped in vacancies, plays a different role than the one suggested by Magnin *et al.* [82, 83]. In this case it may stabilise the vacancies [235, 236] in certain planes and aid substitutional diffusion of Ni. Of course, that does not mean that the decohesion hypothesis is incorrect. It appears that diffusion further into the GB is the favourable path for Ni diffusion after the formation of the half sphere in the top grain. The existence of big Ni particles in some areas ahead of the GB oxide, but very little Ni enrichment in others (see Figure 4.23), supports this theory.

Thomas and Bruemmer and Arioka *et al.* have found Ni enrichment at some crack tips [139, 237]. More Ni enrichment was detected in specimens tested in low-potential hydrogenated water environments. "The cause of the dependence on potential for the nickel enrichment could be due to the difference in stability of nickel oxides at the crack tip, such as nickel oxide (NiO) and iron nickel oxide (Fe2NiO4)" [139]. It appears from Figure 4.41 that the Ni particles are noble compared to the steel matrix and while they can grow, they are very immobile. They do not oxidise and seem to hinder further oxygen diffusion. Oxide can still grow around the particles. However, the vacancies in this area were probably "used up" to accommodate the Ni particle and most diffusion around it will have to be interstitial. In materials without a high density of DBs the formation of such Ni phase particles puts a limit on GB oxidation. If the oxide in a GB became brittle and started to open, the freshly exposed material would be a Ni alloy and no further corrosion would occur.

This situation changes if deformation bands are present and frequently intersect a GB. While Ni diffusion in FeNi is slow, these additional high vacancy regions allow the rejected Ni to be removed from the oxide front. If the Ni concentration does not become high enough, no Ni-rich phase forms in the GB. If the oxide films are ruptured, the underlying steel will be susceptible to corrosion.

The Ni diffusion might be the controlling factor in whether SCC can occur in 304-type stainless steels or not, but it might not have an influence on the actual SCC mechanism. Chapters 4 to 6 report a number of observations, that together with previous reports in the literature [12,110,111,122,123,128,143,163,172,181,238–240], allow conclusions about the properties required of a corrosion mechanism. A mechanism, that describes SCC in

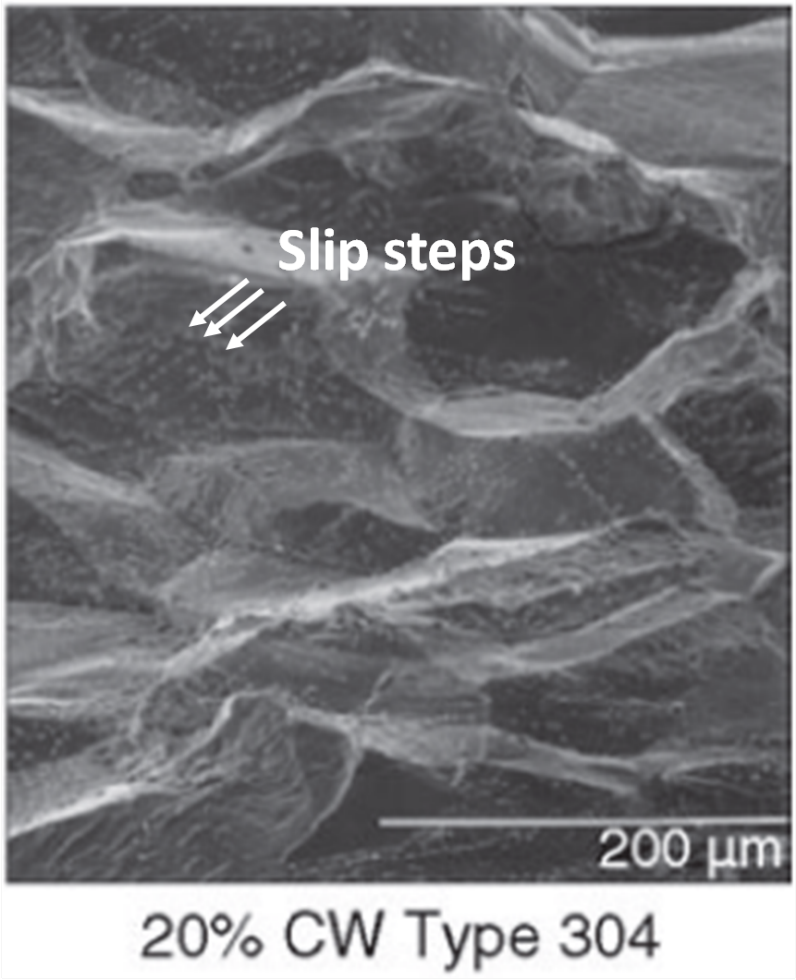

Figure 7.1: Fracture surface of a cold-worked 304 stainless steel tested in hydrogenated water at 320°C studied by Arioka *et al.* [238].

simulated PWR primary water must be in agreement with the following observations:

1. SCC in aqueous solution can only occur in cold deformed SUS304.
2. SCC is mostly intergranular [181, 238].
3. The average crack growth rate for SUS304 in hydrogenated water is in the order of 10^{-7}mm/s at 320°C [238].
4. The exact CGR and the crack path depends on the amount and direction of cold-working [122, 125].
5. Fracture surfaces have a step-like structure, see Figure 7.1 [238].
6. Oxides penetrate GBs and DBs [143].
7. Ni diffuses ahead of oxides in GBs and DBs [143] (this study).

8. B segregates to the GBs and seems to reach especially high concentrations at the crack tip. No B segregation to DBs was observed [143].

9. The oxide at surfaces exposed to the water is a chromite-type spinel. Magnetite-type oxide particles are redeposited on these oxides, they can also be found in the open crack [110] (this study).

10. The oxides in DBs and some GB oxides are more Cr rich than the surface oxides (this study).

11. Li is incorporated in all oxide regions (this study).

12. GB oxides are not homogeneous at the oxidation front, but oxide particles can grow in the GBs disconnected from the bulk oxide (this study).

13. Void formation is possible ahead of oxides and is slightly more frequent in stressed samples (but was not commonly observed) (this study).

14. No GB type could be identified that is resistant to cracking (CSL system) [172].

15. H concentrates in high stress regions [123].

Further considerations should also be included:

- Li may also diffuse along dislocations ahead of the oxidation. (this study)
- H can stabilise vacancies [235, 236].
- H can diffuse anywhere that Li can diffuse to.
- H enrichment is observed in planar features in Ni-rich regions just ahead of the oxidation front.
- Although voids are not commonly observed it is possible that crack embryos as suggested by Magnin [83] would form once actual cracking has started.
- The maximum oxide depth is measured to be 1.4 μm in this study. This corresponds to an oxide growth rate of about $\sim$1 nm/h (compared to a crack growth rate of $\sim$ 360 nm/h). It is however possible, that the oxide growth rate is not linear with time.

- The step patterns on the fracture surfaces suggest that slip plays a role in the formation of the crack. It is possible that slip leads to crack advance or it could be responsible for crack opening. Alternate slip could lead to both at the same time.

- It is fairly certain that hydrogen is present around the crack. It is also likely that it is trapped in vacancies and stabilises them. This leads to more stable fast diffusion paths for larger atoms, that can only diffuse by substitution. It is not certain if the immobility of these vacancies locally increases the plasticity and leads to a decreased fracture toughness.

- Austenitic stainless steels and Ni-alloys have the same crystal structure and exhibit similar mechanical properties [241, 242]. However, the oxidation behaviour is different. Alloy 600 (72 wt.% Ni) for example exhibits only very shallow surface oxides, about one order of magnitude thinner than 304 stainless steel. However, all grain GBs in Alloy 600 will oxidise to a much greater depth [243].

On the basis of the above mentioned considerations a mechanism based on the FRM mechanism as reviewed above (see Section 2.2.1) is suggested for the SUS304/simulated PWR water system. This mechanism is illustrated in Figure 7.2.
It is not proposed that stress and stress-induced higher H concentrations at the crack front locally enhance the plasticity of the material (although it is possible that they do), but that they provide local fast diffusion channels that enhance oxygen and metal diffusion and locally increase the corrosion rate. This way anodic dissolution and "internal oxidation" in the slip planes aid crack advance simultaneously and no exposed metal is necessary for further corrosion. This is supported by the fact that Hou *et al.* have found that hydrogen charging of Alloy 600 enhances cation transport in the oxide film and leads to thicker surface oxides [244]. Jones criticised that anodic dissolution alone cannot account for the high crack growth rates in stainless steels [52]. But with oxidation not relying on exposed metal surfaces this limitation of the FRM can be overcome.

This mechanism explains the intergranular crack surfaces with the step like appearance. It explains the high crack growth rates and includes H stabilised vacancies, which were predicted to exist and which have probably been observed with APT in this research. It also explains why only deformed steels are susceptible to SCC. Cracking following this

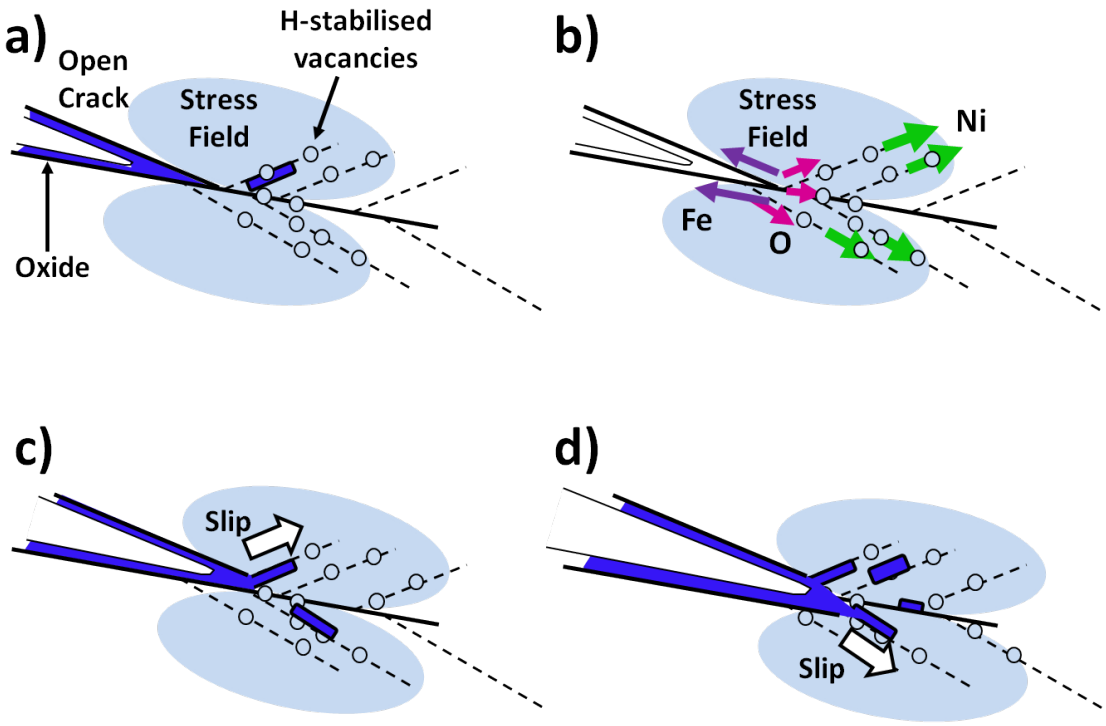

Figure 7.2: Schematic illustrating the suggested mechanism. a) H stabilises vacancies in the stress field around the crack. b) Ni diffuses into the DBs using the stable vacancies. O diffusion into the stress field and Fe outwards diffusion are enhanced. Oxide particles grow ahead of the oxidation front. c) Slip causes crack opening and local stress relief. The advances along the internal oxides and non-passivated metal is exposed. The stress field moves forward and vacancies are stabilised in a new region to form new fast-diffusion paths. d) Alternate slip and cracking of internal oxides lead to further crack advance. The stress field moves further and the process is repeated.

mechanism would lead to the partially oxidised DBs at crack surfaces that Lozano-Perez observed [110]. Although at first glance this appears to be very similar to the internal oxidation mechanism Scott suggested for Ni alloys [101], something different is happening here. H-enhanced fast diffusion in localised regions - GBs -, nucleation sites and local strain fields lead to formation of unconnected oxides. Fe, the main element in the steel is, in this case and contrary to the case of Ni Alloys Scott was describing, part of the oxide particles formed.

Li seems to diffuse along dislocations ahead of the oxides. However, the concentration of Li does not seem to reach concentrations, where it would influence the local potential.

There are four points, from the list above, which are not covered by the suggested mechanism:

1. **The oxides in DBs and some GB oxides are more Cr rich than the surface oxides.** The oxides in the dislocations and DBs may be more Cr-rich, because Fe

outward diffusion is faster in these areas. It appears that the more Fe-rich oxides at the surface form where there are no defects and Fe outward diffusion is slow. The same is probably happening at GBs. Cr-rich oxides grow in the fast diffusion paths, that is usually the GB and dislocation pile-ups. When the undisturbed metal regions between those fast diffusion paths oxidise, (substitutional) Fe outwards diffusion is slower than (interstitial) O inwards diffusion and more Fe is incorporated in the oxide. This is not really relevant at crack tips as the time before rupture is only sufficient to oxidise regions on the fast diffusion paths. Other oxides may form at the crack flanks during crack fatigue, i.e. when the crack tip has moved further into the steel and the crack flanks are exposed to the environment, but these are not relevant for crack advance.

2. **B segregates to the GBs and seems to reach especially high concentrations at the crack tip. No B segregation to DBs was observed.** This point is most likely to be relevant to SCC crack advance. B segregation strengthens GBs in austenitic stainless steels [245, 246], however, it is believed that higher than usual B concentrations can have the opposite effect and in fact embrittle GBs [247]. Generally B addition increases the rupture ductility of iron base super alloys [248]. The B concentration at the crack tip could not be determined accurately, so further investigations are necessary. At this stage, it is not possible to determine, if the effect increases or slows down the crack growth rate. It is not believed that it is essential to the SCC mechanism, but further investigations into crack tip chemistry are desirable for a conclusive argument.

3. **Void formation is possible ahead of oxides (but is not commonly observed).** Formation of bubble-like voids ahead of oxide regions has been observed in a few cases ahead of heavily oxidised DBs. It has not been seen at GBs or ahead of crack oxides in this material. Although in cases of extremely high vacancy density, e.g. where two systems of deformation bands cross, those vacancies may join into a void, this does not seem to be a common enough mechanism to play a role for the SCC mechanism. It is possible however, that regions like the one shown in Figure 4.15 might cause occasional transgranular cracking. At this stage, this remains speculation.

4. **Similarities and differences with SCC in Ni alloys.** The GB oxides in stainless steels are spinels, while the GB oxides in Alloy 600 are a mixture of spinels and Cr_2O_3. While stress and cold-work seem to play a similar role in both systems and the oxide species that form on the surface and grain boundaries are very similar, the extent of intergranular oxidation is remarkably different. This, however, does not seem to have an effect on the appearances of cracks and or the observed crack growth rates.

To further support the suggested mechanism and clarify the role of B segregation to the crack tip it would be desirable to obtain high-resolution and high chemical sensitivity data of an active crack tip. APT is the only technique, that could provide this information, therefore an APT study of crack tips is recommended. This way, the local B concentration could be compared with the concentration along the GBs and its importance could be evaluated.

Further studies on alloys with varying B and Ni concentration are suggested for a better understanding of the processes involved. In those cases EFTEM and NanoSIMS experiments could give the desired information.

Chapter 8

Crack Tip Analysis

The crack tip investigation suggested in Chapter 7 has been attempted for this thesis. Cracks were grown in samples with 5, 10 and 20 % cold-work. The testing method is described in detail in Section 3.1. The crack path was examined in the optical microscope and EBSD strain mapping was performed in the regions of the active crack tips. NanoSIMS was performed in the same regions for chemical analysis. FIB lift-out of the crack tips for TEM and APT sample preparation was attempted, but could not be achieved so far.

8.1 Preliminary Results

The optical micrographs in Figure 8.1 give an idea of the SCC susceptibility at the different CW levels. In the 20 % cold-work sample an extended crack has formed in only 666 h, in the 10 % the crack path remained much shorter even after 982.4 h and in the 5 % cold-work sample a very small crack had formed after 4356 h. The cracks are 3-dimensional and only one plane of the actual crack volume is shown. The stress was applied horizontally, parallel to the image plane. It can be seen, that there is not always only one preferred crack path. At some triple points the cracks continued to grow in both directions.

8.1.1 Electron Backscatter Diffraction and strain analysis

EBSD mapping was performed in the regions marked with the red boxes in Figure 8.1. The results are displayed in Figure 8.2. From left to right image quality (IQ), normal direction (ND) IPF and transverse direction (TD) IPF maps are shown. The dashed lines in the ND IPF maps show the crack paths. In the top right corner in the TD IPF map of

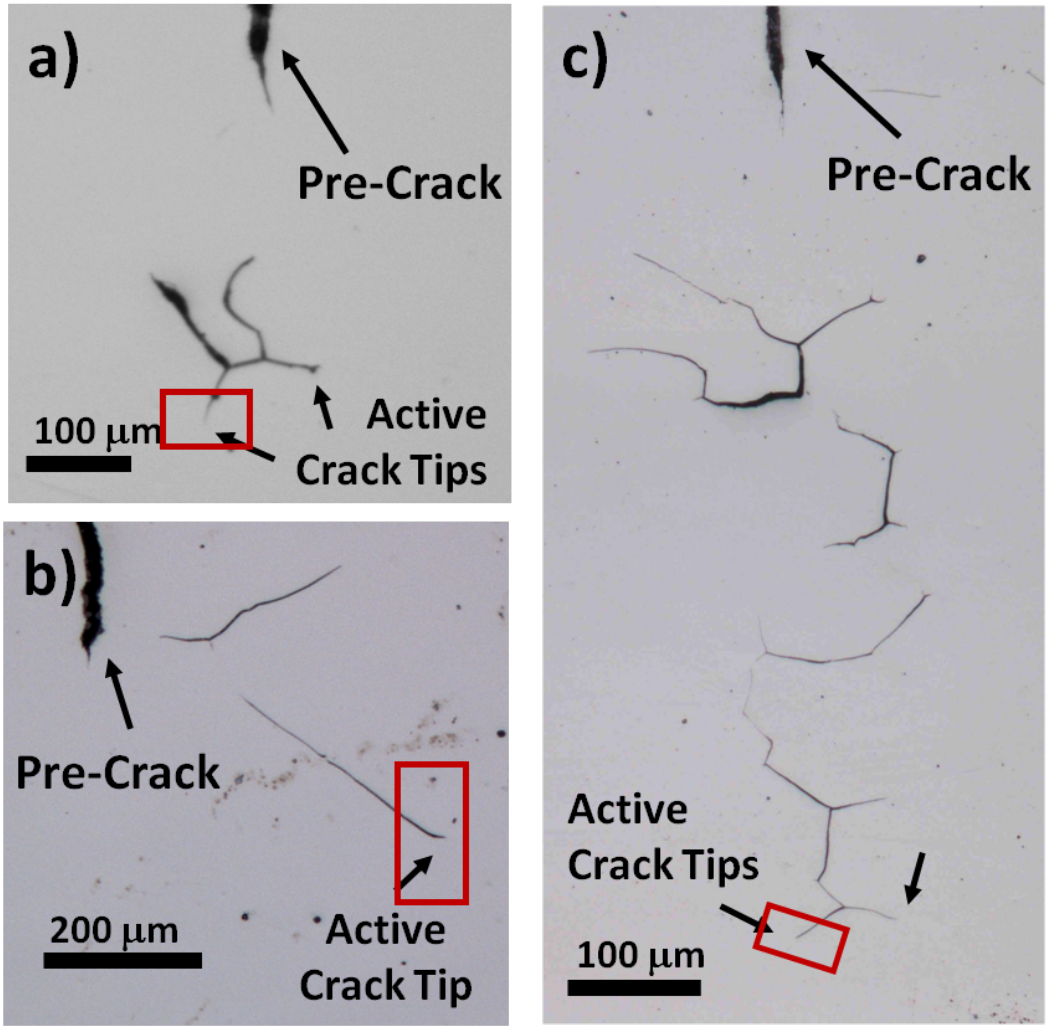

Figure 8.1: Optical Microscopy of cross sections through stress corrosion cracks in samples with different levels of cold-work. In all images pre-cracks are visible at the top edge of the sample. The boxed regions correspond to the areas EBSD maps in Figure 8.2 have been acquired from. a) Crack in the 5% cold-work sample (4356 h). b) Crack in the 10% cold-work sample (982.4 h). c) Crack in the 20% cold-work sample (666 h).

the 5% cold-work sample is the colour key for all IPF maps. While slight colour gradients across the grains of the 5 and 10% cold-work samples are the only sign of deformation in these samples, there are densely packed deformation twins all over the grains of the 20 % cold-work sample.

Pattern saving and cross correlation of the saved EBSD patterns was performed to analyse lattice misorientations and the corresponding strains and rotations in more detail. Details concerning the method can be found in [249]. Maps quantifying relative strains and rotations were generated. Maps showing the Mean Angular Errors (MAE) as a measure of data quality and the reference points chosen for strain evaluation for all samples can be found in appendix A.

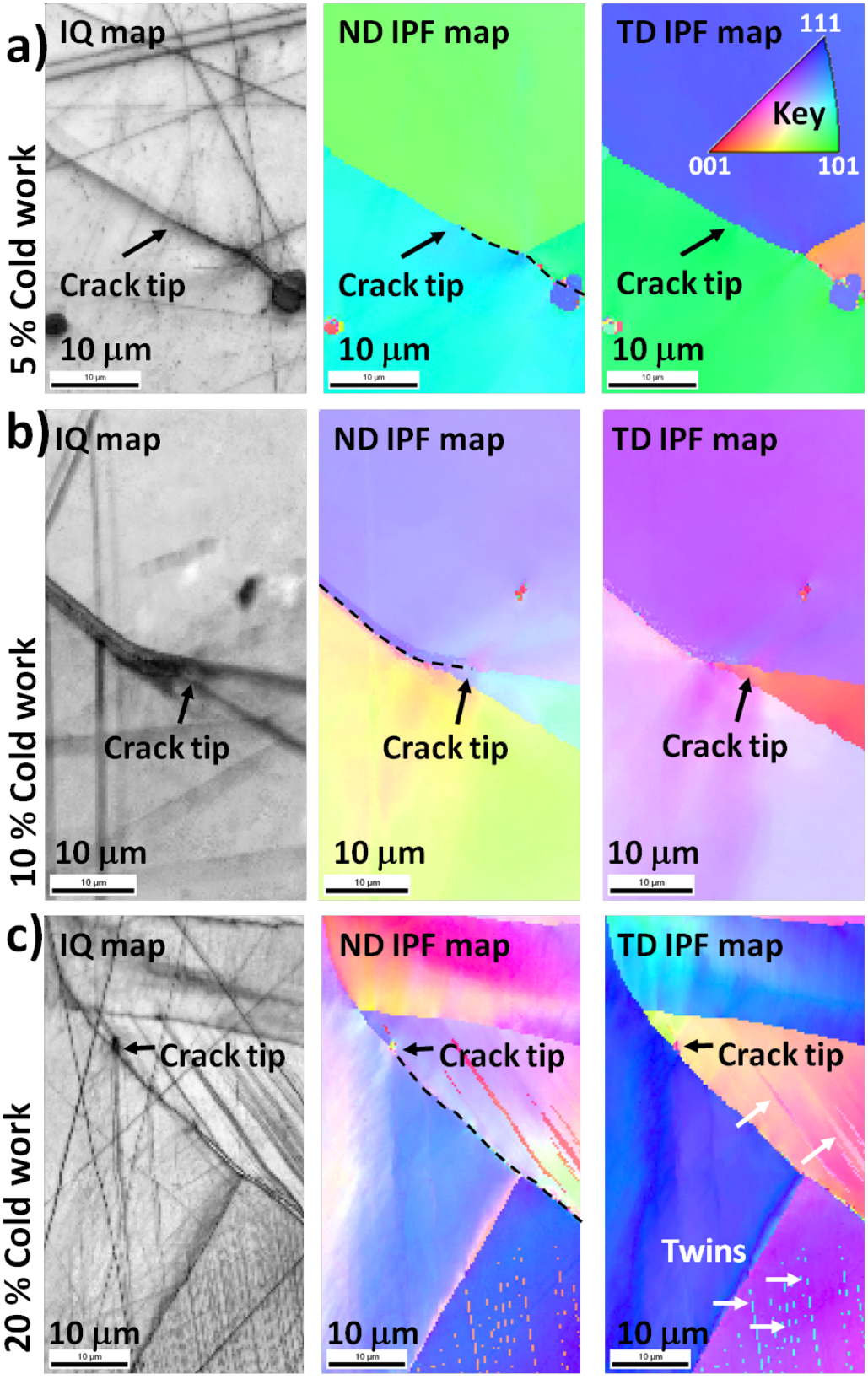

Figure 8.2: EBSD maps of regions containing the active crack tips. a) Crack tip in the 5% cold-work sample. b) Crack tip in the 10% cold-work sample. c) Crack tip in the 20% cold-work sample.

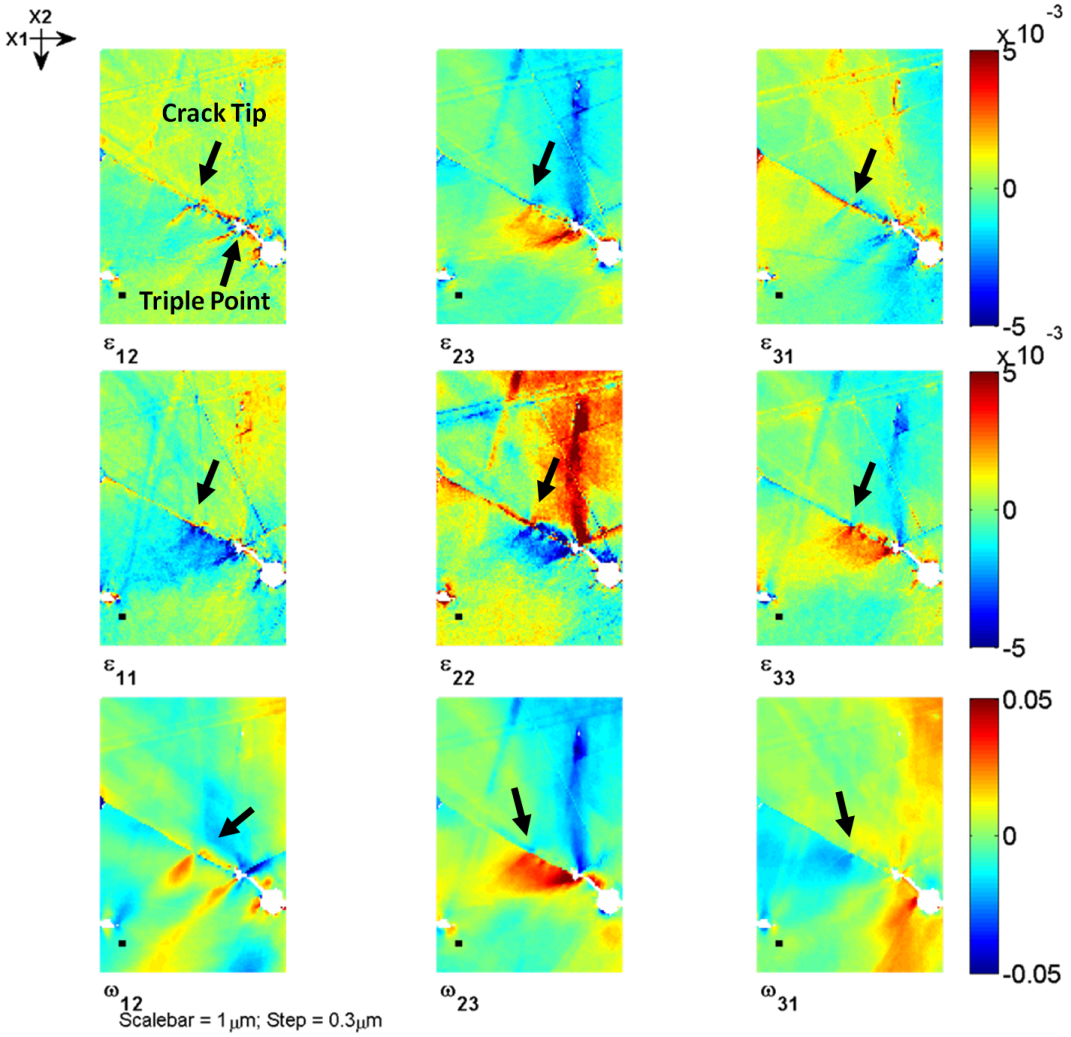

Figure 8.3: Relative strains and rotations in the 5 % cold-work sample (cp. Figure 8.2a). The $\varepsilon_i j$ are the normal elastic strains if $i = j$ and elastic shear strains if $i \neq j$. The ω_{ij} are the rotations.

Figure 8.3 shows the results of the strain analysis for the 5% cold-work sample. The first row illustrates the elastic shear strains, the second row illustrates eleastic normal strains and the third row shows the rotations. It can be seen that strain fields start at the triple point and the crack tip and expand more than 10 μm into the different grains. Particularly in the bottom grain the strain fields starting at the triple point and crack tip have formed a joined strain field. The strain (almost) normal to the GB containing the advancing cracking (ϵ_{22}) seems to have the most extreme values on both sides of the GB, indicating that slip may occur to reduce the local strains and cause crack opening.

Figure 8.4 shows the respective results for the 10 % cold-work sample. The crack is coming into view from the left side. Just as above the crack tip was located close to a triple point and strain fields are expanding into the sample from both features. However, in this case

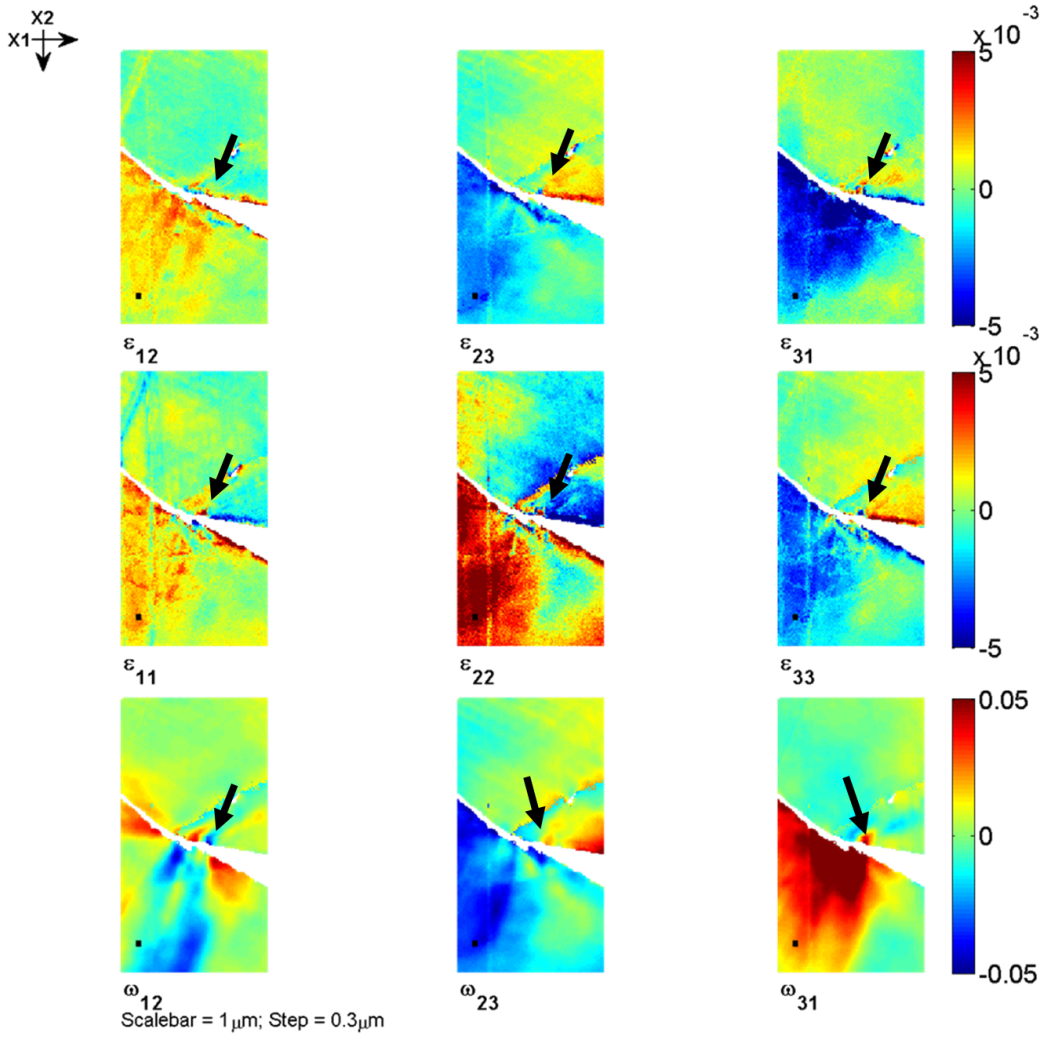

Figure 8.4: Relative strains and rotations in the 10 % cold-work sample (cp. Figure 8.2b). The $\varepsilon_i j$ are the normal elastic strains if $i = j$ and elastic shear strains if $i \neq j$. The ω_{ij} are the rotations.

the top grain seems to be almost free from strain, only the ϵ_{22}, which again shows the elastic normal strain almost perpendicular to the crack path. A large strain field, that extends beyond the edges of the map, can be found in the bottom grain. There seems to be a strain field in the small grain at the right side of the sample, but it is at the edge of the map, so its extent cannot be estimated from the presented data.

The strains and rotations around the crack tip in the 20 % cold-work sample are shown in Figure 8.5. All grains in this sample contain strain fields. There are steep gradients from one side of each grain to the other and twins crossing the different grains. In the area around the crack tip, the disturbance of the lattice was so substantial, that no useful EBSD patterns could be obtained and the strains could not be quantified. The ϵ_{22} map, that is showing the normal strains almost perpendicular to the path of the crack, is almost

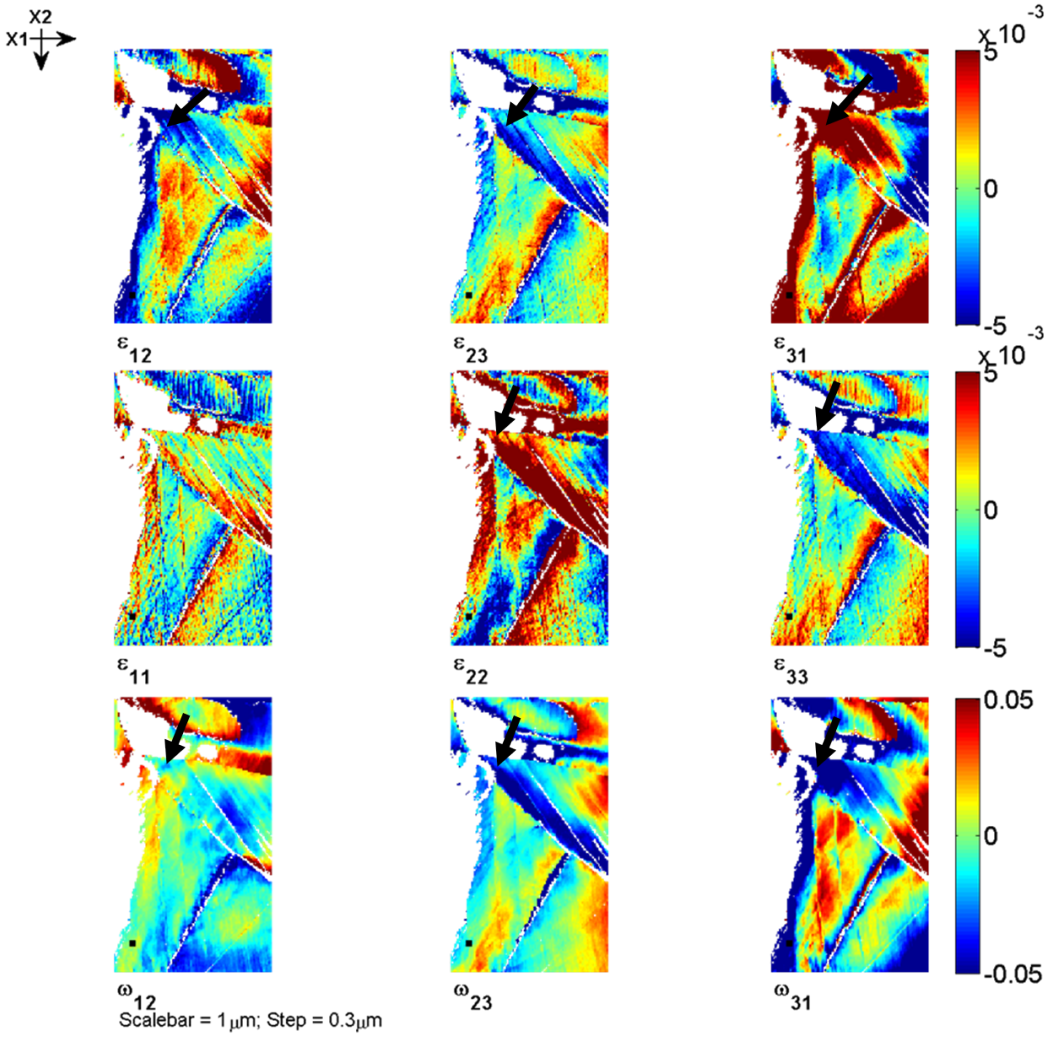

Figure 8.5: Relative strains and rotations in the 20 % cold-work sample (cp. Figure 8.2c). The $\varepsilon_i j$ are the normal elastic strains if $i = j$ and elastic shear strains if $i \neq j$. The ω_{ij} are the rotations.

entirely comprised of dark red and dark blue regions, indicating the greatest amount of strain. However, the strains are not only concentrated in along the crack path, but along all other GBs as well.

8.1.2 NanoSIMS

The same crack tips were also analysed with NanoSIMS. For secondary ion mass spectroscopy (SIMS) a sample surface is bombarded with a primary ion beam, which causes particles to be emitted from the surface. These emitted (secondary) particles will be a combination of electrons, neutral species and ions [250, 251]. The secondary ions are detected and analysed to give information about the chemical composition of the sample. The electrons can also be detected and can give an indication of the surface topography

just as in a SEM (see Section 3.5). SIMS is able to detect all elements (and isotopes) from hydrogen to uranium as well as molecular ions, but it has different sensitivities for different elements and ions [252]. The resolution obtained can be down to 50 nm for some instruments.

One of the major problems with SIMS is that quantification of the sample composition is very difficult because each element and molecular species has a different ion yield. Interestingly for this research, if sputtering is performed with a Cs beam, the yield for BO_2^- is particularly high. Although the instrument was not calibrated to allow quantitative analysis, the distribution of some elements within the sample could be determined qualitatively.

The analyses in this thesis was carried out using a CAMECA NanoSIMS 50 instrument optimised for high lateral resolution analysis while maintaining high mass resolution ($M/\Delta M = 5{,}000$) and high sensitivity (ppb for some elements).

The maps obtained for the crack tip in the 5 % cold-work sample are shown in Figure 8.6. The crack appears to be filled with Fe-rich oxide. No CrO^- or Ni^- enrichment was detected in the crack region. The yield for Ni in the NanoSIMS is particularly low, therefore the Ni maps are not very conclusive, but they are provided for completeness. The lack of CrO^- enrichment is surprising, particularly considering the observations made by Lozano-Perez [143], who found Cr-rich oxides all along crack flanks in a similar alloy. An oxide precipitate in the cracked GB has fractured right through the middle and did not seem to have any influence on the crack path. The particle consists of neither Cr- nor Fe-oxide, other candidate oxide precipitates are TiO or Al_2O_3. The most striking map is the BO_2^- map. B has such a high yield in the NanoSIMS that the smallest enrichment can be detected. It appears that in this case not only the GB ahead of the oxide is B enriched, but also the entire oxide region.

Figure 8.7 shows the NanoSIMS data for the 10 % cold-work sample. Again the corresponding Ni map does not show much signal, which is probably due to the nature of the technique. In this sample, however, the crack seems to be much more open and the crack flanks are lined by a Cr-rich oxide, while the crack is filled with an Fe-rich oxide. B is particularly enriched in the Fe-rich oxides and also in a line crossing the material ahead of the oxidation front.

NanoSIMS data of the crack tip in the 20 % cold-work sample is shown in Figure 8.8.

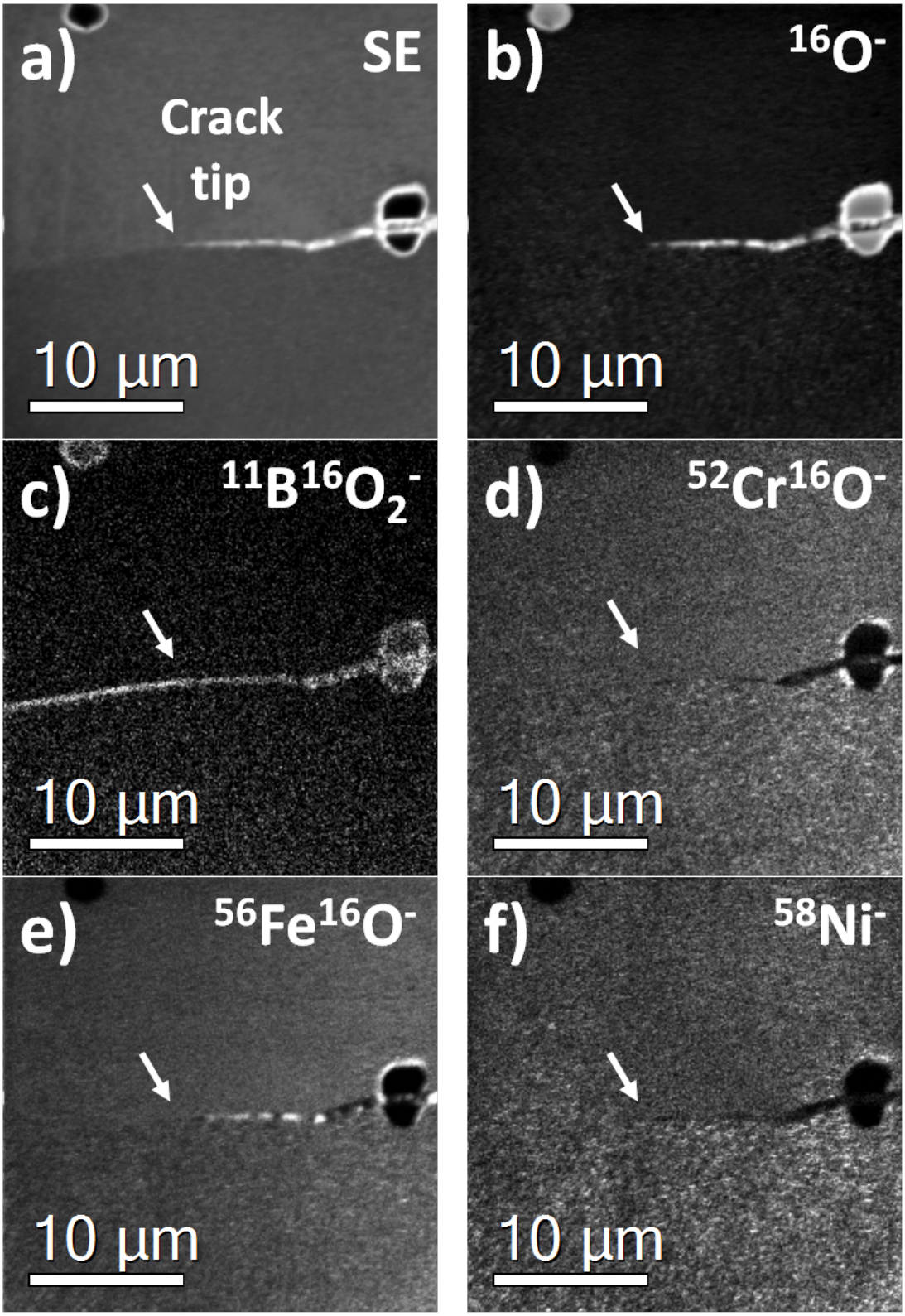

Figure 8.6: NanoSIMS maps of the crack tip in the 5% cold-work sample shown in Figure 8.3.

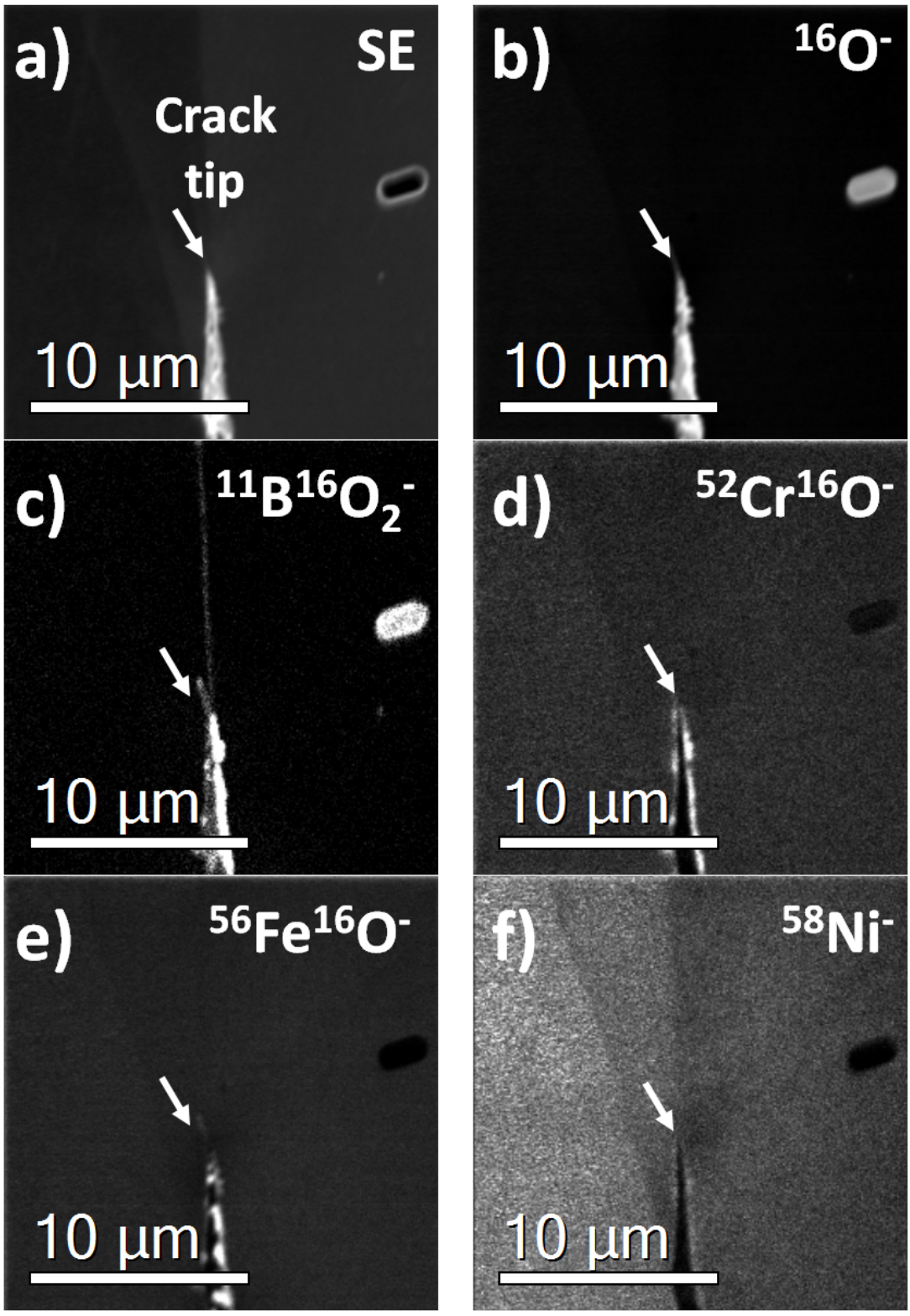

Figure 8.7: NanoSIMS maps of the crack tip in the 10% cold-work sample shown in Figure 8.4

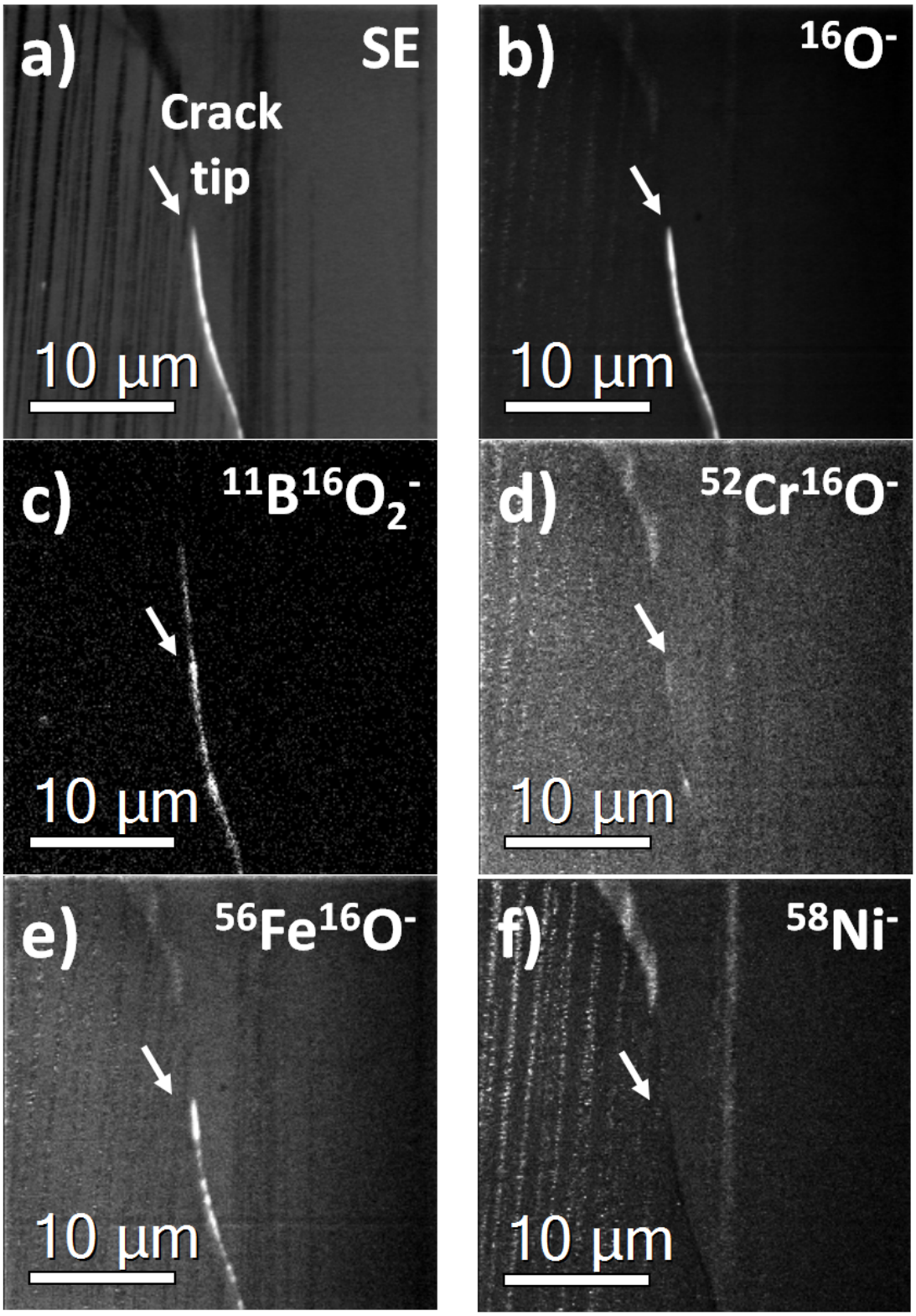

Figure 8.8: NanoSIMS maps of the crack tip in the 20% cold-work sample shown in Figure 8.5

Just as for the 5 % cold-work sample the crack front is not open, so it is assumed that the crack tip is placed at the oxidation front. As in the 5 % cold-work sample, there is no sign of CrO^- or Ni^- enrichment in the crack tip region. Neither oxides nor Ni enrichment were observed in the deformation twins, which can be seen very clearly in the EBSD strain maps in Figure 8.5. In this case B enrichment was observed in the crack oxide and about 8 μm ahead in the GB. The remaining GB looks B depleted.

8.2 Discussion

The results shown above were a preliminary characterisation. APT and ATEM are still to be performed to fully characterise the crack tips.

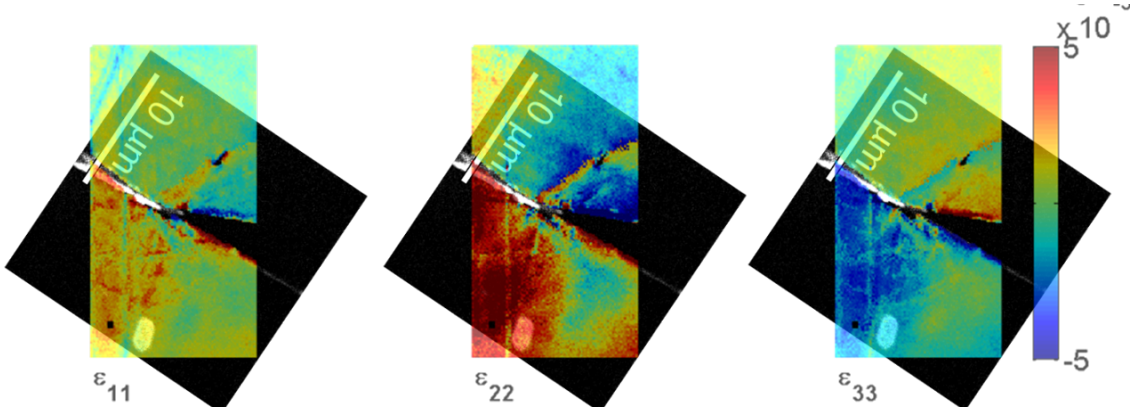

Figure 8.9: Overlay of the normal strain maps in Figure 8.4 and the NanoSIMS BO_2^- elemental map in Figure 8.4c (10% cold-work sample).

The strain maps were compared with the elemental maps from the NanoSIMS and the comparison with the BO_2^- maps provided some interesting observations. An overlay of the BO_2^- and the respective normal strain map from the same area of the 10 % cold-work sample is shown in Figure 8.9. The crack is progressing in to the upper GB at the triple point. B enrichment is mainly observed in the crack oxide and also in the other, lower, GB. It is possible, that the GB which is about to crack is similarly enriched and this was just not detected with the technique. Another explanation is that the B from the cracking GB has diffused to the crack tip and left the GB ahead of the crack depleted.

Another overlay of the normal strain maps and the NanoSIMS BO_2^- map was produced for the 20 % cold-work sample. In this case the B enrichment ahead of the crack tip follows the GB as previously observed [143]. Ahead of the enriched region of the GB, there is a depleted region. This depleted region begins at the triple point ahead of the crack tip.

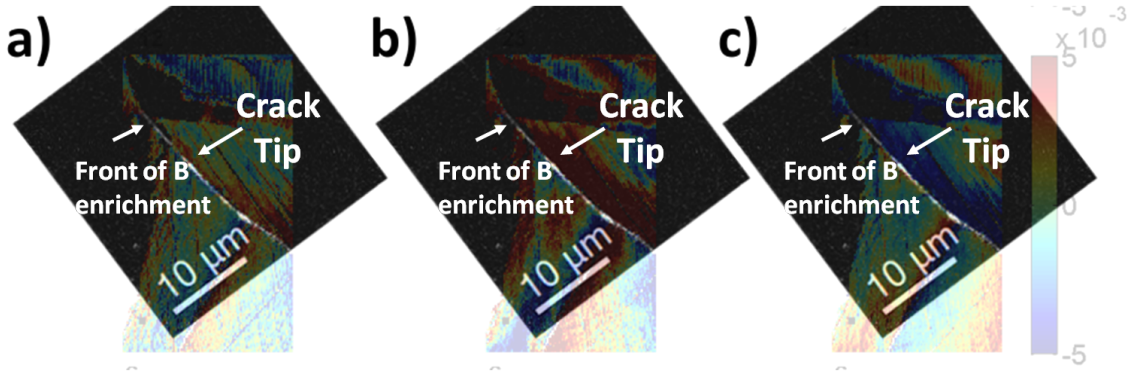

Figure 8.10: Overlay of the normal strain maps in Figure 8.5 and the NanoSIMS BO_2^- elemental map in Figure 8.5c.

However, as this region is at the edge of the map, it is possible, that this is an effect of the technique (trajectory aberrations etc.).

APT experiments containing the crack tip regions are also suggested to further investigate the role of B in SCC in 304 stainless steel and possible B depletion in the GBs ahead of cracks.

Chapter 9

Conclusions

The aim of this thesis was to further determine the influence of stress and cold-work on SCC in 304 stainless steels in PWR primary water conditions. A methodology for the systematic study of surface and grain boundary oxides was developed. Oxides and trace elements were characterised. Ni enrichment and a Ni-rich phase were found ahead of the oxidised portions of GBs and DBs. The implications for current SCC mechanisms were discussed and a modified film-rupture mechanism was suggested.

9.1 New experimental approaches

1. **Systematic characterisation of surface oxides with APT**
   Although it had been shown that the characterisation of surface oxides with APT is possible [211], this is the first systematic characterisation of surface oxides on a set of samples tested under controlled conditions.

2. **Combination of characterisation methods to overcome shortcomings of single techniques and obtain a full picture**
   High spatial resolution EFTEM mapping and the high chemical sensitivity of APT were combined with 3D FIB slicing, which allowed acquisition of statistically relevant amounts of data. Comparison of the data obtained with the different techniques allowed calibration of the reconstruction parameters for the APT data and calibration of the edge-set up for the EELS quantification in the EFTEM maps. Comparison of the features in both types of data with the 3D FIB slicing helped to put the results into a wider context and evaluate their importance and representativeness in

a greater scheme.

3. **Development of a robust methodology for full characterisation of GB oxides**

   A matrix of samples with/without prior cold-work oxidised with/without stress was systematically studied with a range of different techniques. Sectioning of the GB oxides with the FIB allowed the fabrication of several different specimen types optimised for different techniques. The acquisition of much better ATEM data was possible from the TEM foils, than it would have been if APT needles had been studied instead.

4. **Identification of the different oxide phases at the surfaces, in GBs and DBs**

   A range of compositions was found in the surface, GB and DB oxides. The surface is usually covered with spinel oxides with an $Fe_{1+x}Cr_{2-x}O_4$. With $0 < x < 0.5$. The GB and DB oxides are more Cr enriched and probably contain some proportion of Cr_2O_3. The phase diagram in Figure 4.35 shows that these phases are miscible.

9.2 Implications for SCC mechanisms

1. **New evidence for the influence of stress and cold-work**

   It was found that both an applied load (external stress) and cold-work prior to oxidation (internal stress) increase the oxidation rates, generally and at GBs. DBs were observed to form in cold-rolled specimen, but also in samples stressed below the yield strength. Oxides grow in to these DBs, if they are exposed to PWR primary water conditions. Although SCC in 304 stainless steel is mostly intergranular, the deformation bands seem to play a role as fast diffusion paths.

2. **In-depth analysis of oxidation of DBs and TDBs**

   DB oxides were found to contain much greater amounts of Cr than any other oxides analysed in this study. It was found that Ni diffuses ahead of the oxides at single DBs. At TDBs it diffuses along the band edges alloing oxide growth within the TDBs. If sub-cell structures are present in DBs, the sub-cell edges also act as fast diffusion paths for Ni.

3. **Novel characterisation of the distribution of minor additions to the PWR water in the oxides**

   The distribution Li in the surface and GB oxides was studied with APT. B enrichment was not observed. However, B segregation to GBs (prior to autoclave testing) and cracks was observed with NanoSIMS.

   The distribution of these trace elements in the oxides can now be accurately measured, although further investigations are needed to determine if they play a role in SCC of 304 in PWR primary water.

4. **Characterisation of Ni-phase formation ahead of the oxide front**

   The formation of Ni-rich precipitates ahead of the oxide front was observed in all samples that chemical analysis was performed on. These Ni precipitates seem to be of a separate stable phase formed at the testing temperature of 360°C. The phase could not be identified in available phase diagrams and the synthesis of the phase is suggested for a future experiment.

   It appears that these Ni-rich particles can hinder further oxygen diffusion and oxide growth.

5. **Suggestion of a modified film rupture mechanism**

   A modified FRM using H-stabilised vacancies for enhanced diffusion in the crack tip region was suggested. It is suggested that growth of "internal" unconnected oxide particles may lead to faster achievement of greater maximum oxide depths and allow the high crack growth rates measured in [181] and [253].

6. **Detection of H associated with Ni-rich regions ahead of GB oxides at high resolution**

   The detection of NiH^+ ions spatially segregated in Ni enriched regions in APT samples suggests that H can be trapped in high-vacancy regions in Ni-rich alloys. Such vacancy-rich regions are for example the high-stress fields at crack tips.

7. **Preliminary characterisation of crack tips**

   Crack tips in samples with different levels of cold work were studied with EBSD and NanoSIMS. This "non-destructive" characterisation is the first part of a systematic study of the crack tip regions. The same region can be further characterized by TEM and APT. Future APT experiments are promising to lead to new infor-

mation concerning the role of B and maybe the distribution of trapped H and its relationship with the detected strain fields can also be detected. TEM will provide microstructural information of the same region.

Chapter 10

Suggestions for Future Work

Although the systematic characterisation presented in this thesis has answered some questions about the influence of stress and cold-work on corrosion behaviour of 304 stainless steel in PWR primary water conditions, some questions have remained unresolved. Some new types of analysis were shown to be possible and should be exploited, and some new questions have arisen.

1. **Crack tip characterisation**

   Crack tip characterisation has been attempted and could not be completed for this thesis. ATEM and APT analysis are recommended. A larger scale NanoSIMS study is also recommended to evaluate the behaviour of B fully.

2. **EBSD for determination of GB character**

   The chemistry of the GBs and GB oxides in this thesis have been characterised at high resolution and with great accuracy, but the GB orientation was not determined. Although no type of GB was found to be immune to cracking [172], there were differences in oxidation behaviour, which could not be explained by dislocation concentration or chemical differences. A low resolution EBSD map of the sample surface prior to oxidation could easily that information for all surface near GBs.

3. **Diffraction for phase identification**

   The compositions of some of the GB and DB oxides was measured to be more Cr-rich, than expected in a (cubic) spinel oxide. If a (hexagonal) sesquioxide phase was present, it should be possible, to identify this phase with local-area diffraction. This is suggested for future TEM studies.

Diffraction should also be used to identify the structure of the Ni-rich phase. The lattice parameters of austenitic steels and Ni alloys are very similar, but nonetheless diffraction could establish whether a γ phase or an $L1_2$ phase is present.

4. **APT of hydrogen charged specimen**

   Hydrogen is extremely volatile and if not bound chemically, it can diffuse through metal of dimensions of an APT needle in a very short time. Additionally it is present even in ultra-high vacuum systems and condensates on APT specimens during the experiment. However, if the H is trapped in vacancies and weakly bound to the atoms of the APT needle, it might be possible to detect this trapped H. Vacancy concentration could be locally increased by irradiation or deformation. A cool transfer at cryogenic temperatures would reduce H fugacity.

5. **Experiments in deuterated water**

   Even if weakly bound H can be detected with APT, it remains uncertain, whether it was trapped during the corrosion experiment or whether it condensed onto certain planes preferentially. If the corrosion test was conducted with deuterated water, the D could be distinguished from H in the mass spectrum and the source of the signal could be determined conclusively. However, as the m/z peaks for $^{58}NiD^+$ and $^{60}Ni^+$ overlap, it may be difficult to distinguish between these molecular ions.

6. **Testing of samples with varying Ni concentration**

   The results obtained in this study suggest that the precipitation of a Ni-rich phase plays an important role in SCC of 304 stainless steel. Corrosion tests on samples with changing Ni content and the study of GB oxides in these model alloys would help to clarify the role of Ni further.

7. **Synthesis of Ni alloy resembling the phase in the observed Ni-rich particles**

   The isothermal cross section at 400°C of the ternary Fe-Cr-Ni phase diagram does not show a phase that fits the composition measured in the Ni-rich particles. It is suggested that the synthesis of such a phase should be attempted.

In the 139 years since Johnson dropped a bent steel wire in acid and found that it cracked [14] until today, more than 25,000 articles, reviews, letters and books have been published

on SCC [254]. Despite the extensive effort it is still not possible to reliably predict SCC susceptibility and crack growth rates for new systems.

This is why I would like to conclude my DPhil thesis, in the hope of having brought a small ray of light into the dark, with this poem:

"The image of stress corrosion I see
Is that of a huge unwanted tree,
Against whose trunk we chop and chop,
But which outgrows the chips that drop;

And from each gash made in its bark
A new branch grows to make more dark
the shade of ignorance around its base,
Where scientists toil with puzzled face"

On Stress Corrosion, S.P. Rideout

Appendix A

EBSD strain mapping data quality maps

A.1 5 % cold-work sample

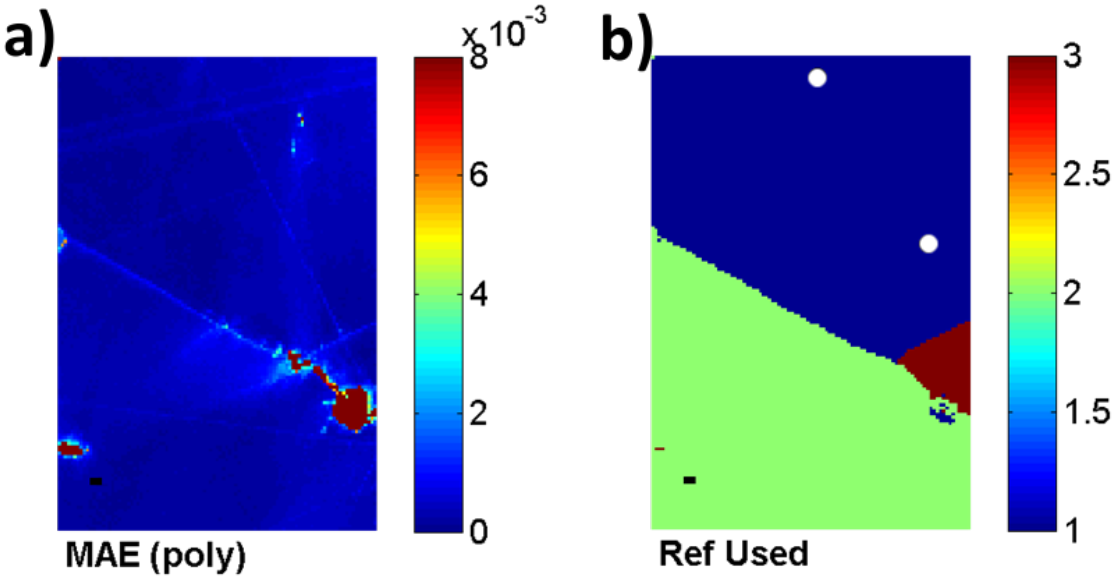

Figure A.1: a) MAE b) Grain map showing the reference points that were chosen to represent 0 strain in the respective grain.

A.2 10 % cold-work sample

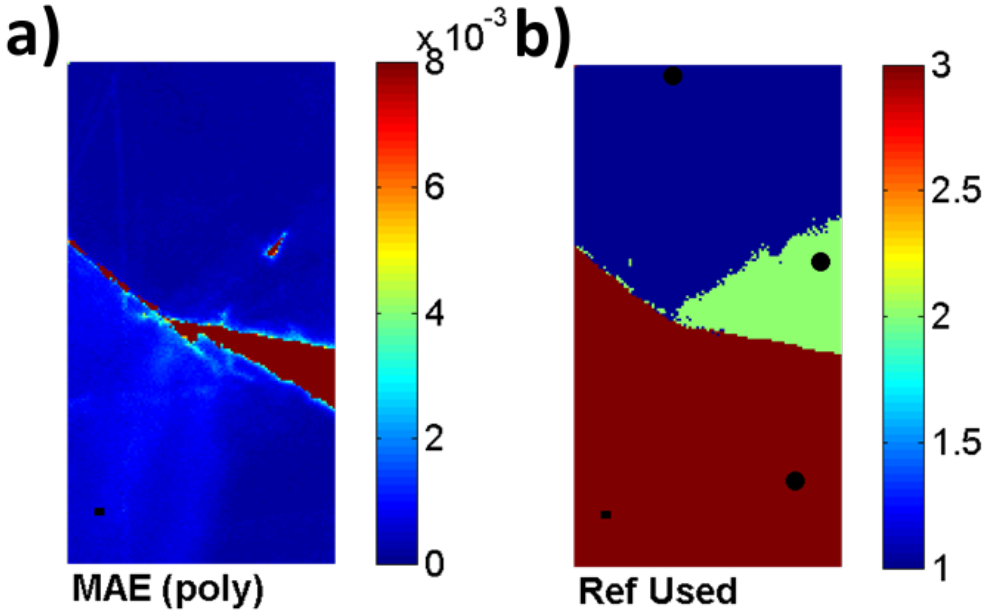

Figure A.2: a) MAE b) Grain map showing the reference points that were chosen to represent 0 strain in the respective grain.

A.3 20 % cold-work sample

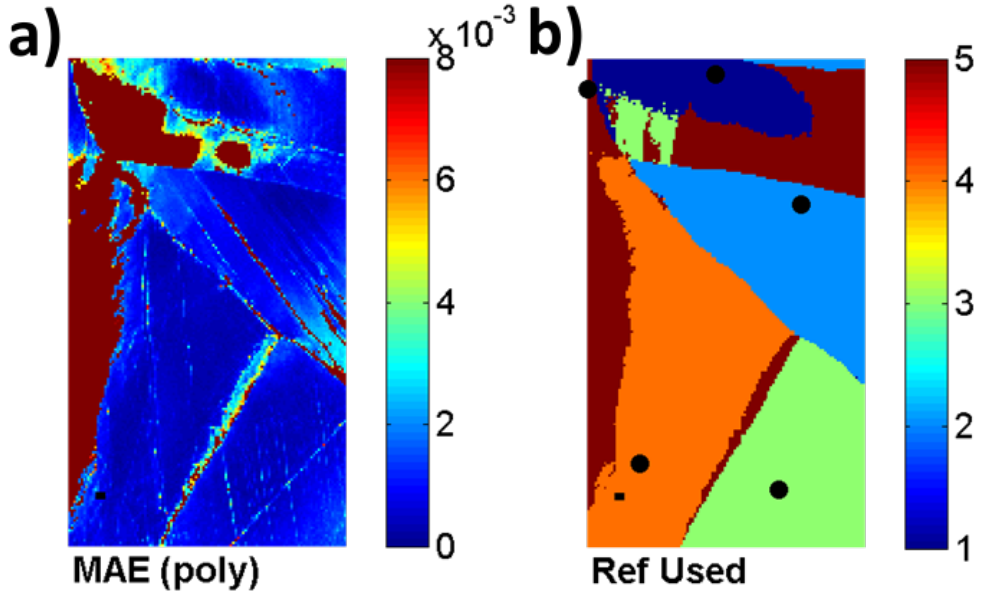

Figure A.3: a) MAE b) Grain map showing the reference points that were chosen to represent 0 strain in the respective grain.

Appendix B

Colour Code for Ions in APT Ion maps

In atom probe tomography ionic species are field evaporated and accelerated towards the detector, where there position and ToF from the sample to the detector are recorded. The ionic species can consist of one or several atoms, that have been part of the sample. The identity of a single ion does not provide information about the stoichiometry of the sample. Ion evaporated from a chromite spinel region ($FeCr_2O_4$), for example, could be Fe^+, Cr^+, O^+, O_2^+, O_2^{2+}, FeO^+, CrO^+, Cr_2O^+, Fe_2O^+ and a number of others. The analysis of the decomposed ions is necessary to determine the local stoichiometry of the sample.
However, oxide regions dominated by light and dark blue regions in the provided ion maps suggest Cr-rich oxides, while oxide regions, that appear purple suggest the a number of FeO^+ ions were evaporated from the area, thus they are Fe-rich. Interface regions may often appear orange, due to Fe_2O^+ ions, which seem to be evaporated from weakly oxidised regions.

Ion	Colour	Intervals ranged in the m/e spectrum
Si		13.98 -14.01 14.48 -14.52
Cr		49.80 - 54.11 24.95 - 25.00 25.93 - 26.04 26.44 - 26.50
Ni		57.81 - 58.26 28.93 - 29.10 29.94 - 31.06 59.78 - 62.05
Fe		26.94 - 27.00 27.93 - 28.54 55.74 - 57.08
O		15.94 - 16.10
OH		17.00 - 17.29
C		17.99 - 18.07
C_2		23.97 - 24.08
H_2O		18.07 - 18.44
Mn		27.44 - 27.51 54.84 - 55.04
NiH		29.44 - 29.57 58.84 - 59.07
O_2		31.91 - 32.23
CrO		33.43 - 35.05 67.72 - 68.29 68.86 - 69.19 69.82 - 70.30
CrO_2		41.79 - 43.73 83.65 - 86.45 81.70 - 82.33 40.85 - 41.28
Mo		46.86 - 49.07 45.83 - 46.18 93.81 - 97.03
Cu		62.86 - 63.27 64.79 - 65.33
Fe_2O		63.81 - 64.12
FeO		71.86 - 72.23 72.82 - 73.17 73.81 - 74.37 35.92 - 37.31
Li		6.98 - 7.03
B		11.00 - 11.04

Figure B.1: The ions in all maps in this thesis are colour coded as shown in this key unless explicitly stated otherwise.

Bibliography

[1] T L Root, J T Price, K R Hall, S H Schneider, C R, and J A Pounds. Fingerprints of Global Warming on Wild Animals and Plants. *Nature*, 421:57 – 60, 2003.

[2] G A Meehl, W M Washington, W D Collins, J M Arblaster, A Hu, L E Buja, W G Strand, and H Teng. How Much More Global Warming and Sea Level Rise? *Science*, 307:1769 – 1772, 2005.

[3] X Zhang, F W Zwiers, G C Hegerl, F H Lambert, N P Gillett, S Solomon, P A Stott, and T Nozawa. Detection of human influence on twentieth-century precipitation trends. *Nature*, 448:461 – 466, 2007.

[4] M T Boykoff and J M Boykoff. Balance as bias: global warming andthe US prestige press. *Global Environmental Change*, 14:125 – 136, 2004.

[5] D J Karoly, K Braganza, P A Stott, J M Arblaster, G A Meehl, A J Broccoli, and K W Dixon. Detection of a Human Influence on North American Climate. *Science*, 302:1200 – 1203, 2003.

[6] W Cramer, A Bondeau, F I Woodward, I C Prentice, R A Betts, V Brovkin, P M Cox, V Fisher, J A Foley, A D Friend, C Kucharik, M R Lomas, N Ramankutty, S Sitch, B Smith, A White, and C Young-Molling. Global response of terrestrial ecosystem structure and function to CO2 and climate change: results from six dynamic global vegetation models. *Global Change Biology*, 7:357 – 373, 2001.

[7] J Mandula, editor. *Nuclear Power Reactors in the World*. Reference Data Series No. 2. International Atomic Energy Agency, Vienna, 2011.

[8] P M Scott. *Corrosion issues in light water reactors : stress corrosion cracking*, chapter An overview of materials degradation by stress corrosion in PWRs, pages 3 – 24. Woodhead Publishing and Maney Publishing on behalf of the Institute of Materials, Minerals & Mining, Cambridge, 2007.

[9] F Cattant, D Crusset, and D Feron. Corrosion Issues in Nuclear Industry Today. *materialstoday*, 11:32 –37, 2008.

[10] D O Sprowls. *Handbook of Materials, Volume 8: Mechanical Testing*, volume t, chapter Tests for Stress Corrsion Cracking, pages 495 – 536. American Society for Metals, 1985.

[11] http://www.nrc.gov/reactors/pwrs.html, Accessed: May 2012.

[12] S M Bruemmer. Microstructural and Microchemical Mechanisms Controlling Intergranular Stress Corrosion Cracking in Light-Water-Reactor Systems. *Journal of Nuclear Materials*, 216:348 – 368, 1994.

[13] S Lozano-Perez and J M Titchmarsh. TEM investigations of intergranular stress corrosion cracking in austenitic alloys in PWR environmental conditions. *Materials at High Temperatures*, 20(4):573 – 579, 2003.

[14] W H Johnson. On the Influence of Sulphuric and Hydrochloric Acids on Iron and Steel. *Proceedings of the Manchester Literary and Philosophical Society*, 12:42, 1873.

[15] W H Johnson. On the influence of acids on iron and steel. *Proceedings of the Manchester Literary and Philosophical Society*, 12:74 – 80, 1873.

[16] O Reynolds. On the effect of acid on the interior of iron wire. *Proceedings of the Manchester Literary and Philosophical Society*, 13:93 – 96, 1874.

[17] W H Johnson. On the Influence of Acids on Iron and Steel. *Proceedings of the Manchester Literary and Philosophical Society*, 13:60 – 61, 1874.

[18] W H Johnson. Further Observation and Experiments on the Influence of Acids on Iron and Steel. *Proceedings of the Manchester Literary and Philosophical Society*, 13:100 – 111, 1874.

[19] W H Johnson. On the Action of nascent Hydrogen on Iron. *Proceedings of the Manchester Literary and Philosophical Society*, 13:130 – 131, 1874.

[20] W H Johnson. Hydrogen and Acids on Iron and Steel. *Proceedings of the Royal Society London*, 23:168 – 179, 1875.

[21] W C Roberts-Austen. *Proceedings of the Royal Institute of Great Britain*, 11:395 – 412, 1886.

[22] A Ledebur. *Stahl Eisen*, 7:681 – 694, 1887.

[23] A Ledebur. *Stahl Eisen*, 9:745 – 755, 1889.

[24] J H Andrew. The embrittlement of iron by caustic soda. *Transaction of the Faraday Society*, 9:316 – 329, 1913.

[25] W C Hothersall. The Spontanious Cracking of the Necks of Small Arm Cartridge Cases. *Transaction of the Faraday Society*, 17:201 –208, 1921.

[26] S A Shipilov. Stress Corrosion Cracking and Corrosion Fatigue: A Record of Progress, 1873 - 1973. In S A Shipilov, R H Jones, J-M Olive, and R B Rebak, editors, *Environment-Induced Cracking of Materials*, volume 1 Chemistry, Mechanics and Mechanisms of *Second International Conference on Environmental Induced Cracking of Metals*, pages 507 – 557, Alberta, Canada, 2004.

[27] W H Hatfield. The Mechanism of Failure of Metals from Internal Stress. *Transactions of the Faraday Society*, 17:36 – 46, 1921.

[28] H Moore and S Beckinsale. The Prevention of Season Cracking in Brass by the Removal of Internal Stress. *Transactions of the Faraday Society*, 17:162 – 189, 1921.

[29] E S Sperry. The Season Cracking of Brass and Bronce Tubing. *Brass World*, 2:39 – 44, 1906.

[30] H Moore, S Beckinsale, and C E Mallinson. The Season Cracking of Brass and other Copper Alloys. *Journal of the Institute of Metal*, 25:35 – 124, 1921.

[31] W H Bassett. The Causes and Prevention of Corrosion Cracking. *Proc. ASTM*, 18:158 – 162, 1918.

[32] W Arthur. *Transactions of the American Institute of Metals*, 10:173 – 177, 1916.

[33] W Rosenhain. The Failure of Metals under Internal and Prologned Stress. *Transaction of the Faraday Society*, 17:2 – 16, 1921.

[34] Symposium on Stress Corrosion Cracking of Metals. Philadelphia, PA, 1945. ASTM.

[35] J C Hodge and J L Miller. Stress Corrosion Cracking of the Austenitic Chromium-Nickel Steels and its Industrial Implications. *Trans ASM*, 28:25 – 81, 1940.

[36] E H Dix Jr. *Proc. ASTM*, 41:928 – 929, 1941.

[37] W J Singley, I H Welinsky, S F Whirl, and H A Klein. Stress Corrsion of Stainless Steel and Boiler Water Treatment in Shippingport Atomic Power Station. In *Proc. American Power Conference*, volume 21, pages 748 – 766, 1959.

[38] D Noel, O de Bouvier, F Foct, T Magnin, J D Mithieux, and F Vaillant. *Corrosion-Deformation Interactions*, chapter 41 Study of the Mechanisms of Stress Corrosion Cracking of Alloys 600 and 690 in Primary Water Reactor Conditions, pages 435 – 452. The Institute of Materials Pub., 1997.

[39] R W Staehle. Critical Analysis of "Tight Cracks". In P King and T Allen, editors, *Canadian Nuclear Society - 13th International Conference on Environmental Degradation of Materials in Nuclear Power Systems 2007*, volume 3 of *Proc. 13th Int. Symp on Environmental Degradation of Materials in Nuclear Power Systems - Water Reactors*, pages 1877–1957. Canadian Nuclear Society, 2007.

[40] H L Logan. Film-rupture mechanism of stress corrosion. *Journal of Research of the National Bureau of Standards*, 48(2):99 – 105, 1952.

[41] E M Gutman. An Inconsistancy in "Film Rapture Model" of Stress Corrosion Cracking. *Corrosion Science*, 49:2289 – 2302, 2007.

[42] J C Scully. Stress Corrosion Crack Propagation: A Constant Charge Criterion. *Corrosion Science*, 15:207 – 224, 1975.

[43] R B Mears, R H Brown, and E H Dix Jr. Symposium on stress corrosion cracking of metals. ASTM-AIME, ASTM Philadelphia, Pa, 1944.

[44] R C Newman and C Healey. Stability, Validity, and Sensitivity to Input Parameters of the Slip-Dissolution Model for Stress Corrosion Cracking . *Corrosion Science*, 49:4040 – 4050, 2007.

[45] D A Vermilyea. A theory for the Propagation of Stress Corrsion Cracks in Metals. *Journal of the Elctrochemical Society*, 119:405 – 407, 1972.

[46] P L Andresen and F P Ford. Life Prediction by Mechanistic Modeling and System Monitoring of Environmental Cracking of Iron and Nickel Alloys in Aqueous Systems. *Materials Science and Engeneering*, A103:167 – 184, 1988.

[47] F P Ford and P L Andresen. Development and use of a Predictive Model of Crack Propagation in 304/316L, A533B/A508 and Inconal 600/182 Alloys in 288°C Water. In *3rd International Conference on Degradation of Materials in Nuclear Power Industry*, 1987.

[48] F P Ford, D F Taylor, P L Andresen, and R G Balinger. Environmentally Controlled Cracking of Stainless and Low Alloy Steels in Light Water Reactor Environments. Technical report, EPRI, 1987.

[49] F P Ford and P L Andresen. The Theoretical Prediction of the Effect of System Variables on the Cracking of Stainless Steel and its use in Design. *Corrosion*, 83, 1987.

[50] P L Andresen and F P Ford. Modelling and Life Prediction of Stress Corrosion Cracking in Sensitized Stainless Steel in High Temperature Water. In *Proc. Symp. on Predictive Capabilities in Environmentally Assisted Cracking*. ASME, 1985.

[51] F P Ford. *Corrosion Processes*, chapter Stress Corrosion Cracking. Sole distributor in the USA and Canada, Elsevier Science Pub., Co. (London, New York, New York, NY, USA), 1982.

[52] D A Jones. A Unified Mechanism of Stress Corrosion and Corrosion Fatigue Cracking. *Metallurgical and Materials Transactions A*, 16:1133 – 1142, 1985.

[53] R C Newman. Developements in the Slip-Dissolution Model of Stress Corrosion Cracking. *Corrosion Science*, 50:682 – 686, 1994.

[54] P L Andresen. Conceptual Similarities and Common Predictive Approaches for SCC in High Temperature Water Systems. In *Corrosion96*. NACE, 1996.

[55] L M Young, P L Andresen, and T M Angeliu. Crack Tip Strain Rate: Estimates Based on Continuum Theory and Experimental Measurement. *Corrsion2001*, page 01131, 2001. NACE.

[56] Z Lu and T Shoji. Unified interpretation of crack Growth Rates of Ni-Base Alloys in LWR Environments. *Journal of Pressure Vessel Technology (Trans. ASME)*, 128:318 – 327, 2006.

[57] K Sieradzki. Atomistic and micromechanical modeling aspects of environment-iduced cracking of metals. In R P Gangloff and M B Ives, editors, *Environment-Induced Cracking of Metals*, pages 125 – 137. NACE, 1990.

[58] A Turnbull. Modelling of Environment Assisted Cracking. *Corrosion Science*, 34:821 – 960, 1993.

[59] M M Hall Jr. An Alternative to the Shoji Crack Tip Strain Rate Equation. *Corrosion Science*, 50:2902 – 2905, 2008.

[60] M M Hall Jr. Critique of the Ford-Andresen Film Rapture Model for Aqueous Stress Corrosion Cracking. *Corrosion Science*, 51:1103 – 1106, 2009.

[61] M M Hall Jr. Film Rapture Model for Aqueous Stress Corrosion Cracking Under Constant and Variable Stress Intensity Factor. *Corrosion Science*, 51:225 – 233, 2009.

[62] M Vankeerberghen, G Weyns, S Gavrilov, B Martens, and J Deconinck. Crack Propagation Rate Modelling for 316SS exposed to PWR-relevant Conditions. *Journal of Nuclear Materials*, 384:274 – 285, 2009.

[63] K Sieradzki and R C Newman. Brittle Behavior of Ductile Metals during Stress Corrosion Cracking. *Philosophical Magazine A*, 51:95 – 132, 1985.

[64] F Friedersdorff and K Sieradzki. Film-induced Brittle Intergranular Cracking of Silver-Gold alloys. *Corrosion*, 52:331 – 336, 1996.

[65] K Sieradzki and R C Newman. Stress Corrosion Cracking. *Journal of Physics and Chemistry of Solids*, 48:1101 – 1113, 1987.

[66] J R Galvele. A Stress Corrosion Cracking Mechanism based on Surface Mobility. *Corrosion Science*, 27(1):1 – 33, 1987.

[67] K Sieradzki and F J Friedersdorff. Notes on the Surface Mobility Mechanism of Stress Corrosion Cracking. *Corrosion Science*, 34:669 – 675, 1994.

[68] E M Gutman. Notes on the Discussion Concerning the "Surface Mobility Mechanism" of Stress Corrosion Cracking. *Corrosion Science*, 45:2105 – 2127, 2003.

[69] E M Gutman. An Inconsistancy in "Surface Mobility Mechanism" of Stress Corrosion Cracking". *Corrosion Science*, 61:197 – 200, 2005.

[70] J R Galvele. Surface Mobility Mechanism of Stress Corrsion Cracking. *Corrosion Science*, 35:419 – 434, 1993.

[71] J R Galvele. Reply to "Notes on the Discussion Concerning 'Surface Mobility Mechanism' of Stress Corrosion Cracking", by E.M. Gutman. *Corrosion Science*, 45:2119 – 2128, 2003.

[72] AR Troiano. The role of hydrogen and other interstitials in the mechanical behavior of metals. *Trans ASM*, 52:54, 1960.

[73] L L Shreir. Übersicht der electrochemischen Methodes zur Untersuchung von Wasserstoffversprödung und Spannungsrisskorrosion. *Werkstoffkunde und Korrosion*, 21:613 – 629, 1970.

[74] S P Lynch. Environmentally Assisted Cracking: Overview of Evidence for an Adsorption-Induced Localized Slip Process. *Acta Metallurgica*, 36:2639 – 2661, 1988.

[75] H W Liu. A Unified Model of Enivironment-Assisted Cracking. *Acta Materialia*, 56:4339 – 4348, 2008.

[76] S P Lynch. Comments on "A Unified Model of Environment-Assisted Cracking". *Scripta Materialia*, 61:331 – 224, 2009.

[77] C F Barth and E A Steigerwald. Evaluation of hydrogen embrittlement mechanisms . *Metallurgical and Materials Transactions B*, 1:3451–3455, 1970.

[78] X Chen, T Foecke, M Lii, Y Katz, and W W Gerberich. The Role of Stress State on Hydrogen Cracking in Fe-Si Single Crystals. *Engeneering Fracture Mechanics*, 35:997 – 1017, 1990.

[79] S L Lee and D J Unger. A Decohesion Model of Hydrogen Assisted Cracking. *Engeneering Fracture Mechanics*, 31:647 – 660, 1988.

[80] I Schneider, M Pfuff, and W Dietzel. Simulation of hydrogen assisted stress corrosion cracking using the cohesive model. *Engeneering Fracture Mechanics*, 75:4283–4291, 2008.

[81] N R Raykar, S K Maiti, and R K Singh Raman. Modelling of mode-I stable crack growth under hydrogen assisted stress corrosion cracking. *Engineering Fracture Mechanics*, 78:3153 – 3165, 2011.

[82] T Magnin, R Chiergatti, and R Oltra. Mechanism of Brittle Fracture in a Ductile 316 Alloy During Stress Corrosion. *Acta Metallurgica and Materialia*, 38:1313 – 1319, 1990.

[83] T Magnin, A Chambreuil, and B Bayle. The Corrosion-Enhanced Plasticity Model for Stress Corrosion Cracking in Ductile FCC Alloys. *Acta Materialia*, 44:1457 –1470, 1996.

[84] D Delafosse and T Magnin. Hydrogen Induced Plasticity in Stress Corrosion Cracking of Engeneering Systems. *Engeneering Fracture Mechanics*, 68:693 – 729, 2001.

[85] C D Beachem. A New Model for Hydrogen -Assisted Cracking (Hydrogen "Embrittlement"). *Metallurgical Transactions*, 3:437 – 450, 1972.

[86] DO Hayward and BMW Trapnell. *Chemisorption*. Butterworth, London, 1964.

[87] C B Gilpin, D H Paul, S K Asunmaa, and N A Tiner. *Advanced Electron Metallography*, chapter Electron microautoradiography and its application to the study of hydrogen distribution in steel, page 720. A.S.T.M. Spec. Tech. Publ. No. 396, 1966.

[88] A Cracknell and N J Petch. Frictional forces on dislocation arrays at the lower yield point in iron. *Acta Metallurgica*, 3:186 – 189, 1955.

[89] R M Vennett and G S Ansell. The effect of high-pressure hydrogen upon the tensile properties and fracture behavior of 304L stainless steel. *Trans ASM*, 60:242 – 251, 1967.

[90] B F Brown, C T Fuji, and E P Dahlberg. Methods for Studying the Solution Chemistry Within Stress Corrosion Cracks. *Journal of the Elctrochemical Society*, 116:218 – 219, 1969.

[91] B F Brown. The role of the occluded corrosion cell in stress-corrosion cracking of high strength steels. Technical Report 112, Centre Belge d'Etude de la Corrosion, 1970.

[92] J A Smith, M H Peterson, and B F Brown. Electrochemical conditions at the tip of an advancing stress corrosion crack in AISI 4340 steel. *Corrosion*, 26:539, 1970.

[93] I M Robertson and H K Birnbaum. An HVEM study of hydrogen effects on the deformation and fracture of nickel. *Acta Metallurgica*, 34:353 – 366, 1986.

[94] G M Bond, I M Robertson, and H K Birnbaum. Effects of hydrogen on deformation and fracture processes in high-purity aluminium. *Acta Metallurgica*, 36:2193 – 2197, 1988.

[95] H K Birnbaum and P Sofronis. Hydrogen-enhanced localized plasticity – a mechanism for hydrogen-related fracture. *Materials Science and Engineering: A*, 176:191 – 202, 1994.

[96] A M Alvarez, I M Robertson, and H K Birnbaum. Hydrogen embrittlement of a metastable β-titanium alloy. *Acta Materialia*, 52:4161 – 4175, 2004.

[97] H K Birnbaum. Mechnisms of hydrogen related fracture of metals. Office of Naval Research contract USN 00014 - 83 - K - 0468, University of Illinois Research Laboratory, 1989.

[98] M L Martin, I M Robertson, and P Sofronis. Interpreting hydrogen-induced fracture surfaces in terms of deformation processes: A new approach. *Acta Materialia*, 59:3680 – 3687, 2011.

[99] Afrooz Barnoush and Horst Vehoff. Recent developments in the study of hydrogen embrittlement: Hydrogen effect on dislocation nucleation. *Acta Materialia*, 58(16):5274 – 5285, 2010.

[100] M Wen, L Zhang, B An, S Fukuyama, and K Yokogawa. Hydrogen-enhanced dislocation activity and vacancy formation during nanoindentation of nickel. *Phys. Rev. B*, 80:094113, 2009.

[101] P M Scott and M Le Calvar. Some possible mechanisms of intergranular stress corrosion cracking of Alloy 600 in PWR primary water. In R E Gold and E P Simonen, editors, *6th International Conference on Environmental Degradation of Materials in Nuclear Power Systems*, pages 657–667, 1993.

[102] J.L Meijering. On the diffusion of oxygen through solid iron. *Acta Metallurgica*, 3(2):157 – 162, 1955.

[103] R B Rebak and Y Szklarska-Smialowska. The mechanism of Stress Corrosion Cracking of Alloy 600 in High Temperature Water. *Corrosion Science*, 38(6):971 – 988, 1996.

[104] L E Thomas and S M Bruemmer. Insights into environmental degradation mechanisms from analytical transmission electron microscopy of scc cracks. In F P Ford, S M Bruemmer, and G S Was, editors, *Proceedings of the 9th International Symposium on Environmental Degradation of Materials in Nuclear Power Systems - Water Reactors*, pages 41–47, 1999.

[105] A J McEvily and I Le May. Hydrogen-assisted cracking. *Materials Characterization*, 26:253 – 268, 1991.

[106] J E Truman. The influence of chloride content, pH and temperature of test solution on the occurrence of stress corrosion cracking with austenitic stainless steel. *Corrosion Science*, 17:737 – 746, 1977.

[107] J N Wanklyn and P J Jones. The aqueous corrosion of reactor metals. *Journal of Nuclear Materials*, 6:291 – 329, 1962.

[108] G S Was and J T Busby. Role of irradiated microstructure and microchemistry in irradiation-assisted stress corrosion cracking. *Philosophical Magazine*, 85(4-7 SPEC. ISS.):443–465, 2005.

[109] S M Bruemmer and L E Thomas. High-Resolution Characterization of Stress Corrosion Cracks in Austenitic Stainless Steel from Crack Growth Tests in BWR-Simulated Environments. In T R Allen, P J King, and L Nelson, editors, *Proceedings of the 12th International Conference on Environmental Degration of Materials in Nuclear Power System - Water Reactors*, 2005.

[110] S Lozano-Perez, T Yamada, T Terachi, M Schröder, C A English, G D W Smith, C R M Grovenor, and B L Eyre. Multi-scale Characterization of Stress Corrosion Cracking of Cold-Worked Stainless Steels and the Influence of Cr Content. *Acta Materialia*, 57:5361 – 5381, 2009.

[111] T Terachi, K Fujii, and K Arioka. Microstructural Characterization of SCC Crack tip and Oxide Film for SUS316 Stainless Steel in Simulated PWR Water at 320°C. *Journal of Nuclear Science and Technology*, 42:225 – 232, 2005.

[112] K Arioka, T Yamada, T Terachi, and T Miyamoto. Temperature, Potential and Sensitization Effects on Intergranular Crack Growth and Crack-Tip Appearance of Cold Worked 316. In *13th International Conference on Environmental Degradation of Materials in Nuclear Power Systems*. Whistler, British Columbia, Paper 3, 2007.

[113] S Lozano-Perez and L C Gontard. Understanding Stress Corrsion Cracking with Electron Tomography. *Journal of Microscopy and Microanalysis*, 14:642 – 643, 2008.

[114] S M Bruemmer, E P Simonen, P M Scott, P L Andresen, G S Was, and J L Nelson. Radiation-induced material changes and susceptibility to intergranular failure of light-water-reactor core internals. *Journal of Nuclear Materials*, 274:299 – 314, 1999.

[115] R Pathania, K Gott, and P Scott. An Overview of the Cooperative IASCC Research (CIR) Programm. In *13th International Conference on Environmental Degradation of Materials in Nuclear Power Systems*. Whistler, British Columbia, Paper 56, 2007.

[116] D D MacDonald and M Urquidi-MacDonald. A Coupled Environment Model for Stress Corrosion Cracking in Sensitized Type 304 Stainless Steel in LWR Environments. *Corrosion Science*, 32:51 – 81, 1991.

[117] M P Manahan Sr., D D MacDonald, and A J Peterson. Determination of the fate of the Current in the Stress Corrosion Cracking of sensitised type 304SS in High Temperature Aquaeous Systems. *Corrosion Science*, 37:189 – 208, 1994.

[118] M Kamaya and T Haruna. Crack Initiation Model for Sensitized 304 Stainless Steel in High Temperature Water. *Corrosion Science*, 48:2442 – 2456, 2006.

[119] M Kamaya and T Haruna. Influence of Local Stress on Initiation Behavior of Stress Corrosion Cracking for Sensitized 304 Stainless Steel. *Corrosion Science*, 49:3303 – 3324, 2007.

[120] S Rahimi, D L Engelberg, J A Duff, and T J Marrow. In situ observation of intergranular crack nucleation in a grain boundary controlled austenitic stainless steel. *Journal of Microscopy*, 233:423 – 431, 2009.

[121] O Raquet, E Herms, F Vaillant, T Couvant, and J-M Boursier. SCC of Cold-Worked Austenitic Stainless Steels in PWR Conditions. In T R Allen, P J King, and L Nelson, editors, *Proceedings of the 12th International Conference on Environmantal Degradation of Materials in Nuclear Power Systems - Water Reactors*, 1049-1059, 2005.

[122] L Tribouilloy, F Vaillant, J-M Olive, M Puigalli, L Legras, T Couvant, J-M Boursier, Y Rouillon, and C Amzallag. Stress Corrosion Cracking on cold-worked Austenitic Stainless Steels in PWR Environment. In *13th International Conference on Environmental Degradation of Materials in Nuclear Power Systems*. Whistler, British Columbia, Paper74, 2007.

[123] S W Sharkawy, Z Xia, and Z Szklarska-Smialowska. Stress corrosion cracking of AISI 304 and 316 stainless steels in lithiated water at 350°C. *Journal of Nuclear Materials*, 195(12):184 – 190, 1992.

[124] Z Szklarska-Smialowska, Z Xia, and S W Sharkawy. Comparative Studies of SCC in Two Austenitic Stainless Steels and Alloy 600 on Exposure to Lithiated Water at 350∘C. *Corrosion*, 48:455–462, 1992.

[125] Yamada T. Miyamoto T. Arioka K. Terachi, T. Scc growth behaviors of austenitic stainless steels in simulated pwr primary water. *Journal of Nuclear Materials*, 426(1-3):59–70, 2012. cited By (since 1996) 0.

[126] T Couvant, D Delafosse, F Vaillant, and J-M Boursier. Effect of Strain-Path on Stress Corrosion Cracking of AISI 304L Stainless Steel in PWR Primary Environment at 360 ° C. *Journal of Corrosion Science and Engineering*, 11:1–14, 2008.

[127] T Couvant, D Delafosse, F Vaillant, and J-M Boursier. Effect of Strain-Path on Stress Corrosion Cracking of AISI 304L Stainless Steel in PWR Primary Environment at 360 ° C. In T R Allen, P J King, and L Nelson, editors, *Proceedings of the 12th International Conference on Environmental Degration of Materials in Nuclear Power System - Water Reactors*, 2005.

[128] T Couvant, L Legras, C Pokor, F Vaillant, Y Brechet, J M Boursier, and P Moulart. Investigations on the mechanisms of PWSCC of strain hardened austenitic stainless steels. *Canadian Nuclear Society 13th International Conference on Environmental Degradation of Materials in Nuclear Power Systems*, 1:499 – 514, 2007.

[129] http://www2.fz-juelich.de/ief/ief-2/datapool/page/401/DSC_0071_470.jpg, Accessed: May 2012.

[130] R G Allen, G I Ogundele, A C Lloyd D K Jain, and A K Järvine. Crack observed within CANDU nuclear power plants under cyclic moist environments. *Canadian Nuclear Society - 29th Annual Conference of the Canadian Nuclear Society and 32nd CNS/CNA Student Conference 2008*, 2:1045–1057, 2008.

[131] S Xu, W Wang, and H Liu. The Stress Corrosion Cracking of austenitic stainless steel heat exchange tubes - Three cases study. *American Society of Mechanical Engineers, Pressure Vessels and Piping Division*, 5:335–343, 2010.

[132] Y Prawoto, A Moin, M Tadjuddin, and W B Wan Nik. Effect of microstructures on SCC of steel: Field failure analysis case study and laboratory test result. *Engineering Fracture Mechanics*, 18:1858 – 1866, 2011.

[133] http://www.astm.org/Standards/G49.htm, Accessed: May 2012.

[134] http://www.astm.org/Standards/G129.htm, Accessed: May 2012.

[135] http://www.matelect.com/files/download/stressapp.pdf, Accessed: August 2012.

[136] P L Andresen, P W Emigh, M M Morra, and J Hickling. Effects of PWR primary water chemistry and deaerated water on SCC. In T R Allen, P J King, and L Nelson, editors, *Proceedings of the 12th International Conference on Environmental Degradation of Materials in Nuclear Power System Water Reactors* , Paper 74, 2005.

[137] P L Andresen. Critical Processes to Model in Predicting SCC Response in Hot Water. In *CORROSION 2005, April 3 - 7, 2005 , Houston (TX),*. NACE International, Paper ID: 05470,2005.

[138] P L Andresen and M M Morra. IGSCC of non-sensitised stainless steels in high temperature water. *Journal of Nuclear Materials*, 383:97–111, 2008.

[139] K Arioka, T Yamada, T Terachi, and Miyamoto T. Dependence of stress corrosion cracking for cold-worked stainless steel on temperature and potential, and role of diffusion of vacancies at crack tips. *Corrosion*, 64 (9):691–706, 2008.

[140] P.L. Andresen, K. Gott, and J.L. Nelson. Stress corrosion cracking of sensitized type 304 stainless steel in 288c water: A five laboratory round robin. pages 423–433, 1999. cited By (since 1996) 12.

[141] D.H. Lister, R.D. Davidson, and E. McAlpine. The mechanism and kinetics of corrosion product release from stainless steel in lithiated high temperature water. *Corrosion Science*, 27(2):113 – 140, 1987.

[142] J Robertson. The Mechanism of High Temperature Aqueous Corrosion of Stainless Steels. *Corrosion Science*, 32:443 – 465, 1991.

[143] S Lozano-Perez, M R Kilburn, T Yamada, T Terachi, C A English, and C R M Grovenor. High-Resolution Imaging of Complex Crack Chemistry in Reactor Steels by NanoSIMS. *Journal of Nuclear Materials*, 374:61 – 68, 2008.

[144] R M Langford and A K Petford-Long. Preparation of Transmission Electron Microscopy Cross-Section Specimens using Focussed Ion Beam Milling. *Journal of Vacuum Science and Technology*, A 19(5):2186 – 2193, 2001.

[145] V G M Sivel, J van den Brand, W R Wang, H Mohdadi, F D Tichelaar, P F A Alkemade, and H W Zandbergen. Application of the Dual-Beam FIB/SEM to Metals Research. *Journal of Microscopy*, 214:237 – 245, 2004.

[146] S Lozano-Perez. A Guide on FIB Preparation of Samples containing Stress Corrosion Crack Tip for TEM and Atom-Probe Analysis. *Micron*, 39:320 – 328, 2008.

[147] M K Miller, K F Russell, and G B Thompson. Strategies for fabricating atom probe specimens with a dual beam FIB. *Ultramicroscopy*, 102:287 – 298, 2005.

[148] D Hudson, N Ni, S Lozano-Perez, D Saxey, C English, G D W Smith, J Sykes, and C Grovenor. The Atomic Scale Structure and Chemistry of the Zircaloy-4 Metal-Oxide Interface. In *14th International Conference of Environmental Degradation of Materials in Nuclear Power Systems*, 2:1407-1418, 2009.

[149] K Thompson, D Lawrence, D J Larson, J D Olson, T F Kelly, and B Gorman. In situ site-specifi specimen preparation for atom probe tomography. *Ultramicroscopy*, 107:131 – 139, 2007.

[150] T Saito, H Masaki, F A Mukhlis, H Tsuchiya, and S Fujimoto. Crystallographic Characterization of Stress Corrosion Cracking Initiation on Type316L Stainless Steel in High Temperature and High Pressure Water. *Journal of Physics: Conference Series*, 165:1 – 4, 2009.

[151] A J Wilkinson, G Meaden, and D J Dingley. High-resolution elastic strain measurement from electron backscatter diffraction patterns: New levels of sesitivity. *Ultramicroscopy*, 106:307 – 313, 2006.

[152] A J Wilkinson, G Meaden, and D J Dingley. High resolution mapping of strains and rotations using electron backscatter diffraction. *Materials Science and Technology*, 22:1271 – 1278, 2006.

[153] G M Scamans and P R Swann. High Voltage Electron Metallography of Stress Corrosion Cracking of Austenitic Stainless Steels. *Corrosion Science*, 18:983 – 995, 1978.

[154] A Cigada, B Mazza, P Pedeferri, G Salvago, D Sinigaglia, and G Zanini. Stress corrosion cracking of cold-worked austenitic stainless steel. *Corrosion Science*, 22:559–578, 1982.

[155] W J Nisbet, G W Lorimer, and R C Newman. A transmission electron microscopy study of stress corrosion cracking in stainless steels. *Corrosion Science*, 35:457 – 469, 1993.

[156] M T Thomas, D R Baer, R H Jones, and S M Bruemmer. Sulfur and Oxygen Chemistry at Free Surfaces and Grain Boundaries of Iron Alloys. *Journal of Vacuum Science and Technology*, 17:25 – 29, 1980.

[157] L E Thomas and S M Bruemmer. High-Resolution Characterization of Intergranular Attack and Stress Corrosion Cracking of Alloy. *Corrosion*, 56:572 – 578, 2000.

[158] L E Thomas, V Y Gertsman, and S M Bruemmer. Crack-Tip Microstructures and Impurities in Stress Corrosion Cracked Alloy 600 from Recirculating and Once Through Steam Generators. In *Proceedings of the 10th International Conference on Environmental Degradation of Materials in Nuclear Power Systems - Water Reactors*, Paper 117, 2002.

[159] Y Takeda, T Shoji, M Bojinov, P Kinnunen, and T Saario. In Situ and Ex Situ Characterization of Oxide Films Formed on Strained Stainless Steel Surfaces in High-Temperature Water. *Applied Surface Science*, 252:8580 – 8588, 2006. l.

[160] B Beverskog, M Bojinov, A Englund, P Kinnunen, T Laitinen, K Mäkelä, T Saario, and P Sirkiä. A mixed-conduction model for oxide films on Fe, Cr and FeCr alloys in high-temperature aqueous electrolytesI. Comparison of the electrochemical behaviour at room temperature and at 200 °C. *Corrosion Science*, 44:1901 – 1921, 2002.

[161] B Beverskog, M Bojinov, P Kinnunen, T Laitinen, K Mäkelä, and T Saario. A mixed-conduction model for oxide films on Fe, Cr and FeCr alloys in high-temperature aqueous electrolytesII. Adaptation and justification of the model. *Corrosion Science*, 44:1923 – 1940, 2002.

[162] I Betova, M Bojinov, P Kinnunen, K Mkel, and T Saario. Conduction mechanism in oxide films on ferrous alloys studied by impedance spectroscopy in symmetrical and asymmetrical configurations. *Journal of Electroanalytical Chemistry*, 572:211 – 223, 2004.

[163] S Lozano-Perez, M Schröder, T Yamada, T Terachi, C A English, and C R M Grovenor. Using NanoSIMS to map trace elements in stainless steels from nuclear reactors. *Applied Surface Science*, 255:1541–1543, 2008.

[164] S Lozano-Perez. Novel characterization of stress corrosion cracks. *Journal of Physics Conference Series*, 126:012078, 2008.

[165] A Cerezo, P H Clifton, M J Galtrey, C J Humphreys, T F Kelly, D J Larsonc, S Lozano-Perez, E A Marquis, R A Oliver, G Sha, K Thompson, M Zandbergen, and R L Alvisc. Atom probe tomography today. *MaterialsToday*, 12:36 – 42, 2007.

[166] M Bachhav, R Danoix, F Danoix, B Hannoyer, S Ogale, and F Vurpillot. Investigation of wüstite ($Fe_{1-x}O$) by femptosecond laser assisted atom probe tomography. *Ultramicroscopy*, 111:584–588, 2010.

[167] M N Bachhav, R Danoix, F Vurpillot, B Hannoyer, S B Ogale, and F Danoix. Evidence of lateral heat transfer during laser assisted atom probe tomography analysis of large band gap materials. *Applied Physics Letters*, 99, 2011.

[168] M Bachhav. Private communication.

[169] D W Saxey. Correlated ion analysis and the interpretation of atom probe mass spectra. *Ultramicroscopy*, 111:473 – 479, 2011.

[170] C A Williams. *Atomic scale characterisation of ODS steels for fusion applications.* PhD thesis, University of Oxford, 2011.

[171] L Viskari and K Stiller. Oxygen influenced intergranular crack propagation: Microstructure and chemistry in the crack tip region. *Presentation at the 8th International Conferenceon the Microscopy of Oxidation, 11-13 April 2011 University of Liverpool, United Kingdom*, 2011.

[172] V Y Gertsman and S M Bruemmer. Study of Grain Boundary Character along Intergranular Stress Corrosion Crack Paths in Austenitic Alloys. *Acta Materialia*, 49:1589 – 1898, 2001.

[173] V Randle. The coincidence site lattice and the 'sigma enigma'. *Materials Characterization*, 47(5):411 – 416, 2001.

[174] T Watanabe. An approach to grain boundary design for strong and ductile polycrystals. *Mechanica*, 11:47, 1984.

[175] V Randle and B Ralph. A practical approach to the determination of the crystallography of grain boundaries. *Journal of Materials Science*, 21:3823–3828, 1986.

[176] V Randle and R More. *The Role of Coincidence Site Lattices in Grain Boundary Engineering.* Woodhead Pub Ltd, 1996.

[177] D C Crawford and G S Was. The Role of Grain Boundary Misorientation in Intergranular Cracking of Ni-16Cr-9Fe in 360°C Argon and High-Purity Water. *Metallurgical Transactions A*, 23A:1195–1206, 1992.

[178] V Y Gertsman, K Tangri, and R Z Valiev. On the Grain Boundary Statistics in Metals and Alloys Susceptible to Annealing Twinning. *Acta Metallurgica and Materialia*, 42:1785–1804, 1994.

[179] Y Pan, B L Adams, T Olson, and N Panayotou. Grain boundary structure effects on Intergranular Stress Corrosion Cracking of Alloy X-750. *Acta Materialia*, 44:4685 – 4695, 1996.

[180] M Vankeerberghen and S Gavrilov. Experimental measurements and numerical simulations to evaluate the electrode kinetics for 316 stainless steel under PWR-relevant conditions. *Journal of Nuclear Materials*, 377:331 – 339, 2008.

[181] K Arioka, T Yamada, T Terachi, and R W Staehle. Intergranular Stress Corrosion Cracking Behavior of Austenitic Stainless Steels in Hydrogenated High-Temperature Water. *Corrosion*, 62:74 – 83, 2006.

[182] R W Staehle. Presentation: Predicting the scc of reactor components from first principles– quantitative micro-nano based prediction (qmn) challenges and approach. *INSS Project Meeting*, 2010.

[183] E Brüche. 25 Jahre Elektronenmikroskop. *Die Naturwissenschaften*, 23:601 – 610, 1957.

[184] http://www.nobelprize.org/, Accessed: May 2012.

[185] M von Ardenne. Das Elektronen-Rastermikroskop. *Zeitschrift für Physik*, 109:37 – 57, 1938.

[186] T E Everton. Persistence pays off: Sir Charles Oatley and the Scanning Electron Microscope. *Journal of Vacuum Science and Technology B*, 14:3620 – 3624, 1996.

[187] A J Wilkinson, G Meaden, and D J Dingley. Mapping strains at the nanoscale using electron back scatter diffraction. *Superlattices and Microstructures*, 45:285 – 294, 2009.

[188] A J Wilkinson and D Randman. Determination of elastic strain fields and geometrically necessary dislocation distributions near nanoindents using electron back scatter diffraction. *Philosophical Magazine*, 90:1159–1177, 2010.

[189] A Wagner. Applications of Focused Ion Beams to Microlithography. *Solid State Technology*, 26:97–103, 1983.

[190] D B Williams and C B Carter. *Transmission Electron Microscopy: A Textbook for Materials Science*. Springer, 2005 (1996).

[191] M Varela, A R Lupini, K van Benthem, A Y Borisevich, M F Chisholm, N Shibata, E Abe, and S J Pennycook. Materials Characterization in the Aberration-Corrected Scanning Transmission Electron Microscope. *Annu. Rev. Mater. Res.*, 35:539 – 569, 2005.

[192] P Trebbia and N Bonnet. EELS elemental mapping with unconventional methods I. Theoretical basis: image analysis with multivariate statistics and entropy concepts. *Ultramicroscopy*, 34:179 – 203, 1990.

[193] X Hu, Y Sun, and J Yuan. Multivariate statistical analysis of electron energy-loss spectroscopy in anisotropic materials. *Ultramicroscopy*, 108:465 – 471, 2008.

[194] C C Ahn and O L Krivanek. *EELS Atlas*. ASU HREM facility and GATAN, 1983.

[195] E W Müller. Das Feldionenmikroskop. *Zeitschrift für Physik*, 131:136 – 142, 1951.

[196] M Drechsler. Erwin Müller and the early development of field emission microscopy. *Surface science*, 70:1 – 18, 1978.

[197] E W Müller. *Zeitschrift für technische Physik*, 17:412, 1936.

[198] E W Müller. Feldemission. In *Ergebnisse der exakten Naturwissenschaften*, volume 27 of *Springer Tracts in Modern Physics*, pages 290 – 360. Springer Berlin / Heidelberg, 1953. 10.1007/BFb0110808.

[199] M K Miller. *Atom-probe Tomography : Analysis at the Atomic Level*. Kluwer Academic/ Plenum Publishes, 2000.

[200] A Cerezo, T J Godfrey, and G D W Smith. Application of a position-sensitive detector to atom-probe microananlysis. *Review of Scientific Instruments*, 59:862 – 866, 1988.

[201] T T Tsong, J H Block, M Nagasaka, and B Viswanathan. Photon stimulated field ionization. *The Journal of Chemical Analysis*, 65:2469 – 2470, 1976.

[202] T F Kelly, V Patrick, P P Camus, D J Larson, and L M Holzman S S Bajikar. On the many advantages of local-electrode atom probes. *Ultramicroscopy*, 62:29 – 42, 1996.

[203] T F Kelly, P P Camus, D J Larson, L M Holzman, and S S Bajikar. Us patent 5,440,124, 1995.

[204] IMAGO Scientific Instruments, 5500 Nobel Drive, Madison WI 53711. *IMAGO Scientific Instruments user Manual LEAP3000X HR.*

[205] M K Miller, A Cerezo, M G Hetherington, and G D W Smith. *Atom Probe Field Ion Microscopy*, pages 447 – 451. Clarendon Press, Oxford, 1996.

[206] S Lozano-Perez, K Kruska, I Iyengar, T Terachi, and T Yamada. The role of cold work and applied stress on surface oxidation of 304 stainless steel. *Corrosion Science*, 56(0):78 – 85, 2012.

[207] J J Mor. *Lecture Notes in Mathematics*, chapter The LevenbergMarquardt algorithm: Implementation and theory, in numerical analysis, pages 105 – 116. Springer-Verlag, Berlin, 1977.

[208] R Bauch, M Cambini, P Weisgerber, C DeAsmundis, and C Plog. Investigations on Oxide Formed in High-Temperature Water on Austenitic Steel. *Journal of Nuclear Materials*, 92:334 – 344, 1980.

[209] J Robertson. The Mechanism of High Temperature Aqueous Corrosion of Steel. *Corrosion Science*, 29:1275 – 1291, 1989.

[210] C Deininger, R F Egerton, F Hofer, B Jouffrey, D Krahl, R D Leapman, J Mayer, H Rose, P Schattschneider, and J C H Spence. *Energy-Filtering Transmission Electron Microscopy (Springer Series in Optical Sciences)*. Springer, 1995.

[211] S Lozano-Perez, D Saxey, T Yamada, and T Terachi. Atom-Probe Tomography Characterization of the Oxidation of Stainless Steel. *Scripta Materialia*, 62:855 – 858, 2010.

[212] E Montoya, S Bals, M D Rossell, D Schryvers, and G Van Tendeloo. Evaluation of top, angle, and side cleaned fib samples for tem analysis. *Microscopy Research and Technique*, 70:1060 – 1071, 2007.

[213] S Schwarz, B Kempshall, L Giannuzzi, and M McCartney. Avoiding the Curtaining Effect: Backside Milling by FIB INLO. *Microscopy and Microanalysis*, 9:116–117, 2003.

[214] Y M Chen, T Ohkubo, M Kodzuka, K Morita, and K Hono. Laser-assisted atom probe analysis of zirconia/spinel nanocomposite ceramics. *Scripta Materialia*, 61:693 – 696, 2009.

[215] M Tsukada, H Tamura, K P McKenna, A L Shluger, Y M Chen, T Ohkubo, and K Hono. Mechanism of laser assisted field evaporation from insulating oxides. *Ultramicroscopy*, 111:567 – 570, 2011.

[216] *H Kreuzer at EUROMAT 2011, Montpellier in a comment to the presentation "Direct excitation mechanism of Laser Assisted Field Evaporation from Insulating Oxides" by M Tsukada.*, 2011.

[217] C-W Yang and D B Williams. A Revision of the Fe-Ni Phase Diagram at Low Temperatures (<400°C). *Journal of Phase Equilibria*, 17:522 – 531, 1996.

[218] D Woodhouse and J White. Phase relationships of iron-oxide-containingspinels. Part III. Further investigations on the systems Fe-Mg-O and Fe-Mg-Cr-O, and general relationships in the system Fe-Mg-Cr-Al-O. *Trans Br Ceram Soc*, 54:333 – 366, 1955.

[219] L Tan, X Ren, and T R Allen. Corrosion behavior of 912 % Cr ferritic – martensitic steels in supercritical water. *Corrosion Science*, 52:1520 – 1528, 2010.

[220] N K Das, K Suzuki, K Ogawa, and T Shoji. Early stage SCC initiation analysis of fcc Fe-Cr-Ni ternary alloy at 288 °C: A quantum chemical molecular dynamics approach. *Corrosion Science*, 51:908–913, 2009.

[221] D Cubicciotti. Potential-pH diagrams for alloy-water systems under LWR conditions. *Journal of Nuclear Materials*, 201:176–183, 1993.

[222] V Raghavan. Cr-Fe-Ni (Chromium-Iron-Nickel). *Journal of Phase Equilibria and Diffusion*, 30:94–95, 2009.

[223] P. Franke and H.J. Seifert. The influence of magnetic and chemical ordering on the phase diagram of crfeni. *Calphad*, 35:148 – 154, 2011.

[224] P Franke and H J Seifert, editors. *Binary Systems and Ternary Systems from C-Cr-Fe to Cr-Fe-W, Thermodynamic Properties of Inorganic Materials Compiled by SGTE, Subvolume C: Ternary Steel Systems, Phase Diagrams and Phase Transition Data.* Landolt-Brnstein: Numerical Data and Functional Relationships in Science and Technology - New Series. Springer, 2012.

[225] N Saunders and A P Miodownik. *CALPHAD (Calculation of Phase Diagrams): A Comprehensive Guide.* Elsevier, 1998.

[226] C M Schillmoller and MR Jasner. High performance alloys for offshore platform piping. *Materials Performance*, 23:45–53, 1984.

[227] G.S. Was and S.M. Bruemmer. Effects of irradiation on intergranular stress corrosion cracking. *Journal of Nuclear Materials*, 216(0):326 – 347, 1994.

[228] H Masuda. SKFM observation of SCC on SUS304 stainless steel. *Corrosion Science*, 49:120 – 129, 2007.

[229] T Onchi, K Dohi, N Soneda, J.R Cowan, R.J Scowen, and M.L Castao. Fractographic and microstructural characterization of irradiated 304 stainless steel intergranularly fractured in inert gas. *Journal of Nuclear Materials*, 320(3):194 – 208, 2003.

[230] D Cubicciotti and L Ljungberg. The Pourbaix Diagram for Cr With Fe and Stress Corrosion Cracking of Stainless Steel. *Journal of the Elctrochemical Society*, 132:987–988, 1985.

[231] R A Langley. Hydrogen trapping, diffusion and recombination in austenitic stainless steels. *Journal of Nuclear Materials*, 128129:622 – 628, 1984.

[232] Yoji Mine and Takashi Kimoto. Hydrogen uptake in austenitic stainless steels by exposure to gaseous hydrogen and its effect on tensile deformation. *Corrosion Science*, 53(8):2619 – 2629, 2011.

[233] Su-Il Pyun and R.A. Oriani. The permeation of hydrogen through the passivating films on iron and nickel. *Corrosion Science*, 29(5):485 – 496, 1989.

[234] J von Pezold, L Lymperakis, and J Neugebeauer. Hydrogen-enhanced local plasticity at dilute bulk H concentrations: The role of HH interactions and the formation of local hydrides. *Acta Materialia*, 59:2969 – 2980, 2011.

[235] Y Fukai. Formation of superabundant vacancies in MH alloys and some of its consequences: a review. *Journal of Alloys and Compounds*, 356357:263 – 269, 2003.

[236] Y Fukai and H Sugimoto. Formation mechanism of defect metal hydrides containing superabundant vacancies. *Journal of Physics: Condensed Matter*, 19:436201, 2007.

[237] L E Thomas and S M Bruemmer. Microstructural and Microchemical Characterization of Intergranular Stress Corrosion Cracks in Irradiated Type 304SS Removed from a BWR Top Guide. In *11th Int. Conf. Environmental Degradation of Materials in Nuclear Systems, Stevenson, WA, Aug. 10-14,*, pages 1049 – 1061, 2003.

[238] K Arioka, T Yamada, T Terachi, and Chiba G. Cold Work and Temperature Dependence of Stress Corrosion Crack Growth of Austenitic Stainless Steels in Hydrogenated and Oxygenated High- Temperature Water. *Corrosion*, 63, No. 12:1114 – 1123, 2007.

[239] T Terachi, T Yamada, T Miyamoto, K Arioka, and K Fokuya. Corrosion Behavior of Stainless Steels in Simulated PWR Primary Water —Effect of Chromium Content in Alloys and Dissolved Hydrogen—. *Journal of Nuclear Science and Technology*, 45:975–984, 2008.

[240] S M Bruemmer and L E Thomas. High-Resolution Analytical Electron Microscopy Characterization of Corrosion and Cracking at buried Interfaces. *Surface and Interface Analysis*, 31:571 – 581, 2001.

[241] *ASM Metals Handbook Volume 02: Properties and Selection: Nonferrous Alloys and Special-Purpose Materials*, chapter Nickel and Nickel Alloys, page 438. ASM International, 1990.

[242] *ASM Metals Handbook Volume 1: Properties and Selection: Irons, Steels, and High-Performance Alloys*, chapter Wrought Stainless Steels, page 854. ASM International, 1990.

[243] T Terachi, T Yamada, K Arioka, and S Lozano-Perez. Role of Corrosion in LPSCC of Fe-and Ni-Based Alloys. In B L Eyre and I Kimura, editors, *Proc. of Int. Conf. of Research for Aging Management of Light water reactors and its future trend*, Fukui, Japan, 2007.

[244] J. Hou, Q.J. Peng, K. Sakaguchi, Y. Takeda, J. Kuniya, and T. Shoji. Effect of hydrogen in inconel alloy 600 on corrosion in high temperature oxygenated water. *Corrosion Science*, 52(3):1098 – 1101, 2010.

[245] W T Geng, A J Freeman, R Wu, C B Geller, and J E Raynolds. Embrittling and strengthening effects of hydrogen, boron, and phosphorus on a $\Sigma 5$ nickel grain boundary. *Phys. Rev. B*, 60:7149–7155, 1999.

[246] M Hashimoto, Y Ishida, S Wakayama, R Yamamoto, M Doyama, and T Fujiwara. Atomistic studies of grain boundary segregation in Fe-P and Fe-B alloysII. Electronic structure and intergranular embrittlement. *Acta Metallurgica*, 32:13 – 20, 1984.

[247] N Totsuka. Private communication at INSS February 2011.

[248] *ASM Metals Handbook Volume 02: Properties and Selection: Nonferrous Alloys and Special-Purpose Materials*, chapter Nickel and Nickel Alloys, page 430. ASM International, 1990.

[249] T B Britton. *A High Resolution Electron Backscatter Diffraction Study of Titanium and its Alloys*. PhD thesis, University of Oxford, 2010.

[250] A Benninghoven, F G Rudenauer, and H W Werner. *Secondary ion mass spectrometry: basic concepts, instrumental aspects, applications and trends*. John Wiley and Sons,New York, NY, 1987.

[251] J C Vickerman, N M Reed, and A Brown. *Secondary Ion Mass Spectroscopy: Principles and Applications (Retroactive Coverage)*. Oxford University Press, 1989.

[252] R G Wilson, F A Stevie, and C W Magee. *Secondary ion mass spectrometry: A practical handbook for depth profiling and bulk impurity analysis*. Wiley (New York), 1989.

[253] P L Andresen, T M Angeliu, W R Catlin, L M Young, and R M Horn. Effect of Deformation on SCC of Unsensitized Stainless Steels. *CORROSION 2000 (Houston, TX: NACE International)*, Paper No. 203, 2000.

[254] http://www.sciencedirect.com, Accessed: May 2012.